

**LATTICE MODELING OF ULTRASONIC
NONDESTRUCTIVE EVALUATION OF ATTENUATING
MATERIALS**

by

Anton F. Thomas

B.S., Mechanical Engineering
Florida Agricultural and Mechanical University (1999)

S.M., Mechanical Engineering
Massachusetts Institute of Technology (2002)

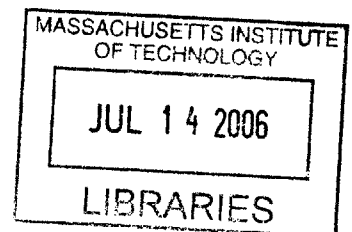
Submitted to the Department of Mechanical Engineering in partial fulfillment of the
requirements for the degree of

DOCTOR OF PHILOSOPHY IN MECHANICAL ENGINEERING

at the

Massachusetts Institute of Technology

June 2006



© 2006, Massachusetts Institute of Technology. All rights reserved.

BARKER

Signature of Author: _____
Department of Mechanical Engineering
March 21, 2006

Certified by: _____
James H. Williams, Jr.
SEPT Professor of Engineering
Professor of Writing and Humanistic Studies
Thesis Supervisor

Accepted by: _____
Lallit Anand
Professor of Mechanical Engineering
Departmental Committee on Graduate Studies



Room 14-0551
77 Massachusetts Avenue
Cambridge, MA 02139
Ph: 617.253.2800
Email: docs@mit.edu
<http://libraries.mit.edu/docs>

DISCLAIMER OF QUALITY

Due to the condition of the original material, there are unavoidable flaws in this reproduction. We have made every effort possible to provide you with the best copy available. If you are dissatisfied with this product and find it unusable, please contact Document Services as soon as possible.

Thank you.

The images contained in this document are of the best quality available.

Lattice Modeling of Ultrasonic Nondestructive Evaluation of Attenuating Materials

by

Anton F. Thomas

Submitted to the Department of Mechanical Engineering on March 21, 2006 in partial fulfillment of the requirements for the degree of Doctor of Philosophy in Mechanical Engineering

ABSTRACT

Theoretical predictions of specific strength and specific stiffness of nanocomposites make them attractive replacements for alloys and fiber reinforced composites in future generations of numerous structures. The reliable and safe utilization of nanocomposites will require their periodic characterization with nondestructive evaluation. When subjected to ultrasonic waves, nanocomposites often exhibit attenuation that is an order of magnitude higher than that of carbon fiber reinforced polymeric composites. Thus, an accurate model of ultrasonic wave propagation in nanocomposites as well as several other modern composites must include attenuation.

Lattice modeling is a heuristic approach that consists of the discretization of solids into regularly spaced particles interconnected via nearest-neighbor interactions. For example, the mass-spring-lattice model (MSLM), a lattice model for the simulation and visualization of elastic wave propagation, has been used in favor of other finite-difference and finite-element methods due to its straightforward implementation of boundary conditions and relatively inexpensive explicit numerical integration.

Its utility notwithstanding, MSLM discretization produces documented, yet previously unresolved and uncharacterized, numerical errors. In addressing errors associated with numerical anisotropy and surface wave propagation, two main points are revealed. (1) For isotropic materials having a Poisson's ratio less than 0.4, 20 grid spaces per shear wavelength are required to ensure phase speed errors of less than 1%. (2) For precise implementation of MSLM traction boundaries, correction terms are formulated.

Further, the MSLM is not capable of modeling ultrasonic wave propagation in nanocomposites and many thick composites, polymers, and nanocrystalline metals, in part, because of the associated losses due to attenuation. The mass-spring-dashpot lattice model (MSDLM) is therefore formulated to simulate and visualize wave phenomena in attenuating, viscoelastic media. Via the dispersion relations for a standard linear solid, the MSDLM spring and dashpot constants are set to match the corresponding wave propagation phase speeds and attenuation. The convergence, stability, and accuracy criteria for the MSDLM are presented for one and two-dimensional models. Additional verification is provided through numerical examples and comparisons with known solutions.

The homogenization of the elastic and viscoelastic mechanical properties of the nanocomposite constituents is implied in the use of the MSDLM. Assuming the characteristic wavelength is much larger than the characteristic length scale of the interrogated nanocomposite phases, interaction of ultrasonic waves with nanometer constituents is captured by the inherent, frequency-dependent attenuation.

To illustrate a practical application of lattice modeling, mass-spring-dashpot lattice models for the ultrasonic nondestructive evaluation of an attenuating nanocomposite containing subsurface cracks are developed. Full-field wave propagation simulations of these models as well as the corresponding model of a pristine nanocomposite are conducted, and their relative surface displacements are presented. These relative surface displacements of the cracked and pristine models reveal guidelines for the identification of subsurface cracks in nanocomposites and other attenuating materials.

Thesis Committee:

Professor James H. Williams, Jr.: Committee Chairman, Department of Mechanical Engineering and Program in Writing and Humanistic Studies, MIT

Professor Kenneth R. Manning: Program in Writing and Humanistic Studies, MIT

Professor Hyunjune Yim: Department of Mechanical & System Design Engineering, Hongik University, Korea

ACKNOWLEDGMENTS

For I know the thoughts that I think toward you, saith the Lord, thoughts of peace, and not of evil, to give you an expected end.

Jeremiah 29:11 (KJV)

I would first like to thank my Lord and Savior Jesus Christ for His provision, blessings, and mercy. When I reflect upon the physical, spiritual and mental journey that I have traveled, it becomes clearer that God's guidance and His placement of special people in my life have permitted me to achieve goals that I would have never thought possible. The completion of this thesis, being the culmination of years of formal education, has been made possible, in part, by those special people—the family, teachers, friends, mentors, administrators and educators—who have touched the course of my life. For the remainder of this section, I would like to acknowledge them in a somewhat unorthodox semi-autobiographical manner.

I am extremely grateful to my parents and first teachers, Mr. William L. Thomas and Mrs. Jacqueline M. Thomas, for their love, encouragement, and instillation of principles for success. My older brothers, Mr. Amman T. Thomas and Mr. Alexi C. Thomas, provided excellent examples for me and became trusted confidants as we approached adulthood.

I would like to acknowledge a few extraordinary primary and secondary educators and administrators: Mrs. Gulosh of High Horizons School (Bridgeport, CT); Mrs. Brown and Mr. McCoy of Baypoint Middle School (St. Petersburg, FL); and Mrs. Diane Church-Smith, Mrs. Jansen, Mr. Launchy, Miss McGarvey, Mr. Oberg and Mr. Watson of Lakewood High School and the Center for Advanced Technologies (St. Petersburg, FL).

I will always have fond memories of life as an undergraduate student at Florida Agricultural & Mechanical University (FAMU) in Tallahassee, FL. I am grateful to the visionary former president of FAMU, Dr. Frederick S. Humphries, for establishing the "Life-Gets-Better" Scholarship, and the accompanying sponsorship of Michelin North America. I was fortunate to establish bonds with FAMU faculty members Dr. Mario Encinosa, Dr. Author G.O. Mutambara and especially Dr. Frederick J. Foreman, who introduced me to the subject of applied mechanics. The summer internship supervision of Mr. Jack Anderson, Mrs. Judy Moss, Mr. Daniel Williamson (Michelin North America) and Dr. Dan Chen (3M Company) is gratefully acknowledged as an important aspect of my education. I am also thankful for the friendship and support of several FAMU alums, especially Mr. Aubrey J. Rembert and Mr. Mathieu A. Thames.

I am deeply indebted to my MIT thesis advisor, Professor James H. Williams, Jr., who possesses a unique combination of precise communication, engineering competency, and educational engagement. He once said that students "are less like buckets to be filled than rockets to be lit." Well, I feel as if I am accelerating toward *warp* speed. I thank him for his mentorship, guidance and patience.

I am also grateful to the other members of my thesis committee, Professor Kenneth R. Manning and Professor Hyunjune Yim (Hongik University, Korea), for their technical support and thoughtful advice.

I am grateful to the members of the Composite Materials and Nondestructive Evaluation Laboratory: Dr. Liang-Wu Cai, LCDR Peter D. Small and LT Marianne Holt-

Pheonix. Additionally, Professor Klaus-Jürgen Bathe, Dr. Irfan Biag, Professor Jiame Peraire, and Dr. Per-Olof Persson are gratefully acknowledged for their technical assistance.

I am also thankful for the following individuals and institutions for their generous financial support of my graduate studies: 3M Company, Ford Motor Company, Dean Isaac Colbert of the MIT Graduate Students Office, The MIT Provost Office, Dean Thomas L. Magnanti and Dean Donna R. Savicki of the MIT College of Engineering, and Mrs. Dorothy Lemelson, Chair of the Lemelson Foundation.

I would like to acknowledge various members of the MIT community who have supported me during my years on campus: Dean Blanche E. Staton, former Dean Roy A. Charles, and Dean Christopher M. Jones of the MIT Graduate Students Office; Mrs. Deborah Alibrandi; Mrs. Kimberly G. Bonnette (Waters); Dr. Louis Defrate and Mrs. Marisa Defrate; Mr. Craig Forest and Mrs. Laura Forest; Ms. Yvonne Gittens; Mr. Lael S. Hebert; Mr. Reginald Hutchinson; Mr. Julius Korley and Dr. Lashanda James-Korley; Dr. Michael Johnson; Dr. LaRuth McAfee; Mr. Ivan Skopovi; Mr. Byron Stancil and the other members of the Black Graduate Student Association.

I am grateful to the Worldwide Church of God congregations in Meriden, CT and Pinellas County, FL; Pastor John M. Borders III of Morning Star Baptist Church (Mattapan, MA); and especially to my church family at Heritage Park Baptist Church (Burlington, MA) led by Pastor Curt Wiedenroth.

I am thankful to my extended family across the country for their support and prayers: the Thomas Family of St. Petersburg, FL, the Larry Family of Tampa, FL, the Thomas/Stanford Family of Orlando/Jacksonville FL, the Thomas/Bell Family of Baltimore County, MD, the Thomas Family of Bridgeport, CT, The Coote/Thomas Family of Marietta, GA, the Jones/Muhajir Family of Washington, DC, and the Johnson Family of Vallejo, CA.

I am so grateful for the love and support of my beautiful daughters, Miss Ayren J. Thomas and Miss Avery L. Thomas, with their beaming faces in the morning and eager inquisitiveness in the evening.

Finally, I can not easily express in words what my wife's support, confidence, advice, motivation, and love have meant to me through these years. So I will simply state that it is to her, Mrs. Jocelyn L. Thomas, that I dedicate this thesis.

To Jocelyn

TABLE OF CONTENTS

Abstract

Acknowledgments

Dedication

Table of Contents

1	Thesis Introduction	11
1-1	Introduction.....	13
1-2	Thesis Organization.....	14
2	Numerical Accuracy of Mass-Spring-Lattice Model	17
2-1	Introduction.....	19
2-2	MSLM Phase Speed Error.....	20
	2-2.1 Continuum.....	20
	2-2.2 MSLM Discretization.....	21
2-3	MSLM Traction Boundary Conditions.....	29
	2-3.1 One-Dimensional MSLM.....	29
	2-3.2 Two-Dimensional MSLM.....	30
	2-3.3 Numerical Example.....	35
	2-3.4 Interface of Dissimilar Materials.....	37
2-4	Conclusions.....	41
2A	Force and Constitutive Expressions for Traction Boundary Conditions.....	42
2B	Lamb's Problem.....	43
2C	Force and Constitutive Expressions for Interface of Dissimilar Materials...	48
3	Formulation of Mass-Spring-Dashpot Lattice Model	51
3-1	Introduction.....	53
3-2	Analytical Model.....	53
	3-2.1 Stress-Dynamic Equations.....	53
	3-2.2 Dispersion Relations.....	55
3-3	Numerical Discretization.....	59
	3-3.1 One-Dimensional MSDLM.....	59
	3-3.2 Two-Dimensional MSDLM.....	62
3-4	Numerical Examples.....	68
	3-4.1 Material Properties.....	68
	3-4.2 One-Dimensional Examples.....	68
	3-4.3 Two-Dimensional Examples.....	71
3-5	Conclusions.....	79
3A	Derivation of Stress-Dynamic Equations and Dispersion Relations for Standard Linear Solid Having Single Relaxation Time.....	81
3B	Four Stage Runge-Kutta Method.....	91

3C	Convergence and Accuracy Criteria for the Mass-Spring-Dashpot Lattice Model.....	93
3D	Two-Dimensional MSDLM Schematic and Stress Dynamic Equations for Longitudinal Interface of Dissimilar Materials.....	129
3E	Steady-State Wave Propagation in One and Two-Dimensional Standard Linear Solids	132
3F	Absorbing Boundaries for Mass-Spring-Dashpot Lattice Model.....	147
4	Ultrasonic Nondestructive Evaluation of Subsurface Cracks in an Attenuating Nanocomposite.....	155
4-1	Introduction.....	157
4-2	Analytical Model.....	159
4-3	Numerical Discretization.....	162
	4-3.1 Mass-Spring-Dashpot Lattice Model.....	162
	4-3.2 Verification.....	163
4-4	Normalized Parameters.....	166
4-5	Material and Interrogation Parameters.....	167
4-6	Displacement Field.....	169
4-7	Required Detection Resolution.....	169
4-8	Initial Relative Surface Disturbance.....	172
4-9	Transient Relative Surface Disturbance.....	176
4-10	Conclusions.....	178
4A	MSDLM Discretizations at Various Boundary and Interaction Conditions.	180
4B	Asymptotic and Numerical Analysis of Scattering and Diffraction of an Incident Longitudinal Wave by a Semi-Infinite Crack.....	190
4C	Spectral Analysis of Transient Relative Vertical Surface Displacement.....	200
5	Thesis Conclusion.....	205
5-1	Summary of Achievements.....	207
5-2	Recommendations.....	207

CHAPTER 1: THESIS INTRODUCTION

CONTENTS:

1-1	Introduction.....	13
1-2	Thesis Organization.....	14

1-1 INTRODUCTION

Modern composites consist of a matrix (generally polymer, metal, or ceramic) and reinforcement (generally fibers, platelets, or spheroids) that are combined to produce materials having mechanical properties tailored for specific applications. Substandard fabrication procedures, environmental exposure, and handling or service deterioration can affect their mechanical properties without effect on their visual appearance.

Because composite components are subjected to increasingly demanding structural requirements, their periodic characterization by various nondestructive evaluation (NDE) techniques is an important aspect of ensuring their reliable performance. In ultrasonic NDE, prescribed time-dependent waves are propagated through the interrogated structure. Due to reflections, scattering, and absorption of these waves, output surface tractions and/or displacements can be detected, and ideally related to deterioration or inherent characteristics of the component.

Theoretical predications for the specific strength and specific stiffness of nanocomposites make this novel class of materials attractive replacements for alloys and modern fiber reinforced composites in a variety of future structures. When subjected to ultrasonic waves, nanocomposites often exhibit attenuation that is an *order of magnitude* higher than that of modern carbon fiber reinforced composites. Thus, an accurate model of ultrasonic wave propagation in nanocomposites must include attenuation.

Numerical methods can provide a powerful tool for simulating ultrasonic waves. The mass-spring lattice model (MSLM), for instance, has been used for modeling, simulating and visualizing elastic wave phenomena by discretizing a material into an assemblage of particles interconnected with springs [1-1 through 1-4]. However, there are unresolved and uncharacterized errors associated with MSLM discretization [1-5, 1-6].

Furthermore, the MSLM is *not* capable of modeling ultrasonics in nanocomposites, largely, because of the associated losses due to attenuation [1-7,1-8].

The objectives of this thesis are summarized in the following four steps.

1. The investigation of the numerical convergence of phase speed and the consistency of traction boundaries in the MSLM.

2. The development of a computational model for simulating broadband ultrasonic wave propagation in highly attenuating media.
3. The presentation of visual simulations of the propagation, scattering and reflection of waves in nanocomposite materials and structures, having both reflecting and absorbing boundaries.
4. The generation of parametric input-output ultrasonic wave spectra due to the presence of overt flaws in nanocomposites and attenuating materials.

1-2 THESIS ORGANIZATION

The thesis is organized into five chapters.

Chapter 1 describes the motivation, outlines the objectives, and describes the organization of the thesis.

Chapter 2 begins by reviewing the historical evolution of the MSLM and describes numerical errors associated with MSLM discretization. It explores the numerical phase speed error for plane waves and offers discretization guidelines on the required number of grid spaces per wavelength. Furthermore, correction terms to precisely implement traction-boundary conditions are formulated and verified.

Chapter 3 formulates the mass-spring-dashpot lattice model (MSDLM) for the simulation and visualization wave phenomena in attenuating viscoelastic media. The exact dispersion relations of a standard linear solid model are presented and rigorous convergence analyses on the corresponding discretization is investigated. Several numerical examples are presented as verification.

In *Chapter 4*, the MSDLM is applied to the modeling of ultrasonic NDE of an attenuating nanocomposite containing subsurface cracks. The full-field displacement field of scattering in the vicinity of horizontal and vertical cracks in an attenuating nanocomposite half-space is explored. Relative surface displacements of the cracked and pristine models reveal guidelines for the identification of subsurface cracks.

Chapter 5 outlines the contributions of the thesis.

References:

- 1-1. K. Harumi, T. Igarashi and T. Saito. *J. Nondestr. Test. Jpn.* **27**: 807 (1978).
- 1-2. J.H. Williams, Jr. *Fundamentals of Applied Dynamics*, pp.717-718. John Wiley & Sons, New York (1996).
- 1-3. H. Yim and Y. Choi. *Mater. Eval.* **58**:889 (2000).
- 1-4. H. Yim and Y. Sohn. *IEEE Trans. Ultrason. Ferroelectr. Freq. Control.* **47**:549 (2000).
- 1-5. Y. Sohn and S. Krishnaswamy. *J. Acoust. Soc. Am.* **115**:172 (2004).
- 1-6. H. Yim and C.-J. Lee. *Review of Quantitative Nondestructive Evaluation*. D.O. Thompson and D.E. Chimenti (eds). **21**:152 (2002).
- 1-7. M.J. Lang, M. Duarte-Dominguez, R. Birringer, R. Hempelmann, H. Natter, and W. Arnold. *NanoStruct. Mater.* **12**:811 (1999).
- 1-8. Z. Bian, R.J. Wang, W.H. Wang, T. Zhang and A. Inoue. *Adv. Funct. Mater.* **14**:55 (2004).

CHAPTER 2: NUMERICAL ACCURACY OF MASS-SPRING-LATTICE MODEL

ABSTRACT: The mass-spring-lattice model (MSLM), a numerical model for the simulation of elastic wave propagation, discretizes an elastic solid into an assemblage of particles interconnected with extensional and rotational springs. The MSLM has been used in favor of other finite-element and finite-difference based methods because of its straight-forward application of boundary conditions and relatively inexpensive explicit numerical integration. However, various MSLM numerical errors have not been fully investigated. A convergence analysis reveals that, for isotropic materials having Poisson's ratio less than 0.4, 20 MSLM grid spaces per shear wavelength are required to ensure phase speed errors of less than 1%. As Poisson's ratio approaches the incompressible limit, the computational expense increases dramatically. Additionally, correction terms necessary for the precise implementation of MSLM traction boundaries are formulated and verified through a numerical example.

CONTENTS:

2-1	Introduction.....	19
2-2	MSLM Phase Speed Error.....	20
	2-2.1 Continuum.....	20
	2-2.2 MSLM Discretization.....	21
2-3	MSLM Traction Boundary Conditions.....	29
	2-3.1 One-Dimensional MSLM.....	29
	2-3.2 Two-Dimensional MSLM.....	30
	2-3.3 Numerical Example.....	35
	2-3.4 Interface of Dissimilar Materials.....	37
2-4	Conclusions.....	41
2A	Force and Constitutive Expressions for Traction Boundary Conditions.....	42
2B	Lamb's Problem.....	43
2C	Force and Constitutive Expressions for Interface of Dissimilar Materials...	48

NOMENCLATURE

Symbols

A	unit area	u, v	displacement
C	Courant number	U, V	Fourier transform of displacement
c	phase speed		
D	unit depth	Δt	numerical time step
F	force	ε	phase speed error
\mathbf{G}	amplification matrix	γ	Gaussian offset
g	extensional spring constant	η	rotational spring constant
h	numerical grid spacing	θ	angle with respect to horizontal
\hat{i}	imaginary number	κ	wavelength
i, j	indicial notation for grid position	λ, μ	Lamé constants
k	wavenumber	ν	Poisson's ratio
N	number of grid spaces per wavelength	π	ratio of circle's circumference to diameter
P	relating to longitudinal waves	ρ	density
Q	peak force per unit depth	σ_{ij}	stress tensor
R	applied force	ξ	eigenvalue of amplification matrix
S	relating to shear waves	ω	circular frequency

Subscripts

<i>center</i>	relating to center
<i>min</i>	relating to minimum
<i>P</i>	relating to longitudinal waves
<i>S</i>	relating to shear waves
<i>std.dev.</i>	relating to standard deviation

2-1 INTRODUCTION

Numerical methods can provide powerful tools for simulating ultrasonic waves. The mass-spring lattice model (MSLM), for instance, has been used for modeling, simulating and visualizing elastic wave phenomena by discretizing a material into an assemblage of particles interconnected with springs. This idea can be traced to Cauchy and Poisson in the 1840s though their models were incomplete [2-1]. The MSLM reemerged in the 1970s, and later extended in the 1980s, through the wave propagation work of Harumi [2-2 through 2-9], in Williams's NDE investigations during the 1980s [2-10], in Ayyadurai's computation and visualization studies in the late 1980s [2-11,2-12], in Yim's formulations for transversely isotropic and dissimilar materials during the 1990s [2-13,2-14], and in Sohn's modeling of the scanning laser source technique in the early 2000s [2-15, 2-16]. A closely related spring model, the local interaction simulation approach (LISA), was developed in the 1990s by Delsanto [2-17, 2-18, 2-19] in order to exploit parallel computing.

In addition to the straightforward implementation of boundary conditions such as free surfaces and material interfaces, relatively inexpensive, explicit integration schemes make the MSLM and LISA attractive alternatives to other finite-difference and finite-element methods for simulating wave propagation.

However, there are computational errors involved in the MSLM discretization that have not been thoroughly studied. For example, Yim and Sohn [2-13] investigated the numerical phase speed error for waves traveling parallel to the MSLM grid, but the numerical phase errors for a wave traveling at an arbitrary angle have not been investigated.

Furthermore, it is known that the heuristic treatment of traction-free boundary conditions in the MSLM leads to errors in wave phenomena such as the reflection of body waves at free surfaces [2-20] and the propagation of surface waves [2-16]. To precisely impose traction-free boundary conditions, Sohn and Krishnaswamy [2-16] used a hybrid higher-order finite difference method [2-21] along the boundaries and MSLM discretization in the interior; however, the stability characteristics of those systems resulted in a less efficient numerical implementation compared to the standard MSLM.

In order to address and characterize the MSLM accuracy, the remainder of this chapter is divided into two main sections: (1) the convergence analysis of the MSLM numerical phase speed error at oblique angles of incidence and (2) the investigation into the precise imposition of traction boundaries.

2-2 MSLM PHASE SPEED ERROR

2-2.1 Continuum

The equations of motion for a plane strain isotropic elastic medium expressed in Cartesian coordinates are

$$\rho \frac{\partial^2 u}{\partial t^2} = (\lambda + 2\mu) \frac{\partial^2 u}{\partial x^2} + (\lambda + \mu) \frac{\partial^2 v}{\partial x \partial y} + \mu \frac{\partial^2 u}{\partial y^2} \quad (2-1)$$

$$\rho \frac{\partial^2 v}{\partial t^2} = (\lambda + 2\mu) \frac{\partial^2 v}{\partial y^2} + (\lambda + \mu) \frac{\partial^2 u}{\partial x \partial y} + \mu \frac{\partial^2 v}{\partial x^2} \quad (2-2)$$

where ρ is the density, u is displacement in the x direction, v is displacement in the y direction, and λ and μ are the Lamé elastic constants.

Consider a plane wave oriented at angle θ with respect to the horizontal that is expressed as

$$u(x, y, t) = \int_{-\infty}^{\infty} U_k \exp[\hat{i}(xk \cos \theta + yk \sin \theta - \omega_k t)] dk \quad (2-3)$$

$$v(x, y, t) = \int_{-\infty}^{\infty} V_k \exp[\hat{i}(xk \cos \theta + yk \sin \theta - \omega_k t)] dk \quad (2-4)$$

where U_k and V_k are the Fourier transforms of u and v , respectively, corresponding to the wavenumber k , $\hat{i} = \sqrt{-1}$, and ω_k is the circular frequency corresponding to k . Substituting eqns. (2-3) and (2-4) into eqns. (2-1) and (2-2) for a generic value of k yields the matrix equation

$$\begin{bmatrix} a_{exact} & b_{exact} \\ c_{exact} & d_{exact} \end{bmatrix} \begin{bmatrix} U_k \\ V_k \end{bmatrix} = \begin{bmatrix} 0 \\ 0 \end{bmatrix} \quad (2-5)$$

where

$$a_{exact} = -\rho\omega^2 + (\lambda + 2\mu)k^2 \cos^2 \theta + \mu k^2 \sin^2 \theta \quad (2-6)$$

$$b_{exact} = (\lambda + \mu)k^2 \sin \theta \cos \theta \quad (2-7)$$

$$c_{exact} = (\lambda + \mu)k^2 \sin \theta \cos \theta \quad (2-8)$$

$$d_{exact} = -\rho\omega^2 + (\lambda + 2\mu)k^2 \sin^2 \theta + \mu k^2 \cos^2 \theta \quad (2-9)$$

In order for solutions to eqn. (2-5) to exist, the determinant must vanish, or

$$ad - bc = (-\rho^2\omega^2 + k^2(\lambda + 2\mu))(-\rho^2\omega^2 + k^2\mu) = 0 \quad (2-10)$$

Solving eqn. (2-10) leads to the dispersion relations for the two fundamental types of wave propagation in an unbounded isotropic linear elastic solid as

$$\omega = c_P k_P \quad (2-11)$$

$$\omega = c_S k_S \quad (2-12)$$

where

$$c_P = \sqrt{\frac{\lambda + 2\mu}{\rho}} \quad (2-13)$$

$$c_S = \sqrt{\frac{\mu}{\rho}} \quad (2-14)$$

Here c is the phase speed, subscript P refers to a longitudinal wave in which the continuum particle displaces parallel to the direction of wave propagation, and subscript S refers to a shear wave in which the continuum particle displaces orthogonal to the direction of wave propagation. (Refer to [2-22] or [2-23] for a detailed discussion of the wave propagation in elastic solids.)

2-2.2 MSLM Dcretization

The MSLM discretization of eqns. (2-1) and (2-2), is shown in Fig. 2-1, yielding the following equations written in component form for a particle at position (i, j) and time t [2-13]

$$\begin{aligned} \rho \frac{{}^{t+\Delta t}u_{i,j} - 2{}^t u_{i,j} + {}^{t-\Delta t}u_{i,j}}{(\Delta t)^2} &= \frac{\lambda + \mu}{h^2} ({}^t u_{i+1,j} - 2{}^t u_{i,j} + {}^t u_{i-1,j}) \\ &+ \frac{\mu}{2h^2} ({}^t u_{i+1,j+1} + {}^t u_{i-1,j-1} + {}^t u_{i+1,j-1} + {}^t u_{i-1,j+1} - 4{}^t u_{i,j}) \quad (2-15) \\ &+ \frac{\lambda + \mu}{4h^2} ({}^t v_{i+1,j+1} + {}^t v_{i-1,j-1} - {}^t v_{i+1,j-1} - {}^t v_{i-1,j+1}) \end{aligned}$$

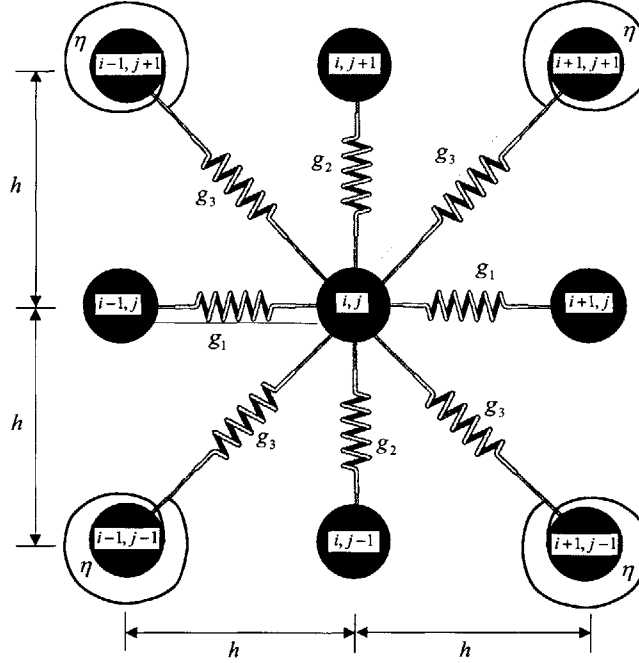


Fig. 2-1—Mass-spring-lattice model at interior plane-strain particle located at position (i, j) . [2-13]

$$\begin{aligned} \rho \frac{{}^{t+\Delta t}v_{i,j} - 2{}^t v_{i,j} + {}^{t-\Delta t}v_{i,j}}{(\Delta t)^2} &= \frac{\lambda + \mu}{h^2} ({}^t v_{i,j+1} - 2{}^t v_{i,j} + {}^t v_{i,j-1}) \\ &+ \frac{\mu}{2h^2} ({}^t v_{i+1,j+1} + {}^t v_{i-1,j-1} + {}^t v_{i+1,j-1} + {}^t v_{i-1,j+1} - 4{}^t v_{i,j}) \\ &+ \frac{\lambda + \mu}{4h^2} ({}^t u_{i+1,j+1} + {}^t u_{i-1,j-1} - {}^t u_{i+1,j-1} - {}^t u_{i-1,j+1}) \end{aligned} \quad (2-16)$$

where h is the grid space and Δt is the numerical time step. Via consistency, the extensional and rotational spring constants are given by

$$g_1 = g_2 = D(\lambda + \mu) \quad (2-17)$$

$$g_3 = \frac{D(\lambda + 3\mu)}{4} \quad (2-18)$$

$$\eta = \frac{h^2 D(\mu - \lambda)}{4} \quad (2-19)$$

where D is the unit depth.

Through von Nuemann analysis [2-13], the stability requirement for the Courant number C is

$$C = \frac{c_p \Delta t}{h} \leq 1 \quad (2-20)$$

The value $C = 1$ has been shown to be optimal in the sense that it minimizes the error in numerical phase speed error for P waves aligned with the x or y -axis and yields the most efficient computation time [2-13].

Consider a discrete plane wave oriented at angle θ with respect to the horizontal and given by

$${}^t u_{i,j} = \sum_k {}^t U_k \exp[\hat{i}(ihk \cos \theta + jhk \sin \theta - \omega_k t)] \quad (2-21)$$

$${}^t v_{i,j} = \sum_k {}^t V_k \exp[\hat{i}(ihk \cos \theta + jhk \sin \theta - \omega_k t)] \quad (2-22)$$

where ${}^t U_k$ and ${}^t V_k$ are the discrete Fourier transforms of ${}^t u_{i,j}$ and ${}^t v_{i,j}$, respectively, corresponding to the wavenumber k . Substituting eqns. (2-21) and (2-22) into eqns. (2-15) and (2-16) yields a matrix equation having the form

$${}^{t+\Delta t} \mathbf{u} = \mathbf{G} {}^t \mathbf{u} \quad (2-23)$$

where

$${}^t \mathbf{u} = [{}^t U \quad {}^t V \quad {}^{t-\Delta t} U \quad {}^{t-\Delta t} V]^T \quad (2-24)$$

$$\mathbf{G} = \begin{bmatrix} a_{MSLM} & b_{MSLM} & -1 & 0 \\ c_{MSLM} & d_{MSLM} & 0 & -1 \\ 1 & 0 & 0 & 0 \\ 0 & 1 & 0 & 0 \end{bmatrix} \quad (2-25)$$

and where

$$a_{MSLM} = \frac{2(\Delta t)^2}{\rho h^2} ((\lambda + \mu)(\cos k_x h - 1) + \mu(\cos k_x h \cos k_y h - 1)) + 2 \quad (2-26)$$

$$b_{MSLM} = -\frac{(\lambda + \mu)(\Delta t)^2}{\rho h^2} \sin k_x h \sin k_y h \quad (2-27)$$

$$c_{MSLM} = -\frac{(\lambda + \mu)(\Delta t)^2}{\rho h^2} \sin k_x h \sin k_y h \quad (2-28)$$

$$d_{MSLM} = \frac{2(\Delta t)^2}{\rho h^2} ((\lambda + \mu)(\cos k_y h - 1) + \mu(\cos k_x h \cos k_y h - 1)) + 2 \quad (2-29)$$

In eqns. (2-26) through (2-29)

$$k_x = k \cos \theta \quad (2-30)$$

$$k_y = k \sin \theta \quad (2-31)$$

The four eigenvalues of the amplification matrix \mathbf{G} are ξ_{+P} , ξ_{+S} , ξ_{-P} and ξ_{-S} , where the subscripts + or – refer to the positive and negative phases.

In light of eqns. (2-11) and (2-12), the positive phase change in one time step is found as

$$\omega_{exact} \Delta t = c_S k_S \Delta t \quad (2-32)$$

$$\omega_{exact} \Delta t = c_S k_S \Delta t \quad (2-33)$$

and the positive phase change from the numerical approximation is [2-24]

$$\omega_{MSLM} \Delta t = \text{Im}\{\ln(\xi_{+P})\} \quad (2-34)$$

$$\omega_{MSLM} \Delta t = \text{Im}\{\ln(\xi_{+S})\} \quad (2-35)$$

To quantify the difference in numerical phase change relative to the exact phase change, the error in phase is defined as

$$\varepsilon = \frac{\omega_{MSLM} \Delta t - \omega_{exact} \Delta t}{\omega_{exact} \Delta t} \cdot \frac{1/k}{1/k} = \frac{c_{MSLM} - c_{exact}}{c_{exact}} \quad (2-36)$$

which is just the error in phase speed. The nondimensional forms for P and S phase speed errors are

$$\varepsilon_P = \frac{c_{P,MSLM} - c_P}{c_P} = fc n_1 \{N_P, C, \nu, \theta\} \quad (2-37)$$

$$\varepsilon_S = \frac{c_{S,MSLM} - c_S}{c_S} = fc n_2 \{N_S, C, \nu, \theta\} \quad (2-38)$$

where N_P and N_S are the number of grid spaces per P and S wavelengths, respectively, and given by

$$N_P = \frac{2\pi}{k_P h} \quad (2-39)$$

$$N_S = \frac{2\pi}{k_S h} \quad (2-40)$$

The errors in wave speed for the case when $\nu = 0.377$, typical of a bulk metallic glass nanocomposite [2-25], for $\theta = 0^\circ$ and $\theta = 45^\circ$ are shown in Figs. 2-4 and 2-5, respectively. A few observations are noted.

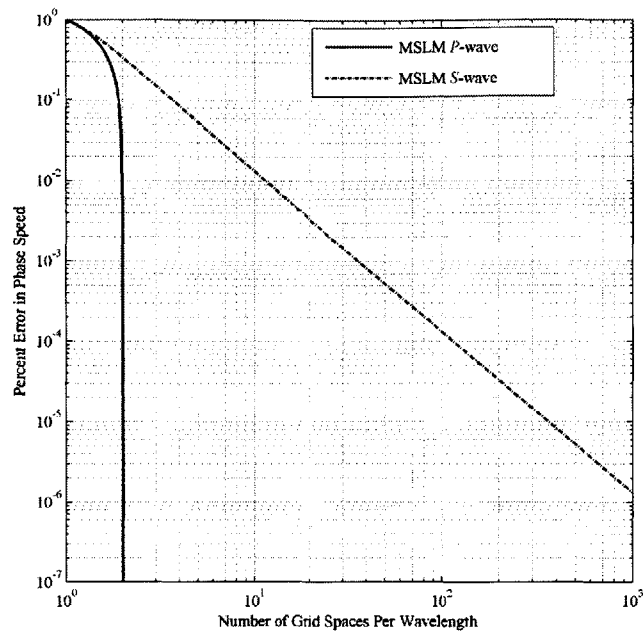


Fig. 2-4—Percent error in phase speed as function of grid spaces per wavelength, where Poisson's ratio $\nu = 0.377$, Courant number $C = 1$, and angle of orientation $\theta = 0^\circ$.

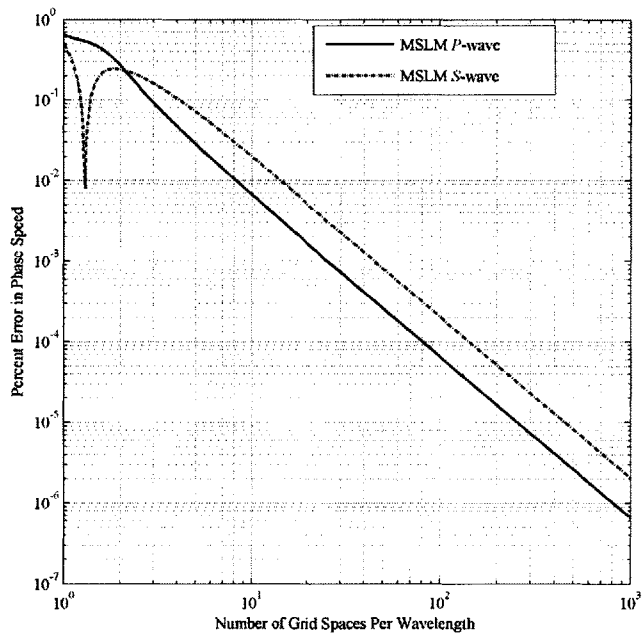


Fig. 2-5—Percent error in phase speed as function of grid spaces per wavelength where Poisson's ratio $\nu = 0.377$, Courant number $C = 1$, and angle of orientation $\theta = 45^\circ$.

First, when $N_S \gg 1$ and $N_P \gg 1$, all phase speed convergence is of second order and is manifested in the slope of two (2) on all the logarithmic plots of Figs. 2-4 and 2-5. Second, as $N_P \gg 1$ in Fig. 2-4, there is no P phase speed error for waves, which is in agreement with [2-13]. In Fig. 2-4, when $N_P = N_S$, the P phase speed error is smaller than the S phase speed error.

Typically in engineering practice, $\varepsilon_P = \varepsilon_S = \varepsilon$ is often specified, and N_P and N_S are adjusted accordingly. According to Figs. 2-4 and 2-5, at $\theta = 0^\circ$, to achieve $\varepsilon_S < 0.01$ requires $N_S \geq 10$; at $\theta = 45^\circ$, to achieve $\varepsilon_P < 0.01$ and $\varepsilon_S < 0.01$ requires $N_P > 8$ and $N_S > 10$, respectively.

The nondimensional form for these requirements is given as

$$N_P = fcn_3\{\varepsilon, C, \nu, \theta\} \quad (2-41)$$

$$N_S = fcn_4\{\varepsilon, C, \nu, \theta\} \quad (2-42)$$

In Fig. 2-6, the numerical evaluation of eqns. (2-41) and (2-42) is achieved for the case of $C = 1$, $0 \leq \theta \leq 90^\circ$, and $0 \leq \nu < 0.5$. (ν can theoretically approach -1 as a lower limit, but most engineering materials have positive values of ν .)

A few observations can be made about Fig. 2-6. First, N_P and N_S are symmetric about the angle $\theta = 45^\circ$, which follows directly from the symmetry of the MSLM for an interior particle as shown in Fig. 2-1. Second, as discussed in [2-13], when $\theta \rightarrow 0^\circ$ and $\theta \rightarrow 90^\circ$ the phase error decays to zero as $N_P \rightarrow 0$. Third, for a fixed ν , as $\theta \rightarrow 45^\circ$ N_P is maximum. Fourth, holding $\theta = 45^\circ$, N_S has a minimum near $\nu = 0.30$ and increases dramatically as $\nu \rightarrow 0.5$. Fifth, holding $\theta \rightarrow 0^\circ$ or $\theta = 90^\circ$, N_S is a monotonically increasing function of ν .

Because there is only a single grid space parameter, for a given error requirement either N_P or N_S will limit the accuracy. Using, the relationship between the P and S phase speeds as

$$\frac{c_S}{c_P} = \sqrt{\frac{1-2\nu}{2(1-\nu)}} \quad (2-43)$$

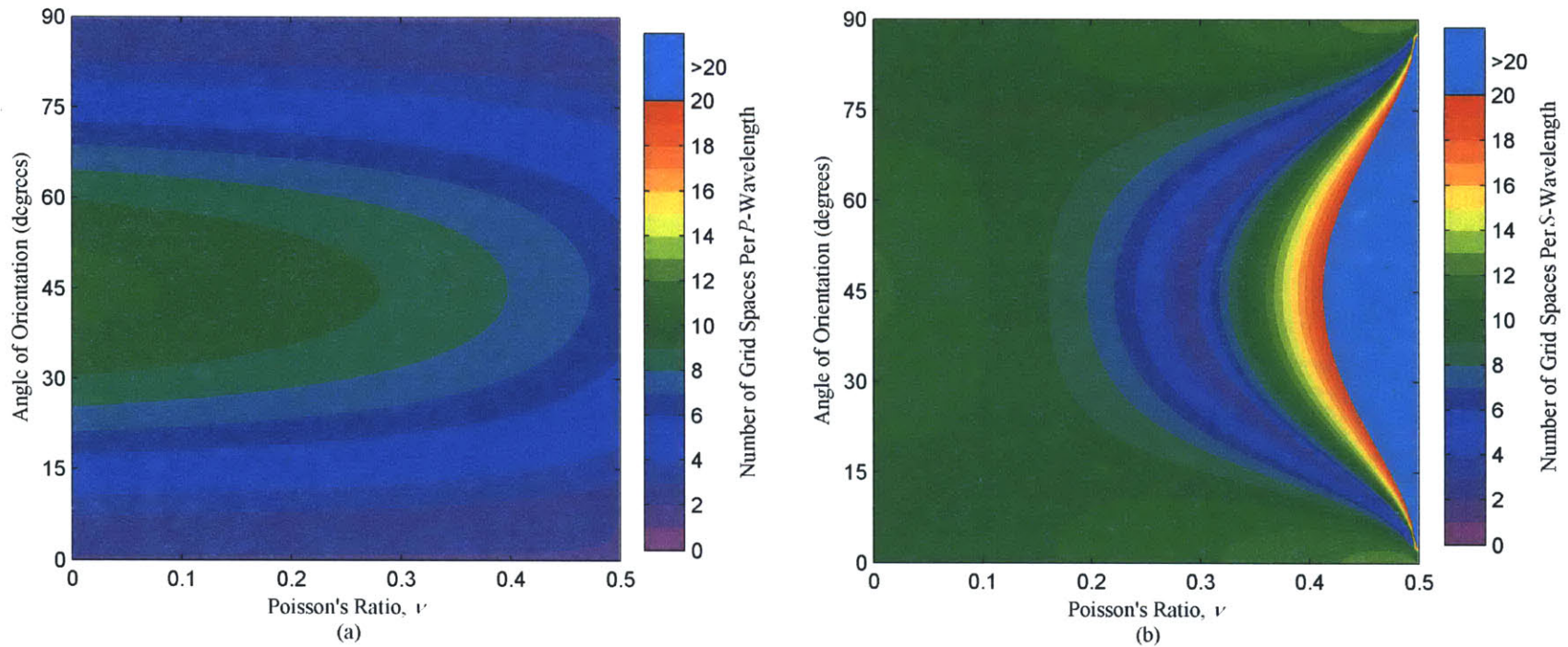


Fig. 2-6—Number of grid spaces per wavelength required to achieve 1% or less phase speed error as function of Poisson's ratio ν and plane wave angle of orientation θ with respect to horizontal axis for (a) P waves and (b) S waves. Here Courant number is equal to unity.

a single parameter \hat{N}_S is defined as

$$\hat{N}_S(\varepsilon, C, \nu) = \max \left\{ \max_{\theta} \{N_p(\varepsilon, C, \nu, \theta)\} \sqrt{\frac{2(1-\nu)}{1-2\nu}}, \max_{\theta} \{N_s(\varepsilon, C, \nu, \theta)\} \right\} \quad (2-44)$$

which represents an equivalent grid spacing per S -wavelength that would result in all waves at all orientations propagated with phase speed error less than ε .

Figure 2-7 shows \hat{N}_S as a function of $\varepsilon = 0.05$, $\varepsilon = 0.01$, and $\varepsilon = 0.005$. The more demanding accuracy requirement shift the curves up to higher required grid spaces per wavelength. In the regions $0 \leq \nu < 0.12$ and $\nu \geq 0.35$, the accuracy is limited by phase error of S -waves propagating at $\theta = 45^\circ$. The relatively shallow line segment from $0.12 \leq \nu \leq 0.35$ is due to accuracy requirements on P -wave propagating at $\theta = 45^\circ$. To require $\varepsilon < 0.01$ for all P and S plane waves in a material where $\nu < 0.40$, a conservative rule is therefore $N_S > 20$.

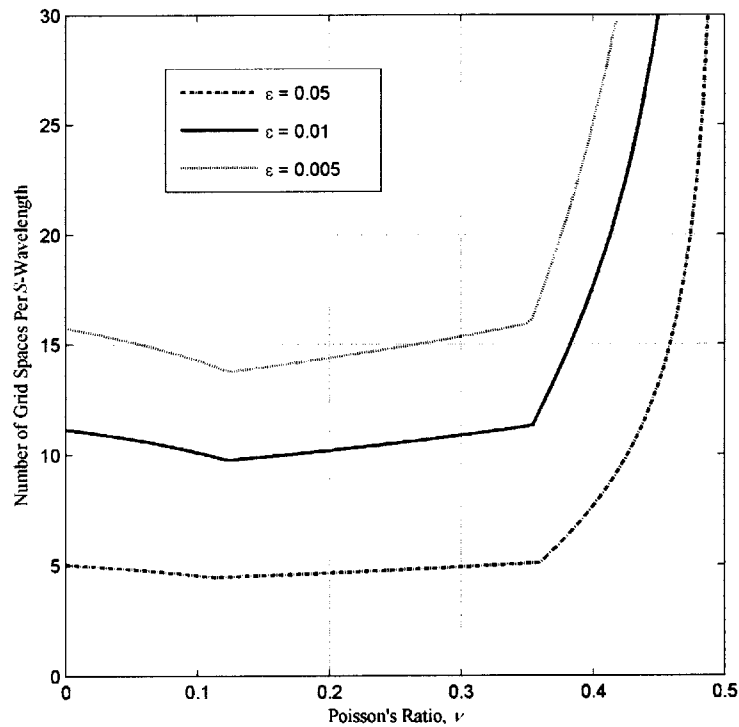


Fig. 2-7—Number of grid spaces per S -wavelength, as functions of Poisson's ratio ν , required for error in phase speed for all P and S waves plane waves to be less than 5.0, 1.0 and 0.5 percent.

2-3 MSLM TRACTION BOUNDARY CONDITIONS

In this section, the consistency of the MSLM traction boundary condition is evaluated via a comparison with various finite continuum elements. This approach has been used previously [2-12], but it was incorrectly applied and led to non-physical results.

2-3.1 One-dimensional MSLM

Before preceding to two-dimensional traction boundaries, a one-dimensional example is explored. A one-dimensional schematic of the MSLM discretization in the vicinity of a boundary is shown in Fig. 2-8a. The corresponding equation of motion is

$$\rho \ddot{u}_N = \frac{2g}{Ah}(u_{N-1} - u_N) + \frac{2R_x}{Ah} \quad (2-45)$$

where g is the spring constant, A is the unit cross-sectional area, and R_x is the surface force applied to the outer particle.

The Taylor series expansion of the difference equation is

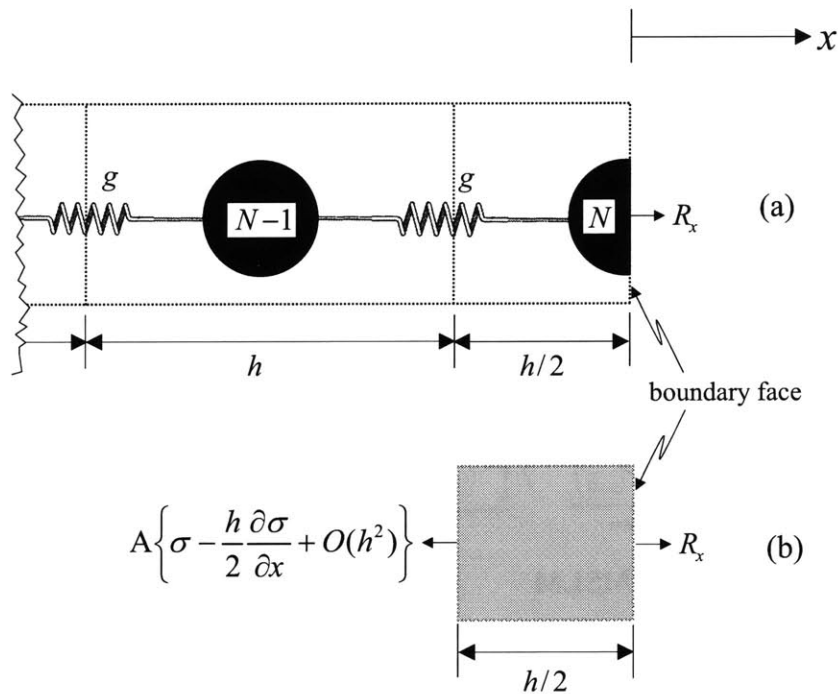


Fig. 2-8—(a) Schematic of one-dimensional MSLM discretization in vicinity of boundary detailing computational cell boundaries and neighbor interactions. (b) Free-body diagram of forces on continuum element. Here spring constant g is related to continuum material constants of elastic solid, R_x is surface force, h is grid space, σ is stress and A is unit cross-sectional area.

$$\frac{u_{N-1} - u_N}{h} = -\left. \frac{\partial u}{\partial x} \right|_{x=0} + \frac{h}{2} \left. \frac{\partial^2 u}{\partial x^2} \right|_{x=0} + O(h^2) \quad (2-46)$$

Substituting eqn. (2-46) into eqn. (2-45) yields

$$\rho \ddot{u} = \frac{2g}{A} \left(-\left. \frac{\partial u}{\partial x} \right|_{x=0} + \frac{h}{2} \left. \frac{\partial^2 u}{\partial x^2} \right|_{x=0} + O(h^2) \right) + \frac{2R_x}{Ah} \quad (2-47)$$

A one-dimensional schematic of a continuum model in the vicinity of a boundary is shown in Fig. 2-8b. The corresponding equation of motion is

$$\rho \ddot{u} = \frac{2}{h} \left\{ \sigma_x(0) - \frac{h}{2} \left. \frac{\partial \sigma_x}{\partial x} \right|_{x=0} \right\} + \frac{2R_x}{Ah} + O(h) \quad (2-48)$$

where σ_x is the stress, given by the constitutive equation, as

$$\sigma_x = (\lambda + 2\mu) \frac{\partial u}{\partial x} \quad (2-49)$$

where λ and μ are the Lamé constants.

Substituting eqn. (2-49) into eqn. (2-48) yields

$$\rho \ddot{u} = -\frac{2(\lambda + 2\mu)}{h} \left. \frac{\partial u}{\partial x} \right|_{x=0} + (\lambda + 2\mu) \left. \frac{\partial^2 u}{\partial x^2} \right|_{x=0} + \frac{2R_x}{Ah} + O(h) \quad (2-50)$$

Comparing eqns. (2-50) and (2-47) yields the consistency requirement on the spring constant as

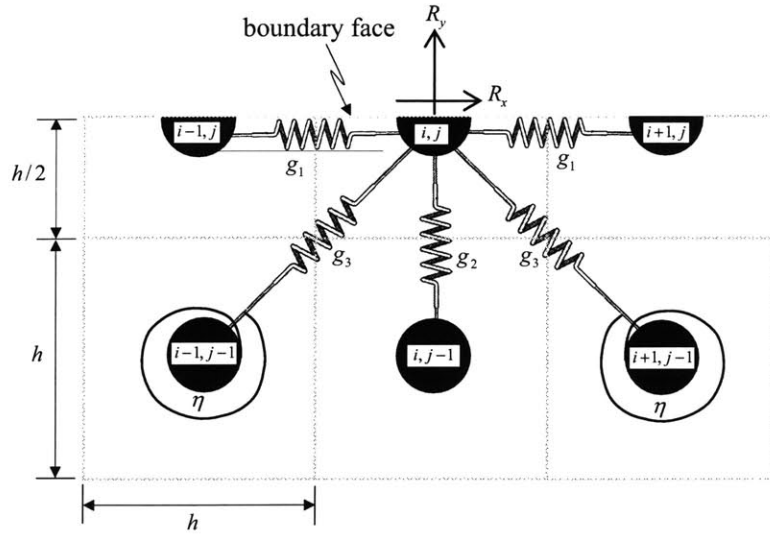
$$g = \frac{(\lambda + 2\mu)A}{h} \quad (2-51)$$

By rewriting eqn. (2-50), the equation of motion contains the traction boundary condition, the governing wave equation, and the truncation error as

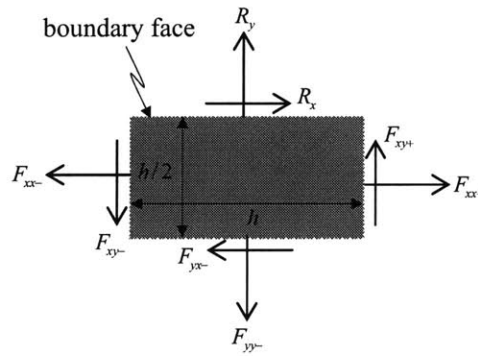
$$\underbrace{\left\{ \frac{F_x}{A} - (\lambda + 2\mu) \left. \frac{\partial u}{\partial x} \right|_{x=0} \right\}}_{\text{traction boundary condition}} + \frac{h}{2} \underbrace{\left\{ (\lambda + 2\mu) \left. \frac{\partial^2 u}{\partial x^2} \right|_{x=0} - \rho \ddot{u}(0) \right\}}_{\text{governing equation}} + \underbrace{O(h^2)}_{\text{truncation error}} = 0. \quad (2-52)$$

2-3.2 Two-Dimensional MSLM

A two-dimensional schematic of the MSLM discretization of a plane strain elastic solid in the vicinity of a longitudinal traction boundary is shown in Fig. 2-9a. The corresponding equations of motion are



(a)



(b)

Fig. 2-9—(a) MSLM schematic at traction boundary at position (i, j) and (b) free body diagram of corresponding finite continuum element.

$$\begin{aligned}
 \rho \ddot{u}_{i,j} = & \frac{2g_1}{h^2 D} (u_{i-1,j} - 2u_{i,j} + u_{i+1,j}) \\
 & + \frac{1}{h^2 D} \left(g_3 + \frac{\eta}{2h^2} \right) (u_{i+1,j-1} + u_{i+1,j-1} - 2u_{i,j}) \\
 & + \frac{1}{h^2 D} \left(g_3 - \frac{\eta}{2h^2} \right) (v_{i-1,j-1} - v_{i+1,j-1}) + \frac{2R_x}{h^2 D}
 \end{aligned} \tag{2-53}$$

$$\begin{aligned}
 \rho \ddot{v}_{i,j} &= \frac{2g_2}{h^2 D} (v_{i,j-1} - v_{i,j}) \\
 &+ \frac{1}{h^2 D} \left(g_3 + \frac{\eta}{2h^2} \right) (v_{i+1,j-1} + v_{i-1,j-1} - 2v_{i,j}) \\
 &+ \frac{1}{h^2 D} \left(g_3 - \frac{\eta}{2h^2} \right) (u_{i-1,j-1} - u_{i+1,j-1}) + \frac{2R_y}{h^2 D}
 \end{aligned} \tag{2-54}$$

where $u_{i,j}$ and $v_{i,j}$ are the horizontal and vertical displacements, respectively, of a particle at location (i, j) , D is the unit depth, g_1 , g_2 and g_3 are extensional spring constants, η is a rotational spring constant, and R_x and R_y are the horizontal and vertical surface forces, respectively, applied to the outer particle.

By taking Taylor series expansions of the difference equations¹, eqns. (2-53) and (2-54) are reformulated as

$$\begin{aligned}
 0 &= \left\{ \frac{R_x}{hD} - \left(\frac{g_3}{D} + \frac{\eta}{2h^2 D} \right) \frac{\partial u}{\partial y} - \left(\frac{g_3}{D} - \frac{\eta}{2h^2 D} \right) \frac{\partial v}{\partial x} \right\} \\
 &+ \frac{h}{2} \left\{ \left(\frac{2g_1}{D} + \frac{g_3}{D} + \frac{\eta}{2h^2 D} \right) \frac{\partial^2 u}{\partial x^2} + \left(\frac{2g_3}{D} - \frac{\eta}{h^2 D} \right) \frac{\partial^2 v}{\partial x \partial y} \right. \\
 &\quad \left. + \left(\frac{g_3}{D} + \frac{\eta}{2h^2 D} \right) \frac{\partial^2 u}{\partial y^2} - \rho \ddot{u}_{i,j} \right\} \\
 &+ O(h^2)
 \end{aligned} \tag{2-55}$$

$$\begin{aligned}
 0 &= \left\{ \frac{R_y}{hD} - \left(\frac{g_2}{D} + \frac{g_3}{D} + \frac{\eta}{2h^2 D} \right) \frac{\partial v}{\partial y} - \left(\frac{g_3}{D} - \frac{\eta}{2h^2 D} \right) \frac{\partial u}{\partial x} \right\} \\
 &+ \frac{h}{2} \left\{ \left(\frac{g_2}{D} + \frac{g_3}{D} + \frac{\eta}{2h^2 D} \right) \frac{\partial^2 v}{\partial y^2} + \left(\frac{2g_3}{D} + \frac{\eta}{h^2 D} \right) \frac{\partial^2 u}{\partial x \partial y} \right. \\
 &\quad \left. + \left(\frac{g_3}{D} + \frac{\eta}{2h^2 D} \right) \frac{\partial^2 v}{\partial x^2} - \rho \ddot{v}_{i,j} \right\} \\
 &+ O(h^2)
 \end{aligned} \tag{2-56}$$

¹ The useful equations are $\frac{p_{i+1,j-1} - 2p_{i,j} + p_{i-1,j-1}}{2h} = \frac{h}{2} \left(\frac{\partial^2 p}{\partial x^2} + \frac{\partial^2 p}{\partial y^2} \right) - \frac{\partial p}{\partial y} + O(h^2)$,

$\frac{p_{i-1,j-1} - p_{i+1,j-1}}{2h} = h \frac{\partial^2 p}{\partial x \partial y} - \frac{\partial p}{\partial x} + O(h^2)$, $\frac{p_{i+1,j} - 2p_{i,j} + p_{i-1,j}}{h^2} = \frac{\partial^2 p}{\partial x^2} + O(h^2)$,

$\frac{p_{i,j-1} - p_{i,j}}{h} = \frac{h}{2} \frac{\partial^2 p}{\partial y^2} - \frac{\partial p}{\partial y} + O(h^2)$ and $\frac{p_{i-1,j} - p_{i+1,j}}{2h} = -\frac{\partial p}{\partial x} + O(h^2)$

A two-dimensional schematic of a continuum model in the vicinity of a longitudinal traction boundary is shown in Fig. 2-9b. The corresponding equations of motion are

$$\rho \ddot{u} = \frac{2}{h^2 D} (F_{xx+} - F_{xx-} - F_{yx-} + R_x) \quad (2-57)$$

$$\rho \ddot{v} = \frac{2}{h^2 D} (F_{xy+} - F_{xy-} - F_{yy-} + R_y) \quad (2-58)$$

where expressions for the forces are given in Appendix 2A. Simplifying eqns. (2-57) and (2-58) yields

$$0 = \underbrace{\left\{ \frac{R_x}{hD} - \mu \frac{\partial u}{\partial y} - \mu \frac{\partial v}{\partial x} \right\}}_{\text{traction boundary condition}} + \underbrace{\frac{h}{2} \left\{ (\lambda + 2\mu) \frac{\partial^2 u}{\partial x^2} + (\lambda + \mu) \frac{\partial^2 v}{\partial x \partial y} + \mu \frac{\partial^2 u}{\partial y^2} - \rho \ddot{u}_{i,j} \right\}}_{\text{governing equation}} \quad (2-59)$$

$$+ \underbrace{O(h^2)}_{\text{truncation error}}$$

$$0 = \underbrace{\left\{ \frac{R_y}{hD} - (\lambda + 2\mu) \frac{\partial v}{\partial y} - \lambda \frac{\partial u}{\partial x} \right\}}_{\text{traction boundary condition}} + \underbrace{\frac{h}{2} \left\{ (\lambda + 2\mu) \frac{\partial^2 v}{\partial y^2} + (\lambda + \mu) \frac{\partial^2 u}{\partial x \partial y} + \mu \frac{\partial^2 v}{\partial x^2} - \rho \ddot{v}_{i,j} \right\}}_{\text{governing equation}} \quad (2-60)$$

$$+ \underbrace{O(h^2)}_{\text{truncation error}}$$

Comparing eqns. (2-55) and (2-56) with eqns. (2-59) and (2-60), requires for consistency

$$\frac{g_3}{D} + \frac{\eta}{2h^2 D} = \mu \quad (2-61)$$

$$\frac{g_2}{D} + \frac{g_3}{D} + \frac{\eta}{2h^2 D} = \lambda + 2\mu \quad (2-62)$$

$$\frac{2g_1}{D} + \frac{g_3}{D} + \frac{\eta}{2h^2 D} = \lambda + 2\mu \quad (2-63)$$

$$\frac{2g_3}{D} - \frac{\eta}{h^2 D} = \lambda + \mu \quad (2-64)$$

$$\frac{g_3}{D} - \frac{\eta}{2h^2D} = \mu \quad (2-65)$$

$$\frac{g_3}{D} - \frac{\eta}{2h^2D} = \lambda \quad (2-66)$$

Equations (2-61) through (2-66) are over constrained: they contain four unknowns in six equations. Upon further observation, eqns. (2-61), (2-62) and (2-63) are dependent. It can be shown that the solutions

$$g_1 = \frac{D(\lambda + \mu)}{2} \quad (2-67)$$

$$g_2 = D(\lambda + \mu) \quad (2-68)$$

$$g_3 = \frac{D(\lambda + 3\mu)}{4} \quad (2-69)$$

$$\eta = \frac{h^2D(\mu - \lambda)}{2} \quad (2-70)$$

are satisfied only for the case when $\lambda = \mu$ or Poission's ratio $\nu = \frac{1}{4}$. (It is noted that the spring constants in eqns. (2-67) through (2-70) are the result of shifting an MSLM interior unit cell to the surface and halving the mass and the longitudinal springs [2-13].)

If eqns. (2-67) through (2-70) are used when $\nu \neq \frac{1}{4}$, the traction boundary condition will not be satisfied².

To precisely impose the traction boundary conditions, correction terms based on finite-difference considerations are added to each of the horizontal and vertical equations of motion. The modified MSLM equations of motion at a longitudinal traction-free boundary are

² In fact, the erroneous stresses evaluated at the surface are $\sigma_{yy} = (\lambda + 2\mu)\frac{\partial v}{\partial y} + \frac{\lambda + \mu}{2}\frac{\partial u}{\partial x}$ and

$$\sigma_{xy} = \frac{\lambda + \mu}{2}\frac{\partial u}{\partial y} + \mu\frac{\partial v}{\partial x}.$$

$$\begin{aligned}
\rho \ddot{u}_{i,j} = & \frac{2g_1}{h^2 D} (u_{i-1,j} - 2u_{i,j} + u_{i+1,j}) \\
& + \frac{1}{h^2 D} \left(g_3 + \frac{\eta}{2h^2} \right) (u_{i+1,j-1} + u_{i-1,j-1} - 2u_{i,j}) \\
& + \frac{1}{h^2 D} \left(g_3 - \frac{\eta}{2h^2} \right) (v_{i-1,j-1} - v_{i+1,j-1}) \\
& + \frac{\mu - \lambda}{2h^2} (v_{i-1,j} - v_{i+1,j}) + \frac{2R_x}{h^2 D}
\end{aligned} \tag{2-71}$$

$$\begin{aligned}
\rho \ddot{v}_{i,j} = & \frac{2g_1}{h^2 D} (v_{i,j-1} - v_{i,j}) \\
& + \frac{1}{h^2 D} \left(g_3 + \frac{\eta}{2h^2} \right) (v_{i+1,j-1} + v_{i-1,j-1} - 2v_{i,j}) \\
& + \frac{1}{h^2 D} \left(g_3 - \frac{\eta}{2h^2} \right) (u_{i-1,j-1} - u_{i+1,j-1}) \\
& + \frac{\mu - \lambda}{2h^2} (u_{i+1,j} - u_{i-1,j}) + \frac{2R_y}{h^2 D}
\end{aligned} \tag{2-72}$$

where the correction terms in eqns. (2-71) and (2-72) are circled. By taking a Taylor series expansion of eqns. (2-71) and (2-72), it can be shown that the spring constants are given by eqns. (2-67) through (2-70) for a precise implementation of traction boundary conditions for all Poisson's ratios. The physical significance of the extra terms, however, is not as straightforward as adding extensional or torsional springs along the surface. A related numerical spring model, LISA [2-19], introduces "tensorial" springs to account for the correction terms.

2-3.3 Numerical Example

Consider a line force, having peak magnitude Q and temporal variation $q(t)$, acting in the negative y -direction at the origin of a half-space ($y < 0$). The resulting transient surface displacements are detailed in a classical paper by Lamb [2-26].

For the case where the temporal variation is a Gaussian-modulated cosinusoidal function

$$q(t) = \exp\left(-\frac{1}{2}(\omega_{std.dev.} t - \gamma)^2\right) \cos\left(\omega_{center} t - \gamma \omega_{center} \omega_{std.dev.}^{-1}\right) \tag{2-73}$$

where $\omega_{std.dev.}$ is the standard deviation frequency, γ is the nondimensional offset, and ω_{center} is the center frequency. Figure 2-10 shows snapshots of the surface displacements

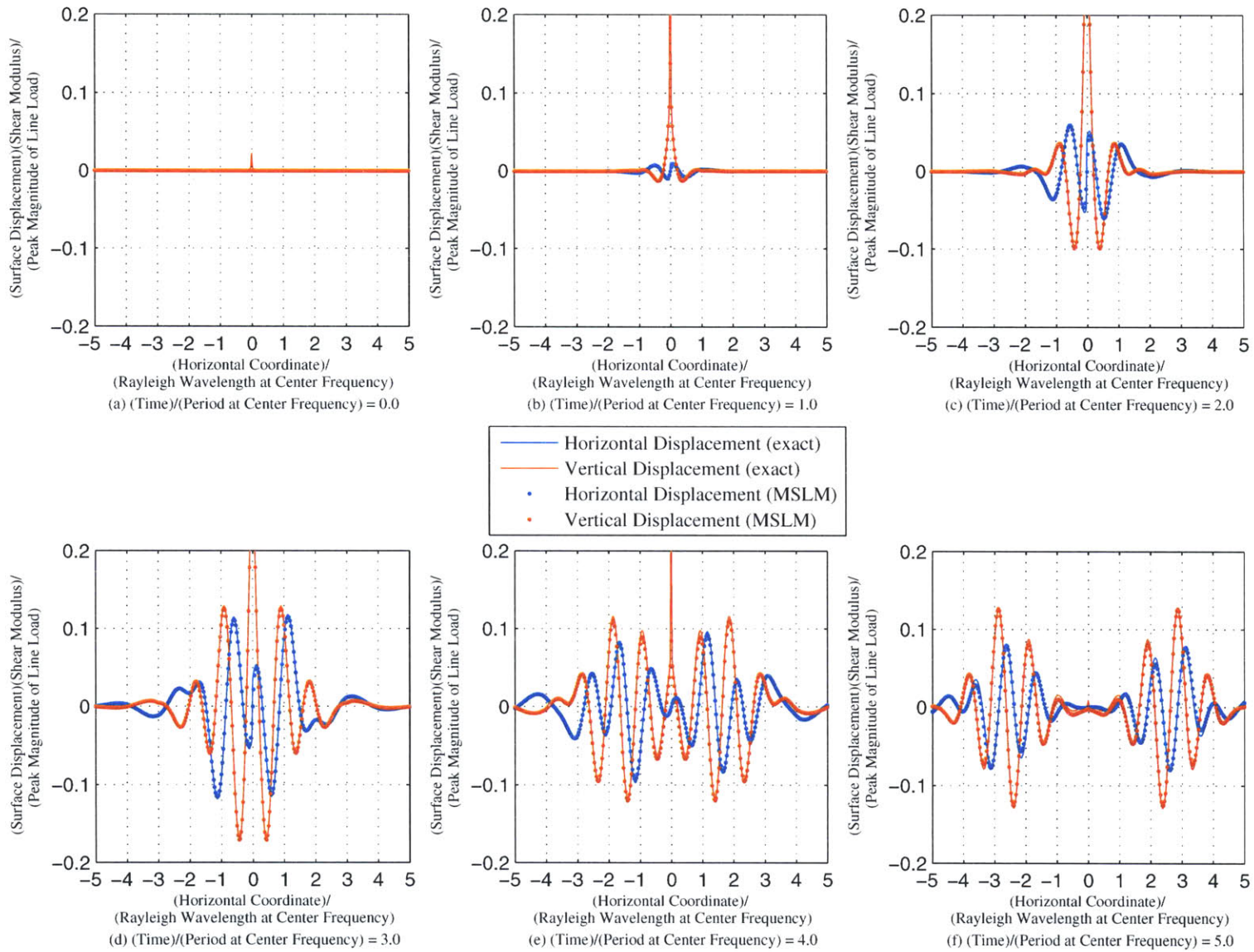


Fig. 2-10—Snapshots of exact and MSLM normalized surface displacements on elastic half-space due to normal point load having Gaussian-modulated cosinusoidal temporal variation. Here Poisson’s ratio is 0.377, nondimensional Gaussian offset is 3, ratio of standard deviation frequency to center frequency is 0.2, and MSLM grid spaces per minimum effective wavelength is 20.

of the exact solution and the MSLM solution in the vicinity of the force application when the normalized bandwidth $\omega_{std.dev.} \omega_{center}^{-1} = 0.2$, offset $\gamma = 3$, N corresponding to minimum effective wavelength, $\kappa_{min} = \frac{2\pi\kappa_R}{\omega_{center} + \gamma\omega_{std.dev.}}$ is equal to 20, and $\nu = 0.377$

(Appendix 2B).

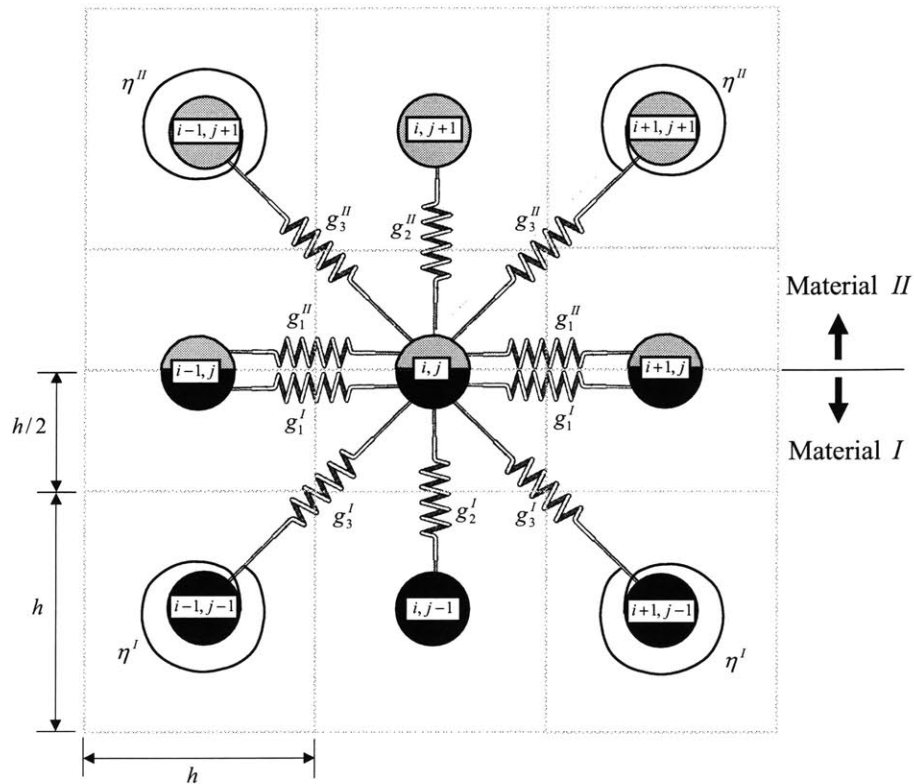
2-3.4 Interface of Dissimilar Materials

Consider a perfect interface between dissimilar materials—Material *I* ($y < 0$) and Material *II* ($y > 0$)—as shown in Fig. 2-11. Via MSLM discretization the uncorrected equations of motion are

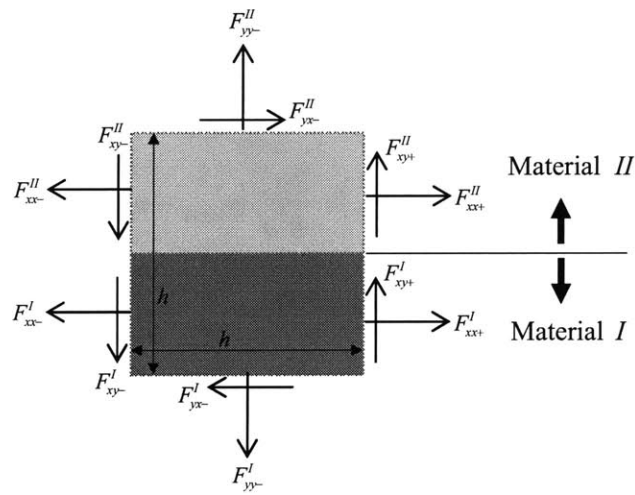
$$\begin{aligned}
 (\rho^I + \rho^{II})\ddot{u}_{i,j} &= \frac{2(g_1^I + g_1^{II})}{h^2 D} (u_{i-1,j} - 2u_{i,j} + u_{i+1,j}) \\
 &+ \frac{1}{h^2 D} \left(g_3^I + \frac{\eta^I}{2h^2} \right) (u_{i+1,j-1} + u_{i-1,j-1} - 2u_{i,j}) \\
 &+ \frac{1}{h^2 D} \left(g_3^{II} + \frac{\eta^{II}}{2h^2} \right) (u_{i+1,j+1} + u_{i-1,j+1} - 2u_{i,j}) \\
 &+ \frac{1}{h^2 D} \left(g_3^I - \frac{\eta^I}{2h^2} \right) (v_{i-1,j-1} - v_{i+1,j-1}) \\
 &+ \frac{1}{h^2 D} \left(g_3^{II} - \frac{\eta^{II}}{2h^2} \right) (v_{i+1,j+1} - v_{i-1,j+1})
 \end{aligned} \tag{2-74}$$

$$\begin{aligned}
 (\rho^I + \rho^{II})\ddot{v}_{i,j} &= \frac{2g_2^I}{h^2 D} (v_{i,j-1} - v_{i,j}) + \frac{2g_2^{II}}{h^2 d} (v_{i,j+1} - v_{i,j}) \\
 &+ \frac{1}{h^2 D} \left(g_3^I + \frac{\eta^I}{4h^2} \right) (v_{i+1,j-1} + v_{i-1,j-1} - 2v_{i,j}) \\
 &+ \frac{1}{h^2 D} \left(g_3^{II} + \frac{\eta^{II}}{4h^2} \right) (v_{i+1,j+1} + v_{i-1,j+1} - 2v_{i,j}) \\
 &+ \frac{1}{h^2 D} \left(g_3^I - \frac{\eta^I}{4h^2} \right) (u_{i-1,j-1} - u_{i+1,j-1}) \\
 &+ \frac{1}{h^2 D} \left(g_3^{II} - \frac{\eta^{II}}{4h^2} \right) (u_{i+1,j+1} - u_{i-1,j+1})
 \end{aligned} \tag{2-75}$$

Assuming the spring constants are determined from the discretization of an interior particle, the spring constants are



(a)



(b)

Fig. 2-11—(a) MSLM schematic in vicinity of perfect interface of dissimilar materials at position (i, j) . (b) Free body diagram of corresponding elastic element.

$$g_1^I = \frac{D(\lambda^I + \mu^I)}{2} \quad (2-76)$$

$$g_2^I = D(\lambda^I + \mu^I) \quad (2-77)$$

$$g_3^I = \frac{D(\lambda^I + 3\mu^I)}{4} \quad (2-78)$$

$$\eta^I = \frac{h^2 D(\mu^I - \lambda^I)}{2} \quad (2-79)$$

$$g_1^{II} = \frac{D(\lambda^{II} + \mu^{II})}{2} \quad (2-80)$$

$$g_2^{II} = D(\lambda^{II} + \mu^{II}) \quad (2-81)$$

$$g_3^{II} = \frac{D(\lambda^{II} + 3\mu^{II})}{4} \quad (2-82)$$

$$\eta^{II} = \frac{h^2 D(\mu^{II} - \lambda^{II})}{2} \quad (2-83)$$

Consider the continuum element in the vicinity of an interface of dissimilar materials as shown in Fig. 2-11b. The equations of motion are

$$(\rho^I + \rho^{II})\ddot{u} = \frac{2}{h^2 D} (F_{xx^+}^I + F_{xx^+}^{II} - F_{xx^-}^I - F_{xx^-}^{II} + F_{yx^+}^{II} - F_{yx^-}^I + F_x) \quad (2-84)$$

$$(\rho^I + \rho^{II})\ddot{v} = \frac{2}{h^2 D} (F_{xy^+}^I + F_{xy^+}^{II} - F_{xy^-}^I - F_{xy^-}^{II} + F_{yy^+}^{II} - F_{yy^-}^I + F_y) \quad (2-85)$$

where the expressions for the various forces are given in Appendix 2C. Simplifying eqns.

(2-84) and (2-85) yields

$$\begin{aligned} 0 = & \underbrace{\mu^{II} \left(\frac{\partial u}{\partial y} + \frac{\partial v}{\partial x} \right) - \mu^I \left(\frac{\partial u}{\partial y} + \frac{\partial u}{\partial y} \right)}_{\text{traction boundary at perfect interface}} \\ & + \frac{h}{2} \underbrace{\left((\lambda^I + 2\mu^I) \frac{\partial^2 u}{\partial x^2} + (\lambda^I + \mu^I) \frac{\partial^2 v}{\partial x \partial y} + \mu^I \frac{\partial^2 u}{\partial y^2} - \rho^I \ddot{u} \right)}_{\text{governing equation in Material I}} \\ & + \frac{h}{2} \underbrace{\left((\lambda^{II} + 2\mu^{II}) \frac{\partial^2 u}{\partial x^2} + (\lambda^{II} + \mu^{II}) \frac{\partial^2 v}{\partial x \partial y} + \mu^{II} \frac{\partial^2 u}{\partial y^2} - \rho^{II} \ddot{u} \right)}_{\text{governing equation in Material II}} \\ & + \underbrace{O(h^2)}_{\text{truncation error}} \end{aligned} \quad (2-86)$$

$$\begin{aligned}
 0 = & \underbrace{(\lambda'' + 2\mu'') \frac{\partial v}{\partial y} + \lambda'' \frac{\partial u}{\partial x} - (\lambda' + 2\mu') \frac{\partial v}{\partial y} - \lambda' \frac{\partial u}{\partial x}}_{\text{traction boundary at perfect interface}} \\
 & + \frac{h}{2} \underbrace{\left((\lambda' + 2\mu') \frac{\partial^2 v}{\partial y^2} + (\lambda' + \mu') \frac{\partial^2 u}{\partial x \partial y} + \mu' \frac{\partial^2 v}{\partial x^2} - \rho' \ddot{v} \right)}_{\text{governing equation in Material I}} \\
 & + \frac{h}{2} \underbrace{\left((\lambda'' + 2\mu'') \frac{\partial^2 v}{\partial y^2} + (\lambda'' + \mu'') \frac{\partial^2 u}{\partial x \partial y} + \mu'' \frac{\partial^2 v}{\partial x^2} - \rho'' \ddot{v} \right)}_{\text{governing equation in Material II}} \\
 & + \underbrace{O(h^2)}_{\text{truncation error}}
 \end{aligned} \tag{2-87}$$

Substituting eqns. (2-76) through (2-83) into eqns. (2-74) and (2-75) and taking the Taylor series expansions³ of the difference terms and comparing the results with eqns. (2-86) and (2-87), it can be shown that in order to satisfy the traction boundary conditions, the MSLM equations must be modified to

$$\begin{aligned}
 (\rho' + \rho'') \ddot{u}_{i,j} = & \frac{2(g_1^I + g_1^{II})}{h^2 d} (u_{i-1,j} - 2u_{i,j} + u_{i+1,j}) \\
 & + \frac{1}{h^2 d} \left(g_3^I + \frac{\eta^I}{2h^2} \right) (u_{i+1,j-1} + u_{i-1,j-1} - 2u_{i,j}) \\
 & + \frac{1}{h^2 d} \left(g_3^{II} + \frac{\eta^{II}}{2h^2} \right) (u_{i+1,j+1} + u_{i-1,j+1} - 2u_{i,j}) \\
 & + \frac{1}{h^2 d} \left(g_3^I - \frac{\eta^I}{2h^2} \right) (v_{i-1,j-1} - v_{i+1,j-1}) \\
 & + \frac{1}{h^2 d} \left(g_3^{II} - \frac{\eta^{II}}{2h^2} \right) (v_{i+1,j+1} - v_{i-1,j+1}) \\
 & + \frac{\mu^I - \lambda^I - \mu^{II} + \lambda^{II}}{2h^2} (v_{i-1,j} - v_{i+1,j})
 \end{aligned} \tag{2-88}$$

³ The useful equations are $\frac{p_{i+1,j-1} - 2p_{i,j} + p_{i-1,j-1}}{2h} = \frac{h}{2} \left(\frac{\partial^2 p}{\partial x^2} + \frac{\partial^2 p}{\partial y^2} \right) - \frac{\partial p}{\partial y} + O(h^2)$,

$\frac{p_{i+1,j+1} - 2p_{i,j} + p_{i-1,j+1}}{2h} = \frac{h}{2} \left(\frac{\partial^2 p}{\partial x^2} + \frac{\partial^2 p}{\partial y^2} \right) + \frac{\partial p}{\partial y} + O(h^2)$, $\frac{p_{i-1,j-1} - p_{i+1,j-1}}{2h} = h \frac{\partial^2 p}{\partial x \partial y} - \frac{\partial p}{\partial x} + O(h^2)$,

$\frac{p_{i+1,j+1} - p_{i-1,j-1}}{2h} = h \frac{\partial^2 p}{\partial x \partial y} + \frac{\partial p}{\partial x} + O(h^2)$, $\frac{p_{i+1,j} - 2p_{i,j} + p_{i-1,j}}{h^2} = \frac{\partial^2 p}{\partial x^2} + O(h^2)$,

$\frac{p_{i,j-1} - p_{i,j}}{h} = \frac{h}{2} \frac{\partial^2 p}{\partial y^2} - \frac{\partial p}{\partial y} + O(h^2)$ and $\frac{p_{i,j+1} - p_{i,j}}{h} = \frac{h}{2} \frac{\partial^2 p}{\partial y^2} + \frac{\partial p}{\partial y} + O(h^2)$.

$$\begin{aligned}
(\rho^I + \rho^{II})\ddot{v}_{i,j} &= \frac{2g_2^I}{h^2d}(v_{i,j-1} - v_{i,j}) + \frac{2g_2^{II}}{h^2d}(v_{i,j+1} - v_{i,j}) \\
&+ \frac{1}{h^2d} \left(g_3^I + \frac{\eta^I}{4h^2} \right) (v_{i+1,j-1} + v_{i-1,j-1} - 2v_{i,j}) \\
&+ \frac{1}{h^2d} \left(g_3^{II} + \frac{\eta^{II}}{4h^2} \right) (v_{i+1,j+1} + v_{i-1,j+1} - 2v_{i,j}) \\
&+ \frac{1}{h^2d} \left(g_3^I - \frac{\eta^I}{4h^2} \right) (u_{i-1,j-1} - u_{i+1,j-1}) \\
&+ \frac{1}{h^2d} \left(g_3^{II} - \frac{\eta^{II}}{4h^2} \right) (u_{i+1,j+1} - u_{i-1,j+1}) \\
&+ \frac{\mu^I - \lambda^I - \mu^{II} + \lambda^{II}}{2h^2} (u_{i+1,j} - u_{i-1,j})
\end{aligned} \tag{2-89}$$

where the correction terms in eqns. (2-88) and (2-89) are circled and the spring constants are given in eqns. (2-76) through (2-83).

2-4 CONCLUSIONS

A mass-spring lattice model (MSLM) convergence analysis reveals that, for materials having Poisson's ratio less than 0.4, 20 grid spaces per S -wavelength are required for the phase speed errors to be less than 1%. As Poisson's ratio approaches the incompressible limit, the computational expense increases dramatically. Additionally, correction terms necessary for the precise implementation of MSLM traction boundaries are formulated and verified through a numerical example.

References:

- 2-1. A.E.H. Love. *A Treatise on the Mathematical Theory of Elasticity* 4th ed., pp. 616-627. Dover Publications, New York (1944).
- 2-2. K. Harumi, T. Igarashi and T. Saito. *J. Nondestr. Test. Jpn.* **27**: 807 (1978).
- 2-3. K. Harumi, H. Okada, T. Saito and T. Fujimori. *10th World Conference on Non-Destructive Testing*, pp. 85-94. (1982).
- 2-4. K. Harumi, H. Okada, T. Saito and T. Fujimori. *10th World Conference on Non-Destructive Testing*, pp. 95-101. (1982).
- 2-5. K. Harumi, H. Okada, T. Saito and T. Fujimori. *10th World Conference on Non-Destructive Testing*, pp. 102-110, (1982).
- 2-6. A. Ohtsuki, and K. Harumi. *Earthqua. Eng. Struct. Dyn.* **11**:441 (1983).
- 2-7. A. Ohtsuki, H. Yamahara and K. Harumi. *Earthqua. Eng. Struct. Dyn.* **12**:37 (1984).

- 2-8. K. Harumi. *NDT Int.* **19**:315 (1986).
- 2-9. K. Harumi, M. Uchida, T. Miyajima and Y. Ogura. *NDT&E Int.* **25**:135 (1992).
- 2-10. J.H. Williams, Jr. *Fundamentals of Applied Dynamics*, pp.717-718. John Wiley & Sons, New York (1996).
- 2-11. S. Ayyadurai. *Visualization of Wave Propagation in Elastic Solids Using a Mass-Spring Lattice Model*. Master's Thesis. M.I.T, Cambridge, MA (1989).
- 2-12. S. Ayyadurai. *Computational Wave Propagation in Isotropic and Anisotropic Media Using the Generalized Mass-Spring Lattice Model*. Master's Thesis. M.I.T, Cambridge, MA (1990).
- 2-13. H. Yim and Y. Choi. *Mater. Eval.* **58**:889 (2000).
- 2-14. H. Yim and Y. Sohn. *IEEE Trans. Ultrason. Ferroelectr. Freq. Control.* **47**:549 (2000).
- 2-15. Y. Sohn and S. Krishnaswamy. *Ultrasonics.* **39**:543 (2002).
- 2-16. Y. Sohn and S. Krishnaswamy. *J. Acoust. Soc. Am.* **115**:172 (2004).
- 2-17. P.P. Delsanto, T. Whitcombe, H.H. Chaskelis and R.B. Mignogna. *Wave Motion* **16**:65 (1992)
- 2-18. P.P. Delsanto, R.S. Schecter, H.H. Chaskelis, R.B. Mignogna and R. Kline. *Wave Motion* **20**:295 (1994).
- 2-19. P.P. Delsanto and M. Scaldierandi. *J. Acoust. Soc. Am.* **104**:2584 (1998).
- 2-20. H. Yim and C.-J. Lee. *Review of Quantitative Nondestructive Evaluation*. D.O. Thompson and D.E. Chimenti (eds). **21**:152 (2002).
- 2-21. H. Yamawaki and T. Saito. *Nondestr. Test. Eval.* **8-9**:379 (1992).
- 2-22. J.D. Achenbach. *Wave Propagation in Elastic Solids*. Amsterdam, North-Holland Publishing Co., New York (1975).
- 2-23. K.F. Graff. *Wave Motion in Elastic Solids*. Dover Publications Inc., New York (1975).
- 2-24. H. Yim. unpublished research (2003).
- 2-25. Z. Bian, R.J. Wang, W.H. Wang, T. Zhang and A. Inoue. *Adv. Funct. Mater.* **14**:55 (2004).
- 2-26. H. Lamb. *Philosophical Transactions of the Royal Society of London. Series A, Containing Papers of a Mathematical or Physical Character.* **203**:1 (1904).

APPENDIX 2A—Force and Constitutive Expressions for Traction Boundary Condition

Consider a finite continuum element in the vicinity of a traction boundary as shown in Fig. 2A-1. The various forces on the element are

$$F_{xx+} = D \left\{ \frac{h\sigma_{xx}}{2} + \frac{h^2}{4} \frac{\partial \sigma_{xx}}{\partial x} \Big|_{i,j} - \frac{h^2}{8} \frac{\partial \sigma_{xx}}{\partial y} \Big|_{i,j} \right\} + O(h^3) \quad (2A-1)$$

$$F_{xx-} = D \left\{ \frac{h\sigma_{xx}}{2} - \frac{h^2}{4} \frac{\partial \sigma_{xx}}{\partial x} \Big|_{i,j} - \frac{h^2}{8} \frac{\partial \sigma_{xx}}{\partial y} \Big|_{i,j} \right\} + O(h^3) \quad (2A-2)$$

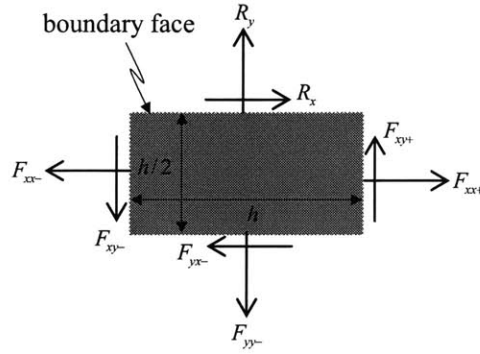


Fig. 2A-1—Free body diagram of element in vicinity of traction boundary.

$$F_{xy+} = D \left\{ \frac{h\sigma_{xy}}{2} + \frac{h^2}{4} \frac{\partial \sigma_{xy}}{\partial x} \Big|_{i,j} - \frac{h^2}{8} \frac{\partial \sigma_{xy}}{\partial y} \Big|_{i,j} \right\} + O(h^3) \quad (2A-3)$$

$$F_{xy-} = D \left\{ \frac{h\sigma_{xy}}{2} - \frac{h^2}{4} \frac{\partial \sigma_{xy}}{\partial x} \Big|_{i,j} + \frac{h^2}{8} \frac{\partial \sigma_{xy}}{\partial y} \Big|_{i,j} \right\} + O(h^3) \quad (2A-4)$$

$$F_{yy-} = D \left\{ h\sigma_{yy} - \frac{h^2}{2} \frac{\partial \sigma_{yy}}{\partial y} \Big|_{i,j} \right\} + O(h^3) \quad (2A-5)$$

$$F_{yx-} = D \left\{ h\sigma_{xy} - \frac{h^2}{2} \frac{\partial \sigma_{xy}}{\partial y} \Big|_{i,j} \right\} + O(h^3) \quad (2A-6)$$

where D is the unit depth, h is the grid space of the finite continuum element (which is significant in numerical modeling but here is arbitrary), and the constitutive equations are

$$\sigma_{xx} = (\lambda + 2\mu) \frac{\partial u}{\partial x} + \lambda \frac{\partial v}{\partial y} \quad (2A-7)$$

$$\sigma_{yy} = (\lambda + 2\mu) \frac{\partial v}{\partial y} + \lambda \frac{\partial u}{\partial x} \quad (2A-8)$$

$$\sigma_{xy} = \mu \left(\frac{\partial u}{\partial y} + \frac{\partial v}{\partial x} \right) \quad (2A-9)$$

APPENDIX 2B—Lamb's Problem

As shown in Fig. 2B-1, consider a normal point line source, having peak magnitude Q and temporal variation $q(t)$, acting at the origin of a half-space ($y < 0$) having

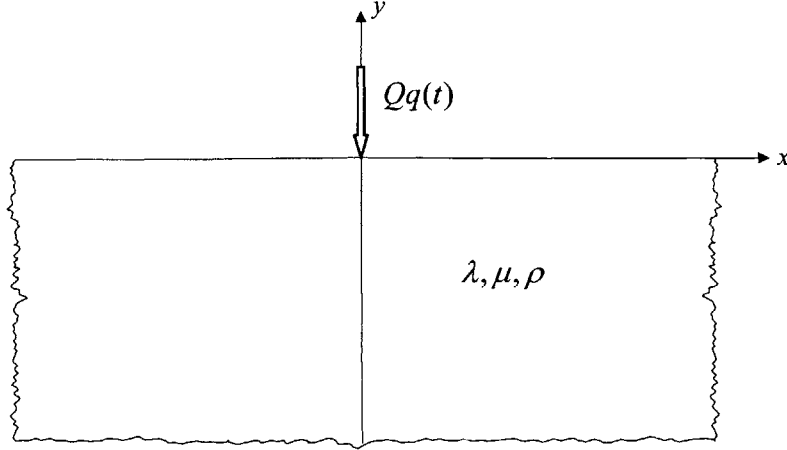


Fig. 2B-1—Point force per unit depth having maximum intensity Q and temporal variation $q(t)$ acting at origin of elastic half-space having Lamé constants λ and μ , and density ρ .

Lamé constants λ and μ , and density ρ . This appendix summarizes Lamb's solution for the resulting surface displacements [2B-1].

Solution [2B-1]

For $x \geq 0$, the horizontal and vertical surface displacements, u and v , respectively, are

$$u = -\frac{Q}{\mu} Hq(t - s_R x) - \frac{Q}{\mu} \frac{2}{\pi} \int_{s_L}^{s_T} \frac{s_T^2 \theta (2\theta^2 - s_T^2) \sqrt{\theta^2 - s_L^2} \sqrt{s_T^2 - \theta^2}}{(2\theta^2 - s_T^2)^4 + 16\theta^4 (\theta^2 - s_L^2)(s_T^2 - \theta^2)} q(t - \theta x) d\theta \quad (2B-1)$$

$$v = \frac{Q}{\mu} \frac{1}{\pi} \int_{s_L}^{s_T} \frac{s_T^2 (2\theta^2 - s_T^2)^2 \sqrt{\theta^2 - s_L^2}}{(2\theta^2 - s_T^2)^4 + 16\theta^4 (\theta^2 - s_L^2)(s_T^2 - \theta^2)} q(t - \theta x) d\theta \quad (2B-2)$$

$$+ \frac{Q}{\mu} \frac{1}{\pi} P \int_{s_T}^{\infty} \frac{s_T^2 \sqrt{\theta^2 - s_L^2}}{(2\theta^2 - s_T^2)^2 - 4\theta^2 \sqrt{\theta^2 - s_L^2} \sqrt{\theta^2 - s_T^2}} q(t - \theta x) d\theta$$

where s_T is the transverse wave slowness (inverse wave velocity) given by

$$s_T = \sqrt{\frac{\rho}{\mu}} \quad (2B-3)$$

s_L is the longitudinal wave slowness given by

$$s_L = \sqrt{\frac{\rho}{\lambda + 2\mu}} \quad (2B-4)$$

s_R is the Rayleigh wave slowness, which is given by the real root of the equation

$$(2s_R^2 - s_T^2)^2 - 4s_R^2 \sqrt{s_R^2 - s_L^2} \sqrt{s_R^2 - s_T^2} = 0 \quad (2B-5)$$

Also,

$$H = -\frac{s_R (2s_R^2 - s_T^2 - 2\sqrt{s_R^2 - s_L^2} \sqrt{s_R^2 - s_T^2})}{F} \quad (2B-6)$$

where

$$F = \frac{4(-2s_L^2 s_T^2 s_R + 3(s_L^2 + s_T^2)s_R^3 - 4s_R^5 + 4s_R^3 \sqrt{s_R^2 - s_L^2} \sqrt{s_R^2 - s_T^2})}{\sqrt{s_R^2 - s_L^2} \sqrt{s_R^2 - s_T^2}} - 8s_T^2 s_R \quad (2B-7)$$

It is noted that P in eqn. (2B-2) denotes the principal value of the integral, which is defined as [2B-2]

$$P \int_a^b f(\xi) d\xi = \lim_{\varepsilon \rightarrow 0} \left(\int_a^{c-\varepsilon} f(\xi) d\xi + \int_{c+\varepsilon}^b f(\xi) d\xi \right) \quad (2B-8)$$

where $a < c < b$ and a non-integrable singularity exists at $f(c)$. (In the second integral of eqn. (2B-2) the non-integrable singularity occurs at $\theta = s_R$.) All the integrals in eqns. (2B-1) and (2B-2) can be evaluated numerically, for example, via adaptive Simpson quadrature as implemented in MATLAB's "quad" function [2B-3].

The surface displacements for $x < 0$ are given by replacing $(t - \zeta x)$ with $(t + \zeta x)$ in eqns. (2B-1) and (2B-2) and reversing the sign of the horizontal displacements in eqn. (2B-1).

Far Field [2B-1]

In the far field, the surface displacements reduce to

$$u = -\frac{Q}{\mu} Hq(t - s_R x) \quad (2B-9)$$

$$v = -\frac{Q}{\mu} Kq'(t - s_R x) \quad (2B-10)$$

where

$$K = -\frac{s_T^2 \sqrt{s_R^2 - s_L^2}}{F} \quad (2B-11)$$

and the complementary temporal function $q'(t)$ satisfies

$$q(t) = \frac{1}{\pi} \int_0^{\infty} d\omega \int_{-\infty}^{\infty} \bar{q}(\omega) \cos \omega(t - \tau) d\tau \quad (2B-12)$$

$$q'(t) = \frac{1}{\pi} \int_0^{\infty} d\omega \int_{-\infty}^{\infty} \bar{q}(\omega) \sin \omega(t - \tau) d\tau \quad (2B-13)$$

Example

Consider, for example, $q(t)$ as a gaussian-modulated cosinusoidal function given by

$$q(t) = \exp\left(-\frac{1}{2}(\omega_{\sigma}t - \eta)^2\right) \cos(\omega_c t - \eta\omega_c\omega_{\sigma}^{-1}) \quad (2B-14)$$

where η is a nondimensional offset, ω_{σ} is the frequency standard deviation, and ω_c is the center frequency. The complementary temporal function $q'(t)$ is

$$q'(t) = \exp\left(-\frac{1}{2}(\omega_{\sigma}t - \eta)^2\right) \sin(\omega_c t - \eta\omega_c\omega_{\sigma}^{-1}) \quad (2B-15)$$

Snapshots of the normalized surface displacements in the vicinity of the line load for the case where Poisson's ratio equals 0.377, $\eta = 3.0$, and the normalized bandwidth parameter $\omega_c\omega_{\sigma}^{-1} = 5.0$ are shown in Fig 2B-2.

References:

- 2B-1. H. Lamb. *Philosophical Transactions of the Royal Society of London. Series A, Containing Papers of a Mathematical or Physical Character.* **203**:1 (1904).
- 2B-2. E. Kreyszig. *Advanced Engineering Mathematics* 7th ed., p. 851. John Wiley & Sons, New York (1993).
- 2B-3. The Mathworks (Natick, MA), MATLAB online support help guide: <http://www.mathworks.com/access/helpdesk/help/techdoc/ref/quad.html>

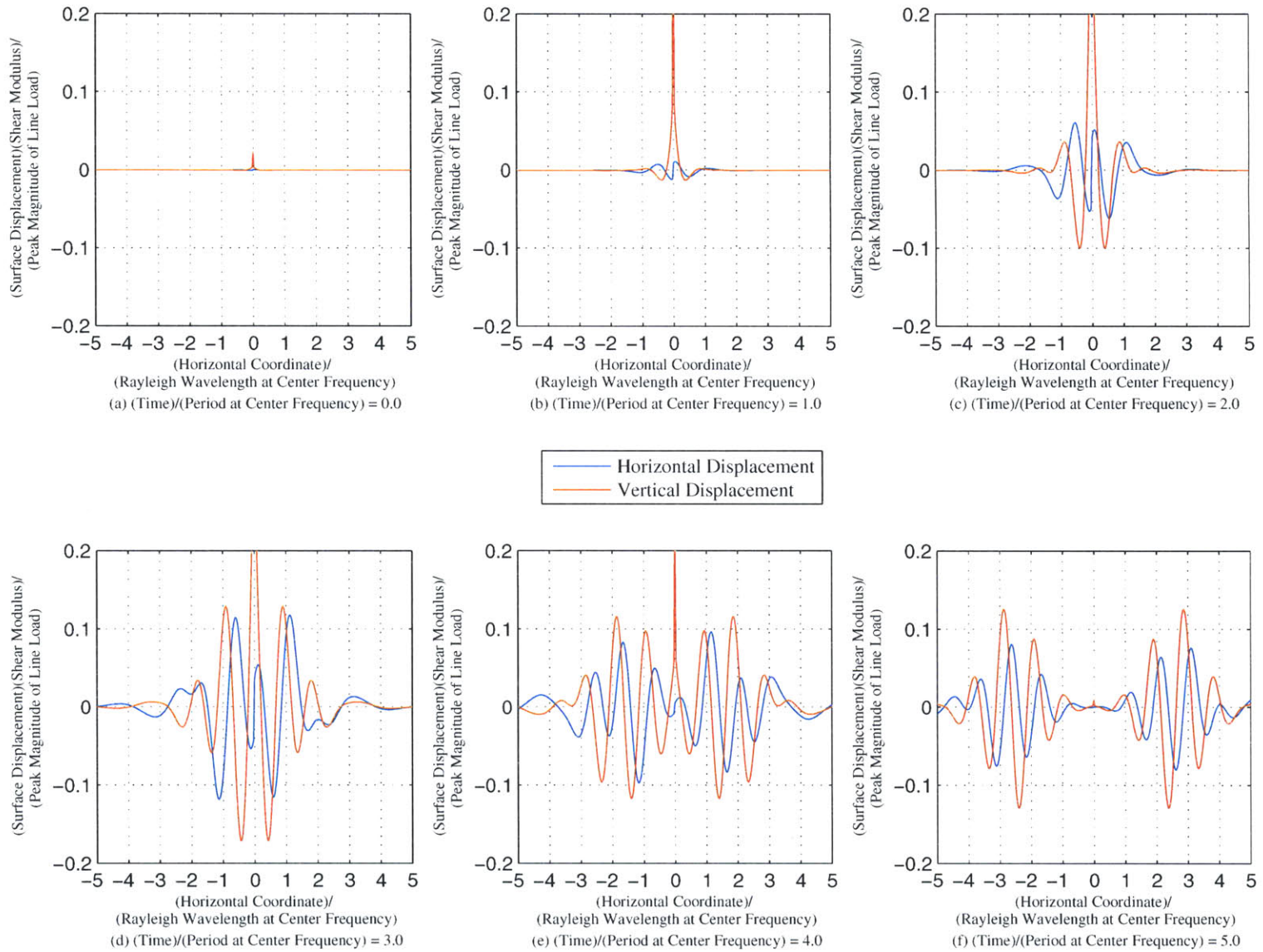


Fig. 2B-2—Snapshots of normalized surface displacements on elastic half-space due to normal line load having temporal variation of Gaussian-modulated cosinusoid. Here Poisson's ratio is 0.377, nondimensional offset is 3, and ratio of standard deviation frequency to center frequency is 0.2.

APPENDIX 2C—Force and Constitutive Expressions for Interface of Dissimilar Materials

Consider a finite heterogeneous continuum element in the vicinity of a perfect interface of dissimilar materials as shown in Fig. 2C-1. The various forces on the element are

$$F_{xx+}^I = D \left\{ \frac{h\sigma_{xx}^I}{2} + \frac{h^2}{4} \frac{\partial \sigma_{xx}^I}{\partial x} \Big|_{i,j} - \frac{h^2}{8} \frac{\partial \sigma_{xx}^I}{\partial y} \Big|_{i,j} \right\} + O(h^3) \quad (2C-1)$$

$$F_{xx-}^I = D \left\{ \frac{h\sigma_{xx}^I}{2} - \frac{h^2}{4} \frac{\partial \sigma_{xx}^I}{\partial x} \Big|_{i,j} - \frac{h^2}{8} \frac{\partial \sigma_{xx}^I}{\partial y} \Big|_{i,j} \right\} + O(h^3) \quad (2C-2)$$

$$F_{xy+}^I = D \left\{ \frac{h\sigma_{xy}^I}{2} + \frac{h^2}{4} \frac{\partial \sigma_{xy}^I}{\partial x} \Big|_{i,j} - \frac{h^2}{8} \frac{\partial \sigma_{xy}^I}{\partial y} \Big|_{i,j} \right\} + O(h^3) \quad (2C-3)$$

$$F_{xy-}^I = D \left\{ \frac{h\sigma_{xy}^I}{2} - \frac{h^2}{4} \frac{\partial \sigma_{xy}^I}{\partial x} \Big|_{i,j} - \frac{h^2}{8} \frac{\partial \sigma_{xy}^I}{\partial y} \Big|_{i,j} \right\} + O(h^3) \quad (2C-4)$$

$$F_{yy-}^I = D \left\{ h\sigma_{yy}^I - \frac{h^2}{2} \frac{\partial \sigma_{yy}^I}{\partial y} \Big|_{i,j} \right\} + O(h^3) \quad (2C-5)$$

$$F_{yy+}^I = D \left\{ h\sigma_{yy}^I - \frac{h^2}{2} \frac{\partial \sigma_{yy}^I}{\partial y} \Big|_{i,j} \right\} + O(h^3) \quad (2C-6)$$

$$F_{xx+}^{II} = D \left\{ \frac{h\sigma_{xx}^{II}}{2} + \frac{h^2}{4} \frac{\partial \sigma_{xx}^{II}}{\partial x} \Big|_{i,j} + \frac{h^2}{8} \frac{\partial \sigma_{xx}^{II}}{\partial y} \Big|_{i,j} \right\} + O(h^3) \quad (2C-7)$$

$$F_{xx-}^{II} = D \left\{ \frac{h\sigma_{xx}^{II}}{2} - \frac{h^2}{4} \frac{\partial \sigma_{xx}^{II}}{\partial x} \Big|_{i,j} + \frac{h^2}{8} \frac{\partial \sigma_{xx}^{II}}{\partial y} \Big|_{i,j} \right\} + O(h^3) \quad (2C-8)$$

$$F_{xy+}^{II} = D \left\{ \frac{h\sigma_{xy}^{II}}{2} + \frac{h^2}{4} \frac{\partial \sigma_{xy}^{II}}{\partial x} \Big|_{i,j} + \frac{h^2}{8} \frac{\partial \sigma_{xy}^{II}}{\partial y} \Big|_{i,j} \right\} + O(h^3) \quad (2C-9)$$

$$F_{xy-}^{II} = D \left\{ \frac{h\sigma_{xy}^{II}}{2} - \frac{h^2}{4} \frac{\partial \sigma_{xy}^{II}}{\partial x} \Big|_{i,j} + \frac{h^2}{8} \frac{\partial \sigma_{xy}^{II}}{\partial y} \Big|_{i,j} \right\} + O(h^3) \quad (2C-10)$$

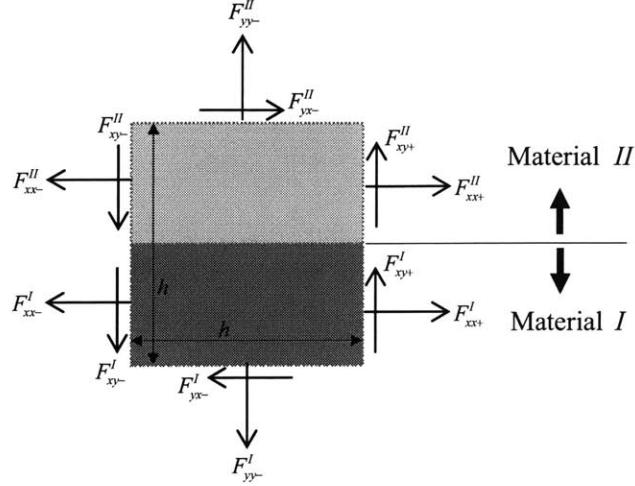


Fig. 2C-1—Free body diagram of heterogeneous continuum element in vicinity of perfect interface of Materials *I* and *II*.

$$F_{yy+}^{II} = D \left\{ h \sigma_{yy}^{II} + \frac{h^2}{2} \frac{\partial \sigma_{yy}^{II}}{\partial y} \Big|_{i,j} \right\} + O(h^3) \quad (2C-11)$$

$$F_{yx+}^{II} = D \left\{ h \sigma_{xy}^{II} + \frac{h^2}{2} \frac{\partial \sigma_{xy}^{II}}{\partial y} \Big|_{i,j} \right\} + O(h^3) \quad (2C-12)$$

where D is the unit depth, h is the grid space of the finite continuum element (which is significant in numerical modeling but here is arbitrary), and the constitutive equations are

$$\sigma_{xx}^I = (\lambda^I + 2\mu^I) \frac{\partial u}{\partial x} + \lambda^I \frac{\partial v}{\partial y} \quad (2C-13)$$

$$\sigma_{yy}^I = (\lambda^I + 2\mu^I) \frac{\partial v}{\partial y} + \lambda^I \frac{\partial u}{\partial x} \quad (2C-14)$$

$$\sigma_{xy}^I = \mu^I \left(\frac{\partial u}{\partial y} + \frac{\partial v}{\partial x} \right) \quad (2C-15)$$

$$\sigma_{xx}^{II} = (\lambda^{II} + 2\mu^{II}) \frac{\partial u}{\partial x} + \lambda^{II} \frac{\partial v}{\partial y} \quad (2C-16)$$

$$\sigma_{yy}^{II} = (\lambda^{II} + 2\mu^{II}) \frac{\partial v}{\partial y} + \lambda^{II} \frac{\partial u}{\partial x} \quad (2C-17)$$

$$\sigma_{xy}^{II} = \mu^{II} \left(\frac{\partial u}{\partial y} + \frac{\partial v}{\partial x} \right) \quad (2C-18)$$

In all the preceding equations, superscripts *I* and *II* denote parameters related to Materials *I* and *II*, respectively.

CHAPTER 3: FORMULATION OF MASS-SPRING-DASHPOT LATTICE MODEL

ABSTRACT: The mass-spring-dashpot lattice model (MSDLM), a numerical model of a viscoelastic standard linear solid, is presented. As an extension of the mass-spring-lattice model (MSLM), the MSDLM discretizes a viscoelastic continuum into an assemblage of particles interconnected with springs and dashpots. Via the dispersion relations of a standard linear solid, the MSDLM spring and dashpot constants are set to match the corresponding wave propagation phase speed and attenuation. The convergence, stability, and accuracy criteria for the MSDLM are presented for one and two-dimensional models. Further verification is provided through numerical examples.

CONTENTS:

3-1	Introduction.....	53
3-2	Analytical Model.....	53
	3-2.1 Stress-Dynamic Equations.....	53
	3-2.2 Dispersion Relations.....	55
3-3	Numerical Discretization.....	59
	3-3.1 One-Dimensional MSDLM.....	59
	3-3.2 Two-Dimensional MSDLM.....	62
3-4	Numerical Examples.....	68
	3-4.1 Material Properties.....	68
	3-4.2 One-Dimensional Examples.....	68
	3-4.3 Two-Dimensional Examples.....	71
3-5	Conclusions.....	79
3A	Derivation of Stress-Dynamic Equations and Dispersion Relations for Standard Linear Solid Having Single Relaxation Time.....	81
3B	Four Stage Runge-Kutta Method.....	91
3C	Convergence and Accuracy Criteria for the Mass-Spring-Dashpot Lattice Model.....	93
3D	Two-Dimensional MSDLM Schematic and Stress Dynamic Equations for Longitudinal Interface of Dissimilar Materials.....	129
3E	Steady-State Wave Propagation in One and Two-Dimensional Standard Linear Solids	132
3F	Absorbing Boundaries for Mass-Spring-Dashpot Lattice Model.....	147

NOMENCLATURE

Symbols

A	unit area	α	attenuation (Np/unit length)
b	extensional dashpot coefficient	Δt	numerical time step
C	Courant number	δ_{ij}	Kronecker delta, $\delta_{ij} = 1$ if $i = j$ and $\delta_{ij} = 0$ otherwise
c	phase speed	ε_{ij}	small strain tensor
e	base of natural logarithm	ϕ	generic elastic constant
D	unit depth	γ	rotational dashpot coefficient
f	force per unit volume	η	rotational spring constant
g	extensional spring constant	κ	wavelength
h	numerical grid space	λ, μ	Lamé constants
\hat{i}	imaginary number	λ', μ'	viscous constants
i, j	indicial notation for grid position	$\tilde{\lambda}, \tilde{\mu}$	relaxation functions
k	wavenumber	ν	Poisson's ratio
M	instantaneous modulus governing shear wave	Π	instantaneous modulus governing longitudinal waves
n	ratio of grid space per wavelength or time step per period	π	ratio of circle's circumference to diameter
P	relating to longitudinal waves	ρ	density
r	dispersion ratio	σ_{ij}	stress tensor
S	relating to shear waves	τ	relaxation time
u, v	displacement	ω	circular frequency

Subscripts

h	relating to numerical grid space
P	relating to longitudinal waves
S	relating to shear waves
max, peak	relating to greatest magnitude in time or frequency
Δt	relating to numerical time step

3-1 INTRODUCTION

The historical evolution of the mass-spring-lattice model (MSLM) [3-1,3-2] as well as an investigation into its numerical accuracy was covered in Chapter 2. Most elastic wave models, including the MSLM and elastic implementations of the local interaction simulation approach (LISA) [3-3,3-4], are not capable of modeling material attenuation during wave propagation. Noncausal attenuation was introduced in a one-dimensional implementation of LISA [3-3]. A two-dimensional viscoelastic implementation of LISA was introduced [3-5], but lacked significant detail. In this chapter, a mass-spring-dashpot lattice model, or MSDLM, is formulated to incorporate viscous losses, thereby being capable of simulating wave phenomena in attenuating and viscoelastic materials, including media containing complex internal interfaces and discontinuities.

3-2 ANALYTICAL MODEL

3-2.1 Stress-Dynamic Equations

For an isotropic, linearly viscoelastic continuum, the constitutive and differential stress-dynamic equations are [3-6]

$$\sigma_{kl} = \tilde{\lambda}(t) * \dot{\varepsilon}_{mm} \delta_{kl} + 2\tilde{\mu}(t) * \dot{\varepsilon}_{kl} \quad (3-1)$$

$$\sigma_{kl,l} + f_k^b = \rho \ddot{u}_k \quad (3-2)$$

where σ_{kl} are the components of the Cauchy stress tensor, and ε_{kl} are the components of small strain given by

$$\varepsilon_{kl} = \frac{1}{2}(u_{k,l} + u_{l,k}) \quad (3-3)$$

δ_{kl} is the Kronecker delta, $*$ denotes a convolution integral, $\tilde{\lambda}(t)$ and $\tilde{\mu}(t)$ are independent stress relaxation functions defined below, f_k^b are the components of the body force per unit volume, ρ is density, and u_k are the components of displacement.

Of the simple spring and dashpot mechanical analogs describing basic viscoelastic behavior—Maxwell, Kelvin-Voigt and the standard linear solid—only the standard linear solid has non-zero bounded phase speeds at extreme frequencies. (A detailed discussion of material behavior based on such mechanical models is given by Kolsky [3-7].) For a

standard linear solid described by a single stress relaxation time τ , the stress relaxation functions have the following form:

$$\tilde{\lambda}(t) = \lambda + \frac{\lambda'}{\tau} \exp\left(-\frac{t}{\tau}\right) \quad (3-4)$$

$$\tilde{\mu}(t) = \mu + \frac{\mu'}{\tau} \exp\left(-\frac{t}{\tau}\right) \quad (3-5)$$

Here, λ and μ are the Lamé constants and λ' and μ' are the analogous viscoelastic constants.

By substituting eqns. (3-3), (3-4) and (3-5) into eqn. (3-1), and applying the Laplace transform, the constitutive and differential stress-dynamic equations can be reformulated as (Appendix 3A)

$$\dot{f}_k = -\frac{1}{\tau} f_k + \frac{r_p \Pi - r_s M}{\tau} u_{l,lk} + \frac{r_s M}{\tau} u_{k,ll} + (\Pi - M) \dot{u}_{l,lk} + M \dot{u}_{k,ll} \quad (3-6)$$

$$\ddot{u}_k = \frac{1}{\rho} (f_k + f_k^b) \quad (3-7)$$

provided the initial condition

$$f_k(0) = (\Pi - M) u_{l,lk}(0) + M u_{k,ll}(0) \quad (3-8)$$

is satisfied and where

$$f_k = \sigma_{kl,l} \quad (3-9)$$

$$r_p = \frac{\tilde{\lambda}(\infty) + 2\tilde{\mu}(\infty)}{\tilde{\lambda}(0) + 2\tilde{\mu}(0)} = \left(1 + \frac{1}{\tau} \frac{\lambda' + 2\mu'}{\lambda + 2\mu}\right)^{-1} \quad (3-10)$$

$$r_s = \frac{\tilde{\mu}(\infty)}{\tilde{\mu}(0)} = \left(1 + \frac{1}{\tau} \frac{\mu'}{\mu}\right)^{-1} \quad (3-11)$$

$$\Pi = \tilde{\lambda}(0) + 2\tilde{\mu}(0) = \lambda + 2\mu + \frac{\lambda' + 2\mu'}{\tau} \quad (3-12)$$

and

$$M = \tilde{\mu}(0) = \mu + \frac{\mu'}{\tau} \quad (3-13)$$

Solving eqns. (3-10) through (3-13) for the Lamé and viscous constants yields

$$\lambda = r_p \Pi - 2r_s M \quad (3-14)$$

$$\mu = r_S M \quad (3-15)$$

$$\lambda' = \tau[(1 - r_P)\Pi - 2(1 - r_S)M] \quad (3-16)$$

$$\mu' = \tau(1 - r_S)M \quad (3-17)$$

Via the uniqueness and thermodynamic conditions listed in [3-6], the following constraints on the standard linear solid parameters must be met:

$$\tau > 0 \quad (3-18)$$

$$\tilde{\mu}(0) > 0 \text{ or } M > 0 \quad (3-19)$$

$$3\tilde{\lambda}(0) + 2\tilde{\mu}(0) > 0 \text{ or } 3\Pi > 4M \quad (3-20)$$

$$1 \geq r_P \geq 0 \quad (3-21)$$

$$1 \geq r_S \geq 0 \quad (3-22)$$

3-2.2 Dispersion Relations

Consider a steady-state longitudinal plane wave attenuated in the direction of wave propagation and having the form

$$u_k(x_1, x_2, x_3, t) = n_k u_0 \exp[-\alpha_P n_m x_m + \hat{i}(k_P n_m x_m - \omega t)] \quad (3-23)$$

and a similar steady-state shear plane wave having the form

$$u_k(x_1, x_2, x_3, t) = n'_k u_0 \exp[-\alpha_S n_m x_m + \hat{i}(k_S n_m x_m - \omega t)] \quad (3-24)$$

where n_k are the components of the unit wave vector, n'_k are the components of a unit vector orthogonal to the wave vector (that is, $n_k n'_k = 0$), u_0 is the wave amplitude at the phase plane containing the origin, α is the attenuation, \hat{i} is equal to $\sqrt{-1}$, k is the wavenumber, subscripts P and S denote the respective properties of longitudinal and shear waves, and ω is the circular frequency.

In the absence of body forces, substituting eqns. (3-23) and (3-24) into eqns. (3-6) and (3-7), and eliminating f_k , give expressions for attenuation and wavenumber of P and S waves as (Appendix A)

$$\alpha_P^2 = \frac{\rho \omega^2}{2r_P \Pi} \left(\sqrt{\frac{1 + \omega^2 \tau^2}{1 + r_P^{-2} \omega^2 \tau^2}} - \frac{1 + r_P^{-1} \omega^2 \tau^2}{1 + r_P^{-2} \omega^2 \tau^2} \right) \quad (3-25)$$

$$\alpha_S^2 = \frac{\rho \omega^2}{2r_S M} \left(\sqrt{\frac{1 + \omega^2 \tau^2}{1 + r_S^{-2} \omega^2 \tau^2}} - \frac{1 + r_S^{-1} \omega^2 \tau^2}{1 + r_S^{-2} \omega^2 \tau^2} \right) \quad (3-26)$$

$$k_p^2 = \frac{\rho\omega^2}{2r_p\Pi} \left(\sqrt{\frac{1+\omega^2\tau^2}{1+r_p^{-2}\omega^2\tau^2}} + \frac{1+r_p^{-1}\omega^2\tau^2}{1+r_p^{-2}\omega^2\tau^2} \right) \quad (3-27)$$

$$k_s^2 = \frac{\rho\omega^2}{2r_s\text{M}} \left(\sqrt{\frac{1+\omega^2\tau^2}{1+r_s^{-2}\omega^2\tau^2}} + \frac{1+r_s^{-1}\omega^2\tau^2}{1+r_s^{-2}\omega^2\tau^2} \right) \quad (3-28)$$

Parameters r_p and r_s represent the extent of dispersion in the standard linear solid; each is equal to the squared ratio of the minimum P or S phase speed (at low frequencies) to the maximum P or S phase speed (at high frequencies). As r_p and r_s approach zero, the minimum phase speed approaches zero (Maxwell model). As r_p and r_s approach one, the phase speed is constant (elastic model).

Table 3-1 gives the wave propagation properties of the standard linear solid in the low frequency limit ($\omega\tau \ll r_p, r_s$), an intermediate frequency limit

$\left(\omega\tau \rightarrow r_p \sqrt{\frac{3+r_p}{1+3r_p}}, r_s \sqrt{\frac{3+r_s}{1+3r_s}} \right)$, and the high frequency limit ($\omega\tau \gg 1$). At the extreme

limits, there is a similarity to elastic wave propagation; the phase speed of the wave is constant and the wave is non-dispersive. The attenuation, on the other hand, is proportional to the square of the frequency at low frequencies and constant at high frequencies. As the frequency approaches the intermediate limit, the attenuation is directly proportional to frequency for a relatively narrow frequency band. The phase speed reveals significant dispersion at the intermediate limit. As a summary, a logarithmic plot of attenuation as a function of frequency and a semi-logarithmic plot of phase speed as a function of frequency are shown in Figs. 3-1 and 3-2, respectively.

The parameters τ , r_p , r_s , Π , and M can be calculated from a numerical fit of frequency-dependent ultrasonic phase speed and attenuation data to approximate the material behavior over a limited frequency range.

Table 3-1—Standard linear solid wave propagation properties at limiting frequencies.

Property	Low Frequency Limit		Intermediate Frequency Limit		High Frequency Limit	
	Longitudinal Wave, P $\omega\tau \ll r_p$	Shear Wave, S $\omega\tau \ll r_s$	Longitudinal Wave, P $\omega\tau \rightarrow r_p \sqrt{\frac{3+r_p}{1+3r_p}}$	Shear Wave, S $\omega\tau \rightarrow r_s \sqrt{\frac{3+r_s}{1+3r_s}}$	Longitudinal Wave, P $\omega\tau \gg 1$	Shear Wave, S $\omega\tau \gg 1$
Phase Speed, c	$c_{\min,P} = \sqrt{\frac{r_p \Pi}{\rho}}$	$c_{\min,S} = \sqrt{\frac{r_s M}{\rho}}$	$c_P \approx c_P(\omega_{P,0}) + (\omega - \omega_{P,0})c'_P(\omega_{P,0})$	$c_S \approx c_S(\omega_{S,0}) + (\omega - \omega_{S,0})c'_S(\omega_{S,0})$	$c_{\max,P} = \sqrt{\frac{\Pi}{\rho}}$	$c_{\max,S} = \sqrt{\frac{M}{\rho}}$
Attenuation, α (Np/unit length)	$\alpha_P = \frac{\omega^2 \tau (1-r_p)}{2r_p c_{\min,P}}$	$\alpha_S = \frac{\omega^2 \tau (1-r_s)}{2r_s c_{\min,S}}$	$\alpha_P \approx \omega \sqrt{\frac{\rho}{\Pi}} \sqrt{\frac{1+2r_p}{8r_p} - \frac{5+r_p}{8(1+r_p)}}$	$\alpha_S \approx \omega \sqrt{\frac{\rho}{M}} \sqrt{\frac{1+2r_s}{8r_s} - \frac{5+r_s}{8(1+r_s)}}$	$\alpha_P = \frac{1-r_p}{2\tau c_{\max,P}}$	$\alpha_S = \frac{1-r_s}{2\tau c_{\max,S}}$

where

$$c(\omega_{P,0}) = \sqrt{\frac{\Pi}{\rho} \left(\frac{5+r_p}{8(1+r_p)} + \frac{3+2r_p}{8r_p} \right)^{-1/2}}, \quad c'(\omega_{P,0}) = \tau(1-r_p) \sqrt{\frac{\Pi}{\rho} \left(\frac{2(5+r_p)}{(1+r_p)} + \frac{2(3+2r_p)}{r_p} \right)^{1/2} \frac{1}{(1+3r_p)^{1/2} (3+r_p)^{3/2}}}, \quad c(\omega_{S,0}) = \sqrt{\frac{M}{\rho} \left(\frac{5+r_s}{8(1+r_s)} + \frac{3+2r_s}{8r_s} \right)^{-1/2}}, \quad c'(\omega_{S,0}) = \tau(1-r_s) \sqrt{\frac{M}{\rho} \left(\frac{2(5+r_s)}{(1+r_s)} + \frac{2(3+2r_s)}{r_s} \right)^{1/2} \frac{1}{(1+3r_s)^{1/2} (3+r_s)^{3/2}}}$$

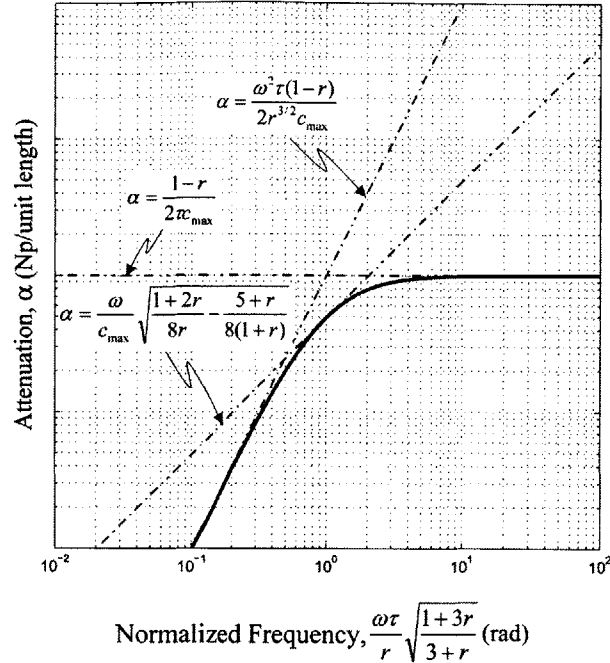


Fig. 3-1—Attenuation of standard linear solid model as function of circular frequency ω , relaxation time τ , dispersion coefficient r , and maximum phase speed c_{\max} , which shows three distinct dependences on frequency: quadratic at low frequencies, proportional at intermediate frequencies, and constant at high frequencies.

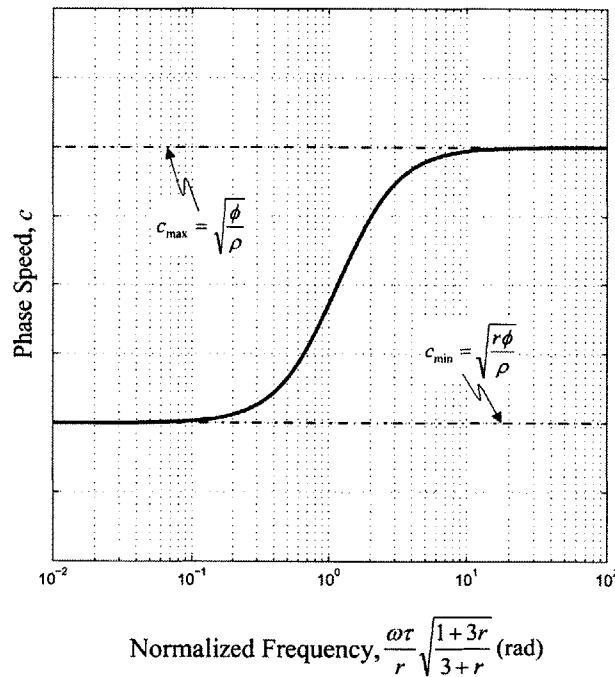


Fig. 3-2—Phase speed of standard linear solid model as function of elastic constant ϕ , which can represent either Π or M for P or S waves, respectively, density ρ , dispersion coefficient r , circular frequency ω , and relaxation time τ , which reveals a minimum phase speed at low frequencies and a maximum phase speed at high frequencies.

3-3 NUMERICAL DISCRETIZATION

Wave phenomena in standard linear solids can be simulated and visualized via the mass-spring-dashpot lattice model (MSDLM). In this section, the numerics of the MSDLM discretization are explored before proceeding to numerical examples.

3-3.1 One-dimensional MSDLM

The numerical discretization via the MSDLM begins with the definition of a unit cell. The MSDLM unit cell specifies the particle positions, particle mass, and all particle neighbor interactions within the cell. Each one-dimensional unit cell contains two half-particles separated by one grid space h . For a MSLM unit cell, the neighbor interaction is simply an extensional linear spring. In the MSDLM, however, the neighbor interaction is physically represented by an extensional standard linear element—an extensional spring in parallel with an extensional dashpot and extensional spring in series.

Schematics and stress-dynamic equations for various interaction and boundary conditions can be realized through the connection of unit cells to form particle-centered computational cells as given in Table 3-2. In the one-dimensional case, a connection is a rigid fusing of adjacent half-particles, where the inertial quantities are averaged according to LISA [3-4] rather than the averaging of neighbor interactions used in MSLM [3-2]*. To discretize an interior particle, identical unit cells are connected around a central particle. At a free surface, no connection is necessary; the stress-dynamic equations are simply formed by updating and summing the forces acting on the particle of interest. Prescribed motion boundaries and the perfect interface of dissimilar materials are also given in Table 3-2. (Imperfect interfaces are incorporated into the MSDLM in [3-8] using a contact quality factor introduced in [3-4].)

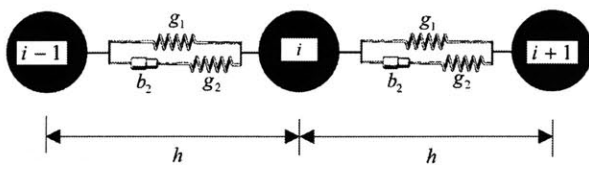
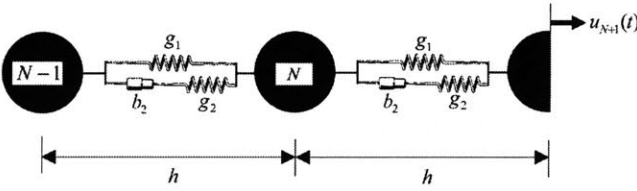
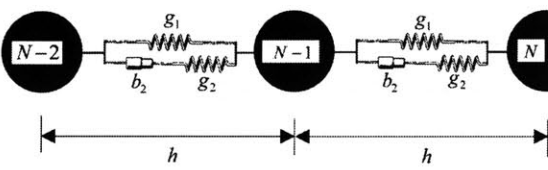
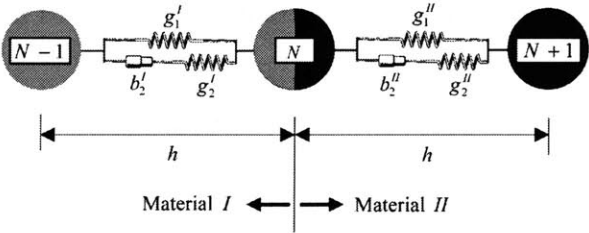
The interior discretized stress-dynamic equations must be consistent with the continuum stress-dynamic equations. Reformulating eqns. (3-6) and (3-7) for wave propagation in the x -direction yields

$$\frac{\partial f}{\partial t} = -\frac{1}{\tau} f + \frac{r\phi}{\tau} \frac{\partial^2 u}{\partial x^2} + \phi \frac{\partial^2 \dot{u}}{\partial x^2} \quad (3-29)$$

$$\frac{\partial u}{\partial t} = \dot{u} \quad (3-30)$$

* This choice allows for a precise imposition of continuity of traction and displacement at longitudinal interfaces.

Table 3-2—One-dimensional MSDLM schematics and stress-dynamic equations for various boundary and interaction configurations.

Schematics	Stress-dynamic equations
<p style="text-align: center;">Interior</p> 	$\frac{df_i}{dt} = -\frac{f_i}{\tau} + \frac{g_1}{\rho h A} (u_{i+1} - 2u_i + u_{i-1}) + \frac{g_1 + g_2}{h A} (\dot{u}_{i+1} - 2\dot{u}_i + \dot{u}_{i-1}) \quad (T2.1)$ $\frac{du_i}{dt} = \dot{u}_i \quad (T2.2)$ $\frac{d\dot{u}_i}{dt} = \frac{1}{\rho} (f_i + f_{bi}) \quad (T2.3)$ <p>where, $\tau = b_2 / g_2$ (T2.4)</p>
<p style="text-align: center;">Prescribed Motion Boundary (for a fixed boundary, $u_{N+1}(t) = 0$)</p> 	$\frac{df_N}{dt} = -\frac{f_N}{\tau} + \frac{g_1}{\rho h A} (u_{N+1}(t) - 2u_N + u_{N-1}) + \frac{g_1 + g_2}{h A} (\dot{u}_{N+1}(t) - 2\dot{u}_N + \dot{u}_{N-1}) \quad (T2.5)$ $\frac{du_N}{dt} = \dot{u}_N \quad (T2.6)$ $\frac{d\dot{u}_N}{dt} = \frac{1}{\rho} (f_N + f_{bN}) \quad (T2.7)$ <p>where, $\tau = b_2 / g_2$ (T2.8)</p>
<p style="text-align: center;">Free Surface</p> 	$\frac{df_{N-\frac{1}{2}}}{dt} = -\frac{f_{N-\frac{1}{2}}}{\tau} + \frac{g_1}{\rho h A} (u_N - u_{N-1}) + \frac{g_1 + g_2}{h A} (\dot{u}_N - \dot{u}_{N-1}) \quad (T2.9)$ $\frac{du_N}{dt} = \dot{u}_N \quad (T2.10)$ $\frac{d\dot{u}_N}{dt} = \frac{2}{\rho} (-f_{N-\frac{1}{2}} + f_{sN}) \quad (T2.11)$ <p>where, $\tau = b_2 / g_2$ (T2.12)</p>
<p style="text-align: center;">Perfect Interface of Dissimilar Materials</p>  <p style="text-align: center;">Material I ← → Material II</p>	$\frac{df_{N-\frac{1}{2}}}{dt} = -\frac{f_{N-\frac{1}{2}}}{\tau^I} + \frac{g_1^I}{\tau^I h A} (u_N - u_{N-1}) + \frac{g_1^I + g_2^I}{h A} (\dot{u}_N - \dot{u}_{N-1}) \quad (T2.13)$ $\frac{df_{N+\frac{1}{2}}}{dt} = -\frac{f_{N+\frac{1}{2}}}{\tau^{II}} + \frac{g_1^{II}}{\tau^{II} h A} (u_{N+1} - u_N) + \frac{g_1^{II} + g_2^{II}}{h A} (\dot{u}_{N+1} - \dot{u}_N) \quad (T2.14)$ $\frac{du_N}{dt} = \dot{u}_N \quad (T2.15)$ $\frac{d\dot{u}_N}{dt} = \frac{2}{\rho^I + \rho^{II}} (f_{N+\frac{1}{2}} - f_{N-\frac{1}{2}} + f_{bN}) \quad (T2.16)$ <p>where $\tau^I = b_2^I / g_2^I$ (T2.17), and $\tau^{II} = b_2^{II} / g_2^{II}$ (T2.18)</p>

Notes: A is unit area orthogonal to direction of force. Each f_{bi} and f_{si} are body force per particle volume and surface traction per particle volume acting on particle i , respectively.

$$\frac{\partial \dot{u}}{\partial t} = \frac{1}{\rho} (f_b + f) \quad (3-31)$$

where u , r and ϕ can respectively represent either u , r_p and Π (longitudinal wave); or v , r_s and M (vertically polarized shear wave); or w , r_s and M (horizontally polarized shear wave). Expanding eqn. (T2.1), located in Table 3-2, via the Taylor series in the limit as $h \rightarrow 0$ and comparing the result with eqn. (3-29), the one-dimensional MSDLM is spatially consistent with the governing PDEs if

$$g_1 = \frac{r\phi A}{h} \quad (3-32)$$

$$g_2 = \frac{(1-r)\phi A}{h} \quad (3-33)$$

and

$$\tau = \frac{b_2}{g_2} \quad (3-34)$$

where A is a unit area.

Equations (T2.1) through (T2.3) can be numerically integrated via the classical fourth-order Runge-Kutta explicit algorithm ([3-9] and Appendix 3B). Von Neumann analysis (Appendix 3C) has shown that for *stability*, the integration numerical time step Δt must satisfy

$$\frac{\Delta t}{\tau} \leq 2.78 \quad (3-35)$$

and the Courant number C corresponding to the highest phase velocity c_{\max} must satisfy

$$C \equiv \frac{c_{\max} \Delta t}{h} \leq 1.30 \quad (3-36)$$

where

$$c_{\max} = \sqrt{\phi / \rho} \quad (3-37)$$

In accordance with the Lax equivalence theorem [3-10], the demonstrated *consistency* and *stability* ensure the MSDLM's *convergence*.

Convergence implies the numerical solution approaches the continuum solution as $h \rightarrow 0$ and $\Delta t \rightarrow 0$. To reduce the numerical phase and dissipation error to less than 1% of the corresponding continuum values in low dispersion materials ($0.25 \leq r \leq 1$), given

the maximum effective circular frequency needed to be accurately propagated through the model ω_{\max} , *accuracy* requires the number of grid spaces per smallest wavelength n_h , or

$$n_h = \frac{2\pi}{k(\omega_{\max})h} \quad (3-38)$$

be at least 20 (Appendix C). Given n_h , eqns. (3-35) and (3-36) represent two (2) conditions on the number of time steps per smallest period $n_{\Delta t}$, or

$$n_{\Delta t} = \frac{2\pi}{\omega_{\max} \Delta t} \quad (3-39)$$

By solving eqns. (3-38) and (3-39) for h and Δt , respectively, and substituting the results into eqn. (3-39), the first condition is found to be

$$n'_{\Delta t} \geq \frac{n_h}{1.30} \quad (3-40)$$

and substituting the result for Δt into eqn. (3-35), the second condition is found to be

$$n''_{\Delta t} \geq \frac{2\pi}{2.78\omega_{\max} \tau} \quad (3-41)$$

For high frequencies ($\omega_{\max} \tau \gg 1$), $n_{\Delta t}$ is approximately equal to n_h , which is numerically satisfactory. However, for low frequencies ($\omega_{\max} \tau \ll 1$), $n_{\Delta t}$ is much greater than n_h ; that is, the integration becomes numerically stiff and much more expensive to evaluate.

3-3.2 Two-Dimensional MSDLM

The unit cell for a two-dimensional discretization via the MSDLM is given by horizontal and vertical neighbor interactions through an extensional standard linear element acting collinearly and diagonal neighbor interactions through an extensional and rotational standard linear element. As in the one-dimensional case, various boundary and interaction conditions are formed through the joining of adjacent unit cells to form particle-centered computational cells. In the two-dimensional case, the forces from neighbor interactions add in parallel. For example, the schematics and stress-dynamic equations for an interior particle are formed by joining four (4) identical unit cells around a central particle as shown in Table 3-3. To precisely impose traction boundary

conditions at a surface of a lattice model discretization, correction terms are necessary (refer to Chapter 2). The schematics and stress-dynamic equations in the vicinity of a particle located on the surface are shown in Table 3-4. (The schematics and stress-dynamic equations in the vicinity of a particle along a longitudinal interface of dissimilar materials are given in Appendix 3D.)

Fig. 3-3 shows a two-dimensional lattice model discretization for interior particles as well as particles having various boundary conditions such as traction free surfaces and interfaces of dissimilar materials.

The interior discretized stress-dynamic equations must be consistent with the continuum stress-dynamic equations. Reformulating eqns. (3-6) and (3-7) for plane strain conditions in the x - y plane yields

$$\begin{aligned} \frac{\partial f_x}{\partial t} = & -\frac{1}{\tau} f_x + \frac{r_p \Pi}{\tau} \frac{\partial^2 u}{\partial x^2} + \frac{r_p \Pi - r_s M}{\tau} \frac{\partial^2 v}{\partial x \partial y} + \frac{r_s M}{\tau} \frac{\partial^2 u}{\partial y^2} \\ & + \Pi \frac{\partial^2 \dot{u}}{\partial x^2} + (\Pi - M) \frac{\partial^2 \dot{v}}{\partial x \partial y} + M \frac{\partial^2 \dot{u}}{\partial y^2} \end{aligned} \quad (3-42)$$

$$\begin{aligned} \frac{\partial f_y}{\partial t} = & -\frac{1}{\tau} f_y + \frac{r_p \Pi}{\tau} \frac{\partial^2 v}{\partial y^2} + \frac{r_p \Pi - r_s M}{\tau} \frac{\partial^2 u}{\partial x \partial y} + \frac{r_s M}{\tau} \frac{\partial^2 v}{\partial x^2} \\ & + \Pi \frac{\partial^2 \dot{v}}{\partial y^2} + (\Pi - M) \frac{\partial^2 \dot{u}}{\partial x \partial y} + M \frac{\partial^2 \dot{v}}{\partial x^2} \end{aligned} \quad (3-43)$$

$$\frac{\partial u}{\partial t} = \dot{u} \quad (3-44)$$

$$\frac{\partial v}{\partial t} = \dot{v} \quad (3-45)$$

$$\frac{\partial \dot{u}}{\partial t} = \frac{1}{\rho} (f_x + f_{bx}) \quad (3-46)$$

and

$$\frac{\partial \dot{v}}{\partial t} = \frac{1}{\rho} (f_y + f_{by}) \quad (3-47)$$

Table 3-3—Schematic and stress-dynamic equations for MSDLM in vicinity of interior particle located at position (i, j) .

Schematic	Stress-dynamic Equations
	$\begin{aligned} \frac{df_{i,j}^x}{dt} = & -\frac{1}{\tau} f_{i,j}^x + \frac{g_1}{th^2 D} (u_{i+1,j} - 2u_{i,j} + u_{i-1,j}) + \frac{1}{th^2 D} \left(\frac{g_3}{2} + \frac{\eta_1}{4h^2} \right) (u_{i+1,j+1} + u_{i-1,j-1} + u_{i+1,j-1} + u_{i-1,j+1} - 4u_{i,j}) \\ & + \frac{1}{th^2 D} \left(\frac{g_3}{2} - \frac{\eta_1}{4h^2} \right) (v_{i+1,j+1} + v_{i-1,j-1} - v_{i+1,j-1} - v_{i-1,j+1}) + \left(\frac{g_1 + g_2}{h^2 D} \right) (\dot{u}_{i+1,j} - 2\dot{u}_{i,j} + \dot{u}_{i-1,j}) \quad (T3.1) \\ & + \frac{1}{h^2 D} \left(\frac{g_3 + g_4}{2} + \frac{\eta_1 + \eta_2}{4h^2} \right) (\dot{u}_{i+1,j+1} + \dot{u}_{i-1,j-1} + \dot{u}_{i+1,j-1} + \dot{u}_{i-1,j+1} - 4\dot{u}_{i,j}) \\ & + \frac{1}{h^2 D} \left(\frac{g_3 + g_4}{2} - \frac{\eta_1 + \eta_2}{4h^2} \right) (\dot{v}_{i+1,j+1} + \dot{v}_{i-1,j-1} - \dot{v}_{i+1,j-1} - \dot{v}_{i-1,j+1}) \\ \frac{df_{i,j}^y}{dt} = & -\frac{f_{i,j}^y}{\tau} + \frac{g_1}{th^2 D} (v_{i,j+1} - 2v_{i,j} + v_{i,j-1}) + \frac{1}{th^2 D} \left(\frac{g_3}{2} + \frac{\eta_1}{4h^2} \right) (v_{i+1,j+1} + v_{i-1,j-1} + v_{i+1,j-1} + v_{i-1,j-1} - 4v_{i,j}) \\ & + \frac{1}{th^2 D} \left(\frac{g_3}{2} - \frac{\eta_1}{4h^2} \right) (u_{i+1,j+1} + u_{i-1,j-1} - u_{i+1,j-1} - u_{i-1,j+1}) + \frac{g_1 + g_2}{h^2 D} (\dot{v}_{i,j+1} - 2\dot{v}_{i,j} - \dot{v}_{i,j-1}) \quad (T3.2) \\ & + \frac{1}{h^2 D} \left(\frac{g_3 + g_4}{2} + \frac{\eta_1 + \eta_2}{4h^2} \right) (\dot{v}_{i+1,j+1} + \dot{v}_{i-1,j-1} + \dot{v}_{i+1,j-1} + \dot{v}_{i-1,j-1} - 4\dot{v}_{i,j}) \\ & + \frac{1}{h^2 D} \left(\frac{g_3 + g_4}{2} - \frac{\eta_1 + \eta_2}{4h^2} \right) (\dot{u}_{i+1,j+1} + \dot{u}_{i-1,j-1} - \dot{u}_{i+1,j-1} - \dot{u}_{i-1,j+1}) \\ \frac{du_{i,j}}{dt} = & \dot{u}_{i,j} \quad (T3.3) \\ \frac{dv_{i,j}}{dt} = & \dot{v}_{i,j} \quad (T3.4) \\ \frac{d\dot{u}_{i,j}}{dt} = & \frac{1}{\rho} (f_{i,j}^{bx} + f_{i,j}^x) \quad (T3.5) \\ \frac{d\dot{v}_{i,j}}{dt} = & \frac{1}{\rho} (f_{i,j}^{by} + f_{i,j}^y) \quad (T3.6) \end{aligned}$
<p>Notes: D is unit depth. $f_{i,j}^{bx}$ and $f_{i,j}^{by}$ are respective x and y-direction body forces per unit particle volume.</p>	<p>where</p> $\tau = \frac{b_2}{g_2} = \frac{b_4}{g_4} = \frac{\gamma_2}{\eta_2} \quad (T3.7)$

Table 3-4—Schematic and stress-dynamic equations for MSDLM in vicinity of particle located on free surface at position (i, j) .

Schematic	Stress-Dynamic Equations
<p>The schematic shows a central particle at position (i, j) on a free surface. It is connected to its horizontal neighbors $(i-1, j)$ and $(i+1, j)$ by springs with stiffness $g_1/2$ and dashpots with coefficient $b_2/2$. It is connected to its vertical neighbor $(i, j-1)$ by a spring with stiffness g_2 and a dashpot with coefficient b_1. It is connected to its diagonal neighbors $(i-1, j-1)$ and $(i+1, j-1)$ by springs with stiffness g_3 and dashpots with coefficient b_4. The lattice spacing is h. The free surface is at the top, and the material is below it. The diagram also shows the parameters η_1, η_2, γ_2 associated with the diagonal connections.</p>	$\begin{aligned} \frac{df_{i,j-\frac{1}{2}}^x}{dt} = & -\frac{f_{i,j-\frac{1}{2}}^x}{\tau} + \frac{g_1}{2\theta h^2 D} (u_{i-1,j} - 2u_{i,j} + u_{i+1,j}) + \frac{1}{\theta h^2 D} \left(\frac{g_3}{2} + \frac{\eta_1}{4h^2} \right) (u_{i+1,j-1} + u_{i-1,j-1} - 2u_{i,j}) \\ & + \frac{1}{\theta h^2 D} \left(\frac{g_3}{2} - \frac{\eta_1}{4h^2} \right) (v_{i-1,j-1} - v_{i+1,j-1}) + \frac{3r_s M - r_p \Pi}{4\theta h^2} (v_{i-1,j} - v_{i+1,j}) \\ & + \frac{g_1 + g_2}{2h^2 D} (\dot{u}_{i-1,j} - 2\dot{u}_{i,j} + \dot{u}_{i+1,j}) + \frac{1}{h^2 D} \left(\frac{g_3 + g_4}{2} + \frac{\eta_1 + \eta_2}{4h^2} \right) (\dot{u}_{i+1,j-1} + \dot{u}_{i-1,j-1} - 2\dot{u}_{i,j}) \\ & + \frac{1}{h^2 D} \left(\frac{g_3 + g_4}{2} - \frac{\eta_1 + \eta_2}{4h^2} \right) (\dot{v}_{i-1,j-1} - \dot{v}_{i+1,j-1}) + \frac{3M - \Pi}{4h^2} (\dot{v}_{i-1,j} - \dot{v}_{i+1,j}) \end{aligned} \quad (T4.1)$ $\begin{aligned} \frac{df_{i,j-\frac{1}{2}}^y}{dt} = & -\frac{f_{i,j-\frac{1}{2}}^y}{\tau} + \frac{g_1}{\theta h^2 D} (v_{i,j-1} - v_{i,j}) + \frac{1}{\theta h^2 D} \left(\frac{g_3}{2} + \frac{\eta_1}{4h^2} \right) (v_{i+1,j-1} + v_{i-1,j-1} - 2v_{i,j}) \\ & + \frac{1}{\theta h^2 D} \left(\frac{g_3}{2} - \frac{\eta_1}{4h^2} \right) (u_{i-1,j-1} - u_{i+1,j-1}) + \frac{3r_s M - r_p \Pi}{4\theta h^2} (u_{i+1,j} - u_{i-1,j}) \\ & + \frac{g_1 + g_2}{h^2 D} (\dot{v}_{i,j-1} - \dot{v}_{i,j}) + \frac{1}{h^2 D} \left(\frac{g_3 + g_4}{2} + \frac{\eta_1 + \eta_2}{4h^2} \right) (\dot{v}_{i+1,j-1} + \dot{v}_{i-1,j-1} - 2\dot{v}_{i,j}) \\ & + \frac{1}{h^2 D} \left(\frac{g_3 + g_4}{2} - \frac{\eta_1 + \eta_2}{4h^2} \right) (\dot{u}_{i-1,j-1} - \dot{u}_{i+1,j-1}) + \frac{3M - \Pi}{4h^2} (\dot{u}_{i+1,j} - \dot{u}_{i-1,j}) \end{aligned} \quad (T4.2)$ $\frac{du_{i,j}}{dt} = \dot{u}_{i,j} \quad (T4.3)$ $\frac{dv_{i,j}}{dt} = \dot{v}_{i,j} \quad (T4.4)$ $\frac{d\dot{u}_{i,j}}{dt} = \frac{2}{\rho} (f_{i,j-\frac{1}{2}}^x + f_{i,j}^{sx}) \quad (T4.5)$ $\frac{d\dot{v}_{i,j}}{dt} = \frac{2}{\rho} (f_{i,j-\frac{1}{2}}^y + f_{i,j}^{sy}) \quad (T4.6)$
<p>Notes: D is unit depth. $f_{i,j}^{sx}$ and $f_{i,j}^{sy}$ are respective x and y-direction surface tractions per unit particle volume. Correction terms necessary to precisely impose traction conditions are boxed.</p>	<p>where,</p> $\tau = \frac{b_2}{g_2} = \frac{b_4}{g_4} = \frac{\gamma_2}{\eta_2} \quad (T4.7)$

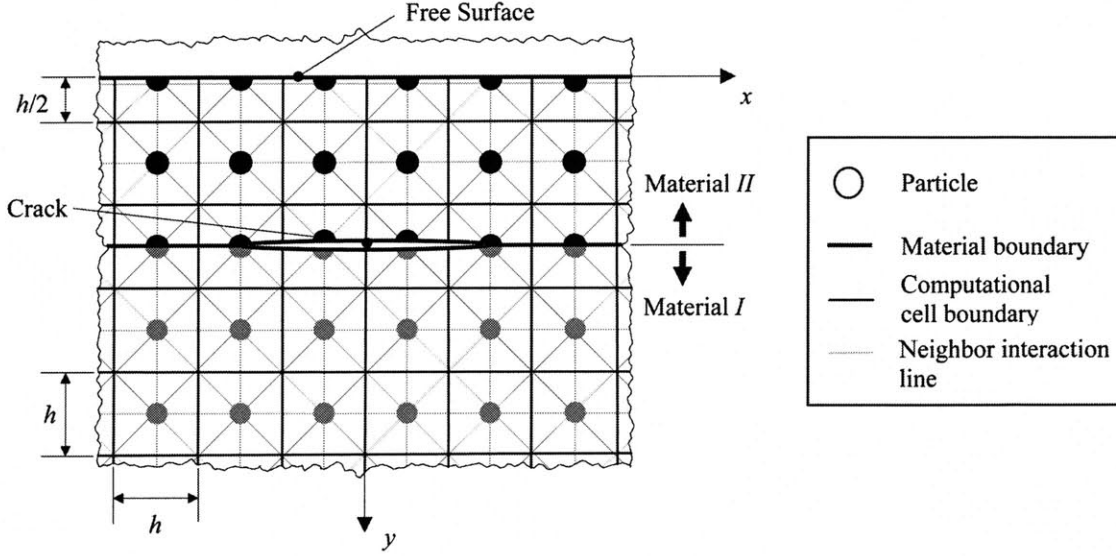


Fig. 3-3—Schematic of two-dimensional lattice model discretization with various boundary and interaction conditions.

Expanding eqns. (T3.1) and (T3.2) via a Taylor series in the limit as $h \rightarrow 0$ and comparing the result with eqns. (3-42) and (3-43), the two-dimensional MSDLM is spatially consistent with the governing PDEs if

$$g_1 = D(r_p \Pi - r_s M) \quad (3-48)$$

$$g_2 = D[(1 - r_p) \Pi - (1 - r_s) M] \quad (3-49)$$

$$g_3 = \frac{D}{4}(r_p \Pi + r_s M) \quad (3-50)$$

$$g_4 = \frac{D}{4}[(1 - r_p) \Pi + (1 - r_s) M] \quad (3-51)$$

$$\eta_1 = \frac{h^2 D}{4}(3r_s M - r_p \Pi) \quad (3-52)$$

$$\eta_2 = \frac{h^2 D}{4}[3(1 - r_s) M - (1 - r_p) \Pi] \quad (3-53)$$

and

$$\tau = \frac{b_2}{g_2} = \frac{b_4}{g_4} = \frac{\gamma_2}{\eta_2} \quad (3-54)$$

where D is the unit depth.

As in the one-dimensional case, eqns. (T3.1) through (T3.6) can be numerically integrated via the classical fourth-order Runge-Kutta explicit algorithm [3-9]. Von Neumann analysis (Appendix 3C) has shown that for *stability*, the numerical time step Δt must satisfy

$$\frac{\Delta t}{\tau} \leq 2.78 \quad (3-55)$$

and the Courant number C corresponding to the maximum P phase velocity must satisfy

$$C \equiv \frac{c_{\max,P} \Delta t}{h} \leq 1.30 \quad (3-56)$$

where

$$c_{\max,P} = \sqrt{\frac{\Pi}{\rho}} \quad (3-57)$$

To this point, it has been assumed the wavevector and attenuation vector were collinear (refer to eqns. (3-23) and (3-24)), a state in which the wave propagation is denoted as being of “simple type”. However, it has been shown that in an isotropic viscoelastic continuum, an obliquely incident P or S wave of simple type on a fixed or traction-free boundary produces reflected waves where the attenuation vector, in general, is in a different direction than the reflected wavevector [3-11,3-12]. In this investigation, only waves of simple type are considered. The requirement that only simple waves are produced at boundaries is given as

$$\frac{\lambda'}{\lambda} = \frac{\mu'}{\mu} \quad \text{or} \quad r_p = r_s = r \quad (3-58)$$

Two consequences of this special case are that Poisson’s ratio ν becomes frequency independent and can be expressed in terms of the elastic constants of the standard linear solid

$$\nu = \frac{1 - 2\frac{M}{\Pi}}{2\left(1 - \frac{M}{\Pi}\right)} \quad (3-59)$$

and the attenuation of S -waves must satisfy

$$\alpha_s = \alpha_p \sqrt{\frac{2 - 2\nu}{1 - 2\nu}} \quad (3-60)$$

To reduce the numerical phase and dissipation error to less than 1% of the corresponding continuum values in low dispersion materials ($r \geq 0.25$) with $\nu \leq 0.40$, accuracy requires the number of grid spacings per wavelength must be at least 20 (Appendix 3C). As $\nu \rightarrow 0.50$, however, the number of grid spacings per wavelength required to maintain a desired level of accuracy increases dramatically due to numerical anisotropy (refer to Chapter 2).

3-4 NUMERICAL EXAMPLES

3-4.1 Material Properties

To validate the MSDLM through numerical examples, wave propagation is studied in a nanocomposite composed of a Zirconium-based bulk metallic glass (Zr-based BMG) reinforced by 3.0% volume of carbon nanotubes (CNTs), having a density of $\rho = 6.61 \times 10^3 \text{ kg/m}^3$. An experimental investigation [3-13] of this nanocomposite at an interrogation frequency of $\omega_c = 6.28 \times 10^7 \text{ rad/s}$ (10 MHz) measured the P and S waves velocities as $5.13 \times 10^3 \text{ m/s}$ and $2.28 \times 10^3 \text{ m/s}$, respectively, and the P and S attenuations as $\alpha_p = 42.6 \text{ Np/m}$ (3.7 dB/cm) and $\alpha_s = 73.7 \text{ Np/m}$ (6.4 dB/cm). The standard linear solid model parameters are calculated by assuming:

- the nanocomposite is isotropic and homogeneous (the wavelengths at this frequency are much larger than the size of a typical CNT),
- the dispersion coefficients for P and S waves are identical $r_p = r_s = r$, yielding a frequency-independent Poisson's ratio ν , and
- the frequency is sufficiently high, say $\omega_c \tau = 50$, such that the frequency independent wave velocity and attenuation asymptotically approach the measured values.

The resulting standard linear solid parameters for the Zr-based BMG nanocomposite, henceforth called “nanocomposite,” are summarized in Table 3-5.

3-4.2 One-dimensional Examples

Steady-State Response

First consider a nanocomposite of finite length subjected to a prescribed harmonic displacement of magnitude u_p and frequency ω . Figure 3-4 shows the agreement of the

Table 3-5—Standard linear solid model of Zirconium-based bulk metallic glass reinforced by 3% volume carbon nanotubes composite [3-13].

Property	Value
Elastic constant, Π ($\text{N}\cdot\text{m}^{-2}$)	1.74×10^{11}
Poisson's ratio, ν	0.377
Dispersion coefficient, r	0.652
Relaxation time, τ (s)	7.96×10^{-7}
Density, ρ ($\text{kg}\cdot\text{m}^{-3}$)	6.61×10^3

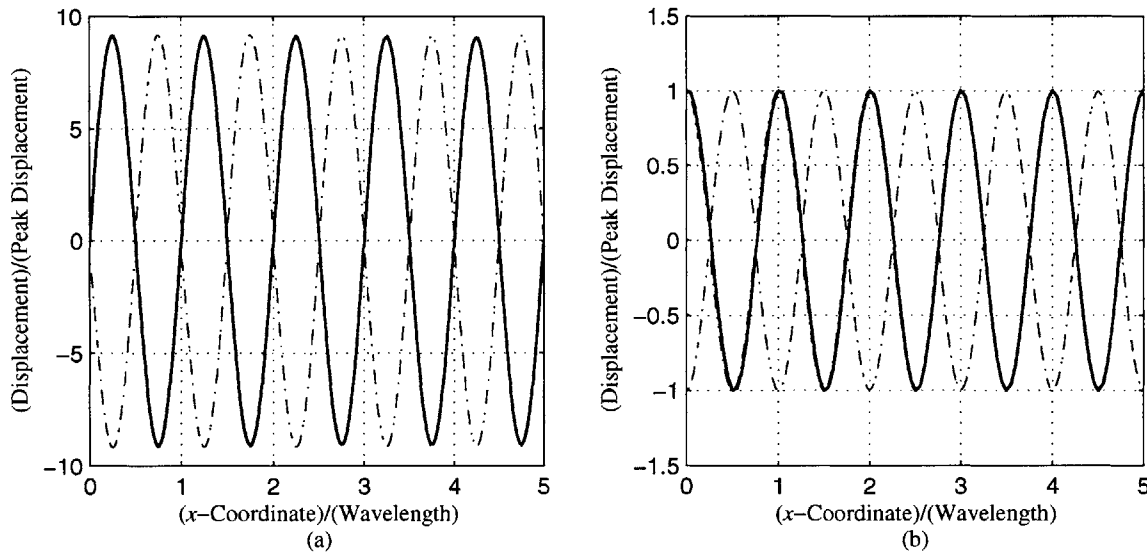


Fig. 3-4—One-dimensional steady state implementation of MSDLM (solid lines) and corresponding steady-state analytical envelopes (dashed lines, Appendix 3E) for prescribed harmonic motion of frequency ω at $x=0$ and (a) fixed boundary at $x=5\kappa$ and (a) free boundary at $x=5\kappa$, where at κ is the wavelength corresponding to ω . Here $r=0.652$, $\omega\tau=50$, $\frac{\kappa}{h}=80$ for (a) and $\frac{\kappa}{h}=20$ for (b).

one-dimensional steady-state implementation of the MSDLM and the corresponding analytical envelope (Appendix 3E) when there is a fixed and free boundary at $x/\kappa=5$, where κ is the wavenumber corresponding to frequency ω . Note that the number of required wavelengths per grid spacing to achieve an accuracy of less than 1% is four times larger for the case with a fixed boundary compared to the case with a free boundary, because the former case is near a natural frequency.

Transient Response

Next, consider a one-dimensional nanocomposite having quiescent initial conditions for $t < 0$. At time $t = 0$, the following Gaussian-modulated cosinusoidal displacement

function $u(t)$, primarily chosen due to its smoothness and well-defined bandwidth, is prescribed at $x = 0$:

$$u(t) = u_{peak} \exp\left[-\frac{1}{2}(\omega_{\sigma}t - 3)^2\right] \cos(\omega_c t - 3\omega_c\omega_{\sigma}^{-1}) \quad (3-61)$$

as shown in Fig. 3-5a, where u_{peak} is the peak magnitude of displacement, ω_{σ} is the frequency standard deviation, and ω_c is the central frequency. The function inputs $\frac{3\omega_c}{\pi\omega_{\sigma}}$ periods of displacements having an envelope greater than $u_p \exp(-\frac{9}{2})$ and thereafter rapidly decays to a rigid boundary condition. The absolute value of the Fourier transform of eqn. (3-61) shows that the frequency content is

$$|U(\omega)| \sim \exp\left[-\frac{(\omega + \omega_c)^2}{2\omega_{\sigma}^2}\right] + \exp\left[-\frac{(\omega - \omega_c)^2}{2\omega_{\sigma}^2}\right] \quad (3-62)$$

and the positive frequency content is shown in Fig. 3-5b. The effective maximum excited frequency can therefore (arbitrarily) be chosen as $\omega_{max} = \omega_c + 3\omega_{\sigma}$, since all higher frequencies excite less than a factor $\exp(-\frac{9}{2})$ or approximately 1.1% of the amplitude of the central frequency. Thus, according to the accuracy condition, the wavelength corresponding to this maximum frequency should be discretized into at least 20 grid spaces.

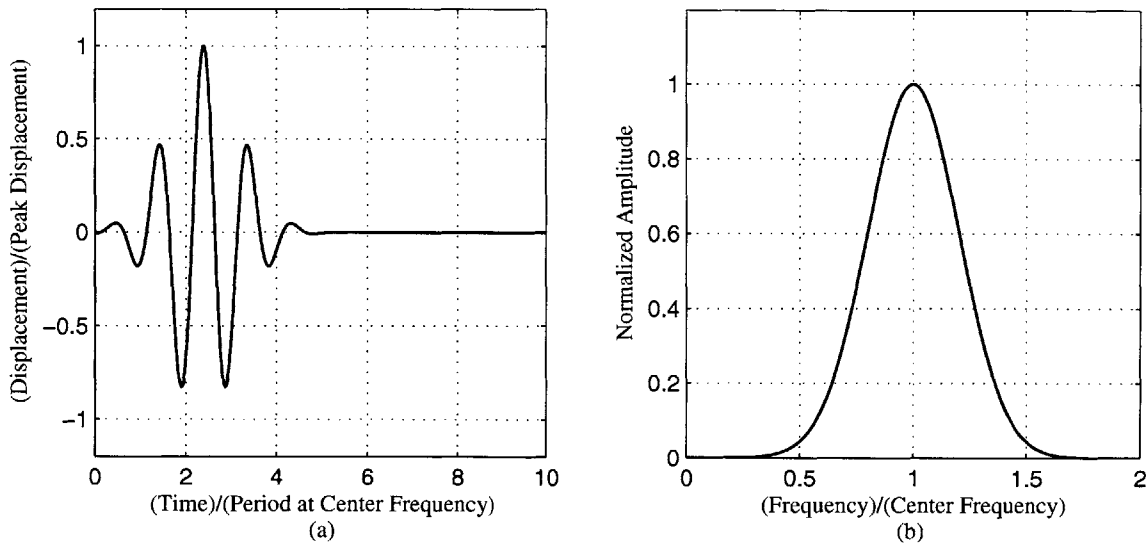


Fig. 3-5—(a) Normalized prescribed displacement of Gaussian-modulated cosinusoidal temporal function having peak amplitude u_p , center frequency ω_c (period at center frequency T_c), standard deviation ω_{σ} and (b) normalized positive frequency content when $\omega_{\sigma} / \omega_c = 0.2$.

Figure 3-6 shows snapshots of the displacement field at various times in a semi-infinite nanocomposite subjected to the prescribed displacement function. To effectively eliminate spurious reflections, an absorbing boundary is placed at $x/\kappa_c = 20$. (Essentially the absorbing boundary is a layer in which the magnitudes of the auxiliary springs and dashpot coefficients are modified to increase the wave attenuation with increasing position. Details are given in Appendix 3F.) The magnitude of the peak wave packet is within 0.5% error of the analytical envelope (dashed line) at a few sampled times (Appendix 3E).

Figure 3-7 shows snapshots of the displacement field at various times near the boundaries of two dissimilar standard linear solids when subjected to the prescribed displacement function. Material *I* ($0 \leq x/\kappa_c < 10$) is the nanocomposite and Material *II* ($10 \leq x/\kappa_c$) has the same properties as the nanocomposite except its relaxation time is five times smaller, and thus, the Material *II* attenuation is five times larger than that of Material *I*. For clarity, an absorbing boundary condition exists at $x/\kappa_c = 20$. The peak magnitudes of the incident and transmitted wave packets are within 0.5% accuracy of the composite analytical envelope (dashed) at a few sampled times (Appendix 3E).

3-4.3 Two-dimensional Examples

Internal Point Loading

Consider a two-dimensional, semi-infinite plane-strain nanocomposite having quiescent initial conditions. At time $t = 0$, the nanocomposite is subjected to a Gaussian-modulated cosinusoidal time-varying radial stress $\sigma_r(t)$ acting at the origin, having peak magnitude $(\sigma_r)_p$, central frequency ω_c , and standard deviation frequency ω_σ . The spatial distribution of forces required to approximate such a stress in the MSDLM is shown in Fig. 3-8a. To effectively eliminate numerical reflections, an absorbing boundary is placed at $x/\kappa_{p,c} = \pm 2.5$ and $y/\kappa_{p,c} = \pm 2.5$, where $\kappa_{p,c}$ is the *P*-wavelength at the center frequency. Figure 3-9 shows snapshots of the resulting displacement field, revealing the circular wave fronts of the *P* waves. Figure 3-10 shows an analogous case for a prescribed circular shear stress $\sigma_{r\theta}(t)$ acting at the origin (with the MSDLM spatial distribution as shown in Fig.3-8b).

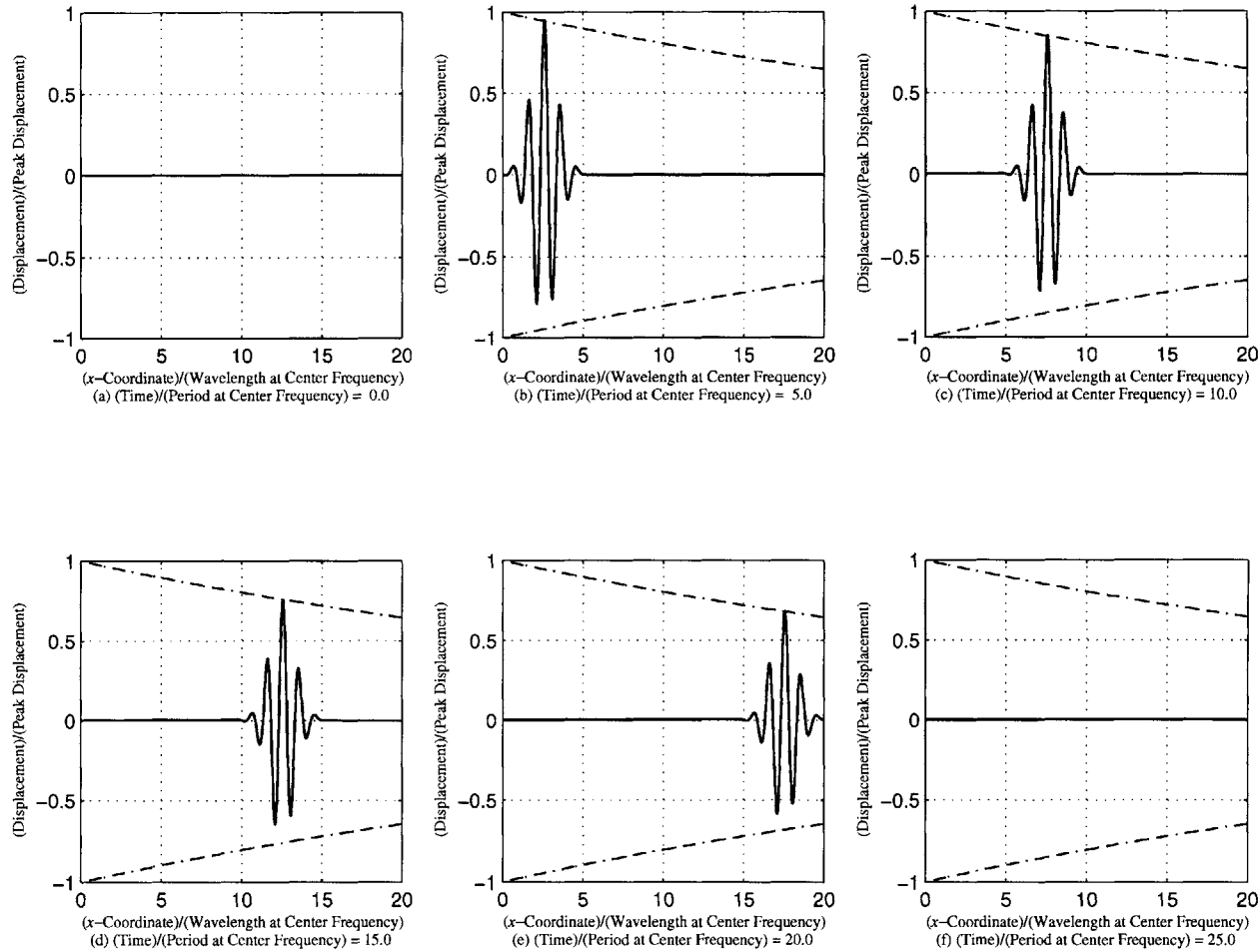


Fig. 3-6—Snapshots of displacement field in one-dimensional standard linear solid numerically simulated via MSDLM, subjected to prescribed Gaussian-modulated cosinusoidal displacement at $x=0$ {peak displacement u_p , central frequency ω_c (period at center frequency T_c), standard deviation ω_σ } and absorbing

boundary at $x/\kappa_c = 20$. Here κ_c is wavelength corresponding to ω_c , $r = 0.652$, $\omega_c \tau = 50$, $\frac{\omega_\sigma}{\omega_c} = 0.20$, $\frac{c_{\max} \Delta t}{h} = 1.30$, and $\frac{\Delta t}{\tau} = 5.1 \times 10^{-3}$.

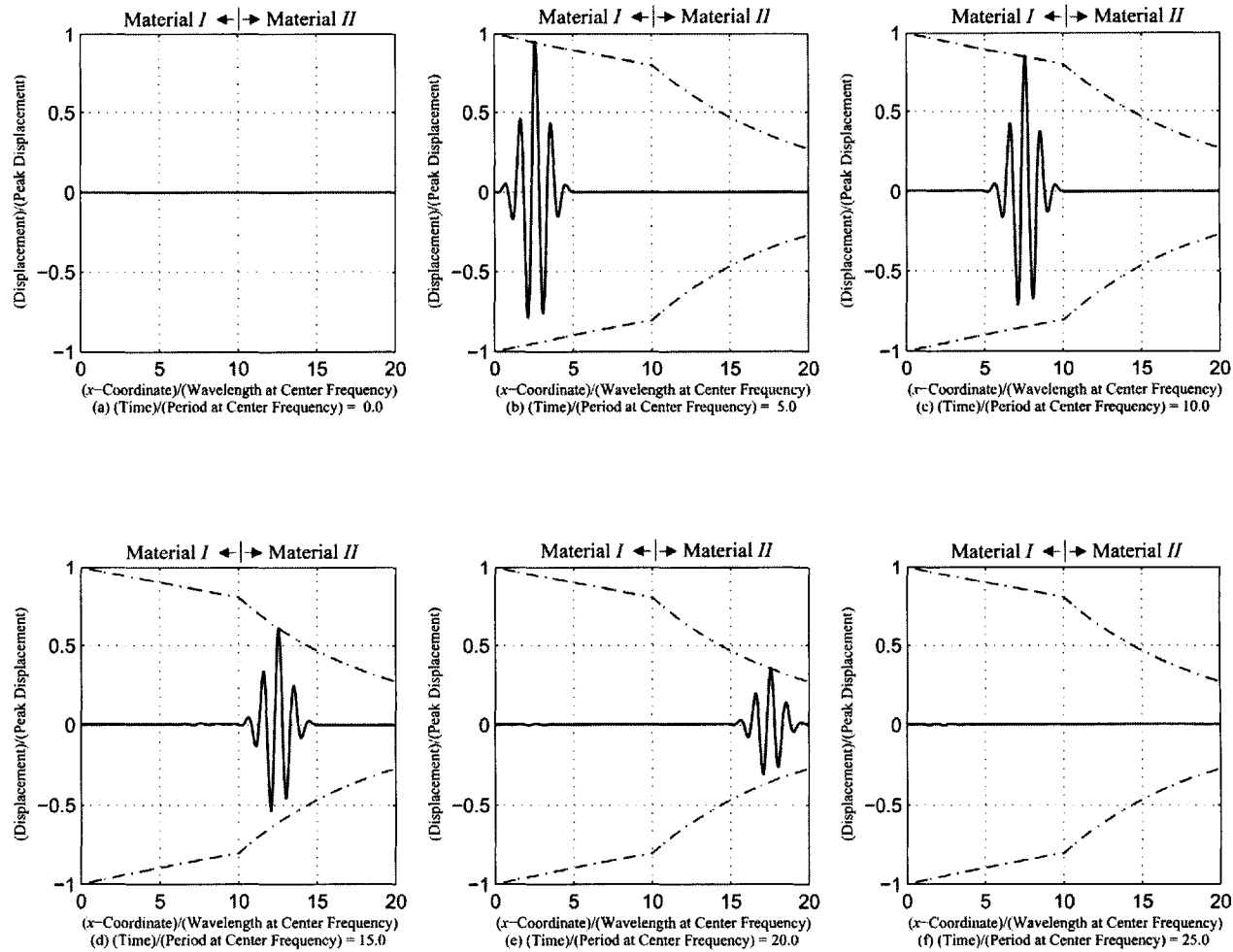


Fig. 3-7—Snapshots of displacement field near interface of dissimilar one dimensional standard linear solids numerically simulated via MSDLM, subjected to prescribed Gaussian-modulated cosinusoidal displacement at $x=0$ (peak displacement u_p , central frequency ω_c , standard deviation ω_σ). Dashed line represents analytical envelope of wave propagation. Nondimensional parameters of Material I, $0 < x/\kappa_c < 10$, and of Material II, $10 < x/\kappa_c$, where κ_c is wavelength corresponding to ω_c , are $\frac{\tau^I}{\tau^{II}} = 5$, $r^I = r^{II} = 0.652$, $\omega_c \tau^I = 50$, $\frac{\omega_\sigma}{\omega_c} = 0.20$, $\frac{c_{\max}^I}{c_{\max}^{II}} = 1$, $\frac{c_{\max}^I \Delta t}{h} = 1.30$, and $\frac{\Delta t}{\tau^I} = 5.1 \times 10^{-3}$.

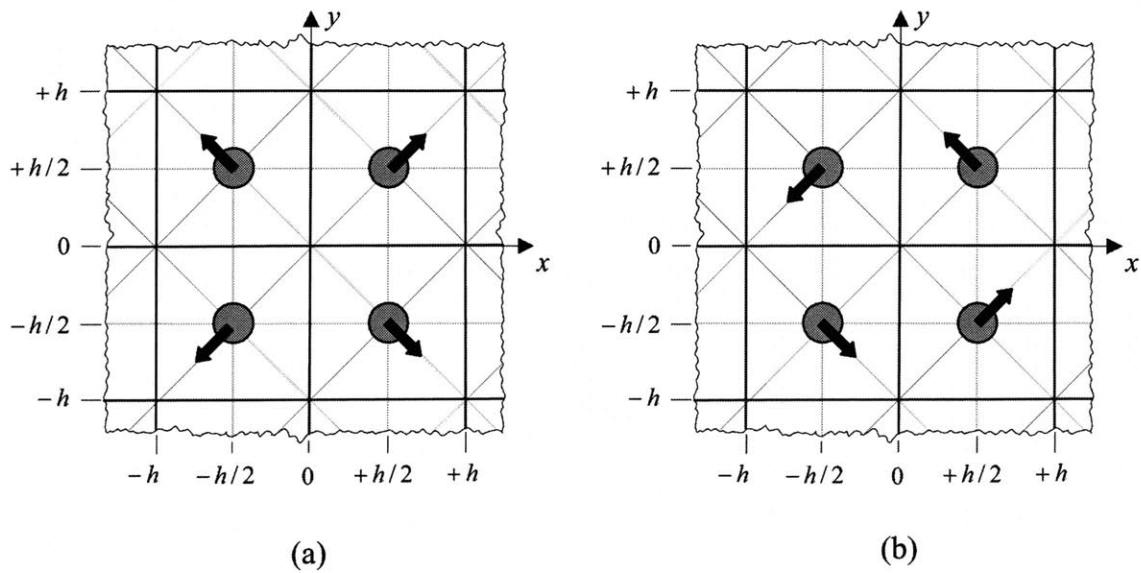


Fig. 3-8—Schematic of spatial distribution of volumetric forces in lattice model to approximate (a) radial pressure point load σ_{rr} and (b) radial shear point load $\sigma_{r\theta}$, where h is grid space.

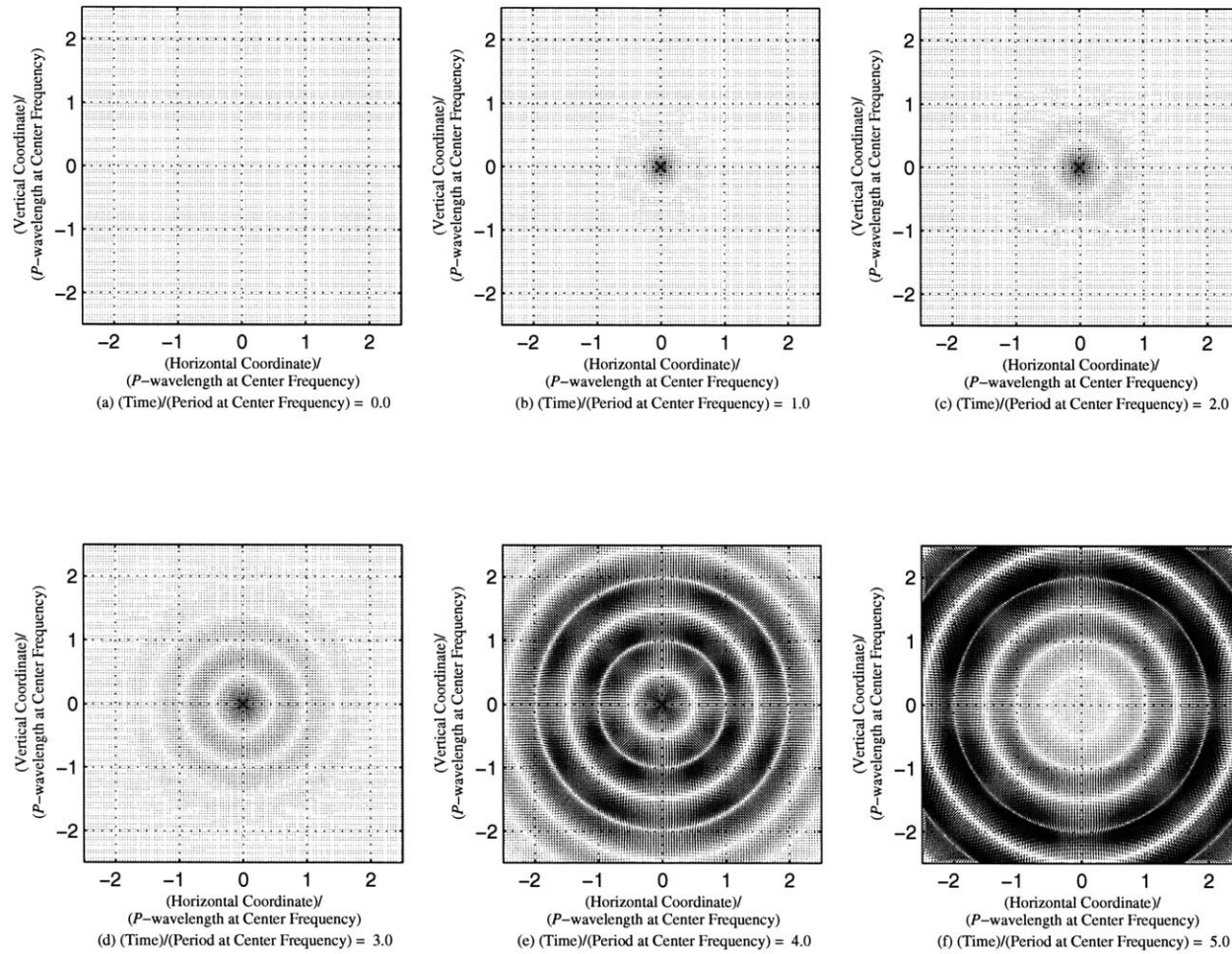


Fig. 3-9—Snapshots of displacement field in two-dimensional, plane strain standard linear solid numerically simulated via MSDLM. Absorbing boundary conditions are at $x/\kappa_{P,c} = \pm 2.5$ and $y/\kappa_{P,c} = \pm 2.5$, and solid is subjected to Gaussian-modulated cosinusoidal time-varying point normal stress $\sigma_{rr}(t)$ (center frequency ω_c , standard deviation ω_σ) acting at origin. Here $\kappa_{P,c}$ is P -wavelength at center frequency, $r_p = r_s = 0.652$, $\nu = 0.377$, $\frac{c_{\max,P}\Delta t}{h} = 1.30$, $\frac{\Delta t}{\tau} = 2.3 \times 10^{-3}$, $\omega_c \tau = 50$, and $\frac{\omega_\sigma}{\omega_c} = 0.2$.

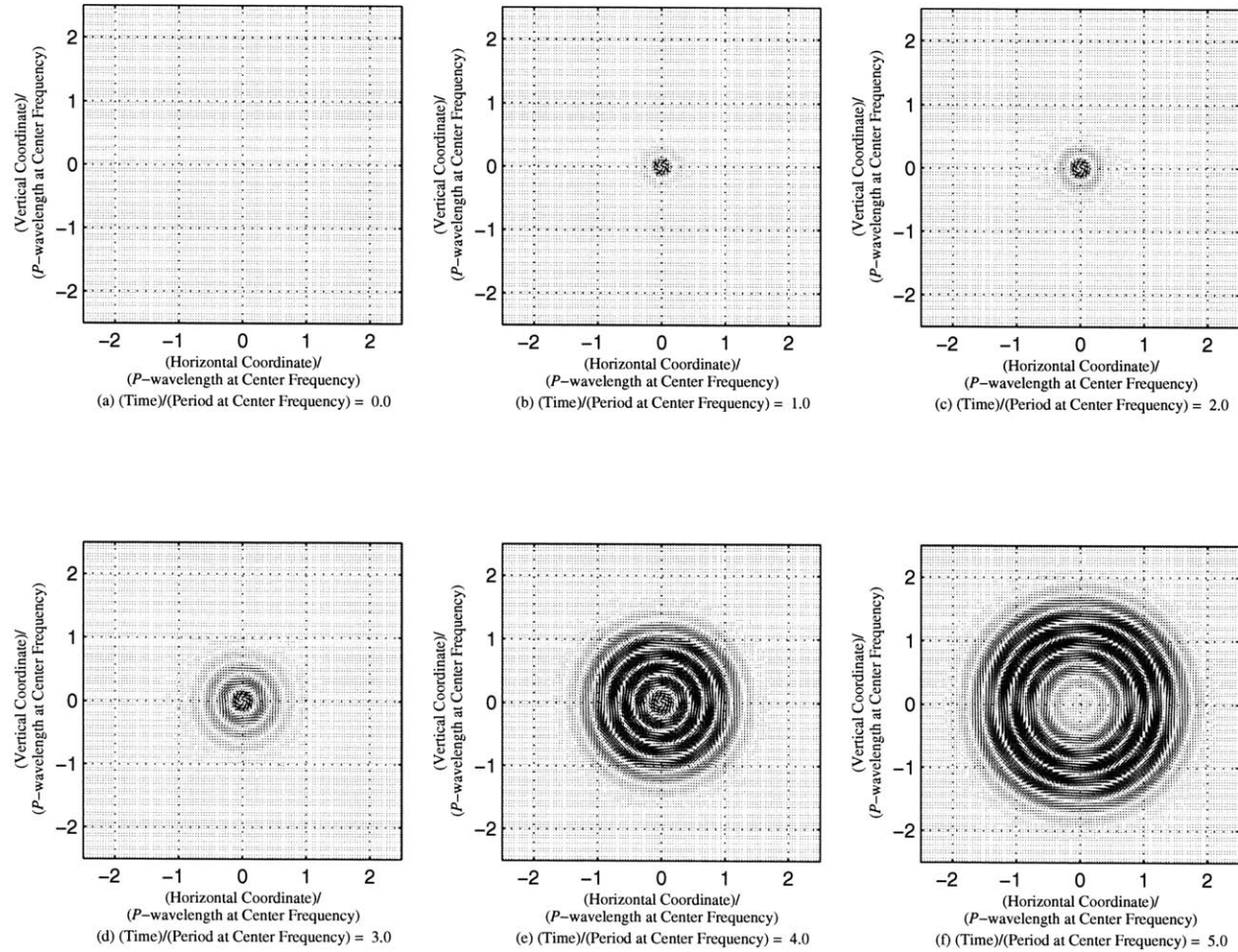


Fig. 3-10—Snapshots of displacement field in two-dimensional, plane strain standard linear solid numerically simulated via MSDLM. Absorbing boundary conditions are at $x/\kappa_{P,c} = \pm 2.5$ and $y/\kappa_{P,c} = \pm 2.5$, and solid is subjected to Gaussian-modulated cosinusoidal time-varying point shear stress $\sigma_{r\theta}(t)$ (center frequency ω_c , standard deviation ω_σ) acting at origin. Here $\kappa_{P,c}$ is P -wavelength at center frequency, $r_p = r_s = 0.652$, $\nu = 0.377$, $\frac{c_{\max,p}\Delta t}{h} = 1.30$, $\frac{\Delta t}{\tau} = 2.3 \times 10^{-3}$, $\omega_c \tau = 50$, and $\frac{\omega_\sigma}{\omega_c} = 0.2$.

Planar Boundary Reflection and Transmission

Consider a nanocomposite half-space ($y < 0$) with a rigid boundary at $y = 0$ containing a 45° obliquely incident P wave comprised of one sinusoidal wavelength at frequency ω_c , emanating from the lower left as shown in Fig. 3-11a. Figure 3-12 shows a snapshot of the displacement field when the incident P wave interacts with the rigid boundary. The magnitude of the reflected P and S waves are within 3% of the analytical steady-state analysis; the orientations of the P and S waves agree well with the predicted angles of 45° and 18° , respectively (Appendix 3E).

Consider the wave propagation near the interface of two material half-spaces at $y = 0$. Material I ($y < 0$) is the nanocomposite and Material II ($y > 0$) has the same material properties as the nanocomposite except $2\Pi'' = \Pi'$ and $\nu'' = 0.300$. In this case, Material I contains a 45° obliquely incident P wave comprised of one wavelength at frequency ω_c , emanating from the lower left as shown in Fig. 3-11b. Figure 3-13 shows the resulting S wave reflection into Material I and P wave transmission into Material II . The orientations with respect to the vertical axis of the reflected P wave, reflected S wave, transmitted P wave and transmitted S wave agree well with the analytical values of 45° , 18° , 30° , and 16° , respectively (Appendix 3E).

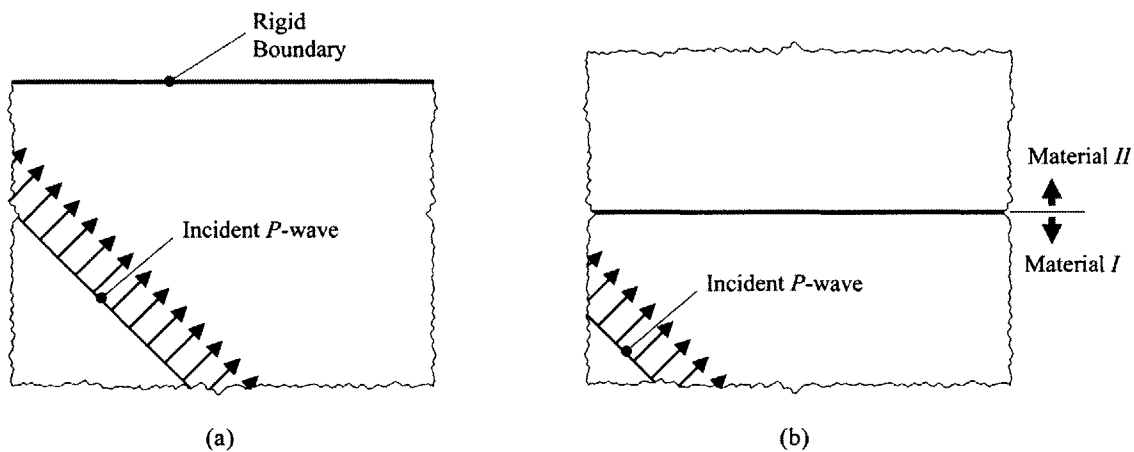


Fig. 3-11—Schematics of 45° longitudinal plane wave propagating in vicinity of (a) rigid boundary and (b) interface of dissimilar materials.

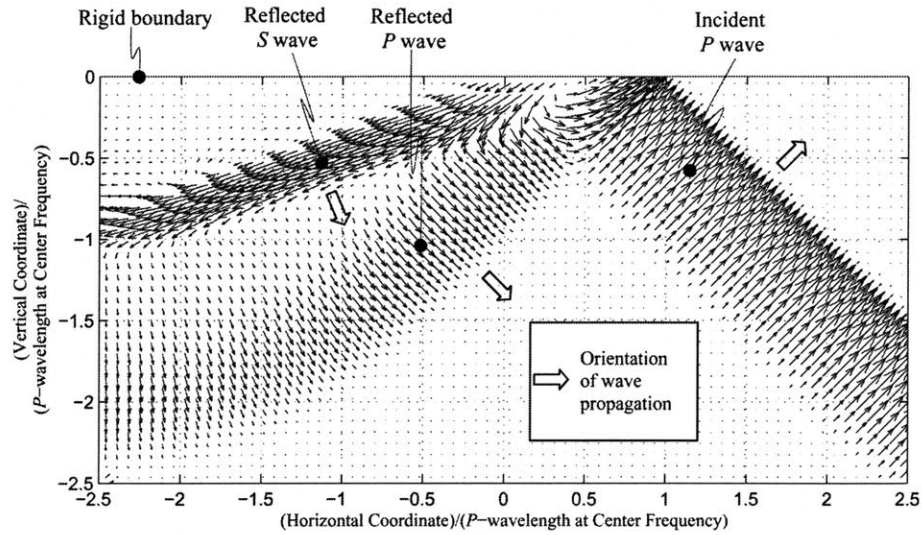


Fig. 3-12—Snapshot of displacement field in two-dimensional, plane strain standard linear solid numerically simulated via MSDLM in vicinity of rigid boundary at $y=0$. One sinusoidal wave length of incident P wave (frequency ω_c) acting at 45° angle of incidence relative to longitudinal boundary produces reflected P and S waves. Here $r_p = r_s = 0.652$, $\nu = 0.377$, $\frac{c_{\max,P}\Delta t}{h} = 1.30$, $\frac{\Delta t}{\tau} = 2.3 \times 10^{-3}$, $\omega\tau = 50$.

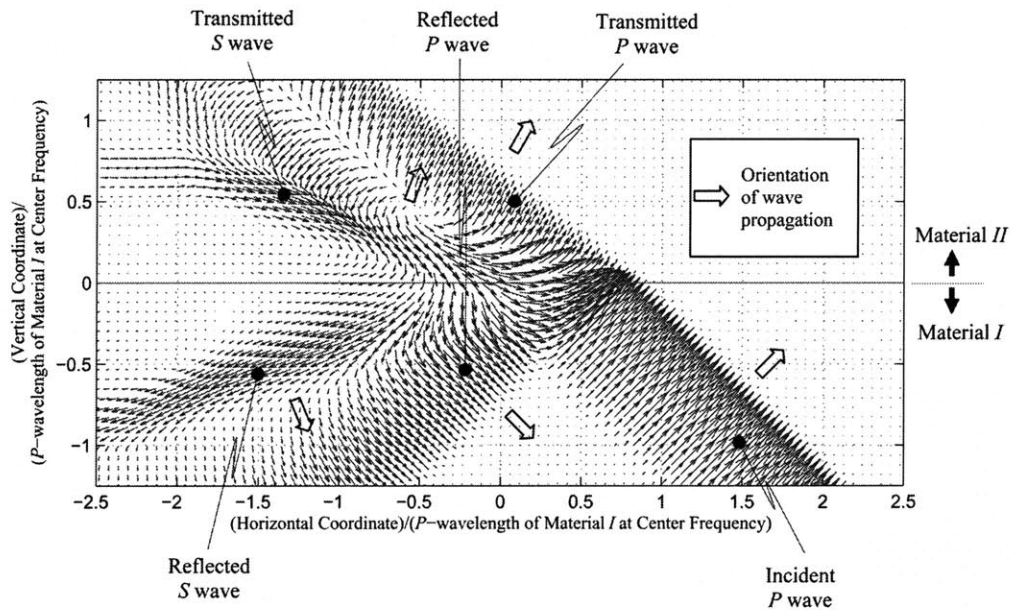


Fig. 3-13—Snapshot of displacement field simulated via MSDLM in vicinity of dissimilar material interface at $y=0$. In Material I , a sinusoidal wave length of incident P wave (frequency ω_c) acting at 45° angle of incidence relative to longitudinal boundary produces reflected P and S waves in Material I and transmitted P and S waves in Material II . Here, $r^I = r^{II} = 0.652$, $\nu^I = 0.377$, $\nu^{II} = 0.300$, $\frac{\tau^I}{\tau^{II}} = 1$,

$$\frac{c_{\max,P}^I}{c_{\max,P}^{II}} = \sqrt{2}, \quad \frac{c_{\max,P}^I \Delta t}{h} = 1.30, \quad \frac{\Delta t}{\tau^I} = 1.9 \times 10^{-3}, \quad \omega\tau^I = 50.$$

Surface Loading

Consider the case of a vertical force, having a Gaussian-modulated cosinusoidal time-variation, concentrated downward at the origin of a two-dimensional plane strain nanocomposite. The loading produces P and S waves radiating into the solid and Rayleigh waves propagating along the surface. Figure 3-14 shows snapshots of the displacement field in the vicinity of the surface loading for the first five periods corresponding to the center frequency. The elastic-like retrograde motion of particles near the surface and exponential decay can be readily verified from the figure and are in good qualitative agreement with analytical steady-state results [3-14]. Because the quality factor of the nanocomposite at the central frequency is 144 (that is, a plane wave must propagate 144 wavelengths to attenuate by a factor $\exp(-\pi)$, or approximately 4.3%), the transient surface displacements on the nanocomposite are within a 10% amplitude of the exact solution for an elastic material [3-15] for the windowed region of interest.

3-5 CONCLUSIONS

The MSDLM was formulated for both one and two dimensions, and the convergence and accuracy criteria were presented. Numerical examples provided further verification of the efficacy of the MSDLM to simulate and visualize wave phenomena in attenuating materials. It is anticipated that the MSDLM can be a useful tool in wave propagation disciplines such as seismology and nondestructive evaluation of materials.

In its present form the MSDLM uses standard linear solid elements, consisting of ideal dashpots and springs, to simulate interactions between particles. In the future, a generalized standard linear solid, containing a fractional derivative dashpot or the so-called spring-pot, can be incorporated into the MSDLM to more realistically model wave phenomena over a broader range of frequencies, albeit with increased numerical complexity. Material nonlinearity can also be incorporated by employing nonlinear springs and power-law dashpots.

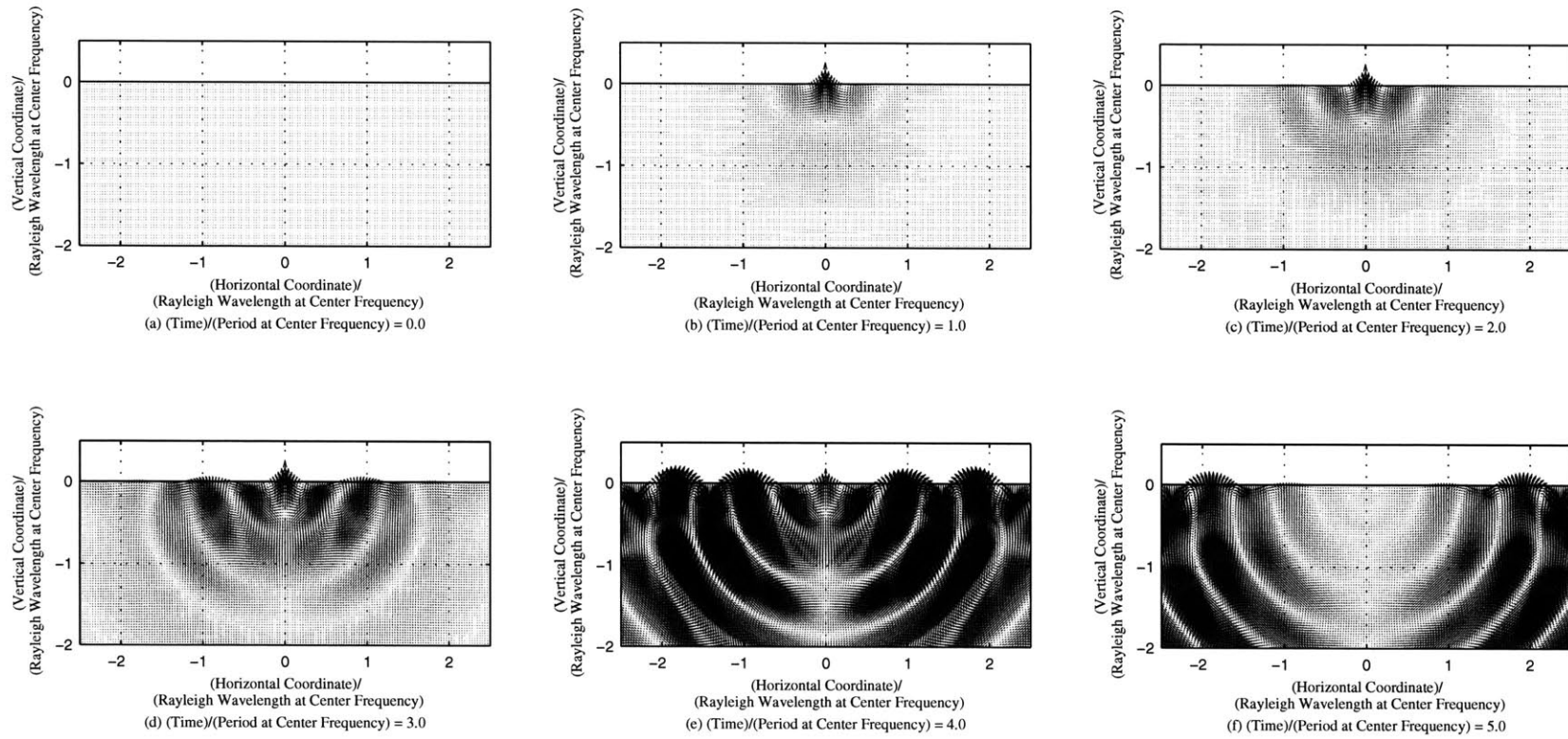


Fig. 3-14—Snapshots of displacement field in two-dimensional, plain strain standard linear solid numerically simulated via MSDLM in vicinity of vertical force concentrated at origin. The Gaussian-modulated time-varying force (center frequency ω_c , standard deviation ω_σ) produces P and S waves radiating into solid and Rayleigh waves propagating along surface. Here $r_p = r_s = 0.652$, $\nu = 0.377$, $\frac{c_{\max,p}\Delta t}{h} = 1.30$, $\frac{\Delta t}{\tau} = 2.1 \times 10^{-3}$, $\omega_c \tau = 50$, and $\frac{\omega_\sigma}{\omega_c} = 0.2$.

References:

- 3-1. H. Yim and Y. Choi. *Mater. Eval.* **58**:889 (2000).
- 3-2. H. Yim and Y. Sohn. *IEEE Trans. Ultrason. Ferroelectr. Freq. Control.* **47**:549 (2000).
- 3-3. P.P. Delsanto, T. Whitcombe, H.H. Chaskelis and R.B. Mignogna. *Wave Motion* **16**:65 (1992)
- 3-4. P.P. Delsanto and M. Scaldierandi. *J. Acoust. Soc. Am.* **104**:2584 (1998).
- 3-5. M. Scalerandi, P.P Delsanto and V. Agostini. *Rev. Prog. Quant. Nondestr. Eval.* **18A**:103 (1999).
- 3-6. R.M. Christensen. *Theory of Viscoelasticity: An Introduction* 2nd ed., pp. 14,15,37,38. Academic Press, New York (1982).
- 3-7. H. Kolsky. *Stress Waves in Solids*, pp. 99-129. Dover, New York (1963).
- 3-8. P.D. Small, A.F. Thomas and J.H. Williams, Jr. to be submitted, (June 2005).
- 3-9. M. Abramowitz and I.A. Stegun (Eds.), *Handbook of Mathematical Functions with Formulas, Graphs and Mathematical Tables*, pp. 896-897. Dover, New York (1965).
- 3-10. L. Lapidus and G.F. Pinder. *Numerical Solution of Partial Differential Equations in Science and Engineering*, pp. 167-168. John Wiley & Sons, New York (1982).
- 3-11. F.J. Lockett. *J. Mech. Phys. Solids.* **10**:53 (1962).
- 3-12. H.F. Cooper, Jr. and E. L. Reiss. *J. Acoust. Soc. Am.* **39**:1133 (1966).
- 3-13. Z. Bian, R.J. Wang, W.H. Wang, T. Zhang and A. Inoue. *Adv. Funct. Mater.* **14**:55 (2004).
- 3-14. P.K. Currie, M. A. Haynes and P. M. O’Leary. *Q. Appl. Math.* **35**:35 (1977).
- 3-15. Lamb, H. *Philosophical Transactions of the Royal Society of London. Series A, Containing Papers of a Mathematical or Physical Character.* **203**:1 (1904).

APPENDIX 3A—Derivation of Stress-Dynamic Equations and Dispersion Relations for Standard Linear Solid Having Single Relaxation Time

In this appendix, the stress-dynamic equations are derived for a standard linear solid having a single stress relaxation time. From the stress-dynamic equations, the attenuation and wavenumber are derived for steady-state harmonic waves and limiting cases are explored.

Derivation of Stress-Dynamic Equations

For a general homogeneous continuum, the equations of motion expressed in Cartesian indicial notation are

$$\sigma_{kl,l} + f_k^b = \rho \ddot{u}_k \tag{3A-1}$$

where σ_{kl} are the components of the Cauchy stress tensor, f_k^b are the components of the body force per unit volume, ρ is the density, u_k are the components of displacement, and

the overdot denotes a partial derivative with respect to time. For an isotropic viscoelastic continuum, the constitutive equations are [3A-1]

$$\sigma_{kl} = \tilde{\lambda}(t) * \varepsilon_{mm} \delta_{kl} + 2\tilde{\mu}(t) * \varepsilon_{kl} \quad (3A-2)$$

where $\tilde{\lambda}(t)$ and $\tilde{\mu}(t)$ are independent stress relaxation functions, $*$ denotes a convolution integral, ε_{kl} are the components of small strain given by

$$\varepsilon_{kl} = \frac{1}{2}(u_{k,l} + u_{l,k}) \quad (3A-3)$$

and δ_{kl} is the Kronecker delta. Equation (3A-2) can be rewritten as [3A-1]

$$\sigma_{kl} = \delta_{kl} \int_{-\infty}^t \tilde{\lambda}(t-t^*) \frac{\partial \varepsilon_{mm}}{\partial t^*} dt^* + 2 \int_{-\infty}^t \tilde{\mu}(t-t^*) \frac{\partial \varepsilon_{kl}}{\partial t^*} dt^* \quad (3A-4)$$

Substituting eqn. (3A-3) into eqn. (3A-4) yields

$$\sigma_{kl} = \delta_{kl} \int_{-\infty}^t \tilde{\lambda}(t-t^*) \frac{\partial u_{m,m}}{\partial t^*} dt^* + \int_{-\infty}^t \tilde{\mu}(t-t^*) \frac{\partial}{\partial t^*} (u_{k,l} + u_{l,k}) dt^* \quad (3A-5)$$

Taking the partial derivative of eqn. (3A-5) with respect to coordinate l yields

$$\sigma_{kl,l} = \delta_{kl} \int_{-\infty}^t \tilde{\lambda}(t-t^*) \frac{\partial u_{m,ml}}{\partial t^*} dt^* + \int_{-\infty}^t \tilde{\mu}(t-t^*) \frac{\partial}{\partial t^*} (u_{k,ll} + u_{l,kl}) dt^* \quad (3A-6)$$

Using the properties

$$\delta_{kl} \frac{\partial u_{m,ml}}{\partial t^*} = \frac{\partial u_{m,mk}}{\partial t^*} = \frac{\partial u_{l,lk}}{\partial t^*} \quad (3A-7)$$

and

$$u_{l,kl} = u_{l,lk} \quad (3A-8)$$

eqn. (3A-5) can be reformulated to yield

$$\sigma_{kl,l} = \int_{-\infty}^t (\tilde{\lambda}(t-t^*) + \tilde{\mu}(t-t^*)) \frac{\partial u_{l,lk}}{\partial t^*} dt^* + \int_{-\infty}^t \tilde{\mu}(t-t^*) \frac{\partial u_{k,ll}}{\partial t^*} dt^* \quad (3A-9)$$

For a standard linear solid described by a single stress relaxation time τ , the stress relaxation functions have the following form:

$$\tilde{\lambda}(t) = \lambda + \frac{\lambda'}{\tau} e^{-t/\tau} \quad (3A-10)$$

$$\tilde{\mu}(t) = \mu + \frac{\mu'}{\tau} e^{-t/\tau} \quad (3A-11)$$

Here, λ and μ are the Lamé constants and λ' and μ' are the analogous viscoelastic constants.

Substituting eqn. (3A-10) and (3A-11) into eqn. (3A-9) yields

$$\begin{aligned} \sigma_{kl,l} = & \int_{-\infty}^t \left(\lambda + \mu + \frac{\lambda' + \mu'}{\tau} e^{-(t-t^*)/\tau} \right) \frac{\partial u_{l,jk}}{\partial t^*} dt^* \\ & + \int_{-\infty}^t \left(\mu + \frac{\mu'}{\tau} e^{-(t-t^*)/\tau} \right) \frac{\partial u_{k,ll}}{\partial t^*} dt^* \end{aligned} \quad (3A-12)$$

If it is assumed that the continuum is initially at rest [3A-1]

$$u_k(t) = \varepsilon_{kl}(t) = \sigma_{kl}(t) = 0, \quad -\infty < t < 0 \quad (3A-13)$$

eqn. (3A-12) becomes

$$\begin{aligned} \sigma_{kl,l} = & \int_0^t \left(\lambda + \mu + \frac{\lambda' + \mu'}{\tau} e^{-(t-t^*)/\tau} \right) \frac{\partial u_{l,jk}}{\partial t^*} dt^* \\ & + \int_0^t \left(\mu + \frac{\mu'}{\tau} e^{-(t-t^*)/\tau} \right) \frac{\partial u_{k,ll}}{\partial t^*} dt^* \end{aligned} \quad (3A-14)$$

taking the Laplace transform of eqn. (3A-14) yields

$$\bar{\sigma}_{kl,l} = s \left(\frac{\lambda + \mu}{s} + \frac{\lambda' + \mu'}{\tau} \frac{1}{s+1/\tau} \right) \bar{u}_{l,jk} + s \left(\frac{\mu}{s} + \frac{\mu'}{\tau} \frac{1}{s+1/\tau} \right) \bar{u}_{k,ll} \quad (3A-15)$$

where the overbar represents the transformed variable and where the following property of the Laplace transform is used

$$L \left\{ \int_0^t f(t)g(t-t^*)dt^* \right\} = \bar{f}(s)\bar{g}(s) \quad (3A-16)$$

Equation (3A-15) can be reformulated to yield

$$\bar{\sigma}_{kl,l} = \frac{(\tau(\lambda + \mu) + \lambda' + \mu')s + \lambda + \mu}{\tau s + 1} \bar{u}_{l,jk} + \frac{(\tau\mu + \mu')s + \mu}{\tau s + 1} \bar{u}_{k,ll} \quad (3A-17)$$

A differential series is introduced as

$$\sigma_{kl,l} + a\dot{\sigma}_{kl,l} = bu_{l,jk} + cu_{k,ll} + d\dot{u}_{l,jk} + e\dot{u}_{k,ll} \quad (3A-18)$$

where a , b , c , d and e are constants yet to be determined. Taking the Laplace transform of eqn. (3A-18) yields

$$\begin{aligned} \bar{\sigma}_{kl,l} - \frac{a}{as+1} \sigma_{kl,l}(0) &= \frac{ds+b}{as+1} \bar{u}_{l,lk} - \frac{d}{as+1} u_{l,lk}(0) \\ &+ \frac{es+c}{as+1} \bar{u}_{k,ll} - \frac{e}{as+1} u_{k,ll}(0) \end{aligned} \quad (3A-19)$$

The differential form of eqn. (3A-18) is equivalent to the convolution form of eqn. (3A-14) if[†]

$$a = \tau \quad (3A-20)$$

$$b = \lambda + \mu \quad (3A-21)$$

$$c = \mu \quad (3A-22)$$

$$d = \tau(\lambda + \mu) + \lambda' + \mu' \quad (3A-23)$$

$$e = \tau\mu + \mu' \quad (3A-24)$$

and provided that the following initial condition is satisfied

$$\sigma_{kl,l}(0) = \left(\lambda + \mu + \frac{\lambda' + \mu'}{\tau} \right) u_{l,lk}(0) + \left(\mu + \frac{\mu'}{\tau} \right) u_{k,ll}(0) \quad (3A-25)$$

Substituting eqns. (3A-20) through (3A-24) into eqn. (3A-18) yields

$$\begin{aligned} \dot{\sigma}_{kl,l} &= -\frac{1}{\tau} \sigma_{kl,l} + \frac{\lambda + \mu}{\tau} u_{l,lk} + \frac{\mu}{\tau} u_{k,ll} \\ &+ \left(\lambda + \mu + \frac{\lambda' + \mu'}{\tau} \right) \dot{u}_{l,lk} + \left(\mu + \frac{\mu'}{\tau} \right) \dot{u}_{k,ll} \end{aligned} \quad (3A-26)$$

The following constants are defined:

$$f_k = \sigma_{kl,l} \quad (3A-27)$$

$$r_P = \left(1 + \frac{1}{\tau} \frac{\lambda' + 2\mu'}{\lambda + 2\mu} \right)^{-1} \quad (3A-28)$$

$$r_S = \left(1 + \frac{1}{\tau} \frac{\mu'}{\mu} \right)^{-1} \quad (3A-29)$$

$$\Pi = \lambda + 2\mu + \frac{\lambda' + 2\mu'}{\tau} \quad (3A-30)$$

and

[†] Simply a term by term comparison of eqns. (3A-17) and (3A-19).

$$M = \mu + \frac{\mu'}{\tau} \quad (3A-31)$$

Finally, eqns. (3A-26), (3A-1) and (3A-25) are rewritten to form the stress-dynamic equations and initial condition as

$$\dot{f}_k = -\frac{1}{\tau} f_k + \frac{r_P \Pi - r_S M}{\tau} u_{l,ik} + \frac{r_S M}{\tau} u_{k,ll} + (\Pi - M) \dot{u}_{l,ik} + M \dot{u}_{k,ll} \quad (3A-29)$$

$$\ddot{u}_k = \frac{1}{\rho} (f_k + f_k^b) \quad (3A-30)$$

$$f_k(0) = (\Pi - M) u_{l,ik}(0) + M u_{k,ll}(0) \quad (3A-31)$$

Derivation of Dispersion Relations

In the absence of body forces, eliminating f_k from eqns. (3A-29) and (3A-30) yields an equation expressed in terms of displacement

$$\tau \rho \ddot{u}_k + \rho \ddot{u}_k = (r_P \Pi - r_S M) u_{l,ik} + (r_S M) u_{k,ll} + \tau (\Pi - M) \dot{u}_{l,ik} + \tau M \dot{u}_{k,ll} \quad (3A-32)$$

Consider a steady-state longitudinal plane wave attenuated in the direction of wave propagation and having the form

$$u_k(x_1, x_2, x_3, t) = n_k u_0 e^{-\alpha_P n_m x_m} e^{\hat{i}(k_P n_m x_m - \omega t)} \quad (3A-33)$$

and a similar steady-state shear plane wave having the form

$$u_k(x_1, x_2, x_3, t) = n'_k u_0 e^{-\alpha_S n_m x_m} e^{\hat{i}(k_S n_m x_m - \omega t)} \quad (3A-34)$$

where n_k are the components of the unit wave vector \mathbf{n} , n'_k are the components of a unit vector orthogonal to the wave vector \mathbf{n}_\perp (that is, $\mathbf{n} \cdot \mathbf{n}_\perp = n_k n'_k = 0$), u_0 is the wave amplitude at the phase plane containing the origin, α is the attenuation coefficient, \hat{i} is equal to $\sqrt{-1}$, k is the wavenumber, subscripts P and S denote the respective properties of longitudinal and shear waves, and ω is the circular frequency.

Longitudinal Waves

Substituting eqn. (3A-33) into eqn. (3A-32) yields

$$\begin{aligned}
 \tau\rho n_k u_0 (-\hat{i}\omega)^3 + \rho n_k u_0 (-\hat{i}\omega)^2 &= (r_p \Pi - r_s \mathbf{M}) n_l n_l n_k u_0 (-\alpha_p + \hat{i}k_p)^2 \\
 &+ (r_s \mathbf{M}) n_k n_l n_l u_0 (-\alpha_p + \hat{i}k_p)^2 \\
 &+ \tau(\Pi - \mathbf{M}) n_l n_l n_k u_0 (-\alpha_p + \hat{i}k_p)^2 (-\hat{i}\omega) \\
 &+ \tau \mathbf{M} n_k n_l n_l u_0 (-\alpha_p + \hat{i}k_p)^2 (-\hat{i}\omega)
 \end{aligned} \tag{3A-35}$$

where the common exponential terms have been ignored. Using the property that

$$\mathbf{n} \cdot \mathbf{n} = n_l n_l = 1 \tag{3A-36}$$

and factoring out the common terms n_k and u_0 , eqn. (3A-35) can be simplified to

$$\tau\rho(-\hat{i}\omega)^3 + \rho(-\hat{i}\omega)^2 = r_p \Pi (-\alpha_p + \hat{i}k_p)^2 + \tau \Pi (-\alpha_p + \hat{i}k_p)^2 (-\hat{i}\omega) \tag{3A-37}$$

Simplifying the real part of eqn. (3A-37) yields

$$-\rho\omega^2 = -2\Pi\omega\tau\alpha_p k_p + r_p \Pi (\alpha_p^2 - k_p^2) \tag{3A-38}$$

Simplifying the imaginary part of eqn. (3A-37) yields

$$\tau\rho\omega^3 = -2r_p \Pi \alpha_p k_p - \omega \tau \Pi (\alpha_p^2 - k_p^2) \tag{3A-39}$$

Solving eqns. (3A-38) and (3A-39) for $\alpha_p k_p$ and $\alpha_p^2 - k_p^2$ yields

$$\alpha_p k_p = \frac{(1-r_p)\tau\rho\omega^3}{2\Pi(r_p^2 + \omega^2\tau^2)} \tag{3A-40}$$

and

$$\alpha_p^2 - k_p^2 = -\frac{\rho\omega^2(r_p + \omega^2\tau^2)}{\Pi(r_p^2 + \omega^2\tau^2)} \tag{3A-41}$$

Solving for k_p in eqn. (3A-40) and substituting the result in eqn. (3A-41) yields

$$\alpha_p^4 + \frac{\rho\omega^2(r_p + \omega^2\tau^2)}{\Pi(r_p^2 + \omega^2\tau^2)}\alpha_p^2 - \frac{\tau^2\rho^2\omega^6(1-r_p)^2}{4\Pi^2(r_p^2 + \omega^2\tau^2)^2} = 0 \tag{3A-42}$$

Equation (3A-42) is quadratic in α_p^2 , thus solving via the quadratic equation yields

$$\alpha_p^2 = -\frac{\rho\omega^2(r_p + \omega^2\tau^2)}{2\Pi(r_p^2 + \omega^2\tau^2)} \pm \frac{1}{2} \sqrt{\frac{\rho^2\omega^4(r_p + \omega^2\tau^2)^2}{\Pi^2(r_p^2 + \omega^2\tau^2)^2} + \frac{\tau^2\rho^2\omega^6(1-r_p)^2}{\Pi^2(r_p^2 + \omega^2\tau^2)^2}} \tag{3A-43}$$

$$\alpha_p^2 = -\frac{\rho\omega^2(r_p + \omega^2\tau^2)}{2\Pi(r_p^2 + \omega^2\tau^2)} \pm \frac{1}{2} \left(\frac{\rho\omega^2}{\Pi} \right) \sqrt{\frac{(r_p + \omega^2\tau^2)^2 + \tau^2\omega^2(1-r_p)^2}{(r_p^2 + \omega^2\tau^2)^2}} \tag{3A-44}$$

$$\alpha_p^2 = \frac{\rho\omega^2}{2\Pi} \left(-\frac{r_p + \omega^2\tau^2}{r_p^2 + \omega^2\tau^2} \pm \sqrt{\frac{(r_p + \omega^2\tau^2)^2 + \tau^2\omega^2(1-r_p)^2}{(r_p^2 + \omega^2\tau^2)^2}} \right) \tag{3A-45}$$

Discarding the negative root of eqn. (3A-45) to avoid α_p being an imaginary number yields

$$\alpha_p^2 = \frac{\rho\omega^2}{2\Pi} \left(\sqrt{\frac{(r_p^2 + \omega^2\tau^2)(1 + \omega^2\tau^2)}{(r_p^2 + \omega^2\tau^2)^2}} - \frac{r_p + \omega^2\tau^2}{r_p^2 + \omega^2\tau^2} \right) \quad (3A-46)$$

$$\alpha_p^2 = \frac{\rho\omega^2}{2\Pi} \left(\sqrt{\frac{1 + \omega^2\tau^2}{r_p^2 + \omega^2\tau^2}} - \frac{r_p + \omega^2\tau^2}{r_p^2 + \omega^2\tau^2} \right) \quad (3A-47)$$

Multiplying eqn. (3A-47) by r_p/r_p yields

$$\alpha_p^2 = \frac{\rho\omega^2}{2r_p\Pi} \left(\sqrt{r_p^2 \frac{1 + \omega^2\tau^2}{r_p^2 + \omega^2\tau^2}} - r_p \frac{r_p + \omega^2\tau^2}{r_p^2 + \omega^2\tau^2} \right) \quad (3A-48)$$

$$\alpha_p^2 = \frac{\rho\omega^2}{2r_p\Pi} \left(\sqrt{\frac{1 + \omega^2\tau^2}{1 + r_p^{-2}\omega^2\tau^2}} - \frac{r_p^2 + r_p\omega^2\tau^2}{r_p^2 + \omega^2\tau^2} \right) \quad (3A-49)$$

Finally,

$$\alpha_p^2 = \frac{\rho\omega^2}{2r_p\Pi} \left(\sqrt{\frac{1 + \omega^2\tau^2}{1 + r_p^{-2}\omega^2\tau^2}} - \frac{1 + r_p^{-1}\omega^2\tau^2}{1 + r_p^{-2}\omega^2\tau^2} \right) \quad (3A-50)$$

Reformulating eqn. (3A-41) yields

$$k_p^2 = \frac{\rho\omega^2(1 + r_p^{-1}\omega^2\tau^2)}{r_p\Pi(1 + r_p^{-2}\omega^2\tau^2)} + \alpha_p^2 \quad (3A-51)$$

Substituting eqn. (3A-50) into eqn. (3A-51) and simplifying yields

$$k_p^2 = \frac{\rho\omega^2}{2r_p\Pi} \left(\sqrt{\frac{1 + \omega^2\tau^2}{1 + r_p^{-2}\omega^2\tau^2}} + \frac{1 + r_p^{-1}\omega^2\tau^2}{1 + r_p^{-2}\omega^2\tau^2} \right) \quad (3A-52)$$

Shear Waves

Substituting eqn. (3A-34) into eqn. (3A-32) yields

$$\begin{aligned} \tau\rho n'_k u_0 (-\hat{i}\omega)^3 + \rho n'_k u_0 (-\hat{i}\omega)^2 &= (r_p\Pi - r_s\mathbf{M})n'_i n_i n_k u_0 (-\alpha_s + \hat{i}k_s)^2 \\ &+ (r_s\mathbf{M})n'_k n_i n_i u_0 (-\alpha_s + \hat{i}k_s)^2 \\ &+ \tau(\Pi - \mathbf{M})n'_i n_i n_k u_0 (-\alpha_s + \hat{i}k_s)^2 (-\hat{i}\omega) \\ &+ \tau\mathbf{M}n'_k n_i n_i u_0 (-\alpha_s + \hat{i}k_s)^2 (-\hat{i}\omega) \end{aligned} \quad (3A-53)$$

where the common exponential terms have been ignored. Using the properties

$$\mathbf{n}_\perp \cdot \mathbf{n} = n'_i n_i = 0 \quad (3A-54)$$

$$\mathbf{n} \cdot \mathbf{n} = n_i n_i = 1 \quad (3A-55)$$

and factoring out the common terms n'_k and u_0 , eqn. (3A-53) can be simplified to

$$\tau\rho(-\hat{i}\omega)^3 + \rho(-\hat{i}\omega)^2 = r_s M(-\alpha_s + \hat{i}k_s)^2 + \tau M(-\alpha_s + \hat{i}k_s)^2 (-\hat{i}\omega) \quad (3A-56)$$

The form of eqn. (3A-56) is similar in form to the longitudinal wave case in eqn. (3A-37). Thus the attenuation and wavenumber of shear waves is similarly found to be

$$\alpha_s^2 = \frac{\rho\omega^2}{2r_s M} \left(\sqrt{\frac{1 + \omega^2\tau^2}{1 + r_s^{-2}\omega^2\tau^2}} - \frac{1 + r_s^{-1}\omega^2\tau^2}{1 + r_s^{-2}\omega^2\tau^2} \right) \quad (3A-57)$$

$$k_s^2 = \frac{\rho\omega^2}{2r_s M} \left(\sqrt{\frac{1 + \omega^2\tau^2}{1 + r_s^{-2}\omega^2\tau^2}} + \frac{1 + r_s^{-1}\omega^2\tau^2}{1 + r_s^{-2}\omega^2\tau^2} \right) \quad (3A-58)$$

Limiting Cases of Attenuation and Wavenumber

The attenuation and wavenumber of both P and S waves have a similar form. Henceforth, the limiting cases of the general dispersion characteristics for the following equations will be identified

$$\alpha^2 = \frac{\rho\omega^2}{2r\phi} \left(\sqrt{\frac{1 + \omega^2\tau^2}{1 + r^{-2}\omega^2\tau^2}} - \frac{1 + r^{-1}\omega^2\tau^2}{1 + r^{-2}\omega^2\tau^2} \right) \quad (3A-59)$$

$$k^2 = \frac{\rho\omega^2}{2r\phi} \left(\sqrt{\frac{1 + \omega^2\tau^2}{1 + r^{-2}\omega^2\tau^2}} + \frac{1 + r^{-1}\omega^2\tau^2}{1 + r^{-2}\omega^2\tau^2} \right) \quad (3A-60)$$

where α , k , r , and ϕ can respectively represent either α_p , k_p , r_p , and Π or α_s , k_s , r_s , and M .

In the high frequency limit ($\omega\tau \gg 1$), eqns. (3A-59) and (3A-60) can be conveniently expressed as

$$\alpha^2 = \frac{\rho\omega^2}{2\phi} \left(\left(1 + \omega^{-2}\tau^{-2}\right)^{1/2} \left(1 + r^2\omega^{-2}\tau^{-2}\right)^{-1/2} - (1 + r\omega^{-2}\tau^{-2})(1 + r^2\omega^{-2}\tau^{-2})^{-1} \right) \quad (3A-61)$$

$$k^2 = \frac{\rho\omega^2}{2\phi} \left(\left(1 + \omega^{-2}\tau^{-2}\right)^{1/2} \left(1 + r^2\omega^{-2}\tau^{-2}\right)^{-1/2} + (1 + r\omega^{-2}\tau^{-2})(1 + r^2\omega^{-2}\tau^{-2})^{-1} \right) \quad (3A-62)$$

Using the approximation

$$(1 + \varepsilon)^p \approx 1 + p\varepsilon, \quad \varepsilon \ll 1, \quad (3A-63)$$

eqn. (3A-61) can be simplified to by keeping all terms up to $O(\tau^{-2})$ as

$$\alpha^2 = \frac{\rho\omega^2}{2\phi} \left(1 + \frac{\omega^{-2}\tau^{-2}}{2} - \frac{r^2\omega^{-2}\tau^{-2}}{2} - 1 - r\omega^{-2}\tau^{-2} + r^2\omega^{-2}\tau^{-2} \right) \quad (3A-64)$$

$$\alpha^2 = \frac{\rho}{2\tau^2\phi} \left(\frac{r^2}{2} - r + \frac{1}{2} \right) \quad (3A-65)$$

$$\alpha^2 = \frac{\rho(1-r)^2}{4\tau^2\phi} \quad (3A-66)$$

Finally

$$\alpha = \frac{1-r}{2\tau c_{\max}} \quad (3A-67)$$

where

$$c_{\max} = \sqrt{\phi/\rho} \quad (3A-68)$$

Equation (3A-62) can be simplified by keeping all terms up to $O(\omega^2)$ as

$$k^2 = \frac{\rho\omega^2}{2\phi} (2) \quad (3A-69)$$

$$k = \frac{\omega}{c_{\max}} \quad (3A-70)$$

In the low frequency limit ($\omega\tau \ll r$), eqns. (3A-59) and (3A-60) can be conveniently expressed as

$$\alpha^2 = \frac{\rho\omega^2}{2r\phi} \left((1 + \omega^2\tau^2)^{1/2} (1 + r^{-2}\omega^2\tau^2)^{-1/2} - (1 + r^{-1}\omega^2\tau^2)(1 + r^{-2}\omega^2\tau^2)^{-1} \right) \quad (3A-71)$$

$$k^2 = \frac{\rho\omega^2}{2r\phi} \left((1 + \omega^2\tau^2)^{1/2} (1 + r^{-2}\omega^2\tau^2)^{-1/2} + (1 + r^{-1}\omega^2\tau^2)(1 + r^{-2}\omega^2\tau^2)^{-1} \right) \quad (3A-72)$$

Equation (3A-71) can be simplified by keeping all terms up to $O(\omega^4\tau^2)$ as

$$\alpha^2 = \frac{\rho\omega^2}{2r\phi} \left(\frac{\omega^2\tau^2}{2} - \frac{\omega^2\tau^2}{2r^2} - \frac{\omega^2\tau^2}{r} + \frac{\omega^2\tau^2}{r^2} \right) \quad (3A-73)$$

$$\alpha^2 = \frac{\rho\omega^4\tau^2}{2r\phi} \left(\frac{1}{2} - \frac{1}{r} + \frac{1}{2r^2} \right) \quad (3A-74)$$

$$\alpha^2 = \frac{\rho\omega^4\tau^2(1-r)^2}{4r^3\phi} \quad (3A-75)$$

Finally,

$$\alpha = \frac{\omega^2 \tau (1-r)}{2rc_{\min}} \quad (3A-76)$$

where

$$c_{\min} = \sqrt{r\phi/\rho} \quad (3A-77)$$

Equation (3A-72) can be simplified by keeping all terms up to $O(\omega^2)$ as

$$k^2 = \frac{\rho\omega^2}{2r\phi} \quad (2) \quad (3A-78)$$

$$k = \frac{\omega}{c_{\min}} \quad (3A-79)$$

There is also an intermediate frequency at which the attenuation is approximately proportional to the frequency. This limit is derived by requiring the attenuation tangent line in the $\alpha - \omega$ plane to contain the origin, or

$$\left. \frac{\partial \alpha}{\partial \omega} \right|_{\omega=\omega_0} = \frac{\alpha}{\omega_0} \quad (3A-80)$$

Equation (3A-80) was solved with *Mathematica 5* software [3A-2], to yield the intermediate frequency

$$\omega_0 = \frac{r}{\tau} \sqrt{\frac{3+r}{1+3r}} \quad (3A-81)$$

As $\omega \rightarrow \omega_0$ the attenuation coefficient is

$$\alpha \approx \omega \sqrt{\frac{\rho}{\phi}} \sqrt{\frac{1+2r}{8r} - \frac{5+r}{8(1+r)}} \quad (3A-82)$$

The phase speed in the vicinity of ω_0 is approximated by using a Taylor series expansion truncated after the linear term as

$$c(\omega) \approx c(\omega_0) + (\omega - \omega_0) \left. \frac{\partial c}{\partial \omega} \right|_{\omega=\omega_0} \quad (3A-83)$$

where

$$c(\omega_0) = \sqrt{\frac{\phi}{\rho}} \left(\frac{5+r}{8(1+r)} + \frac{3+2r}{8r} \right)^{-1/2} \quad (3A-84)$$

and

$$\left. \frac{\partial c}{\partial \omega} \right|_{\omega=\omega_0} = (1-r)\tau \sqrt{\frac{\phi \left(\frac{2(5+r)}{(1+r)} + \frac{2(3+2r)}{r} \right)^{1/2}}{\rho (1+3r)^{1/2} (3+r)^{3/2}}} \quad (3A-85)$$

It is clear from the first term in eqn. (3A-85) that slope in the phase speed decreases to zero as the dispersion coefficient approaches its elastic limit. In general, however, when $\omega \rightarrow \omega_0$ the wave propagation is dispersive for $0 \leq r < 1$.

References:

- 3A-1. R.M. Christensen. *Theory of Viscoelasticity: An Introduction* 2nd ed., pp. 14,15,37,38. Academic Press, New York (1982).
 3A-2. Wolfram Research, Inc. (Champaign, IL), *Mathematica* documentation: <http://documents.wolfram.com/mathematica/>

APPENDIX 3B—Four Stage Runge-Kutta Method

In this appendix, the four stage Runge-Kutta numerical integration for a set of linear, discrete dynamic system of equations is outlined.

Consider a matrix equation given by

$$\dot{\mathbf{u}} = \mathbf{A}\mathbf{u} + \mathbf{f} \quad (3B-1)$$

where \mathbf{u} is the state vector, \mathbf{A} is a matrix and \mathbf{f} is a prescribed forcing vector. The Four Stage Runge-Kutta method [3B-1] is given by

$${}^1\mathbf{u} = \Delta t (\mathbf{A}^t \mathbf{u} + \mathbf{f}) \quad (3B-2)$$

$${}^2\mathbf{u} = \Delta t \mathbf{A} \left({}^t\mathbf{u} + \frac{{}^1\mathbf{u}}{2} \right) + \Delta t \left({}^{t+\frac{\Delta t}{2}}\mathbf{f} \right) \quad (3B-3)$$

$${}^3\mathbf{u} = \Delta t \mathbf{A} \left({}^t\mathbf{u} + \frac{{}^2\mathbf{u}}{2} \right) + \Delta t \left({}^{t+\frac{\Delta t}{2}}\mathbf{f} \right) \quad (3B-4)$$

$${}^4\mathbf{u} = \Delta t \mathbf{A} ({}^t\mathbf{u} + {}^3\mathbf{u}) + \Delta t ({}^{t+\Delta t}\mathbf{f}) \quad (3B-5)$$

$${}^{t+\Delta t}\mathbf{u} = {}^t\mathbf{u} + \frac{1}{6} ({}^1\mathbf{u} + 2 \cdot {}^2\mathbf{u} + 2 \cdot {}^3\mathbf{u} + {}^4\mathbf{u}) \quad (3B-6)$$

where left superscripts 1, 2, 3 and 4 denote intermediate steps.

The time stepping procedure for the one-dimensional mass-spring-lattice model (MSDLM) as shown in Fig. 3B-1, for example, is given by

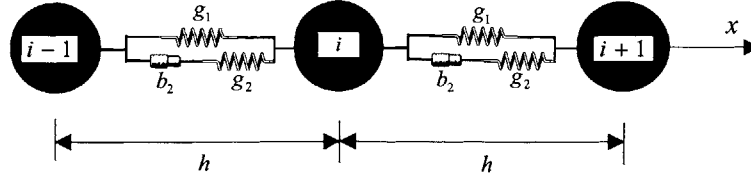


Fig. 3B-1—Schematic of MSDLM for one-dimensional standard linear solid, where each interior particle has mass per unit area (orthogonal to plane of page) equal to ρh .

Step 1:

$${}^1f_i = \Delta t \left(-\frac{1}{\tau} {}^t f_i + \frac{g_1}{\tau h A} ({}^t u_{i+1} - 2 {}^t u_i + {}^t u_{i-1}) + \frac{g_1 + g_2}{h A} ({}^t \dot{u}_i - 2 {}^t \dot{u}_{i+1} + {}^t \dot{u}_{i-1}) \right) \quad (3B-7)$$

$${}^1u_i = \Delta t {}^t \dot{u}_i \quad (3B-8)$$

$${}^1\dot{u}_i = \Delta t \left(\frac{{}^t f_i + {}^t f_{bi}}{\rho} \right) \quad (3B-9)$$

Step 2:

$${}^2f_i = \Delta t \left(-\frac{1}{\tau} {}^t f_i + \frac{g_1}{\tau h A} ({}^t u_{i+1} - 2 {}^t u_i + {}^t u_{i-1}) + \frac{g_1 + g_2}{h A} ({}^t \dot{u}_i - 2 {}^t \dot{u}_{i+1} + {}^t \dot{u}_{i-1}) \right) + \frac{\Delta t}{2} \left(-\frac{1}{\tau} {}^1f_i + \frac{g_1}{\tau h A} ({}^1u_{i+1} - 2 {}^1u_i + {}^1u_{i-1}) + \frac{g_1 + g_2}{h A} ({}^1\dot{u}_i - 2 {}^1\dot{u}_{i+1} + {}^1\dot{u}_{i-1}) \right) \quad (3B-10)$$

$${}^2u_i = \Delta t {}^t \dot{u}_i + \frac{\Delta t}{2} {}^1\dot{u}_i \quad (3B-11)$$

$${}^2\dot{u}_i = \Delta t \left(\frac{{}^t f_i}{\rho} \right) + \frac{\Delta t}{2} \left(\frac{{}^1f_i}{\rho} \right) + \Delta t \left(\frac{{}^{t+\frac{\Delta t}{2}} f_{bi}}{\rho} \right) \quad (3B-12)$$

Step 3:

$${}^3f_i = \Delta t \left(-\frac{1}{\tau} {}^t f_i + \frac{g_1}{\tau h A} ({}^t u_{i+1} - 2 {}^t u_i + {}^t u_{i-1}) + \frac{g_1 + g_2}{h A} ({}^t \dot{u}_i - 2 {}^t \dot{u}_{i+1} + {}^t \dot{u}_{i-1}) \right) + \frac{\Delta t}{2} \left(-\frac{1}{\tau} {}^2f_i + \frac{g_1}{\tau h A} ({}^2u_{i+1} - 2 {}^2u_i + {}^2u_{i-1}) + \frac{g_1 + g_2}{h A} ({}^2\dot{u}_i - 2 {}^2\dot{u}_{i+1} + {}^2\dot{u}_{i-1}) \right) \quad (3B-13)$$

$${}^3u_i = \Delta t {}^t \dot{u}_i + \frac{\Delta t}{2} {}^2\dot{u}_i \quad (3B-14)$$

$${}^3\dot{u}_i = \Delta t \left(\frac{{}^t f_i}{\rho} \right) + \frac{\Delta t}{2} \left(\frac{{}^2f_i}{\rho} \right) + \Delta t \left(\frac{{}^{t+\frac{\Delta t}{2}} f_{bi}}{\rho} \right) \quad (3B-15)$$

Step 4:

$$\begin{aligned}
 {}^4f_i = \Delta t \left(-\frac{1}{\tau} {}^t f_i + \frac{g_1}{hA} ({}^t u_{i+1} - 2 {}^t u_i + {}^t u_{i-1}) + \frac{g_1 + g_2}{hA} ({}^t \dot{u}_i - 2 {}^t \dot{u}_{i+1} + {}^t \dot{u}_{i-1}) \right) \\
 + \Delta t \left(-\frac{1}{\tau} {}^3 f_i + \frac{g_1}{hA} ({}^3 u_{i+1} - 2 {}^3 u_i + {}^3 u_{i-1}) + \frac{g_1 + g_2}{hA} ({}^3 \dot{u}_i - 2 {}^3 \dot{u}_{i+1} + {}^3 \dot{u}_{i-1}) \right)
 \end{aligned} \quad (3B-16)$$

$${}^4 u_i = \Delta t {}^t \dot{u}_i + \Delta t {}^3 \dot{u}_i \quad (3B-17)$$

$${}^4 \dot{u}_i = \Delta t \left(\frac{{}^t f_i}{\rho} \right) + \Delta t \left(\frac{{}^3 f_i}{\rho} \right) + \Delta t \left(\frac{{}^{t+\Delta t} f_{bi}}{\rho} \right) \quad (3B-18)$$

Update

$${}^{t+\Delta t} f_i = {}^t f_i + \frac{1}{6} ({}^1 f_i + 2 {}^2 f_i + 2 {}^3 f_i + {}^4 f_i) \quad (3B-19)$$

$${}^{t+\Delta t} u_i = {}^t u_i + \frac{1}{6} ({}^1 u_i + 2 {}^2 u_i + 2 {}^3 u_i + {}^4 u_i) \quad (3B-20)$$

$${}^{t+\Delta t} \dot{u}_i = {}^t \dot{u}_i + \frac{1}{6} ({}^1 \dot{u}_i + 2 {}^2 \dot{u}_i + 2 {}^3 \dot{u}_i + {}^4 \dot{u}_i). \quad (3B-21)$$

Reference:

- 3B-1. M. Abramowitz and I.A. Stegun (Eds.), *Handbook of Mathematical Functions with Formulas, Graphs and Mathematical Tables*, pp. 896-897. Dover, New York (1965).

APPENDIX 3C—Convergence and Accuracy Criteria for the Mass-Spring-Dashpot Lattice Model

In this appendix, the convergence and accuracy criteria are derived via von Neumann analysis for the one and two-dimensional mass-spring-dashpot lattice model (MSDLM).

One-Dimensional MSDLM
Convergence Criteria

The stress-dynamic equations for a one-dimensional standard linear solid viscoelastic continuum described by a single relaxation time can be expressed as [3C-1]

$$\frac{\partial f}{\partial t} = -\frac{1}{\tau} f + \frac{r\phi}{\tau} \frac{\partial^2 u}{\partial x^2} + \phi \frac{\partial^2 \dot{u}}{\partial x^2} \quad (3C-1)$$

$$\frac{\partial u}{\partial t} = \dot{u} \quad (3C-2)$$

$$\frac{\partial \dot{u}}{\partial t} = \frac{1}{\rho}(f + f_b) \quad (3C-3)$$

where f is the force per unit volume, τ is the stress relaxation time, r is the squared ratio of the minimum to maximum phase speeds ($0 < r \leq 1$), ϕ is the governing elastic constant, u is the displacement, ρ is the density, and f_b is the body force per unit volume.

Taking the Fourier transform of eqns. (3C-1) through (3C-3) yields a matrix equation

$$\frac{d}{dt} \begin{bmatrix} F_k \\ U_k \\ \dot{U}_k \end{bmatrix} = \begin{bmatrix} -\frac{1}{\tau} & -\frac{k^2 r \phi}{\tau} & -k^2 \phi \\ 0 & 0 & 1 \\ \frac{1}{\rho} & 0 & 0 \end{bmatrix} \begin{bmatrix} F_k \\ U_k \\ \dot{U}_k \end{bmatrix} \quad (3C-4)$$

where F_k , U_k and \dot{U}_k are the respective complex amplitudes of the force per unit volume, displacement, and velocity corresponding to the wavenumber k . Equation (3C-4) can be rewritten as

$$\dot{\mathbf{u}}_{exact} = \mathbf{A}_{exact}^{1-D} \mathbf{u}_{exact} \quad (3C-5)$$

The eigenvalues of \mathbf{A}_{exact}^{1-D} are given by

$$\left| \lambda_{\mathbf{A}_{exact}^{1-D}} \mathbf{I} - \mathbf{A}_{exact}^{1-D} \right| = 0 \quad (3C-6)$$

which satisfies the characteristic equation

$$\lambda_{\mathbf{A}_{exact}^{1-D}}^3 + \frac{1}{\tau} \lambda_{\mathbf{A}_{exact}^{1-D}}^2 + \frac{Z}{\tau^2} \lambda_{\mathbf{A}_{exact}^{1-D}} + \frac{rZ}{\tau^3} = 0 \quad (3C-7)$$

where

$$Z \equiv \frac{Ek^2\tau^2}{\rho} \quad (3C-8)$$

The eigenvalues of \mathbf{A}_{exact} are

$$\lambda_{1, \mathbf{A}_{exact}^{1-D}} = -\frac{1}{3\tau} - \frac{\sqrt[3]{2}(3Z-1)}{3\tau D_{\mathbf{A}_{exact}^{1-D}}} + \frac{D_{\mathbf{A}_{exact}^{1-D}}}{3\sqrt[3]{2}\tau} \quad (3C-9a)$$

$$\lambda_{2, \mathbf{A}_{exact}^{1-D}} = -\frac{1}{3\tau} + \frac{(1 + \hat{i}\sqrt{3})(3Z - 1)}{3\sqrt[3]{4\tau} D_{\mathbf{A}_{exact}^{1-D}}} - \frac{(1 - \hat{i}\sqrt{3}) D_{\mathbf{A}_{exact}^{1-D}}}{6\sqrt[3]{2\tau}} \quad (3C-9b)$$

$$\lambda_{3, \mathbf{A}_{exact}^{1-D}} = -\frac{1}{3\tau} + \frac{(1 - \hat{i}\sqrt{3})(3Z - 1)}{3\sqrt[3]{4\tau} D_{\mathbf{A}_{exact}^{1-D}}} - \frac{(1 + \hat{i}\sqrt{3}) D_{\mathbf{A}_{exact}^{1-D}}}{6\sqrt[3]{2\tau}} \quad (3C-9c)$$

where \hat{i} is equal to $\sqrt{-1}$

$$D_{\mathbf{A}_{exact}^{1-D}} = \left(Z(9 - 27r) - 2 + 3\sqrt{(3Z)(4Z^2 + 27Zr^2 - 18Zr - Z + 4r)} \right)^{1/3} \quad (3C-9d)$$

The exact time evolution of eqn. (3C-5) is given by

$$\mathbf{u}_{exact}(t) = \mathbf{G}_{exact}^{1-D} \mathbf{u}_{exact}(0) \quad (3C-10)$$

where

$$\mathbf{G}_{exact}^{1-D} = e^{t\mathbf{A}_{exact}^{1-D}} \quad (3C-11)$$

Here \mathbf{G}_{exact}^{1-D} is the amplification matrix, $e^{t\mathbf{A}_{exact}^{1-D}}$ is the matrix exponential of \mathbf{A}_{exact}^{1-D} and $\mathbf{u}_{exact}(0)$ is the initial conditions vector. The dimensionless eigenvalues of \mathbf{G}_{exact}^{1-D} are called amplification factors and are simply related by the expression $\xi_{l, \mathbf{G}_{exact}^{1-D}} = e^{\lambda_{l, \mathbf{A}_{exact}^{1-D}}}$, where l represents any of 1, 2 or 3.

Equations (3C-1), (3C-2), and (3C-3) are discretized via the one-dimensional mass-spring-dashpot lattice model (MSDLM) in Fig. 3C-1. The stress-dynamic equations for the discretized model are

$$\frac{df_i}{dt} = -\frac{1}{\tau} f_i + \frac{g_1}{\hbar A} (u_{i+1} - 2u_i + u_{i-1}) + \frac{g_1 + g_2}{hA} (\dot{u}_{i+1} - 2\dot{u}_i + \dot{u}_{i-1}) \quad (3C-12)$$

$$\frac{du_i}{dt} = \dot{u}_i \quad (3C-13)$$

$$\frac{d\dot{u}_i}{dt} = \frac{1}{\rho} (f_i + f_{bi}) \quad (3C-14)$$

where

$$\frac{b_2}{g_2} = \tau \quad (3C-15)$$

f_i is the force per particle volume due to the internal strain on particle i , g_1 and g_2 are spring constants, h is the grid space, A is a unit cross-sectional area normal to direction of

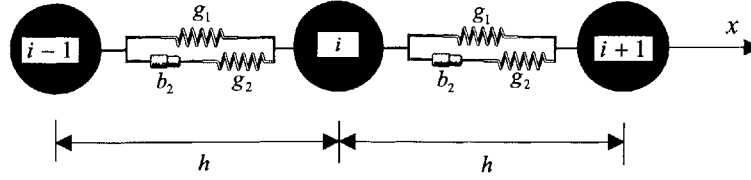


Fig. 3C-1—Schematic of MSDLM for one-dimensional standard linear solid, where each interior particle has mass per unit area (orthogonal to plane of page) equal to ρh .

force, and u_i is the displacement of particle i , and f_{bi} is the body force per unit particle volume on particle i

Expanding eqn. (3C-12) via the Taylor's series in the limit as $h \rightarrow 0$ and comparing the result with eqn. (3C-1), the one-dimensional MSDLM is spatially *consistent* with the governing PDEs if

$$g_1 = \frac{r\phi A}{h} \quad (3C-16)$$

$$g_2 = \frac{(1-r)\phi A}{h} \quad (3C-17)$$

Taking the discrete Fourier transform of eqns. (3C-12) through (3C-14), in light of eqns. (3C-16) and (3C-17), yields a matrix equation

$$\frac{d}{dt} \begin{bmatrix} F_k \\ U_k \\ \dot{U}_k \end{bmatrix} = \begin{bmatrix} -\frac{1}{\tau} & -\frac{2r\phi}{\tau h^2}(1 - \cos kh) & -\frac{2\phi}{h^2}(1 - \cos kh) \\ 0 & 0 & 1 \\ \frac{1}{\rho} & 0 & 0 \end{bmatrix} \begin{bmatrix} F_k \\ U_k \\ \dot{U}_k \end{bmatrix} \quad (3C-18)$$

or

$$\dot{\mathbf{u}}_{msdlm} = \mathbf{A}_{msdlm}^{1-D} \mathbf{u}_{msdlm} \quad (3C-19)$$

The eigenvalues for \mathbf{A}_{msdlm}^{1-D} satisfy the characteristic equation

$$\lambda_{\mathbf{A}_{msdlm}^{1-D}}^3 + \frac{1}{\tau} \lambda_{\mathbf{A}_{msdlm}^{1-D}}^2 + \frac{Z'}{\tau^2} \lambda_{\mathbf{A}_{msdlm}^{1-D}} + \frac{Z'r}{\tau^3} = 0 \quad (3C-20)$$

where

$$Z' \equiv \frac{2\phi\tau^2}{\rho h^2}(1 - \cos kh) \quad (3C-21)$$

The eigenvalues of \mathbf{A}_{msdlm}^{1-D} are

$$\lambda_{1, \mathbf{A}_{msdlm}^{1-D}} = -\frac{1}{3\tau} - \frac{\sqrt[3]{2}(3Z' - 1)}{3\tau D_{\mathbf{A}_{msdlm}^{1-D}}} + \frac{D_{\mathbf{A}_{msdlm}^{1-D}}}{3\sqrt[3]{2}\tau} \quad (3C-22a)$$

$$\lambda_{2, \mathbf{A}_{msdlm}^{1-D}} = -\frac{1}{3\tau} + \frac{(1 + \hat{i}\sqrt{3})(3Z' - 1)}{3\sqrt[3]{4\tau} D_{\mathbf{A}_{msdlm}^{1-D}}} - \frac{(1 - \hat{i}\sqrt{3})D_{\mathbf{A}_{msdlm}^{1-D}}}{6\sqrt[3]{2}\tau} \quad (3C-22b)$$

$$\lambda_{3, \mathbf{A}_{msdlm}^{1-D}} = -\frac{1}{3\tau} + \frac{(1 - \hat{i}\sqrt{3})(3Z' - 1)}{3\sqrt[3]{4\tau} D_{\mathbf{A}_{msdlm}^{1-D}}} - \frac{(1 + \hat{i}\sqrt{3})D_{\mathbf{A}_{msdlm}^{1-D}}}{6\sqrt[3]{2}\tau} \quad (3C-22c)$$

where

$$D_{\mathbf{A}_{msdlm}^{1-D}} = \left(Z'(9 - 27r) - 2 + 3\sqrt{(3Z')(4Z'^2 + 27Z'r^2 - 18Z'r - Z' + 4r)} \right)^{1/3} \quad (3C-22d)$$

The exact solution to eqn. (3C-23) is

$${}^{t+\Delta t} \mathbf{u}_{msdlm} = \mathbf{G}_{msdlm}^{1-D} {}^t \mathbf{u}_{msdlm} \quad (3C-23)$$

where

$$\mathbf{G}_{msdlm}^{1-D} = e^{\Delta t \mathbf{A}_{msdlm}^{1-D}} \quad (3C-24)$$

In numerical computations, the \mathbf{G}_{msdlm}^{1-D} must be approximated. Using a four stage Runge-Kutta integration method [3C-2], the numerical amplification matrix is written as

$$\mathbf{G}_{numerical}^{1-D} = \mathbf{I} + \frac{1}{1!} \Delta t \mathbf{A}_{msdlm}^{1-D} + \frac{1}{2!} (\Delta t \mathbf{A}_{msdlm}^{1-D})^2 + \frac{1}{3!} (\Delta t \mathbf{A}_{msdlm}^{1-D})^3 + \frac{1}{4!} (\Delta t \mathbf{A}_{msdlm}^{1-D})^4 \quad (3C-25)$$

$\mathbf{G}_{numerical}^{1-D}$ is equal to the Taylor series expansion of \mathbf{G}_{msdlm}^{1-D} truncated before the term of order $(\Delta t)^5$. As $h \rightarrow 0$ and $\Delta t \rightarrow 0$ the solution approaches the exact continuum solution, eqn. (3C-10); thus, the MSDLM discretization in space combined with the Runge-Kutta temporal integration yield a *consistent* numerical scheme. Equation (3C-25) can be rewritten as

$$\mathbf{G}_{numerical}^{1-D} = \begin{bmatrix} a_{11} & a_{12} & a_{13} \\ a_{21} & a_{22} & a_{23} \\ a_{31} & a_{32} & a_{33} \end{bmatrix} \quad (3C-26a)$$

where

$$\begin{aligned}
 a_{11} = & 1 - \frac{\Delta t}{\tau} + \frac{(\Delta t)^2}{2} \left(\frac{1}{\tau^2} - \frac{2\phi(1-\cos kh)}{\rho h^2} \right) \\
 & + \frac{(\Delta t)^3}{6} \left(-\frac{1}{\tau^3} + \frac{2\phi(2-r)(1-\cos kh)}{\rho \tau h^2} \right) \\
 & + \frac{(\Delta t)^4}{24} \left(\left(\frac{1}{\tau^2} - \frac{2\phi(1-\cos kh)}{\rho h^2} \right)^2 - \frac{2\phi(1-\cos kh)}{\rho h^2 \tau^2} \right)
 \end{aligned} \tag{3C-26b}$$

$$\begin{aligned}
 a_{12} = & -\frac{2r\phi\Delta t(1-\cos kh)}{\tau h^2} + \frac{r\phi(\Delta t)^2(1-\cos kh)}{\tau^2 h^2} \\
 & + \frac{(\Delta t)^3}{3} \left(\frac{\phi r(1-\cos kh)}{h^2 \tau^2} \right) \left(-\frac{1}{\tau^2} + \frac{2\phi(1-\cos kh)}{h^2 \rho} \right) \\
 & + \frac{(\Delta t)^4}{24} \left(\frac{2\phi r(1-\cos kh)}{h^2 \tau} \right) \left(\frac{1}{\tau^3} - \frac{2\phi r(1-\cos kh)}{\rho \tau} \right)
 \end{aligned} \tag{3C-26c}$$

$$\begin{aligned}
 a_{13} = & \frac{2\phi\Delta t(1-\cos kh)}{h^2} + \frac{\phi(1-r)(\Delta t)^2(1-\cos kh)}{\tau h^2} \\
 & + \frac{(\Delta t)^3}{6} \left(-\frac{2\phi(1-r)(1-\cos kh)}{h^2 \rho} + \frac{4\phi^2(1-\cos kh)^2}{h^2 \rho} \right) \\
 & + \frac{(\Delta t)^4}{24} \left(\frac{2\phi(1-r)(1-\cos kh)}{h^2 \tau} \right) \left(\frac{1}{\tau^2} - \frac{4\phi(1-\cos kh)}{h^2 \rho} \right)
 \end{aligned} \tag{3C-26d}$$

$$a_{21} = \frac{(\Delta t)^2}{2\rho} - \frac{(\Delta t)^3}{6\rho\tau} + \frac{(\Delta t)^4 \phi r(1-\cos kh)}{12h^2 \rho \tau^2} \tag{3C-26e}$$

$$a_{22} = 1 - \frac{(\Delta t)^3 \phi r(1-\cos kh)}{3h^2 \rho \tau} + \frac{(\Delta t)^4 \phi r(1-\cos kh)}{12h^2 \rho \tau^2} \tag{3C-26f}$$

$$a_{23} = \Delta t - \frac{(\Delta t)^3 \phi(1-\cos kh)}{3h^2 \rho} + \frac{(\Delta t)^4 \phi(1-r)(1-\cos kh)}{12h^2 \rho \tau} \tag{3C-26g}$$

$$\begin{aligned}
 a_{31} = & \frac{\Delta t}{\rho} - \frac{(\Delta t)^2}{2\tau\rho} + \frac{(\Delta t)^3}{6} \left(\frac{1}{\tau^2} - \frac{2\phi(1-\cos kh)}{h^2 \rho} \right) \\
 & + \frac{(\Delta t)^4}{24} \left(-\frac{1}{\rho \tau^3} + \frac{2\phi(2-r)(1-\cos kh)}{\rho^2 h^2 \tau} \right)
 \end{aligned} \tag{3C-26h}$$

$$\begin{aligned}
 a_{32} = & -\frac{(\Delta t)^2 \phi r(1-\cos kh)}{\rho \tau h^2} + \frac{(\Delta t)^3 \phi r(1-\cos kh)}{3h^2 \rho \tau^2} \\
 & + \frac{(\Delta t)^4 \phi r(1-\cos kh)}{12h^2 \rho \tau} \left(-\frac{1}{\tau^2} + \frac{2\phi(1-\cos kh)}{h^2 \rho} \right)
 \end{aligned} \tag{3C-26i}$$

$$\begin{aligned}
 a_{33} = & 1 - \frac{(\Delta t)^2 \phi(1 - \cos kh)}{h^2 \rho} + \frac{(\Delta t)^3 \phi(1-r)(1 - \cos kh)}{3h^2 \rho \tau} \\
 & + \frac{(\Delta t)^4}{24} \left(-\frac{2\phi(1-r)(1 - \cos kh)}{\rho h^2 \tau^2} + \frac{4\phi^2(1 - \cos kh)^2}{h^2 \rho^2} \right)
 \end{aligned} \tag{3C-26j}$$

The amplification factors of $\mathbf{G}_{numerical}^{1-D}$ are

$$\begin{aligned}
 \xi_{1,numerical} = & \frac{(a_{11} + a_{22} + a_{33})}{3} + \frac{\sqrt[3]{2}d_2}{3(d_1 + \sqrt{d_1^2 + 4d_2^3})^{1/3}} \\
 & + \frac{(d_1 + \sqrt{d_1^2 + 4d_2^3})^{1/3}}{3\sqrt[3]{2}}
 \end{aligned} \tag{3C-26k}$$

$$\begin{aligned}
 \xi_{2,numerical} = & \frac{(a_{11} + a_{22} + a_{33})}{3} - \frac{(\hat{i} + \sqrt{3})d_2}{3\sqrt[3]{4}(d_1 + \sqrt{d_1^2 + 4d_2^3})^{1/3}} \\
 & + \frac{(\hat{i} - \sqrt{3})(d_1 + \sqrt{d_1^2 + 4d_2^3})^{1/3}}{6\sqrt[3]{2}}
 \end{aligned} \tag{3C-26l}$$

$$\begin{aligned}
 \xi_{3,numerical} = & \frac{(a_{11} + a_{22} + a_{33})}{3} - \frac{(\hat{i} - \sqrt{3})d_2}{3\sqrt[3]{4}(d_1 + \sqrt{d_1^2 + 4d_2^3})^{1/3}} \\
 & + \frac{(\hat{i} + \sqrt{3})(d_1 + \sqrt{d_1^2 + 4d_2^3})^{1/3}}{6\sqrt[3]{2}}
 \end{aligned} \tag{3C-26m}$$

where

$$\begin{aligned}
 d_1 = & 2(a_{11}^3 + a_{22}^3 + a_{33}^3) - 3(a_{11}^2 a_{22} + a_{11}^2 a_{33} + a_{22}^2 a_{33} + a_{11} a_{22}^2 + a_{22} a_{33}^2) \\
 & + 9 \left(\begin{aligned} & a_{11} a_{12} a_{21} + a_{12} a_{21} a_{22} + a_{11} a_{13} a_{31} \\ & + a_{22} a_{23} a_{32} + a_{13} a_{31} a_{33} + a_{23} a_{32} a_{33} \end{aligned} \right)
 \end{aligned} \tag{3C-26n}$$

$$\begin{aligned}
 & + 12a_{11} a_{22} a_{33} - 18(a_{13} a_{22} a_{31} + a_{11} a_{23} a_{32} + a_{12} a_{21} a_{33}) \\
 & + 27(a_{12} a_{23} a_{31} + a_{13} a_{21} a_{32})
 \end{aligned}$$

$$\begin{aligned}
 d_2 = & -(a_{11}^2 + a_{22}^2 + a_{33}^2) - 3(a_{12} a_{21} + a_{13} a_{31} + a_{23} a_{32}) + a_{11} a_{22} \\
 & + a_{11} a_{33} + a_{22} a_{33}
 \end{aligned} \tag{3C-26o}$$

The amplification factors of $\mathbf{G}_{numerical}^{1-D}$ must lie within the stability region expressed in terms of the amplification factors of $\Delta t \mathbf{A}_{msdlm}^{1-D}$ as

$$\left| 1 + \xi_{\Delta t \mathbf{A}_{msdlm}^{1-D}} + \frac{\xi_{\Delta t \mathbf{A}_{msdlm}^{1-D}}^2}{2} + \frac{\xi_{\Delta t \mathbf{A}_{msdlm}^{1-D}}^3}{6} + \frac{\xi_{\Delta t \mathbf{A}_{msdlm}^{1-D}}^4}{24} \right| \leq 1 \tag{3C-27}$$

The amplification factors of $\Delta t \mathbf{A}_{msdlm}^{1-D}$ satisfy the following characteristic equation

$$\left| \xi_{\Delta t \mathbf{A}_{msdlm}^{1-D}} \mathbf{I} - \Delta t \mathbf{A}_{msdlm}^{1-D} \right| = 0 \quad (3C-28)$$

or

$$\xi_{\Delta t \mathbf{A}_{msdlm}^{1-D}}^3 + w \xi_{\Delta t \mathbf{A}_{msdlm}^{1-D}}^2 + z^2 \xi_{\Delta t \mathbf{A}_{msdlm}^{1-D}} + r w z^2 = 0 \quad (3C-29)$$

where

$$w = \frac{\Delta t}{\tau} \quad (3C-30)$$

and

$$z = \frac{\sqrt{2} c_{\max} \Delta t}{h} \sqrt{1 - \cos kh} \quad (3C-31)$$

Here c_{\max} is given by

$$c_{\max} \equiv \sqrt{\frac{\phi}{\rho}} \quad (3C-32)$$

The amplification factors of $\Delta t \mathbf{A}_{msdlm}^{1-D}$ are

$$\xi_{1, \Delta t \mathbf{A}_{msdlm}^{1-D}} = -\frac{w}{3} - \frac{\sqrt[3]{2}(3z^2 - w^2)}{3d_{\Delta t \mathbf{A}_{msdlm}^{1-D}}} + \frac{d_{\Delta t \mathbf{A}_{msdlm}^{1-D}}}{3\sqrt[3]{2}} \quad (3C-33a)$$

$$\xi_{2, \Delta t \mathbf{A}_{msdlm}^{1-D}} = -\frac{w}{3} + \frac{(1 + i\sqrt{3})(3z^2 - w^2)}{3\sqrt[3]{4}d_{\Delta t \mathbf{A}_{msdlm}^{1-D}}} - \frac{(1 - i\sqrt{3})d_{\Delta t \mathbf{A}_{msdlm}^{1-D}}}{6\sqrt[3]{2}} \quad (3C-33b)$$

$$\xi_{3, \Delta t \mathbf{A}_{msdlm}^{1-D}} = -\frac{w}{3} + \frac{(1 - i\sqrt{3})(3z^2 - w^2)}{3\sqrt[3]{4}d_{\Delta t \mathbf{A}_{msdlm}^{1-D}}} - \frac{(1 + i\sqrt{3})d_{\Delta t \mathbf{A}_{msdlm}^{1-D}}}{6\sqrt[3]{2}} \quad (3C-33c)$$

where

$$d_{\Delta t \mathbf{A}_{msdlm}^{1-D}} = \left(\frac{w(9z^2 - 27rz^2 - 2w^2) + \sqrt{4(3z^2 - w^2)^3 + w^2(9z^2 - 27rz^2 - 2w^2)^2}}{\sqrt[3]{2}} \right)^{\frac{1}{3}} \quad (3C-33d)$$

The special case of amplification factors of $\Delta t \mathbf{A}_{msdlm}^{1-D}$ lying on the real axis requires

$$-2.78 \leq \xi_{\Delta t \mathbf{A}_{msdlm}^{1-D}} \leq 0^\ddagger \quad (3C-34)$$

The special case of amplification factors of $\Delta t \mathbf{A}_{msdlm}^{1-D}$ lying on the imaginary axis requires

$$-\hat{i}2\sqrt{2} \leq \xi_{\Delta t \mathbf{A}_{msdlm}^{1-D}} \leq \hat{i}2\sqrt{2} \quad (3C-35)$$

where \hat{i} is equal to $\sqrt{-1}$.

As r approaches unity, the amplification factors of $\Delta t \mathbf{A}_{msdlm}^{1-D}$ reduce to one real and one pair of imaginary complex conjugates.

$$\xi_{1, \Delta t \mathbf{A}_{msdlm}^{1-D}} = -w \quad (3C-36)$$

$$\xi_{2, \Delta t \mathbf{A}_{msdlm}^{1-D}} = \hat{i}z \quad (3C-37)$$

$$\xi_{3, \Delta t \mathbf{A}_{msdlm}^{1-D}} = -\hat{i}z \quad (3C-38)$$

Thus, from eqns. (3C-34) and (3C-36)

$$-2.78 \leq -\frac{\Delta t}{\tau} \leq 0 \quad (3C-39)$$

or

$$\frac{\Delta t}{\tau} \leq 2.78 \quad (3C-40)$$

and, from eqns. (3C-34), (3C-36) and (3C-37)

$$|z| \leq 2\sqrt{2} \quad (3C-41)$$

or

$$\left| \frac{\sqrt{2}c_{\max}\Delta t}{h} \sqrt{1 - \cos kh} \right| \leq 2\sqrt{2} \quad (3C-42)$$

Because eqn. (3C-41) must be satisfied for all kh , it follows that

$$\frac{c_{\max}\Delta t}{h} \leq \sqrt{2} \approx 1.41 \quad (3C-43)$$

[‡]Approximation -2.78 results from requiring $\xi_{\Delta t \mathbf{A}_{msdlm}^{1-D}}$ to lie on the real axis in eqn. (C.27). Exact expression

for lower limit is $-\frac{4}{3} - \frac{10}{3} \frac{\sqrt[3]{2}}{\sqrt[3]{9\sqrt{29} - 43}} + \frac{1}{3} \sqrt[3]{4(9\sqrt{29} - 43)}$.

The nondimensional number $\frac{c_{\max}\Delta t}{h}$ is often important in wave propagation problems and is defined as the Courant number [3C-4].

The above stability analysis is valid as r approaches unity. To generalize, Fig. 3C-2 shows boundaries of stability regions in the z - w plane for various values of r . The stability condition in eqn. (3C-39) is applicable for all valid r ; the stability condition in eqn. (3C-42) is valid for $0.13 < r < 1$. However, for $0 < r < 0.13$, a conservative stability limit requires the Courant number to be less than 1.30.

In summary, for a one-dimensional MSDLM the stability conditions for all r are given by

$$\frac{\Delta t}{\tau} \leq 2.78 \quad 0 < r \leq 1 \quad (3C-44)$$

$$\frac{c_{\max}\Delta t}{h} \leq \sqrt{2} \approx 1.41 \quad 0.13 < r \leq 1 \quad (3C-45)$$

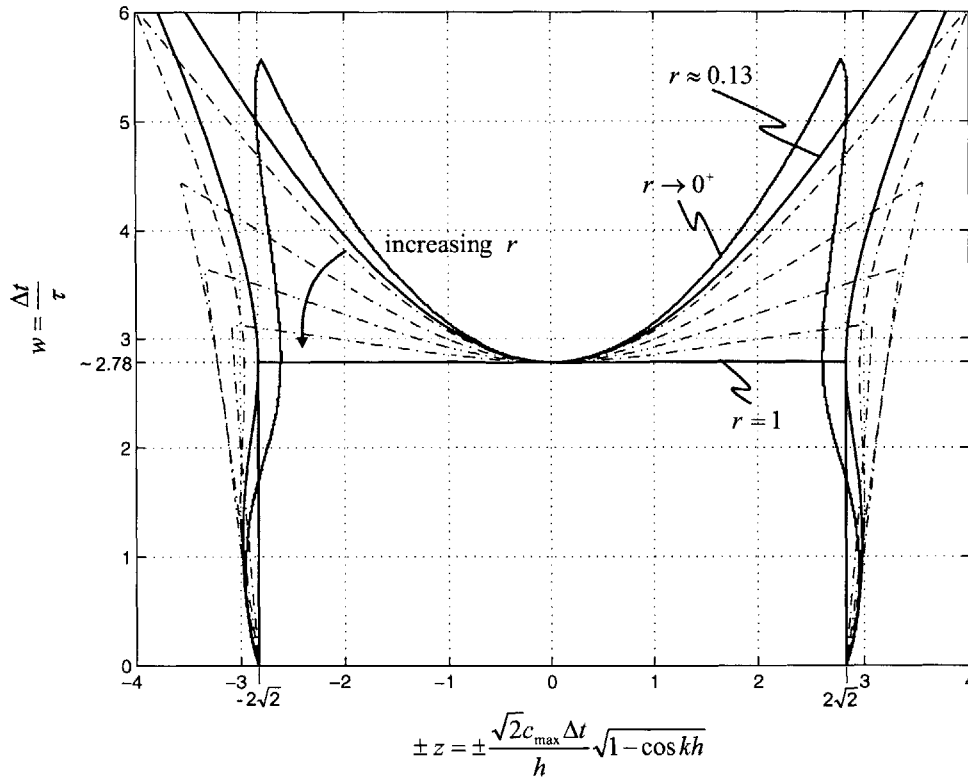


Fig. 3C-2—Stability region boundaries for fourth order Runge-Kutta method on z - w plane for various values of r . For given r , all points that lie between stability boundary and origin are stable.

$$\frac{c_{\max} \Delta t}{h} \leq 1.30 \quad 0 < r \leq 0.13 \quad (3C-46)$$

In accordance with the Lax equivalence theorem [3C-4], the demonstrated *consistency* and *stability* ensure the MSDLM's *convergence*.

Accuracy Criteria

The accuracy of the MSDLM is determined by a comparison of the amplification factor of the exact solution of the continuum model, ξ_{exact} , and the amplification factor due to the Runge-Kutta numerical integration of the MSDLM, $\xi_{numerical}$. In general the amplification factors are complex, and it is often easier to compare their magnitudes and the phases. The respective magnitudes of the exact and numerical amplification factors are given by

$$|\xi_{exact}| = e^{\text{Re}\{\lambda_{exact}\}\Delta t} \quad (3C-46)$$

where λ_{exact} represents any eigenvalues from eqns. (3C-9a), (3C-9b) and (3C-9c),

and

$$|\xi_{numerical}| = \sqrt{\xi_{numerical} \bar{\xi}_{numerical}} \quad (3C-47)$$

where $\xi_{numerical}$ represents any of amplification factors from eqns. (3C-26k), (3C-26l) and (3C-26m) and the overbar denotes complex conjugation. The respective phase angles of the exact and numerical amplification factors are given by

$$\langle \xi_{exact} \rangle = \text{Im}\{\lambda_{exact}\}\Delta t \quad (3C-48)$$

and

$$\langle \xi_{numerical} \rangle = \text{Im}\{\ln(\xi_{numerical})\} \quad (3C-49)$$

(It is noted that the phase angle for the numerical amplification factor will always lie in the range $-\frac{\pi}{2} < \langle \xi_{numerical} \rangle \leq \frac{\pi}{2}$.)

Figure 3C-3 shows the magnitude and phase of the exact and numerical amplification factors as a function of normalized wavenumber when $r = 0.55$, $C = \sqrt{2}$, $\Delta t/\tau = 2.78/4$. For the exact and numerical amplification factors, it is clear that each falls the following categories: a purely real amplification factor corresponding to non-

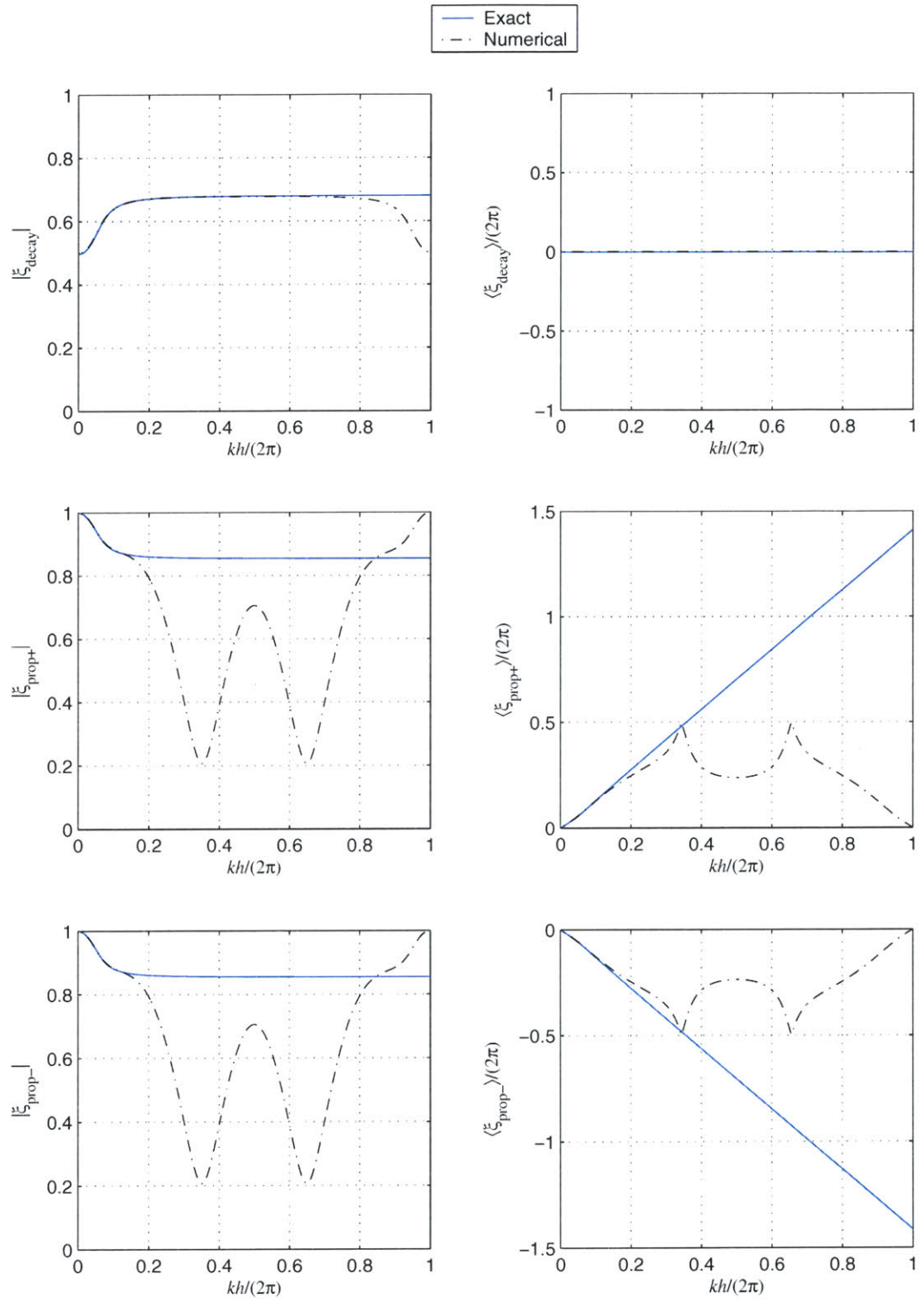


Fig. 3C-3—One-dimensional exact and numerical (MSDLM) magnitudes and phase angles as function of normalized wave number k , for $r = 0.55$, $C = \sqrt{2}$, and $\Delta t/\tau = 0.70$.

propagating decay, denoted by ξ_{decay} , or a complex conjugate pair of amplification factors corresponding to decayed propagation with positive phase and negative phase, denoted by $\xi_{\text{prop+}}$ and $\xi_{\text{prop-}}$, respectively. It is noted that the category for each into one of amplification factor is *not* determined by the order of the subscripts listed in eqns. (3C-9a), (3C-9b), (3C-9c), (3C-26k), (3C-26l) and (3C-26m).

At small kh , the numerical amplification factors approach the exact values; as kh grows larger, the error increases. To quantify this behavior, the error in magnitude and phase of the amplification factors are expressed as

$$\text{Percent Error in Magnitude} = \left| \frac{|\xi_{\text{exact}}| - |\xi_{\text{numerical}}|}{|\xi_{\text{exact}}|} \right| \times 100\% \quad (3C-50)$$

$$\text{Percent Error in Phase} = \left| \frac{\langle \xi_{\text{exact}} \rangle - \langle \xi_{\text{numerical}} \rangle}{\langle \xi_{\text{exact}} \rangle} \right| \times 100\% \quad (3C-51)$$

For the case where $r = 0.55$, $C = \sqrt{2}$, and $\Delta t/\tau = 2.78/4$, Fig. 3C-4 shows the percent error in magnitude for ξ_{decay} as a function of kh . The plot reveals that, to achieve a 1% error or less in the magnitude of ξ_{decay} , the maximum allowable $kh/2\pi$ is ~ 0.75 . For the same case, Fig. 3C-5 shows the percent error in magnitude and phase for $\xi_{\text{prop+/-}}$ as a function of kh . To achieve less than 1% error in magnitude for ξ_{prop} requires $kh/2\pi$ to be less than ~ 0.15 ; however, to achieve less than 1% error in phase for $\xi_{\text{prop+/-}}$ requires $kh/2\pi$ to be less than ~ 0.07 . For this example, one can conclude that the grid spacing should be set according to the error in phase.

The ordinate and abscissa labels in Fig. 3C-4 have a more physical meaning. From the definition of wavenumber, recall that

$$\frac{kh}{2\pi} = \frac{h}{\kappa} \quad (3C-52)$$

where κ is the wavelength. If N_s is defined as ratio of the wavelength κ per grid spacing h , the following relationship exists

$$N_s = \left(\frac{kh}{2\pi} \right)^{-1} \quad (3C-53)$$

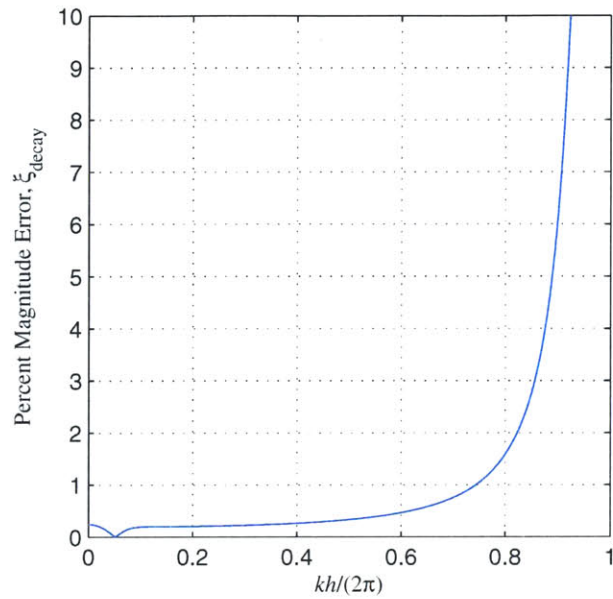


Fig. 3C-4—Percent error in magnitude of amplification factor corresponding to pure decay as function of normalized wave number k , for $r = 0.55$, $C = \sqrt{2}$, and $\Delta t/\tau = 0.70$.

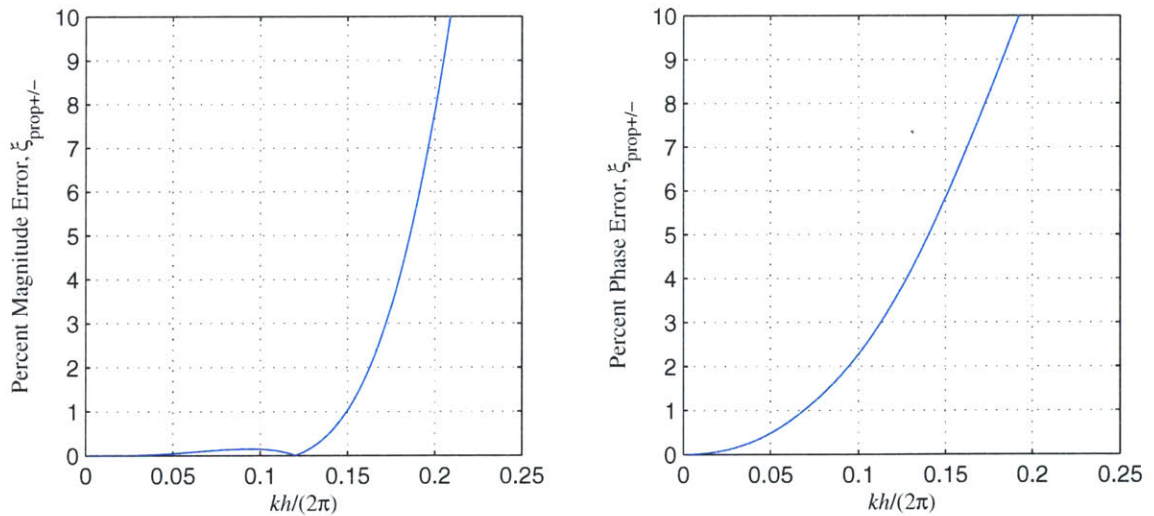


Fig. 3C-5—Percent error in magnitude and phase angle of amplification factor corresponding to wave propagation as function of normalized wave number k , for $r = 0.55$, $C = \sqrt{2}$, and $\Delta t/\tau = 0.70$.

Thus, if $kh/2\pi$ must be less than, say, 0.05 to achieve the required accuracy in phase, it requires a discretization of at least 20 (1/0.05) grid spacings per wavelength.

The phase value of the exact and numerical amplification factors, can be described as the circular frequency multiplied by the time step [3C-3], or

$$\langle \xi_{exact} \rangle = \omega_{exact} \Delta t \quad (3C-54)$$

$$\langle \xi_{numerical} \rangle = \omega_{numerical} \Delta t \quad (3C-55)$$

The relationship between phase speed, circular frequency, and wavenumber is

$$c_{exact} = \frac{\omega_{exact}}{k} \quad (3C-56)$$

$$c_{numerical} = \frac{\omega_{numerical}}{k} \quad (3C-57)$$

Hence, in light of eqns. (3C-54) through (3C-57), eqn. (3C-51) can be rewritten as

$$\left| \frac{\langle \xi_{exact} \rangle - \langle \xi_{numerical} \rangle}{\langle \xi_{exact} \rangle} \right| \times 100\% = \left| \frac{c_{exact} - c_{numerical}}{c_{exact}} \right| \times 100\% \quad (3C-58)$$

Thus, the phase error is also equal to the error in wave speed.

Combining these concepts, Fig. 3C-6 shows contour plots of the minimum number of grid spacings per wavelength required to achieve less than a 1% error in phase speed as functions of C and $\Delta t/\tau$ for various values of r ranging from 0.25 to 1. (These values of r were chosen to be representative of the behavior of real materials subject to ultrasonic waves. Generally, large variations of phase speed as functions of frequency are not expected, and here the lower limit, $r=0.25$, corresponds to the case when the ratio of minimum phase speed to maximum phase speed is 0.5.) Fig. 3C-6 reveals that a conservative estimate to achieve less than a 1% error in phase speed requires a minimum of 20 grid spacings per wavelength.

To ensure errors in magnitude below 1%, it has been found numerically to require

$$\frac{\Delta t}{\tau} \leq \frac{2.78}{3}. \quad (3C-59)$$

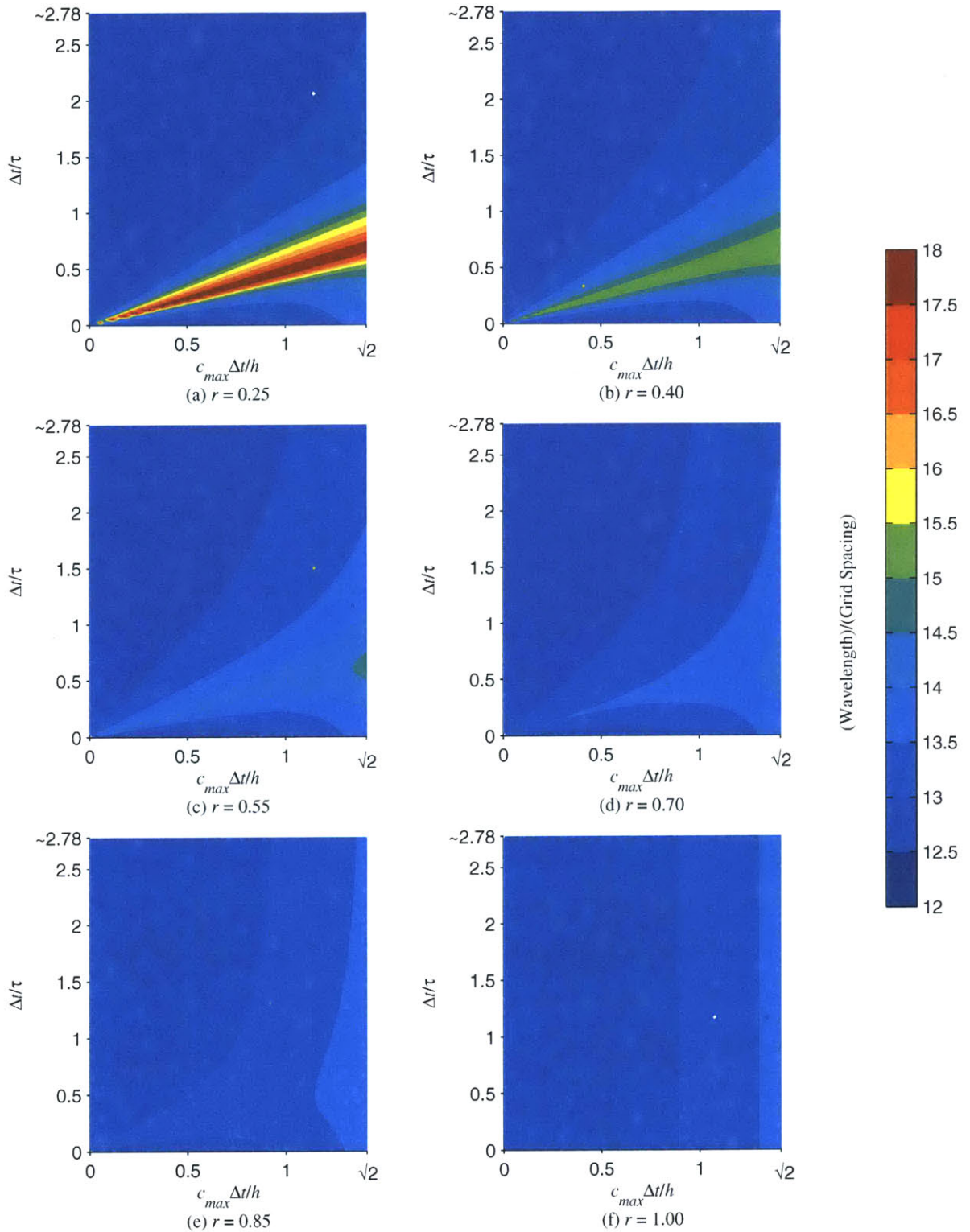


Fig. 3C-6— Minimum number of one-dimensional MSDLM grid spacings per wavelength required to achieve less than 1% error in phase speed as functions of Courant number C , and normalized time step, $\Delta t/\tau$, for various values of r , squared ratio of minimum to maximum phase speeds.

Two-Dimensional MSDLM*Convergence Criteria*

The stress-dynamic equations for a two-dimensional, linear viscoelastic continuum described by a single relaxation time under plane strain conditions in the x - y plane ($w=0$) can be expressed as [3C-1]

$$\begin{aligned} \frac{\partial f_x}{\partial t} = & -\frac{1}{\tau} f_x + \frac{r_p \Pi}{\tau} \frac{\partial^2 u}{\partial x^2} + \frac{r_p \Pi - r_s M}{\tau} \frac{\partial^2 v}{\partial x \partial y} + \frac{r_s M}{\tau} \frac{\partial^2 u}{\partial y^2} \\ & + \Pi \frac{\partial^2 \dot{u}}{\partial x^2} + (\Pi - M) \frac{\partial^2 \dot{v}}{\partial x \partial y} + M \frac{\partial^2 \dot{u}}{\partial y^2} \end{aligned} \quad (3C-60)$$

$$\begin{aligned} \frac{\partial f_y}{\partial t} = & -\frac{1}{\tau} f_y + \frac{\Pi}{\tau} \frac{\partial^2 v}{\partial y^2} + \frac{r_p \Pi - r_s M}{\tau} \frac{\partial^2 u}{\partial x \partial y} + \frac{r_s M}{\tau} \frac{\partial^2 v}{\partial x^2} \\ & + \Pi \frac{\partial^2 \dot{v}}{\partial y^2} + (\Pi - M) \frac{\partial^2 \dot{u}}{\partial x \partial y} + M \frac{\partial^2 \dot{v}}{\partial x^2} \end{aligned} \quad (3C-61)$$

$$\frac{\partial u}{\partial t} = \dot{u} \quad (3C-62)$$

$$\frac{\partial v}{\partial t} = \dot{v} \quad (3C-63)$$

$$\frac{\partial \dot{u}}{\partial t} = \frac{1}{\rho} (f_x + f_{bx}) \quad (3C-64)$$

$$\frac{\partial \dot{v}}{\partial t} = \frac{1}{\rho} (f_y + f_{by}) \quad (3C-65)$$

where

$$r_p = \left(1 + \frac{1}{\tau} \frac{\lambda' + 2\mu'}{\lambda + 2\mu} \right)^{-1} \quad (3C-66)$$

$$r_s = \left(1 + \frac{1}{\tau} \frac{\mu'}{\mu} \right)^{-1} \quad (3C-67)$$

$$E_p = \lambda + 2\mu + \frac{\lambda' + 2\mu'}{\tau} \quad (3C-68)$$

and

$$E_s = \mu + \frac{\mu'}{\tau} \quad (3C-69)$$

Here, λ and μ are the Lamé constants and λ' and μ' are the analogous viscous constants.

Taking the two-dimensional discrete Fourier transform of eqns. (3C-60) through (3C-65) yields a matrix equation

$$\frac{d}{dt} \begin{bmatrix} F^x \\ F^y \\ U \\ V \\ \dot{U} \\ \dot{V} \end{bmatrix} = \begin{bmatrix} -\frac{1}{\tau} & 0 & a_{13,A_{exact}^{2-D}} & a_{14,A_{exact}^{2-D}} & a_{15,A_{exact}^{2-D}} & a_{16,A_{exact}^{2-D}} \\ 0 & -\frac{1}{\tau} & a_{23,A_{exact}^{2-D}} & a_{24,A_{exact}^{2-D}} & a_{25,A_{exact}^{2-D}} & a_{26,A_{exact}^{2-D}} \\ 0 & 0 & 0 & 0 & 1 & 0 \\ 0 & 0 & 0 & 0 & 0 & 1 \\ \frac{1}{\rho} & 0 & 0 & 0 & 0 & 0 \\ 0 & \frac{1}{\rho} & 0 & 0 & 0 & 0 \end{bmatrix} \begin{bmatrix} F^x \\ F^y \\ U \\ V \\ \dot{U} \\ \dot{V} \end{bmatrix} \quad (3C-70)$$

or

$$\dot{\mathbf{u}}_{exact} = \mathbf{A}_{exact}^{2-D} \mathbf{u}_{exact} \quad (3C-71)$$

where

$$a_{13,A_{exact}^{2-D}} = -\frac{k_x^2 r_p \Pi + k_y^2 r_s M}{\tau} \quad (3C-72)$$

$$a_{14,A_{exact}^{2-D}} = -\frac{k_x k_y (r_p \Pi - r_s M)}{\tau} \quad (3C-73)$$

$$a_{15,A_{exact}^{2-D}} = -(k_x^2 \Pi + k_y^2 M) \quad (3C-74)$$

$$a_{16,A_{exact}^{2-D}} = -k_x k_y (\Pi - M) \quad (3C-75)$$

$$a_{23,A_{exact}^{2-D}} = -\frac{k_x k_y (r_p \Pi - r_s M)}{\tau} \quad (3C-76)$$

$$a_{24,A_{exact}^{2-D}} = -k_x k_y (\Pi - M) \quad (3C-77)$$

$$a_{25,A_{exact}^{2-D}} = -\frac{k_x^2 r_p \Pi + k_y^2 r_s M}{\tau} \quad (3C-78)$$

$$a_{26,A_{exact}^{2-D}} = -(k_y^2 \Pi + k_x^2 M) \quad (3C-79)$$

The eigenvalues of \mathbf{A}_{exact}^{2-D} are given by

$$\left| \lambda_{A_{exact}^{2-D}} \mathbf{I} - \mathbf{A}_{exact}^{2-D} \right| = 0 \quad (3C-80)$$

which satisfies the characteristic equation

$$\begin{aligned} & \left(\lambda_{A_{exact}^{2-D}}^3 + \frac{1}{\tau} \lambda_{A_{exact}^{2-D}}^2 + \frac{\hat{Z}_P}{\tau^2} \lambda_{A_{exact}^{2-D}} + \frac{r_P \hat{Z}_P}{\tau^3} \right) \\ & \left(\lambda_{A_{exact}^{2-D}}^3 + \frac{1}{\tau} \lambda_{A_{exact}^{2-D}}^2 + \frac{\hat{Z}_S}{\tau^2} \lambda_{A_{exact}^{2-D}} + \frac{r_S \hat{Z}_S}{\tau^3} \right) = 0 \end{aligned} \quad (3C-81)$$

where

$$\hat{Z}_P = \frac{\Pi k^2 \tau^2}{\rho} \quad (3C-82)$$

$$\hat{Z}_S = \frac{M k^2 \tau^2}{\rho} \quad (3C-83)$$

and

$$k^2 = k_x^2 + k_y^2 \quad (3C-84)$$

The eigenvalues of the exact two-dimensional problem (satisfying eqn. (3C-81)) are two sets of eigenvalues of the exact one dimensional problem (satisfying eqn. (3C-7))—one set for a P wave and one set for an S wave.

Equations (3C-60) through (3C-65), have been discretized according to the two-dimensional MSDLM in Fig. 3C-7. The discretized dynamic equations have been written in component form for a generic particle position (i, j)

$$\begin{aligned} \frac{df_{i,j}^x}{dt} = & -\frac{1}{\tau} f_{i,j}^x + \frac{g_1}{\pi h^2 D} (u_{i+1,j} - 2u_{i,j} + u_{i-1,j}) \\ & + \frac{1}{\pi h^2 D} \left(\frac{\eta_1}{4h^2} + \frac{g_3}{2} \right) (u_{i+1,j+1} + u_{i-1,j-1} + u_{i+1,j-1} + u_{i-1,j+1} - 4u_{i,j}) \\ & + \frac{1}{\pi h^2 D} \left(-\frac{\eta_1}{4h^2} + \frac{g_3}{2} \right) (v_{i+1,j+1} + v_{i-1,j-1} - v_{i+1,j-1} - v_{i-1,j+1}) \\ & + \left(\frac{g_1 + g_2}{h^2 D} \right) (\dot{u}_{i+1,j} - 2\dot{u}_{i,j} + \dot{u}_{i-1,j}) \\ & + \frac{1}{h^2 D} \left(\frac{\eta_1 + \eta_2}{4h^2} + \frac{g_3 + g_4}{2} \right) (\dot{u}_{i+1,j+1} + \dot{u}_{i-1,j-1} + \dot{u}_{i+1,j-1} + \dot{u}_{i-1,j+1} - 4\dot{u}_{i,j}) \\ & + \frac{1}{h^2 D} \left(-\frac{\eta_1 + \eta_2}{4h^2} + \frac{g_3 + g_4}{2} \right) (\dot{v}_{i+1,j+1} + \dot{v}_{i-1,j-1} - \dot{v}_{i+1,j-1} - \dot{v}_{i-1,j+1}) \end{aligned} \quad (3C-85)$$

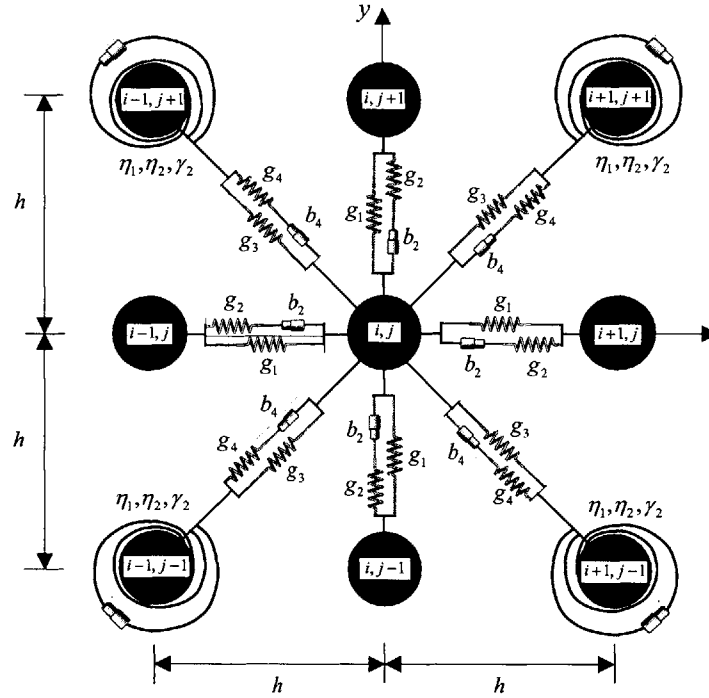


Fig. 3C-7—Schematic for two-dimensional MSDLM in vicinity of interior particle at position (i, j) , where each interior particle has mass per unit depth equal to ρh^2 .

$$\begin{aligned}
 \frac{df_{i,j}^y}{dt} = & -\frac{1}{\tau} f_{i,j}^y + \frac{g_1}{\tau h^2 D} (v_{i,j+1} - 2v_{i,j} + v_{i,j-1}) \\
 & + \frac{1}{\tau h^2 D} \left(\frac{\eta_1}{4h^2} + \frac{g_3}{2} \right) (v_{i+1,j+1} + v_{i-1,j-1} + v_{i+1,j-1} + v_{i-1,j+1} - 4v_{i,j}) \\
 & + \frac{1}{\tau h^2 D} \left(-\frac{\eta_1}{4h^2} + \frac{g_3}{2} \right) (u_{i+1,j+1} + u_{i-1,j-1} - u_{i+1,j-1} - u_{i-1,j+1}) \\
 & + \left(\frac{g_1 + g_2}{h^2 D} \right) (\dot{v}_{i,j+1} - 2\dot{v}_{i,j} + \dot{v}_{i,j-1}) \\
 & + \frac{1}{h^2 D} \left(\frac{\eta_1 + \eta_2}{4h^2} + \frac{g_3 + g_4}{2} \right) (\dot{v}_{i+1,j+1} + \dot{v}_{i-1,j-1} + \dot{v}_{i+1,j-1} + \dot{v}_{i-1,j+1} - 4\dot{v}_{i,j}) \\
 & + \frac{1}{h^2 D} \left(-\frac{\eta_1 + \eta_2}{4h^2} + \frac{g_3 + g_4}{2} \right) (\dot{u}_{i+1,j+1} + \dot{u}_{i-1,j-1} - \dot{u}_{i+1,j-1} - \dot{u}_{i-1,j+1})
 \end{aligned} \tag{3C-86}$$

$$\frac{du_{i,j}}{dt} = \dot{u}_{i,j} \tag{3C-87}$$

$$\frac{dv_{i,j}}{dt} = \dot{v}_{i,j} \tag{3C-88}$$

$$\frac{du_{i,j}}{dt} = \frac{1}{\rho} (f_{i,j}^{bx} + f_{i,j}^x) \quad (3C-89)$$

$$\frac{dv_{i,j}}{dt} = \frac{1}{\rho} (f_{i,j}^{by} + f_{i,j}^y) \quad (3C-90)$$

where h is the grid space, D is the unit depth, $u_{i,j}$ and $v_{i,j}$ are the respective x and y -direction displacements, $f_{i,j}^{bx}$ and $f_{i,j}^{by}$ are the respective x and y -direction volumetric body forces, $f_{i,j}^x$ and $f_{i,j}^y$ are the respective volumetric forces due to internal strain, g_1 , g_2 , g_3 , and g_4 are the extensional spring constants, and η_1 and η_2 are the rotational spring constants.

Because only a single stress relaxation time is defined in the theoretical model, all the force relaxation times in the extensional and rotational elements used in the MSDLM must also equal this single relaxation time. Thus, the extensional dashpots b_2 and b_4 and rotational dashpot γ_2 must satisfy the expression

$$\frac{b_2}{g_2} = \frac{b_4}{g_4} = \frac{\gamma_2}{\eta_2} = \tau \quad (3C-91)$$

Expanding eqns. (3C-85) and (3C-90) via a Taylor's series in the limit as $h \rightarrow 0$ and comparing the result[§] with eqns. (3C-60) and (3C-65), the two-dimensional MSDLM is spatially *consistent* with the governing PDEs if

$$g_1 = D(r_p \Pi - r_s M) \quad (3C-92)$$

$$g_2 = D((1 - r_p) \Pi - (1 - r_s) M) \quad (3C-93)$$

$$g_3 = \frac{D}{4} (r_p \Pi + r_s M) \quad (3C-94)$$

[§] The useful equations are

$$\frac{\partial^2 p}{\partial x^2} = \frac{p_{i+1,j} - 2p_{i,j} + p_{i,j}}{h^2} + O(h^2), \quad \frac{\partial^2 p}{\partial y^2} = \frac{p_{i,j+1} - 2p_{i,j} + p_{i,j-1}}{h^2} + O(h^2),$$

$$\frac{\partial^2 p}{\partial x^2} + \frac{\partial^2 p}{\partial y^2} = \frac{p_{i+1,j+1} + p_{i-1,j+1} + p_{i-1,j-1} + p_{i+1,j-1} - 4p_{i,j}}{2h^2} + O(h^2), \text{ and}$$

$$\frac{\partial^2 p}{\partial x \partial y} = \frac{p_{i+1,j+1} - p_{i-1,j+1} - p_{i+1,j-1} + p_{i-1,j-1}}{4h^2} + O(h^2)$$

$$g_4 = \frac{D}{4}((1-r_p)\Pi + (1-r_s)M) \quad (3C-95)$$

$$\eta_1 = \frac{h^2 D}{4}(3r_s\Pi - r_p M) \quad (3C-96)$$

$$\eta_2 = \frac{h^2 D}{4}(3(1-r_s)\Pi - (1-r_p)M) \quad (3C-97)$$

Substituting eqns. (3C-92) through (3C-97) into eqns. (3C-85) through (3C-90) and taking the two-dimensional, discrete Fourier transform yields a matrix equation

$$\frac{d}{dt} \begin{bmatrix} F_x \\ F_y \\ U \\ V \\ \dot{U} \\ \dot{V} \end{bmatrix} = \begin{bmatrix} -\frac{1}{\tau} & 0 & a_{13,A^{2-D}} & a_{14,A^{2-D}} & a_{15,A^{2-D}} & a_{16,A^{2-D}} \\ 0 & -\frac{1}{\tau} & a_{23,A^{2-D}} & a_{24,A^{2-D}} & a_{25,A^{2-D}} & a_{26,A^{2-D}} \\ 0 & 0 & 0 & 0 & 1 & 0 \\ 0 & 0 & 0 & 0 & 0 & 1 \\ \frac{1}{\rho} & 0 & 0 & 0 & 0 & 0 \\ 0 & \frac{1}{\rho} & 0 & 0 & 0 & 0 \end{bmatrix} \begin{bmatrix} F_x \\ F_y \\ U \\ V \\ \dot{U} \\ \dot{V} \end{bmatrix} \quad (3C-98)$$

or

$$\dot{\mathbf{u}}_{msdlm} = \mathbf{A}_{msdlm}^{2-D} \mathbf{u}_{msdlm} \quad (3C-99)$$

where

$$a_{13,A^{2-D}} = \frac{2}{\tau h^2}((r_p\Pi - r_s M)(\cos k_x h - 1) + r_s M(\cos k_x h \cos k_y h - 1)) \quad (3C-100)$$

$$a_{14,A^{2-D}} = \frac{1}{\tau h^2}(r_s M - r_p \Pi) \sin k_x h \sin k_y h \quad (3C-101)$$

$$a_{15,A^{2-D}} = \frac{2}{h^2}((\Pi - M)(\cos k_x h - 1) + M(\cos k_x h \cos k_y h - 1)) \quad (3C-102)$$

$$a_{16,A^{2-D}} = \frac{1}{h^2}(M - \Pi) \sin k_x h \sin k_y h \quad (3C-103)$$

$$a_{23,A^{2-D}} = \frac{1}{\tau h^2}(r_s M - r_p \Pi) \sin k_x h \sin k_y h \quad (3C-104)$$

$$a_{24,A^{2-D}} = \frac{2}{\tau h^2}((r_p \Pi - r_s M)(\cos k_y h - 1) + r_s M(\cos k_x h \cos k_y h - 1)) \quad (3C-105)$$

$$a_{25,A^{2-D}} = \frac{1}{h^2}(M - \Pi) \sin k_x h \sin k_y h \quad (3C-106)$$

$$a_{26, \mathbf{A}_{msdlm}^{2-D}} = \frac{2}{h^2} \left((\Pi - M)(\cos k_y h - 1) + M(\cos k_x h \cos k_y h - 1) \right) \quad (3C-107)$$

For the special case when the wavenumber is along the x or y axis, that is $k = k_x$ or $k = k_y$, the eigenvalues of \mathbf{A}_{msdlm}^{2-D} satisfy the characteristic equation

$$\left(\lambda_{\mathbf{A}_{msdlm}^{2-D}}^3 + \frac{1}{\tau} \lambda_{\mathbf{A}_{msdlm}^{2-D}}^2 + \frac{\hat{Z}'_P}{\tau^2} \lambda_{\mathbf{A}_{msdlm}^{2-D}} + \frac{r_P \hat{Z}'_P}{\tau^3} \right) \cdot \left(\lambda_{\mathbf{A}_{msdlm}^{2-D}}^3 + \frac{1}{\tau} \lambda_{\mathbf{A}_{msdlm}^{2-D}}^2 + \frac{\hat{Z}'_S}{\tau^2} \lambda_{\mathbf{A}_{msdlm}^{2-D}} + \frac{r_S \hat{Z}'_S}{\tau^3} \right) = 0 \quad (3C-108)$$

where

$$\hat{Z}'_P = \frac{2\Pi \tau^2}{h^2 \rho} (1 - \cos kh) \quad (3C-109)$$

$$\hat{Z}'_S = \frac{2M \tau^2}{h^2 \rho} (1 - \cos kh) \quad (3C-110)$$

The eigenvalues of the two-dimensional MSDLM (satisfying eqn. (3C-108)) are two sets of eigenvalues of the corresponding one-dimensional problem (satisfying eqn. (3C-20))—one set for a P wave and one set for an S wave.

The amplification factors of $\Delta t \mathbf{A}_{msdlm}^{2-D}$ satisfy

$$\left| \xi_{\Delta t \mathbf{A}_{msdlm}^{2-D}} \mathbf{I} - \Delta t \mathbf{A}_{msdlm}^{2-D} \right| = 0 \quad (3C-111)$$

or

$$\left(\xi_{\Delta t \mathbf{A}_{msdlm}^{2-D}}^3 + w \xi_{\Delta t \mathbf{A}_{msdlm}^{2-D}}^2 + z_P^2 \xi_{\Delta t \mathbf{A}_{msdlm}^{2-D}} + w r_P z_P^2 \right) \cdot \left(\xi_{\Delta t \mathbf{A}_{msdlm}^{2-D}}^3 + w \xi_{\Delta t \mathbf{A}_{msdlm}^{2-D}}^2 + z_S^2 \xi_{\Delta t \mathbf{A}_{msdlm}^{2-D}} + w r_S z_S^2 \right) = 0 \quad (3C-112)$$

where

$$w = \frac{\Delta t}{\tau} \quad (3C-113)$$

$$z_P = \frac{\sqrt{2} c_{\max, P} \Delta t}{h} \sqrt{1 - \cos kh} \quad (3C-114)$$

$$z_S = \sqrt{\frac{2M}{\Pi}} \frac{c_{\max, P} \Delta t}{h} \sqrt{1 - \cos kh} \quad (3C-115)$$

The amplification factors of the two-dimensional MSDLM (satisfying eqn. (3C-112)) are two sets of eigenvalues of the corresponding one dimensional problem (eqn. (3C-29)). Thus, the stability criteria are

$$\frac{\Delta t}{\tau} \leq 2.78 \quad (3C-116)$$

and

$$\frac{c_{\max,P}\Delta t}{h} \leq 1.30 \quad (3C-117)$$

In the case of a general orientation of wavevector,

$$k_x = k \cos \theta \quad (3C-118)$$

$$k_y = k \sin \theta \quad (3C-119)$$

where θ is the angle the wavevector makes with the positive x -axis. In the special case of $\theta = 45^\circ$ and $r_s = r_p = r$,

$$\begin{aligned} & \left(\xi_{\Delta t \Lambda_{msdlm}^{2-D}}^3 + w \xi_{\Delta t \Lambda_{msdlm}^{2-D}}^2 + z_+^2 \xi_{\Delta t \Lambda_{msdlm}^{2-D}} + r w z_+^2 \right) \\ & \left(\xi_{\Delta t \Lambda_{msdlm}^{2-D}}^3 + w \xi_{\Delta t \Lambda_{msdlm}^{2-D}}^2 + z_-^2 \xi_{\Delta t \Lambda_{msdlm}^{2-D}} + r w z_-^2 \right) = 0 \end{aligned} \quad (3C-120)$$

where

$$z_+ = \frac{c_{\max,P}\Delta t}{h} \sqrt{2 - 2 \left(1 - \frac{M}{\Pi}\right) \cos kh + \left(1 - \frac{M}{\Pi}\right) \sin^2 kh - 2 \frac{M}{\Pi} \cos^2 kh} \quad (3C-121)$$

$$z_- = \frac{c_{\max,P}\Delta t}{h} \sqrt{2 - 2 \left(1 - \frac{M}{\Pi}\right) \cos kh - \left(1 - \frac{M}{\Pi}\right) \sin^2 kh - 2 \frac{M}{\Pi} \cos^2 kh} \quad (3C-122)$$

Again, the amplification factors of eqn. (3C-120) are two sets of eigenvalues of the corresponding one-dimensional problem, eqn. (3C-29). Requiring the expressions beneath the radical in eqns. (3C-121) and (3C-122) satisfy the stability conditions for all kh yields the following stability criteria:

$$\frac{\Delta t}{\tau} \leq 2.78 \quad (3C-123)$$

and

$$\frac{c_{\max,P}\Delta t}{h} \leq \min \left\{ 1.30 \sqrt{\frac{M}{\Pi}}, \frac{2.61}{\sqrt{2(2-M/\Pi)}} \right\} \quad (3C-124)$$

Because $0 < \frac{M}{\Pi} < \frac{1}{2}$, the stability criterion in eqn. (3C-124) is satisfied by eqn. (3C-117).

Accuracy Criteria

Accuracy criteria is investigated for the special case of $r_s = r_p = r$, or alternatively for a frequency-independent Poisson's ratio, which is defined as

$$\nu = \frac{1 - 2M/\Pi}{2(1 - M/\Pi)} \quad (3C-125)$$

Additionally, for the special case when the wave number is along the x or y axis, that is $k = k_x$ or $k = k_y$, the accuracy of the P and S waves are directly found from the one-dimensional analysis.

Figure 3C-8 shows the magnitude and phase of the exact and numerical amplification factors as a function of normalized wavenumber when $r = 0.55$, $C = 1.30$, $\Delta t/\tau = 2.78/4$ and the wavevector is aligned at 45° with respect to horizontal springs in the MSDLM. As in the one-dimensional case, the exact and numerical amplification factors for P and S waves fall into one of the following categories: a purely real amplification factor corresponding to non-propagating decay, denoted by ξ_{decay} , and a complex conjugate pair of amplification factors corresponding to decayed propagation with positive phase and negative phase, denoted by ξ_{prop} and ξ_{prop}^* , respectively.

According to eqn. (3C-58) the percent error in the phase is equal to the percent error in wave speed. Figures 3C-9 through 3C-18 detail the minimum number of grid spacings per wavelength that result in an error in P or S wave speeds less than 1 percent as a function of ν , r , $\frac{c_{\text{max},P}\Delta t}{h}$ and $\frac{\Delta t}{\tau}$. From the figures, the accuracy requirement would be fulfilled for $0 < \nu < 0.40$ when there are 23 grid spacings per wavelength.

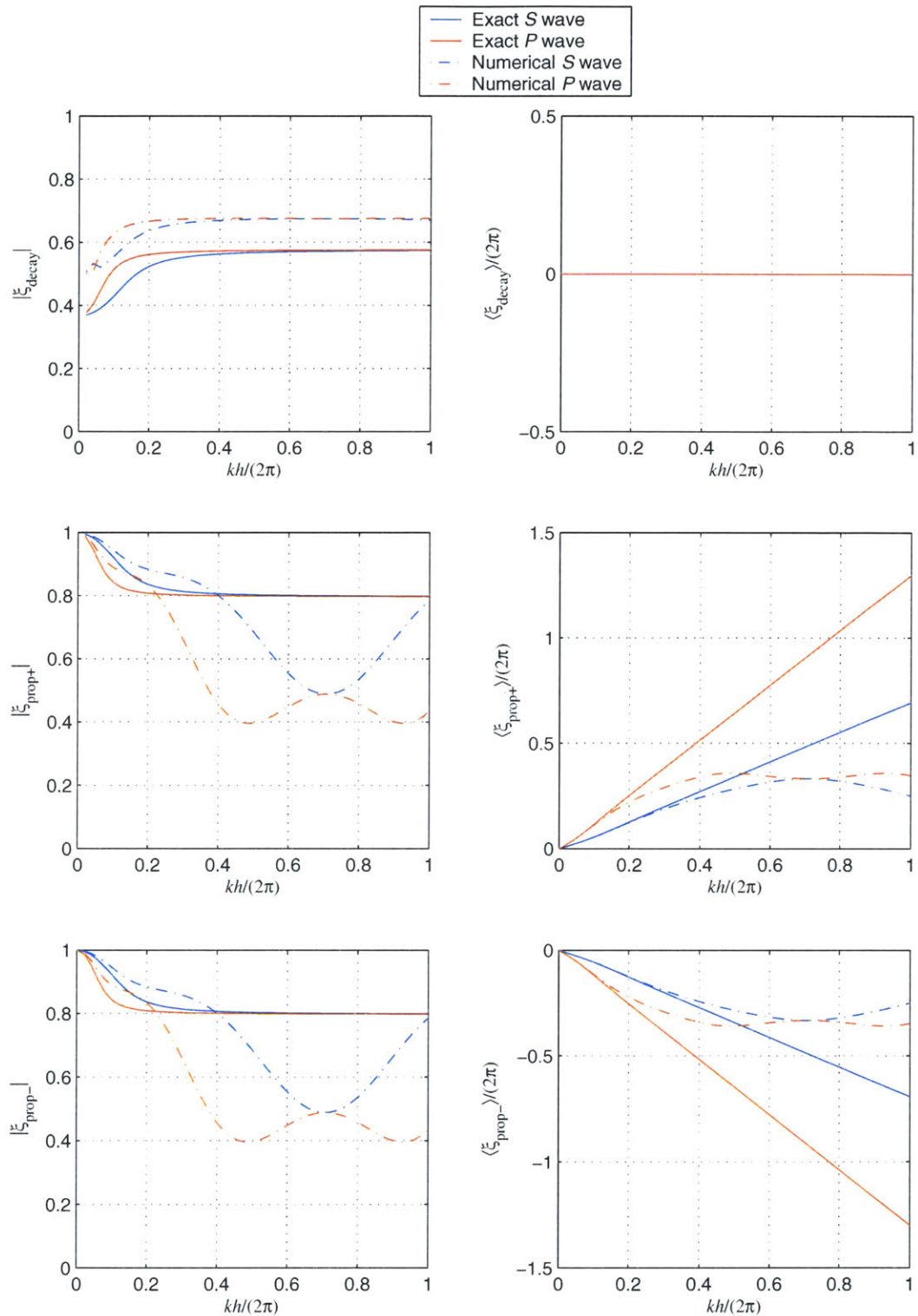


Fig. 3C-8—Two-dimensional exact and numerical (MSDLM) magnitude and phase angles for P and S waves as function of normalized wave number k , oriented at 45° with respect to horizontal axis when $r = 0.55$, $\frac{c_{\max,P}\Delta t}{h} = 1.30$, $\Delta t/\tau = 2.78/4$ and $\nu = 0.30$.

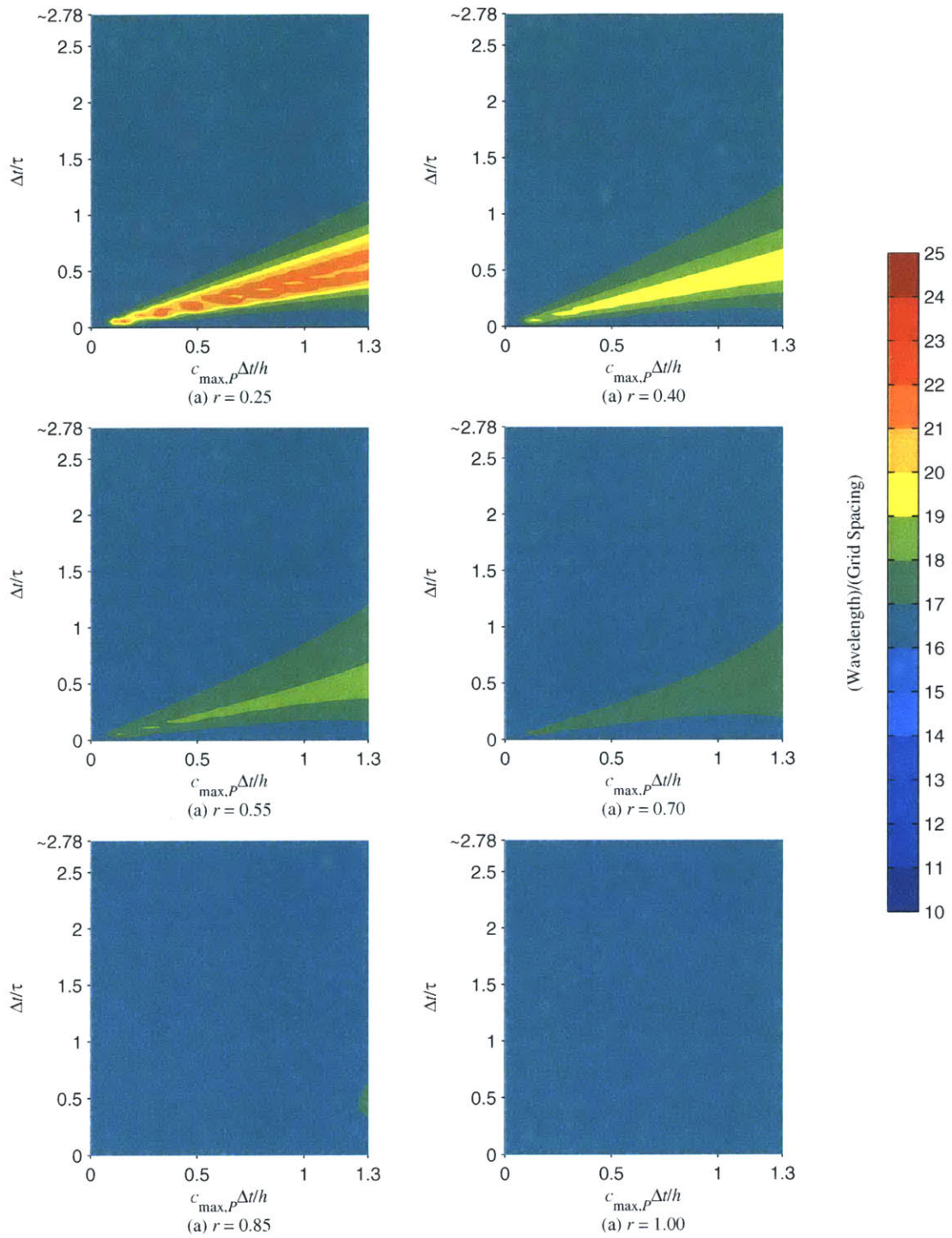


Fig. 3C-9—Minimum number of two-dimensional MSDLM grid spacings per wavelength required to achieve less than 1% error in P phase speed as functions of Courant number C , normalized time step $\Delta t/\tau$, and various values of $r_p = r_s = r$, squared ratio of minimum to maximum phase speeds, when $\nu = 0.00$.

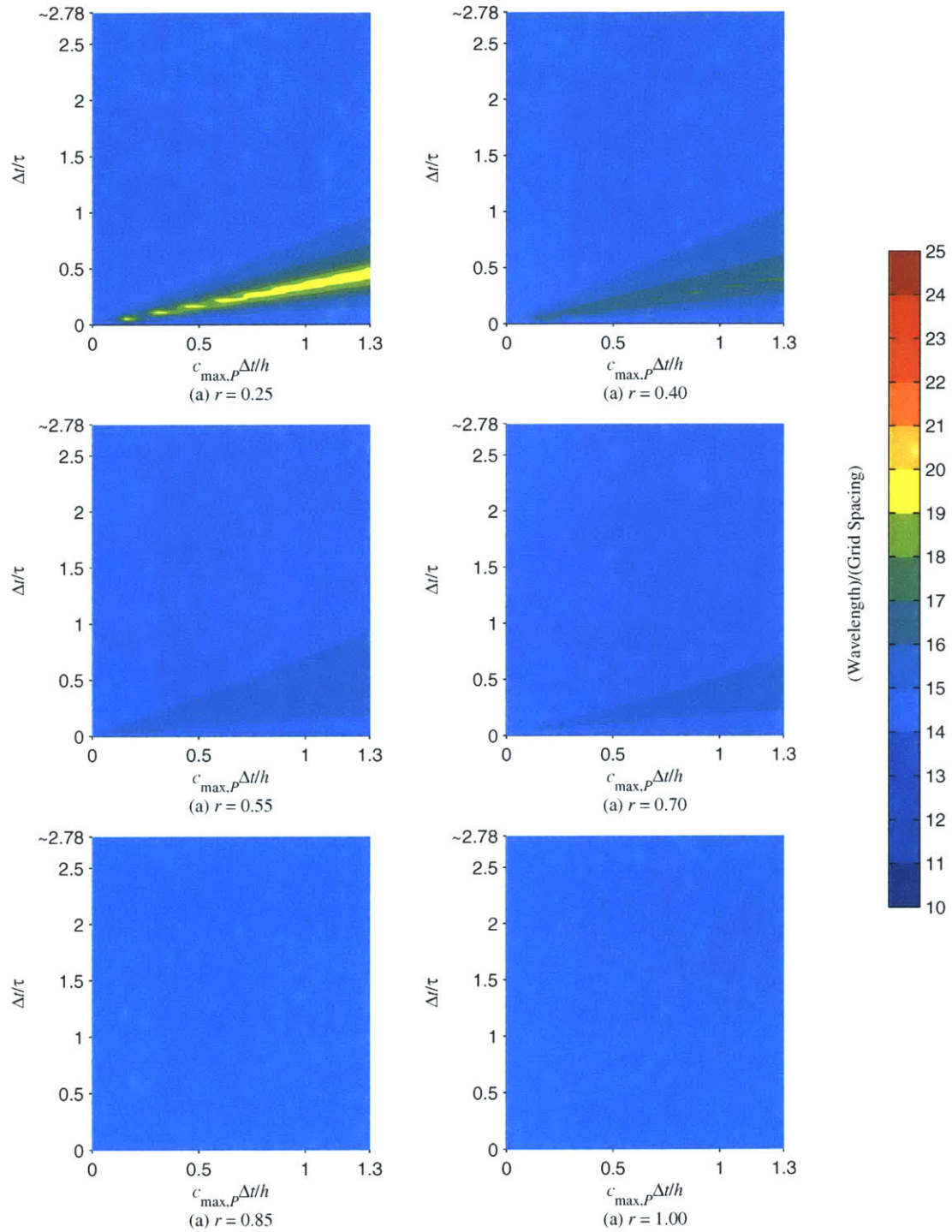


Fig. 3C-10—Minimum number of two-dimensional MSDLM grid spacings per wavelength required to achieve less than 1% error in S phase speed as functions of Courant number C , normalized time step $\Delta t/\tau$, and various values of $r_p = r_s = r$, squared ratio of minimum to maximum phase speeds, when $\nu = 0.00$.

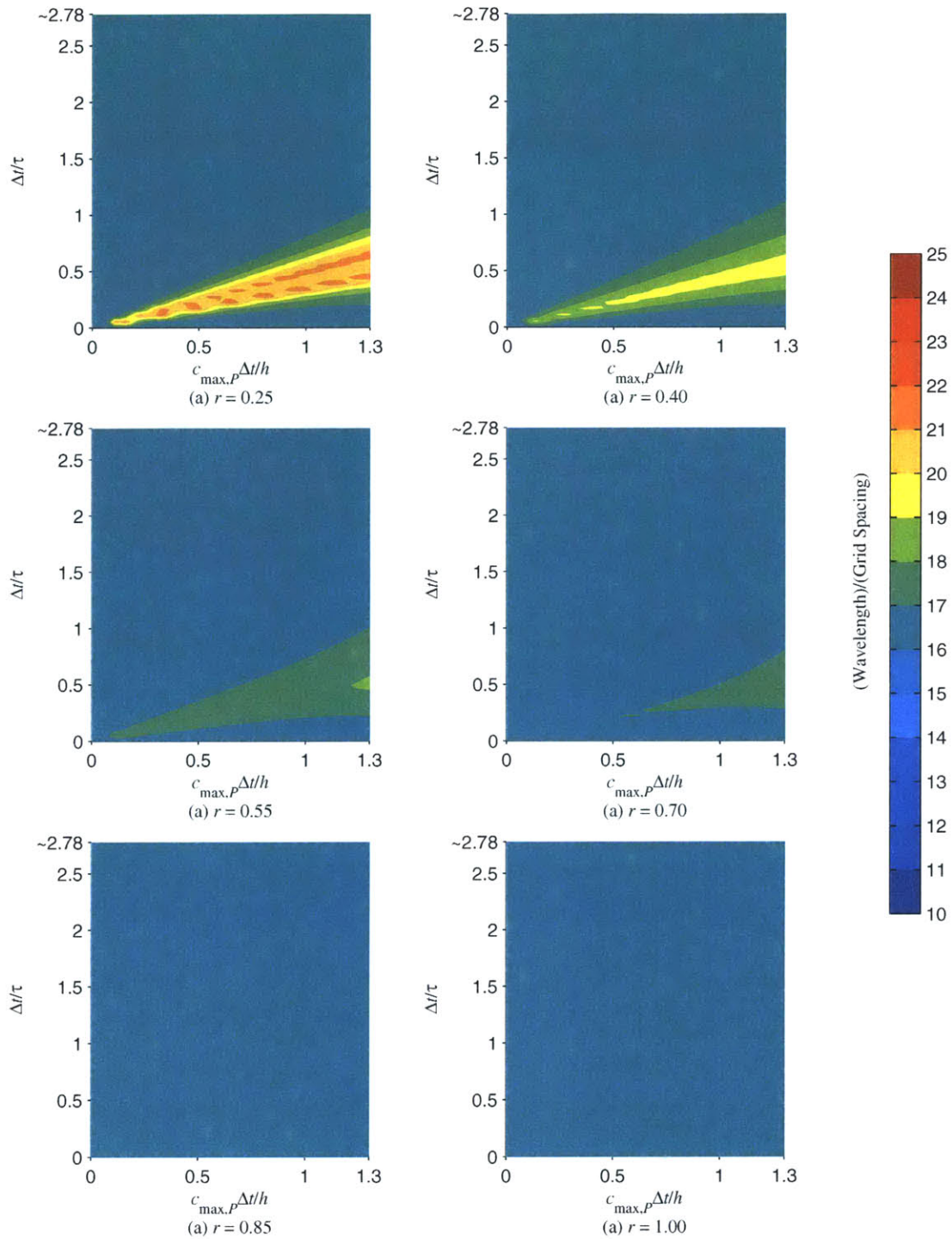


Fig. 3C-11—Minimum number of two-dimensional MSDLM grid spacings per wavelength required to achieve less than 1% error in P phase speed as functions of Courant number C , normalized time step $\Delta t/\tau$, and various values of $r_p = r_s = r$, squared ratio of minimum to maximum phase speeds, when $\nu = 0.10$.

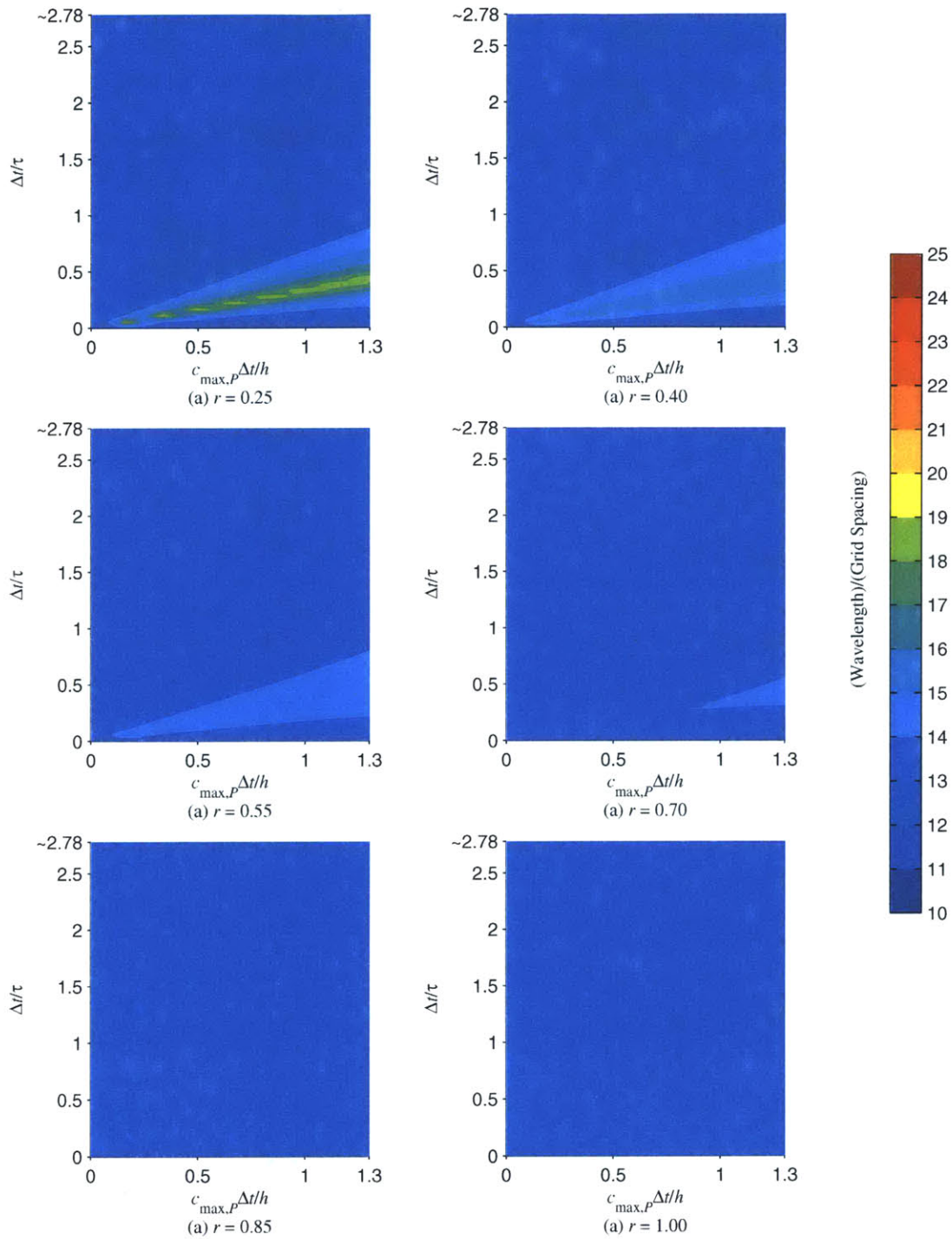


Fig. 3C-12—Minimum number of two-dimensional MSDLM grid spacings per wavelength required to achieve less than 1% error in S phase speed as functions of Courant number C , normalized time step $\Delta t/\tau$, and various values of $r_p = r_s = r$, squared ratio of minimum to maximum phase speeds, when $\nu = 0.10$.

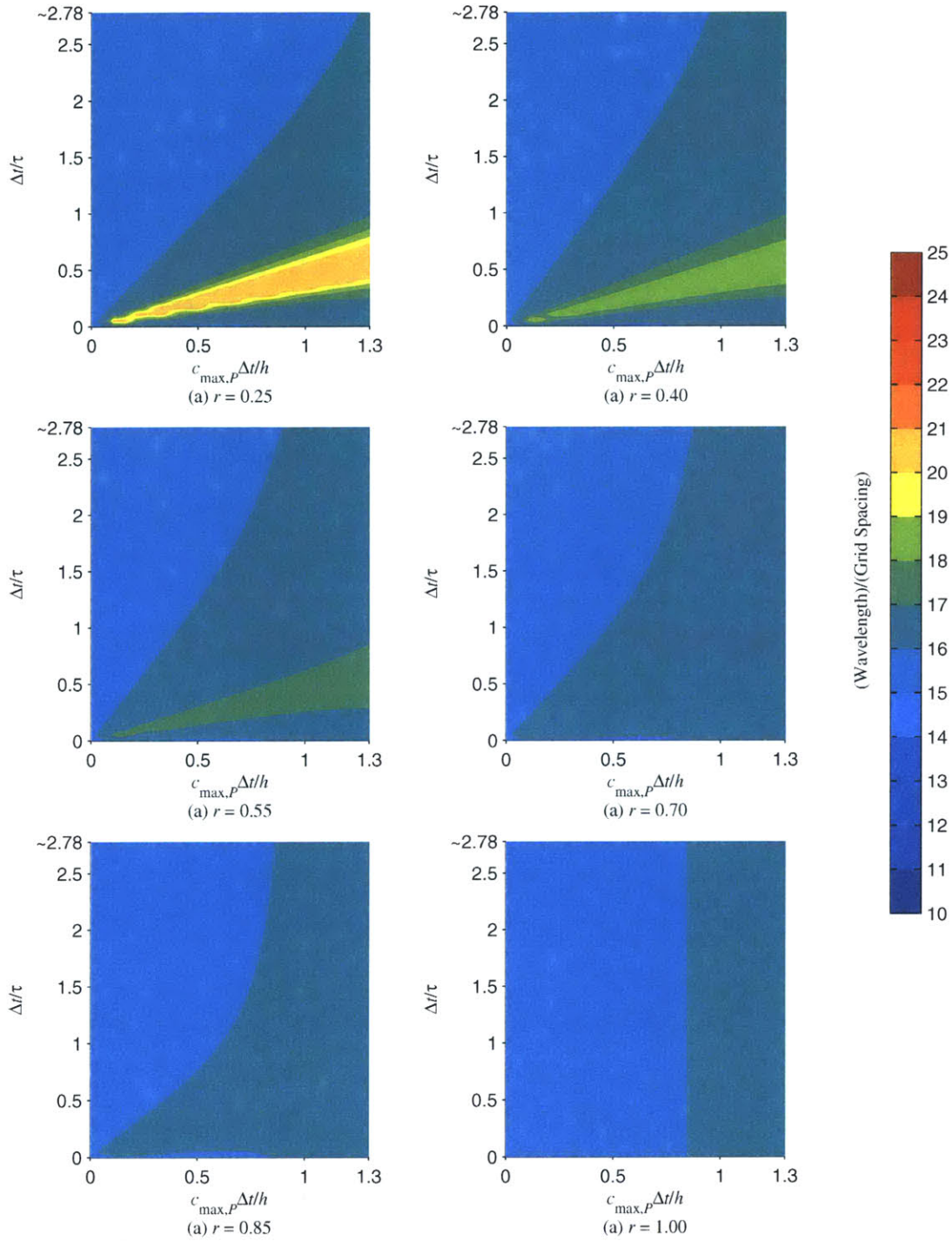


Fig. 3C-13—Minimum number of two-dimensional MSDLM grid spacings per wavelength required to achieve less than 1% error in P phase speed as functions of Courant number C , normalized time step $\Delta t/\tau$, and various values of $r_p = r_s = r$, squared ratio of minimum to maximum phase speeds, when $\nu = 0.20$.

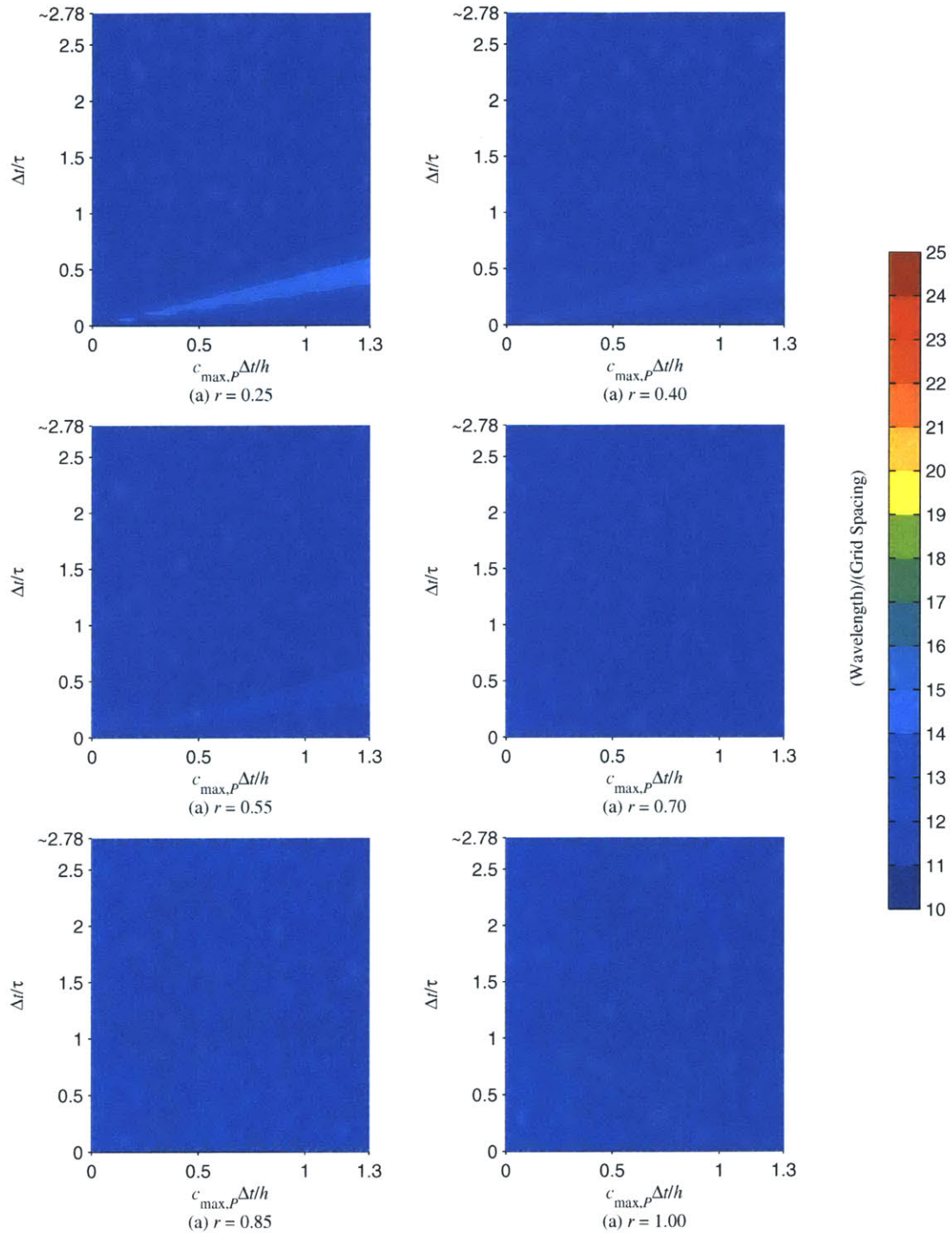


Fig. 3C-14—Minimum number of two-dimensional MSDLM grid spacings per wavelength required to achieve less than 1% error in S phase speed as functions of Courant number C , normalized time step $\Delta t/\tau$, and various values of $r_p = r_s = r$, squared ratio of minimum to maximum phase speeds, when $\nu = 0.20$.

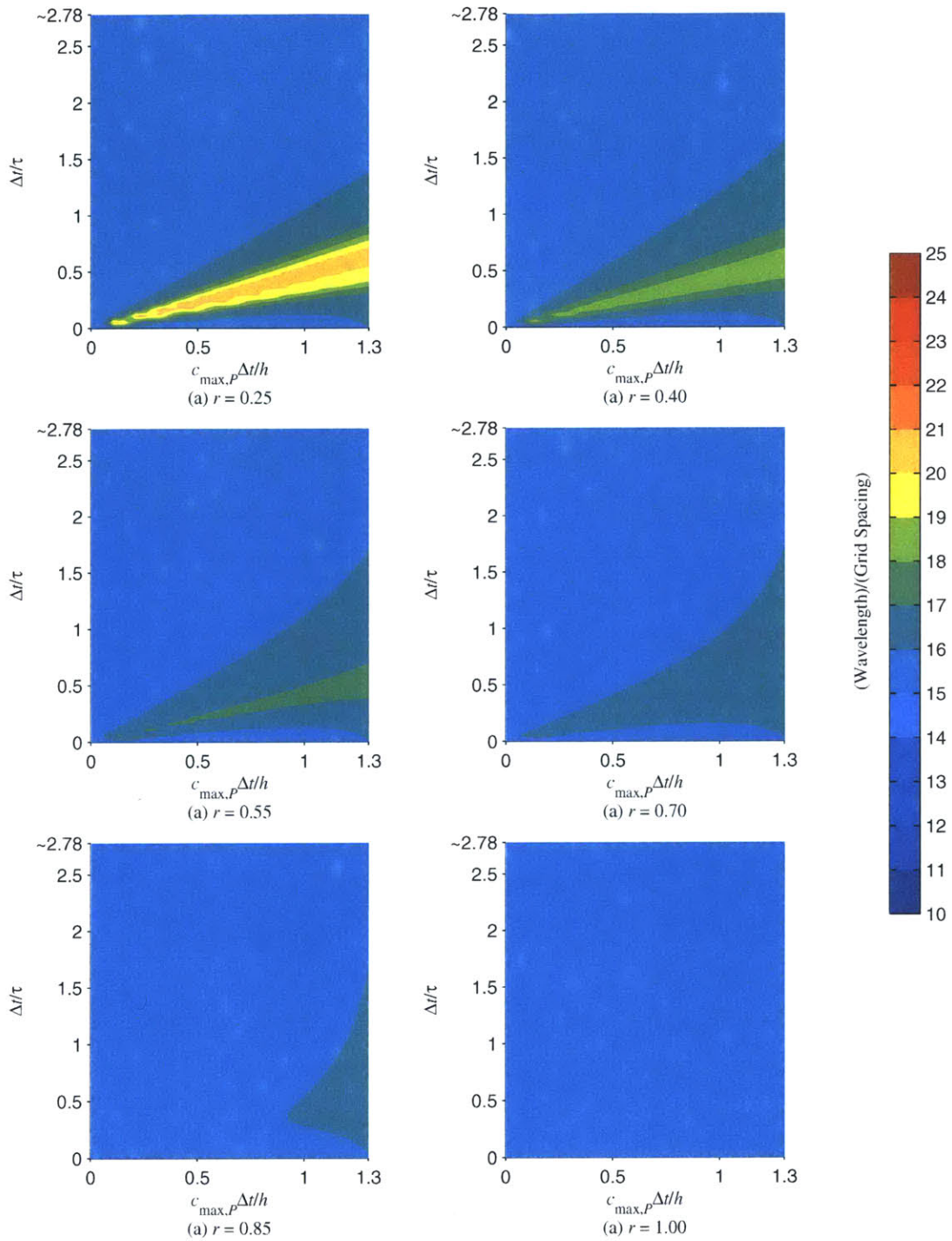


Fig. 3C-15—Minimum number of two-dimensional MSDLM grid spacings per wavelength required to achieve less than 1% error in P phase speed as functions of Courant number C , normalized time step $\Delta t / \tau$, and various values of $r_p = r_s = r$, squared ratio of minimum to maximum phase speeds, when $\nu = 0.30$.

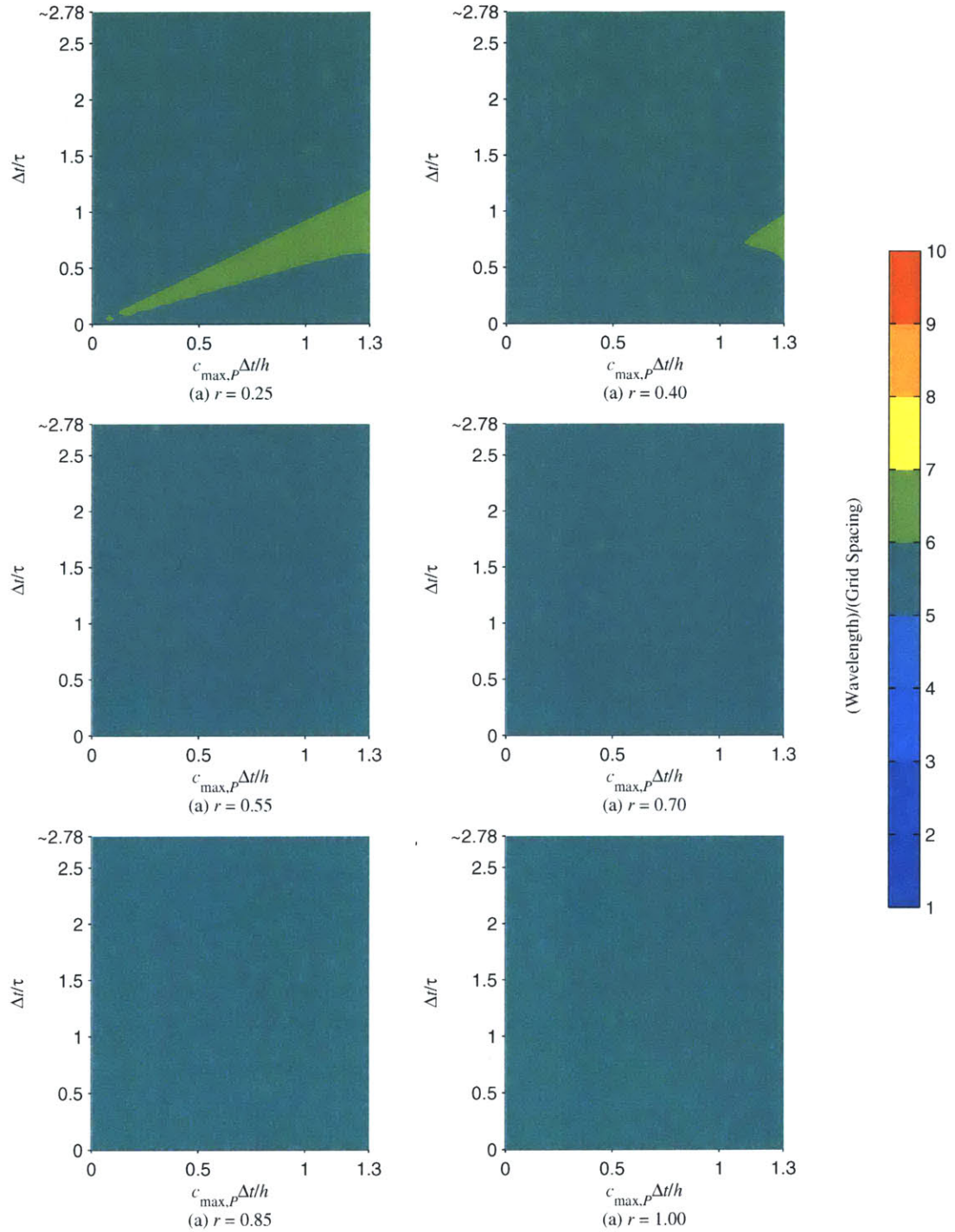


Fig. 3C-16—Minimum number of two-dimensional MSDLM grid spacings per wavelength required to achieve less than 1% error in S phase speed as functions of Courant number C , normalized time step $\Delta t / \tau$, and various values of $r_p = r_s = r$, squared ratio of minimum to maximum phase speeds, when $\nu = 0.30$.

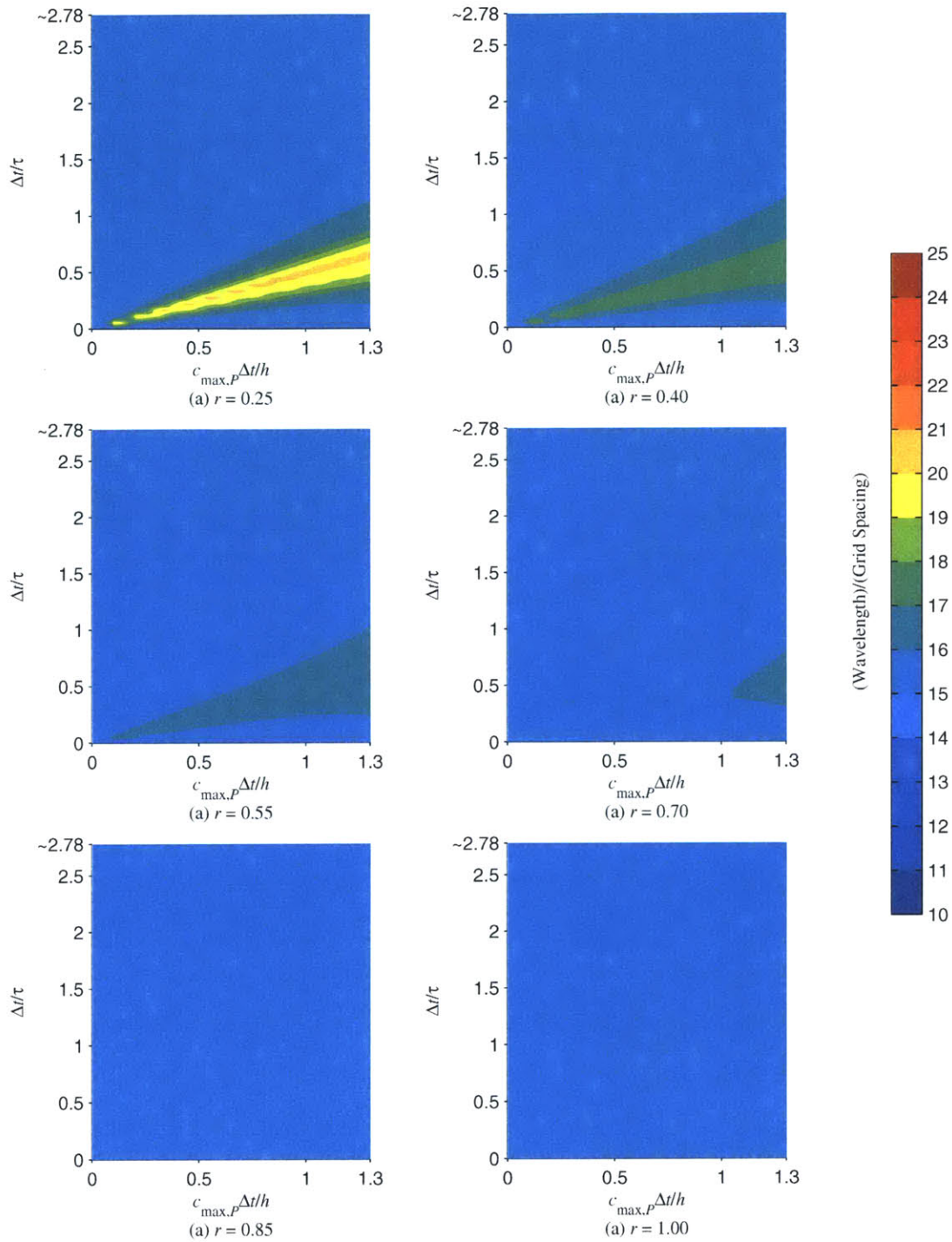


Fig. 3C-17—Minimum number of two-dimensional MSDLM grid spacings per wavelength required to achieve less than 1% error in P phase speed as functions of Courant number C , normalized time step $\Delta t/\tau$, and various values of $r_p = r_s = r$, squared ratio of minimum to maximum phase speeds, when $\nu = 0.40$.

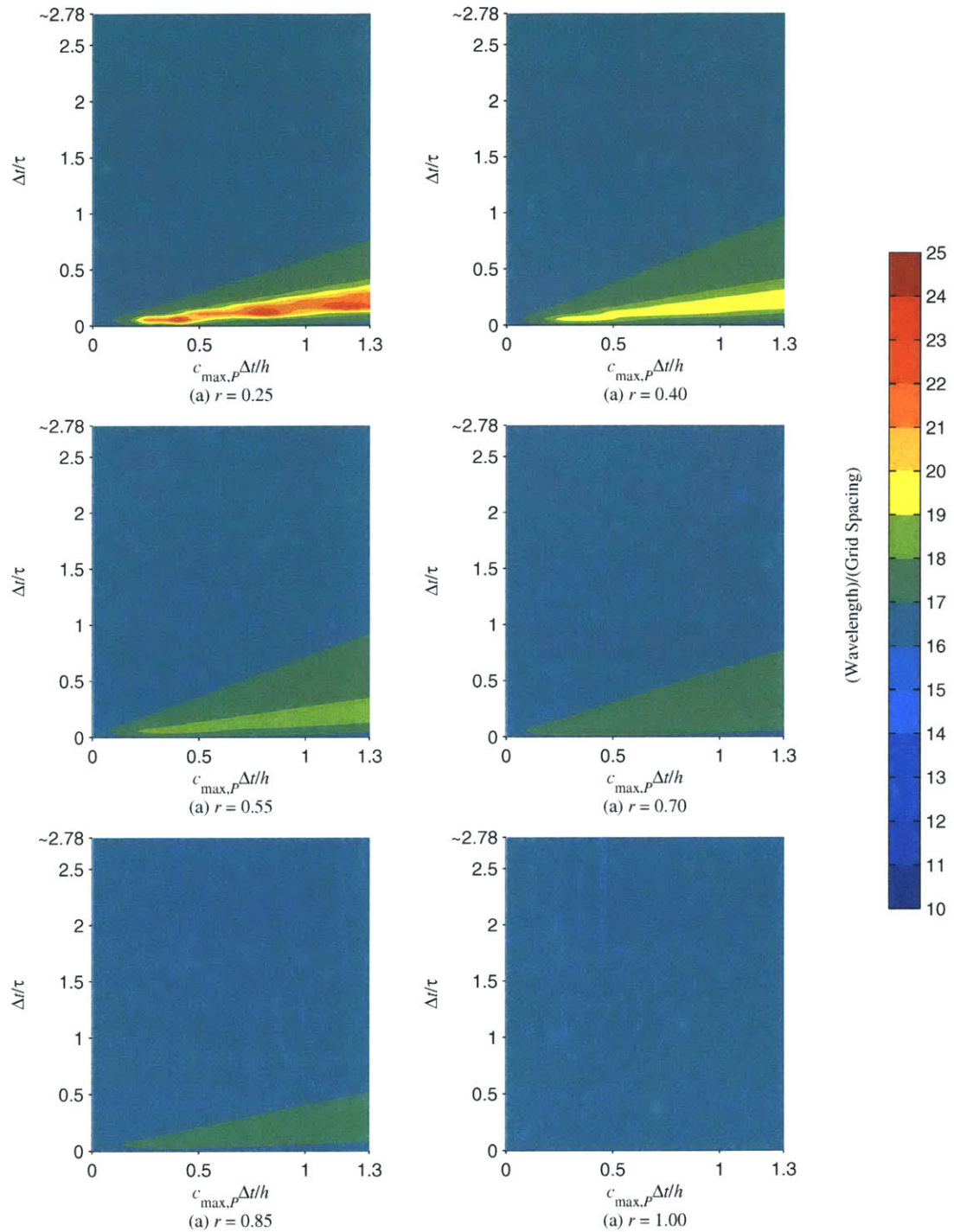


Fig. 3C-18—Minimum number of two-dimensional MSDLM grid spacings per wavelength required to achieve less than 1% error in S phase speed as functions of Courant number C , normalized time step $\Delta t/\tau$, and various values of $r_p = r_s = r$, squared ratio of minimum to maximum phase speeds, when $\nu = 0.40$.

References:

- 3C-1. R.M. Christensen. *Theory of Viscoelasticity: An Introduction* 2nd ed., pp. 14,15,37,38. Academic Press, New York (1982).
 3C-2. M. Abramowitz and I.A. Stegun (Eds.), *Handbook of Mathematical Functions with Formulas, Graphs and Mathematical Tables*, pp. 896-897. Dover, New York (1965).
 3C-3. H. Yim, unpublished research, April, 2003.
 3C-4. L. Lapidus and G.F. Pinder. *Numerical Solution of Partial Differential Equations in Science and Engineering*, pp. 167-168. John Wiley & Sons, New York (1982).

APPENDIX 3D—Two-dimensional MSDLM Schematic and Stress Dynamic Equations for a Longitudinal Interface of Dissimilar Materials.

Consider a longitudinal interface of dissimilar standard linear solids, Material *I* and Material *II*, as illustrated in Fig. 3D-1. The stress-dynamic equations of motion are

$$\begin{aligned}
 \frac{df_{i,j+\frac{1}{2}}^x}{dt} = & -\frac{1}{\tau^I} f_{i,j+\frac{1}{2}}^x + \frac{g_1^I}{2\tau^I h^2 D} (u_{i+1,j} - 2u_{i,j} + u_{i-1,j}) \\
 & + \frac{1}{\tau^I h^2 D} \left(\frac{\eta_1^I}{4h^2} + \frac{g_3^I}{2} \right) (u_{i+1,j+1} + u_{i-1,j+1} - 2u_{i,j}) \\
 & + \frac{1}{\tau^I h^2 D} \left(-\frac{\eta_1^I}{4h^2} + \frac{g_3^I}{2} \right) (v_{i+1,j+1} - v_{i-1,j+1}) + \frac{3r_S^{II} M^{II} - r_P^{II} \Pi^{II}}{4\tau h^2} (-v_{i-1,j} + v_{i+1,j}) \\
 & + \left(\frac{g_1^I + g_2^I}{2h^2 D} \right) (\dot{u}_{i+1,j} - 2\dot{u}_{i,j} + \dot{u}_{i-1,j}) \\
 & + \frac{1}{h^2 D} \left(\frac{\eta_1^I + \eta_2^I}{4h^2} + \frac{g_3^I + g_4^I}{2} \right) (\dot{u}_{i+1,j+1} + \dot{u}_{i-1,j+1} - 2\dot{u}_{i,j}) \\
 & + \frac{1}{h^2 D} \left(-\frac{\eta_1^I + \eta_2^I}{4h^2} + \frac{g_3^I + g_4^I}{2} \right) (\dot{v}_{i+1,j+1} - \dot{v}_{i-1,j+1}) + \frac{3M^{II} - \Pi^{II}}{4h^2} (-\dot{v}_{i-1,j} + \dot{v}_{i+1,j})
 \end{aligned} \tag{3D-1}$$

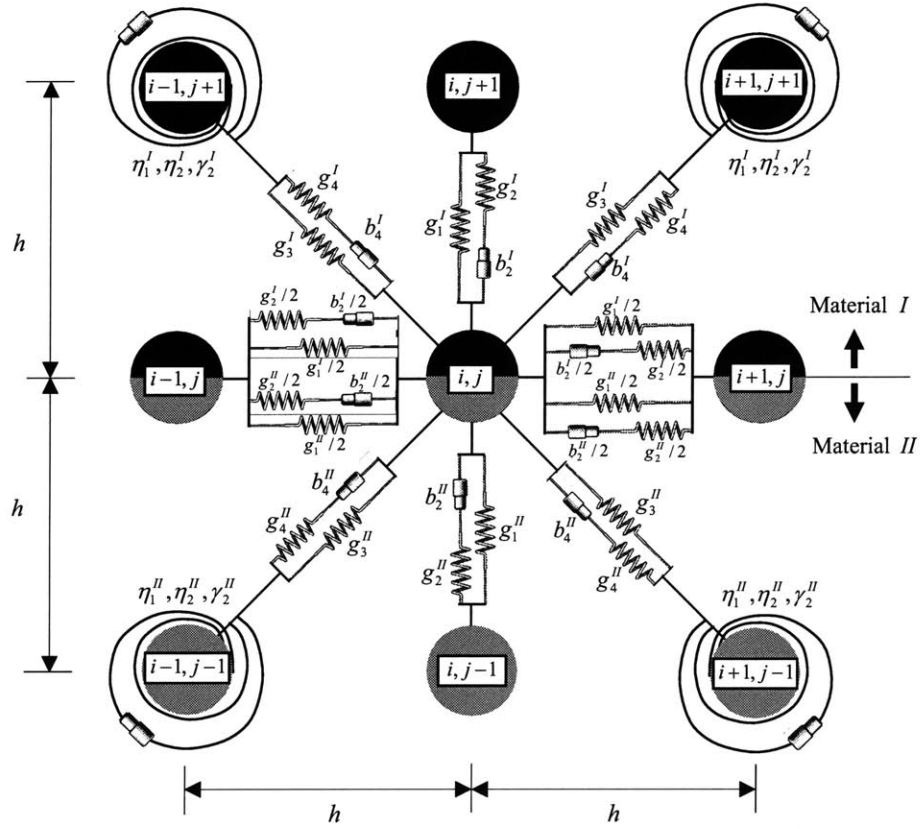


Fig. 3D-1—Schematic of mass-spring-dashpot lattice model (MSDLM) near longitudinal interface dissimilar materials.

$$\begin{aligned}
 \frac{df_{i,j+\frac{1}{2}}^y}{dt} = & -\frac{1}{\tau^I} f_{i,j+\frac{1}{2}}^y + \frac{g_1^I}{\tau^I h^2 D} (v_{i,j+1} - v_{i,j}) \\
 & + \frac{1}{\tau^I h^2 D} \left(\frac{\eta_1^I}{4h^2} + \frac{g_3^I}{2} \right) (v_{i+1,j+1} + v_{i-1,j+1} - 2v_{i,j}) \\
 & + \frac{1}{\tau^I h^2 D} \left(-\frac{\eta_1^I}{4h^2} + \frac{g_3^I}{2} \right) (u_{i+1,j+1} - u_{i-1,j+1}) + \frac{3r_s^{II} M^{II} - r_p^{II} \Pi^{II}}{4th^2} (-u_{i+1,j} + u_{i-1,j}) \\
 & + \left(\frac{g_1^I + g_2^I}{h^2 D} \right) (\dot{v}_{i,j+1} - \dot{v}_{i,j}) \\
 & + \frac{1}{h^2 D} \left(\frac{\eta_1^I + \eta_2^I}{4h^2} + \frac{g_3^I + g_4^I}{2} \right) (\dot{v}_{i+1,j+1} + \dot{v}_{i-1,j+1} - 2\dot{v}_{i,j}) \\
 & + \frac{1}{h^2 D} \left(-\frac{\eta_1^I + \eta_2^I}{4h^2} + \frac{g_3^I + g_4^I}{2} \right) (\dot{u}_{i+1,j+1} - \dot{u}_{i-1,j+1}) + \frac{3M^{II} - \Pi^{II}}{4h^2} (-\dot{u}_{i+1,j} + \dot{u}_{i-1,j})
 \end{aligned} \tag{3D-2}$$

$$\begin{aligned}
 \frac{df_{i,j-\frac{1}{2}}^x}{dt} = & -\frac{1}{\tau''} f_{i,j-\frac{1}{2}}^x + \frac{g_1''}{2\tau''h^2D} (u_{i+1,j} - 2u_{i,j} + u_{i-1,j}) \\
 & + \frac{1}{\tau''h^2D} \left(\frac{\eta_1''}{4h^2} + \frac{g_3''}{2} \right) (u_{i-1,j-1} + u_{i+1,j-1} - 2u_{i,j}) \\
 & + \frac{1}{\tau''h^2D} \left(-\frac{\eta_1''}{4h^2} + \frac{g_3''}{2} \right) (v_{i-1,j-1} - v_{i+1,j-1}) + \frac{3r_S^l M^l - r_P^l \Pi^l}{4\tau h^2} (v_{i-1,j} - v_{i+1,j}) \\
 & + \left(\frac{g_1'' + g_2''}{2h^2D} \right) (\dot{u}_{i+1,j} - 2\dot{u}_{i,j} + \dot{u}_{i-1,j}) \\
 & + \frac{1}{h^2D} \left(\frac{\eta_1'' + \eta_2''}{4h^2} + \frac{g_3'' + g_4''}{2} \right) (\dot{u}_{i-1,j-1} + \dot{u}_{i+1,j-1} - 2\dot{u}_{i,j}) \\
 & + \frac{1}{h^2D} \left(-\frac{\eta_1'' + \eta_2''}{4h^2} + \frac{g_3'' + g_4''}{2} \right) (\dot{v}_{i-1,j-1} - \dot{v}_{i+1,j-1}) + \frac{3M^l - \Pi^l}{4h^2} (\dot{v}_{i-1,j} - \dot{v}_{i+1,j})
 \end{aligned} \tag{3D-3}$$

$$\begin{aligned}
 \frac{df_{i,j-\frac{1}{2}}^y}{dt} = & -\frac{1}{\tau''} f_{i,j-\frac{1}{2}}^y + \frac{g_1''}{\tau''h^2D} (-v_{i,j} + v_{i,j-1}) \\
 & + \frac{1}{\tau''h^2D} \left(\frac{\eta_1''}{4h^2} + \frac{g_3''}{2} \right) (v_{i-1,j-1} + v_{i+1,j-1} - 2v_{i,j}) \\
 & + \frac{1}{\tau''h^2D} \left(-\frac{\eta_1''}{4h^2} + \frac{g_3''}{2} \right) (u_{i-1,j-1} - u_{i+1,j-1}) + \frac{3r_S^l M^l - r_P^l \Pi^l}{4\tau h^2} (u_{i+1,j} - u_{i-1,j}) \\
 & + \left(\frac{g_1'' + g_2''}{h^2D} \right) (-\dot{v}_{i,j} + \dot{v}_{i,j-1}) \\
 & + \frac{1}{h^2D} \left(\frac{\eta_1'' + \eta_2''}{4h^2} + \frac{g_3'' + g_4''}{2} \right) (\dot{v}_{i-1,j-1} + \dot{v}_{i+1,j-1} - 2\dot{v}_{i,j}) \\
 & + \frac{1}{h^2D} \left(-\frac{\eta_1'' + \eta_2''}{4h^2} + \frac{g_3'' + g_4''}{2} \right) (\dot{u}_{i-1,j-1} - \dot{u}_{i+1,j-1}) + \frac{3M^l - \Pi^l}{4h^2} (\dot{u}_{i+1,j} - \dot{u}_{i-1,j})
 \end{aligned} \tag{3D-4}$$

$$\frac{du_{i,j}}{dt} = \dot{u}_{i,j} \tag{3D-5}$$

$$\frac{dv_{i,j}}{dt} = \dot{v}_{i,j} \tag{3D-6}$$

$$\frac{d\dot{u}_{i,j}}{dt} = \frac{2}{\rho^l + \rho''} (f_{i,j+\frac{1}{2}}^x + f_{i,j-\frac{1}{2}}^x + f_{i,j}^{bx}) \tag{3D-7}$$

$$\frac{d\dot{v}_{i,j}}{dt} = \frac{2}{\rho^l + \rho''} (f_{i,j+\frac{1}{2}}^y - f_{i,j-\frac{1}{2}}^y + f_{i,j}^{by}) \tag{3D-8}$$

where

$$g_1^I = D(r_p^I \Pi^I - r_s^I M^I) \quad (3D-9)$$

$$g_2^I = D((1 - r_p^I) \Pi^I - (1 - r_s^I) M^I) \quad (3D-10)$$

$$g_3^I = \frac{D}{4} (r_p^I \Pi^I + r_s^I M^I) \quad (3D-11)$$

$$g_4^I = \frac{D}{4} ((1 - r_p^I) \Pi^I + (1 - r_s^I) M^I) \quad (3D-12)$$

$$\eta_1^I = \frac{h^2 D}{4} (3r_s^I M^I - r_p^I \Pi^I) \quad (3D-13)$$

$$\eta_2^I = \frac{h^2 D}{4} (3(1 - r_s^I) M^I - (1 - r_p^I) \Pi^I) \quad (3D-14)$$

$$g_1^{II} = D(r_p^{II} \Pi^{II} - r_s^{II} M^{II}) \quad (3D-15)$$

$$g_2^{II} = D((1 - r_p^{II}) \Pi^{II} - (1 - r_s^{II}) M^{II}) \quad (3D-16)$$

$$g_3^{II} = \frac{D}{4} (r_p^{II} \Pi^{II} + r_s^{II} M^{II}) \quad (3D-17)$$

$$g_4^{II} = \frac{D}{4} ((1 - r_p^{II}) \Pi^{II} + (1 - r_s^{II}) M^{II}) \quad (3D-18)$$

$$\eta_1^{II} = \frac{h^2 D}{4} (3r_s^{II} \Pi^{II} - r_p^{II} M^{II}) \quad (3D-19)$$

$$\eta_2^{II} = \frac{h^2 D}{4} (3(1 - r_s^{II}) \Pi^{II} - (1 - r_p^{II}) M^{II}) \quad (3D-20)$$

and where h is the grid spacing, D is the unit depth, and ρ^I and ρ^{II} are respective densities of Material I and Material II .

APPENDIX 3E—Steady-State Wave Propagation in One and Two-Dimensional Standard Linear Solids

In this appendix, the steady-state displacement field is derived for various boundary conditions in one and two-dimensional standard linear solids.

One-Dimensional Standard Linear Solids

Prescribed Displacement Slab of Length l

Consider a one-dimensional standard linear solid of length l as shown in Fig. 3E-

1. Given the excitation circular frequency ω , the elastic constant ϕ , the squared ratio of

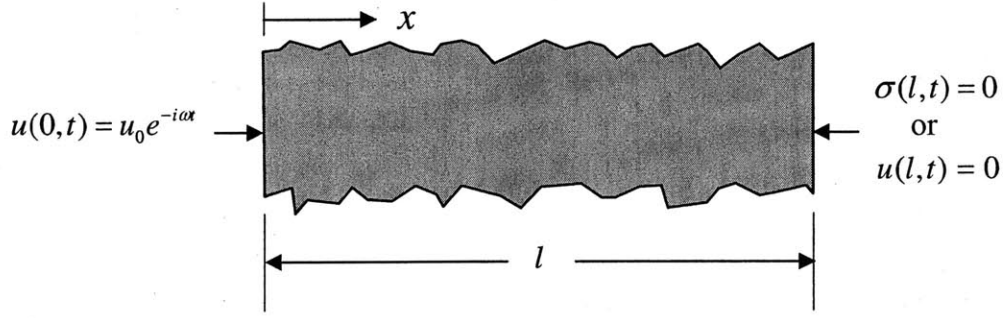


Fig. 3E-1—Prescribed harmonic displacement/fixed or displacement/free boundary conditions on one-dimensional standard linear solid.

minimum to maximum phase speed r , the stress relaxation time τ , and density ρ , the governing equation of wave propagation in a standard linear solid is given by

$$u(x,t) = Ae^{-\alpha x} e^{\hat{i}(kx-\alpha t)} + Be^{\alpha x} e^{\hat{i}(-kx-\alpha t)} \quad (3E-1)$$

where A and B are the complex amplitudes of the damped waves propagating in the positive and negative directions, respectively, α is the attenuation coefficient given by the positive root of

$$\alpha^2 = \frac{\rho\omega^2}{2r\phi} \left(\sqrt{\frac{1+\omega^2\tau^2}{1+r^{-2}\omega^2\tau^2}} - \frac{1+r^{-2}\omega^2\tau^2}{1+r^{-2}\omega^2\tau^2} \right) \quad (3E-2)$$

\hat{i} is equal to $\sqrt{-1}$, and k is the wavenumber given by the positive root of

$$k^2 = \frac{\rho\omega^2}{2r\phi} \left(\sqrt{\frac{1+\omega^2\tau^2}{1+r^{-2}\omega^2\tau^2}} + \frac{1+r^{-2}\omega^2\tau^2}{1+r^{-2}\omega^2\tau^2} \right) \quad (3E-3)$$

Consider the boundary condition at $x = 0$ is a prescribed displacement given by

$$u(x,t) = u_0 e^{-i\alpha t} \quad (3E-4)$$

where u_0 is the amplitude.

Consider a fixed boundary condition at $x = l$

$$u(l,t) = 0 \quad (3E-5)$$

Substituting eqn. (3E-1) into eqns. (3E-4) and (3E-5) and solving the resulting simultaneous system of equations yield

$$A_{fixed} = u_0 \frac{1 - e^{-2\alpha l} \cos 2kl + \hat{i} e^{-2\alpha l} \sin 2kl}{1 - 2e^{-2\alpha l} \cos 2kl + e^{-4\alpha l}} \quad (3E-6)$$

$$B_{fixed} = u_0 \frac{e^{-4\alpha l} - e^{-2\alpha l} \cos 2kl - \hat{i} e^{-2\alpha l} \sin 2kl}{1 - 2e^{-2\alpha l} \cos 2kl + e^{-4\alpha l}} \quad (3E-7)$$

Consider a free boundary condition or the steady-state stress at $x=l$ is given by

$$\sigma(l, t) = \phi \frac{r + \omega^2 \tau^2 + \hat{i} \omega \tau (r-1)}{1 + \omega^2 \tau^2} \frac{\partial u}{\partial x} \Big|_{x=l} = 0 \quad (3E-8)$$

Substituting eqn. (3E-1) into eqns. (3E-4) and (3E-8) and solving the simultaneous system of equations yield

$$A_{free} = u_0 \frac{1 + e^{-2\alpha l} \cos 2kl - \hat{i} e^{-2\alpha l} \sin 2kl}{1 + 2e^{-2\alpha l} \cos 2kl + e^{-4\alpha l}} \quad (3E-9)$$

$$B_{free} = u_0 \frac{e^{-4\alpha l} + e^{-2\alpha l} \cos 2kl + \hat{i} e^{-2\alpha l} \sin 2kl}{1 + 2e^{-2\alpha l} \cos 2kl + e^{-4\alpha l}} \quad (3E-10)$$

The steady-state envelope, or maximum amplitude at a given location, is given by

$$|u(x)| = |Ae^{-\alpha x} e^{ikx} + Be^{\alpha x} e^{-ikx}| \quad (3E-11)$$

It is noted that, for either fixed or free boundary conditions, as the length become very long ($\alpha l \gg 1$), the solution reduces to

$$u(x, t) = u_0 e^{-\alpha x} e^{i(kx - \omega t)} \quad (3E-12)$$

Only right-going waves exist when the length becomes very long because all left-going waves dissipate completely and no reflection occurs at the boundary.

Transmission and reflection coefficients at interface of semi-infinite standard linear solids

Consider the displacement field in steady-state, one-dimensional wave propagation near the interface of two standard linear solids as shown in Fig. 3E-2

$$u_I(x, t) = u_0 e^{-\alpha_I x} e^{i(k_I x - \omega t)} + R u_0 e^{\alpha_I x} e^{i(-k_I x - \omega t)}, \quad -\infty < x \leq 0 \quad (3E-13)$$

$$u_{II}(x, t) = T u_0 e^{-\alpha_{II} x} e^{i(k_{II} x - \omega t)}, \quad 0 \leq x < \infty \quad (3E-14)$$

where u_0 is the amplitude of the incoming wave at $x = 0$, α_I and α_{II} are the respective attenuation coefficients of Materials *I* and *II*, given by

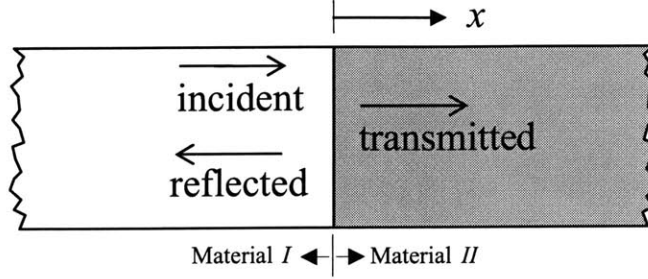


Fig. 3E-2—Schematic of reflection and transmission of waves at interface of dissimilar materials.

$$\alpha_I^2 = \frac{\rho_I \omega^2}{2r_I \phi_I} \left(\sqrt{\frac{1 + \omega^2 \tau_I^2}{1 + r_I^{-2} \omega^2 \tau_I^2}} - \frac{1 + r_I^{-1} \omega^2 \tau_I^2}{1 + r_I^{-2} \omega^2 \tau_I^2} \right) \quad (3E-15)$$

$$\alpha_{II}^2 = \frac{\rho_{II} \omega^2}{2r_{II} \phi_{II}} \left(\sqrt{\frac{1 + \omega^2 \tau_{II}^2}{1 + r_{II}^{-2} \omega^2 \tau_{II}^2}} - \frac{1 + r_{II}^{-1} \omega^2 \tau_{II}^2}{1 + r_{II}^{-2} \omega^2 \tau_{II}^2} \right) \quad (3E-16)$$

\hat{i} is $\sqrt{-1}$, k_I and k_{II} are the respective wavenumbers of material *I* and *II*, given by

$$k_I^2 = \frac{\rho_I \omega^2}{2r_I \phi_I} \left(\sqrt{\frac{1 + \omega^2 \tau_I^2}{1 + r_I^{-2} \omega^2 \tau_I^2}} + \frac{1 + r_I^{-1} \omega^2 \tau_I^2}{1 + r_I^{-2} \omega^2 \tau_I^2} \right) \quad (3E-17)$$

$$k_{II}^2 = \frac{\rho_{II} \omega^2}{2r_{II} \phi_{II}} \left(\sqrt{\frac{1 + \omega^2 \tau_{II}^2}{1 + r_{II}^{-2} \omega^2 \tau_{II}^2}} + \frac{1 + r_{II}^{-1} \omega^2 \tau_{II}^2}{1 + r_{II}^{-2} \omega^2 \tau_{II}^2} \right) \quad (3E-18)$$

and R and T are the reflection and transmission coefficients, respectively.

The boundary conditions at $x = 0$ are a continuity of displacement and that of normal and axial stress

$$u_I(0, t) = u_{II}(0, t) \quad (3E-19)$$

$$\sigma_I(0, t) = \sigma_{II}(0, t) \quad (3E-20)$$

or, expressing the steady-state stress as the product of a complex modulus and strain,

$$\phi_I \frac{r_I - \hat{i} \omega \tau_I}{1 - \hat{i} \omega \tau_I} \frac{\partial u_I}{\partial x} \Big|_{x=0} = \phi_{II} \frac{r_{II} - \hat{i} \omega \tau_{II}}{1 - \hat{i} \omega \tau_{II}} \frac{\partial u_{II}}{\partial x} \Big|_{x=0} \quad (3E-21)$$

Inserting eqns. (3E-13) and (3E-14) into eqns. (3E-19) and (3E-21) yields

$$1 + R = T \quad (3E-22)$$

$$1 - R = XT \quad (3E-23)$$

where

$$X = \frac{\phi_{II}(r_{II} - \hat{i}\omega\tau_{II})(-\alpha_{II} + \hat{i}k_{II})(1 - \hat{i}\omega\tau_I)}{\phi_I(r_I - \hat{i}\omega\tau_I)(-\alpha_I + \hat{i}k_I)(1 - \hat{i}\omega\tau_{II})} \quad (3E-24)$$

Thus, expressions for $|T|$ and $|R|$ are

$$|T| = \left| \frac{2}{1 + X} \right| \quad (3E-25)$$

$$|R| = \left| \frac{1 - X}{1 + X} \right| \quad (3E-26)$$

Reflection coefficient due to absorbing boundary conditions

Consider a semi-infinite standard linear solid defined for $-\infty < x < 0$ with the following boundary condition at $x = 0$:

$$\left. \frac{\partial u(x,t)}{\partial x} \right|_{x=0} + c \left. \frac{\partial u(x,t)}{\partial t} \right|_{x=0} = 0 \quad (3E-27)$$

where c is a characteristic velocity. Consider the displacement field of an incoming attenuating wave traveling in the positive x -direction and a reflected outgoing wave traveling in the negative x -direction given as

$$u(x,t) = u_0 e^{-\alpha x} e^{i(kx - \omega t)} + R u_0 e^{\alpha x} e^{i(-kx - \omega t)} \quad (3E-28)$$

where u_0 is the amplitude of the incoming wave at the origin and R is the reflection coefficient. Substituting eqn. (3E-28) into (3E-27) yields the following expression for the reflection coefficient

$$|R| = \sqrt{\frac{\alpha^2 c^2 + (\omega - ck)^2}{\alpha^2 c^2 + (\omega + ck)^2}} \quad (3E-29)$$

In the high frequency limit ($\omega\tau \gg 1$), c is set equal to $\sqrt{E/\rho}$ and the reflection coefficient is

$$|R| = \frac{1-r}{4\omega\tau} \text{ for } \omega\tau \gg 1 \quad (3E-30)$$

In the low frequency limit ($\omega\tau \ll r$), c is set equal to $\sqrt{rE/\rho}$ and the reflection coefficient is

$$|R| = \frac{\omega\tau(1-r)}{4r} \text{ for } \omega\tau \ll r \quad (3E-31)$$

Two-Dimensional Standard Linear Solid

Consider a half space of a two-dimensional standard linear solid (described by a single relaxation time τ and squared ratio of minimum to maximum P and S wave speeds r) defined by $-\infty < y < 0$ as shown in Fig. C.3.

Reflection at Fixed Surface

First consider a fixed boundary at $y = 0$, that is,

$$u(x,0,t) = v(x,0,t) = 0 \quad (3E-32)$$

A plane strain displacement field in the x - y plane, formed from an incident P plane wave (angle of incidence $\theta_{P,i}$), reflected P plane wave (angle of reflection $\theta_{P,r}$), and a reflected S plane wave (angle of refraction $\theta_{S,r}$), is described in ray form in Fig. C.3.

The displacement field is described by the following combination a P plane wave attenuated in the direction of wave propagation,

$$u_{P,i}(x, y, t) = u_0(\sin \theta_{P,i}) e^{-\alpha_P(x \sin \theta_{P,i} + y \cos \theta_{P,i})} e^{i(k_P(x \sin \theta_{P,i} + y \cos \theta_{P,i}) - \omega t)} \quad (3E-33)$$

$$v_{P,i}(x, y, t) = u_0(\cos \theta_{P,i}) e^{-\alpha_P(x \sin \theta_{P,i} + y \cos \theta_{P,i})} e^{i(k_P(x \sin \theta_{P,i} + y \cos \theta_{P,i}) - \omega t)} \quad (3E-34)$$

a reflected P plane wave attenuated in the direction of wave propagation,

$$u_{P,r}(x, y, t) = R_{P,r} u_0(\sin \theta_{P,r}) e^{-\alpha_P(x \sin \theta_{P,r} - y \cos \theta_{P,r})} e^{i(k_P(x \sin \theta_{P,r} - y \cos \theta_{P,r}) - \omega t)} \quad (3E-35)$$

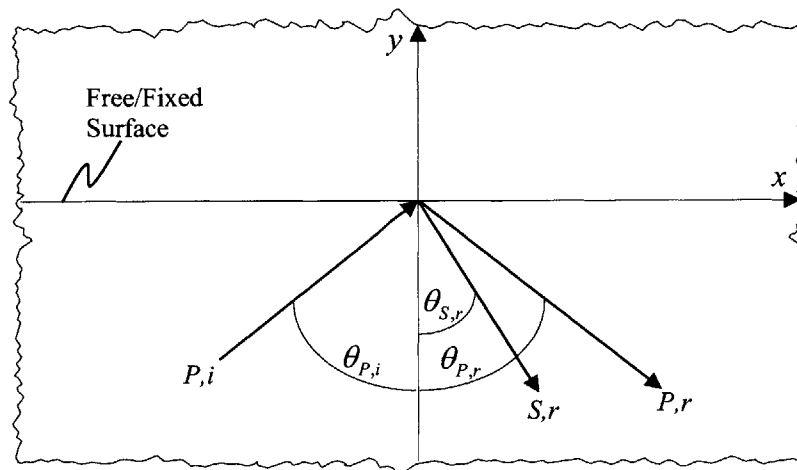


Fig. 3E-3—Ray representation of incident P plane wave, reflected P plane wave and reflected S plane wave near free/fixed surface of standard linear solid.

$$v_{P,r}(x, y, t) = -R_{P,r}u_0(\cos\theta_{P,r})e^{-\alpha_P(x\sin\theta_{P,r}-y\cos\theta_{P,r})}e^{i(k_P(x\sin\theta_{P,r}-y\cos\theta_{P,r})-\omega t)} \quad (3E-36)$$

and a reflected S plane wave attenuated in the direction of wave propagation,

$$u_{S,r}(x, y, t) = R_{S,r}u_0(\cos\theta_{S,r})e^{-\alpha_S(x\sin\theta_{S,r}-y\cos\theta_{S,r})}e^{i(k_S(x\sin\theta_{S,r}-y\cos\theta_{S,r})-\omega t)} \quad (3E-37)$$

$$v_{S,r}(x, y, t) = R_{S,r}u_0(\sin\theta_{S,r})e^{-\alpha_S(x\sin\theta_{S,r}-y\cos\theta_{S,r})}e^{i(k_S(x\sin\theta_{S,r}-y\cos\theta_{S,r})-\omega t)} \quad (3E-38)$$

where

$$\alpha_P^2 = \frac{\rho\omega^2}{2r\Pi} \left(\sqrt{\frac{1+\omega^2\tau^2}{1+r^{-2}\omega^2\tau^2}} - \frac{1+r^{-1}\omega^2\tau^2}{1+r^{-2}\omega^2\tau^2} \right) \quad (3E-39)$$

$$\alpha_S^2 = \frac{\rho\omega^2}{2rM} \left(\sqrt{\frac{1+\omega^2\tau^2}{1+r^{-2}\omega^2\tau^2}} - \frac{1+r^{-1}\omega^2\tau^2}{1+r^{-2}\omega^2\tau^2} \right) \quad (3E-40)$$

$$k_P^2 = \frac{\rho\omega^2}{2r\Pi} \left(\sqrt{\frac{1+\omega^2\tau^2}{1+r^{-2}\omega^2\tau^2}} + \frac{1+r^{-1}\omega^2\tau^2}{1+r^{-2}\omega^2\tau^2} \right) \quad (3E-41)$$

and

$$k_S^2 = \frac{\rho\omega^2}{2rM} \left(\sqrt{\frac{1+\omega^2\tau^2}{1+r^{-2}\omega^2\tau^2}} + \frac{1+r^{-1}\omega^2\tau^2}{1+r^{-2}\omega^2\tau^2} \right) \quad (3E-42)$$

Thus, the total displacement field is

$$u = u_{P,i} + u_{P,r} + u_{S,r} \quad (3E-43)$$

$$v = v_{P,i} + v_{P,r} + v_{S,r} \quad (3E-44)$$

In the above equations, the subscripts P and S denote respective properties of longitudinal and shear waves. Subscripts i and r denote incident and reflected waves, respectively, and superscripts α and k denote the angle of the attenuation and wave propagation, respectively.

Substituting eqns. (3E-43) and (3E-44) into eqn. (3E-32), yields

$$\theta_{P,i} = \theta_{P,r} \quad (3E-45)$$

$$\frac{\sin\theta_{S,r}^k}{\sin\theta_{P,i}^k} = \sqrt{\frac{M}{\Pi}} \quad (3E-46)$$

$$|R_{P,r}| = \left| \frac{-\sin \theta_{P,i} \sin \theta_{S,r} + \cos \theta_{P,i} \cos \theta_{S,r}}{\sin \theta_{P,r} \sin \theta_{S,r} + \cos \theta_{P,r} \cos \theta_{S,r}} \right| \quad (3E-47)$$

$$|R_{S,r}| = \left| \frac{-\sin \theta_{P,r} \cos \theta_{P,i} - \cos \theta_{P,r} \sin \theta_{P,i}}{\sin \theta_{P,r} \sin \theta_{S,r} + \cos \theta_{P,r} \cos \theta_{S,r}} \right| \quad (3E-48)$$

Reflection at Free Surface

The relevant in-plane stresses in a plane strain standard linear solid can be expressed as [3C-1]

$$\sigma_{yy} + \tau\sigma_{yy} = r\Pi \frac{\partial v}{\partial y} + r(\Pi - 2M) \frac{\partial u}{\partial x} + r\Pi \frac{\partial v}{\partial y \partial t} + \tau(\Pi - 2M) \frac{\partial u}{\partial x \partial t} \quad (3E-49)$$

$$\sigma_{xy} + \tau\sigma_{xy} = rM \left(\frac{\partial u}{\partial y} + \frac{\partial v}{\partial x} \right) + rM \left(\frac{\partial u}{\partial y \partial t} + \frac{\partial v}{\partial x \partial t} \right) \quad (3E-50)$$

where σ_{xy} is not needed to derive the reflection coefficient.

At the traction-free surface ($y=0$), σ_{yy} and σ_{xy} must be equal to zero. Substituting eqns. (3E-43) and (3E-44) into eqns. (3E-49) and (3E-50), evaluating all terms at $y=0$, and requiring the boundary condition to be independent of x yield

$$\theta_{P,i} = \theta_{P,r} \quad (3E-51)$$

$$\frac{\sin \theta_{S,r}^k}{\sin \theta_{P,i}} = \sqrt{\frac{M}{\Pi}} \quad (3E-52)$$

$$|R_{P,r}| = \left| \frac{(1 - M/\Pi) \cos 2\theta_{S,r} - (M/\Pi) \cos 2(\theta_{P,i} + \theta_{S,r})}{(1 - M/\Pi) \cos 2\theta_{S,r} - (M/\Pi) \cos 2(\theta_{P,i} - \theta_{S,r})} \right| \quad (3E-53)$$

$$|R_{S,r}| = \left| \frac{2\sqrt{M/\Pi} (1 + (M/\Pi)(1 + \cos 2\theta_{P,i})) \sin 2\theta_{P,i}}{(1 - M/\Pi) \cos 2\theta_{S,r} - (M/\Pi) \cos 2(\theta_{P,i} - \theta_{S,r})} \right| \quad (3E-54)$$

Reflection at Interface of Dissimilar Materials

Consider two dissimilar two-dimensional standard linear solids, Material I, $-\infty < y < 0$, and Material II, $0 < y < \infty$. A plane strain displacement field in the x - y

plane, formed from an incident P plane wave (angle of incidence $\theta_{P,i}$), reflected P plane wave (angle of reflection $\theta_{P,r}$), reflected S plane wave (angle of reflection $\theta_{S,r}$), transmitted P plane wave (angle of transmission $\theta_{P,t}$), and a transmitted S plane wave (angle of refraction $\theta_{S,t}$), is shown in ray form in Fig. 3E-4.

The displacement field in Material I is described by a combination of a P plane wave attenuated in the direction of wave propagation,

$$u_{P,i}(x, y, t) = u_0(\sin \theta_{P,i})e^{-\alpha_P^I(x \sin \theta_{P,i} + y \cos \theta_{P,i})}e^{i(k_P^I(x \sin \theta_{P,i} + y \cos \theta_{P,i}) - \omega t)} \quad (3E-28)$$

$$v_{P,i}(x, y, t) = u_0(\cos \theta_{P,i})e^{-\alpha_P^I(x \sin \theta_{P,i} + y \cos \theta_{P,i})}e^{i(k_P^I(x \sin \theta_{P,i} + y \cos \theta_{P,i}) - \omega t)} \quad (3E-29)$$

a reflected P plane wave attenuated in the direction of wave propagation,

$$u_{P,r}(x, y, t) = R_{P,i}u_0(\sin \theta_{P,r})e^{-\alpha_P^I(x \sin \theta_{P,r} - y \cos \theta_{P,r})}e^{i(k_P^I(x \sin \theta_{P,r} - y \cos \theta_{P,r}) - \omega t)} \quad (3E-30)$$

$$v_{P,r}(x, y, t) = -R_{P,i}u_0(\cos \theta_{P,r})e^{-\alpha_P^I(x \sin \theta_{P,r} - y \cos \theta_{P,r})}e^{i(k_P^I(x \sin \theta_{P,r} - y \cos \theta_{P,r}) - \omega t)} \quad (3E-40)$$

and a reflected S plane wave attenuated in the direction of wave propagation,

$$u_{S,r}(x, y, t) = R_{S,i}u_0(\cos \theta_{S,r})e^{-\alpha_S^I(x \sin \theta_{S,r} - y \cos \theta_{S,r})}e^{i(k_S^I(x \sin \theta_{S,r} - y \cos \theta_{S,r}) - \omega t)} \quad (3E-41)$$

$$v_{S,r}(x, y, t) = R_{S,i}u_0(\sin \theta_{S,r})e^{-\alpha_S^I(x \sin \theta_{S,r} - y \cos \theta_{S,r})}e^{i(k_S^I(x \sin \theta_{S,r} - y \cos \theta_{S,r}) - \omega t)} \quad (3E-43)$$

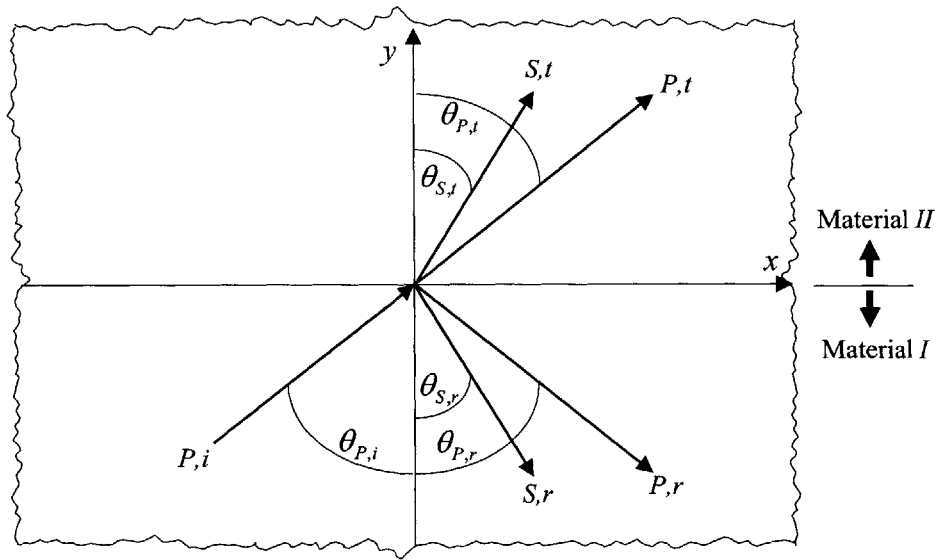


Fig. 3E-4—Ray representation of incident P plane wave and reflected and transmitted P and S plane waves near interface of two dissimilar standard linear solids.

where

$$(\alpha_P^I)^2 = \frac{\rho^I \omega^2}{2r^I \Pi^I} \left(\sqrt{\frac{1 + \omega^2 \tau^2}{1 + (r^I)^{-2} \omega^2 \tau^2}} - \frac{1 + (r^I)^{-1} \omega^2 \tau^2}{1 + (r^I)^{-2} \omega^2 \tau^2} \right) \quad (3E-45)$$

$$(\alpha_S^I)^2 = \frac{\rho^I \omega^2}{2r^I M^I} \left(\sqrt{\frac{1 + \omega^2 \tau^2}{1 + (r^I)^{-2} \omega^2 \tau^2}} - \frac{1 + (r^I)^{-1} \omega^2 \tau^2}{1 + (r^I)^{-2} \omega^2 \tau^2} \right) \quad (3E-46)$$

$$(k_P^I)^2 = \frac{\rho^I \omega^2}{2r^I \Pi^I} \left(\sqrt{\frac{1 + \omega^2 \tau^2}{1 + (r^I)^{-2} \omega^2 \tau^2}} + \frac{1 + (r^I)^{-1} \omega^2 \tau^2}{1 + (r^I)^{-2} \omega^2 \tau^2} \right) \quad (3E-47)$$

and

$$(k_S^I)^2 = \frac{\rho^I \omega^2}{2r^I M^I} \left(\sqrt{\frac{1 + \omega^2 \tau^2}{1 + (r^I)^{-2} \omega^2 \tau^2}} - \frac{1 + (r^I)^{-1} \omega^2 \tau^2}{1 + (r^I)^{-2} \omega^2 \tau^2} \right) \quad (3E-48)$$

The displacement field in Material *I* is

$$u^I = u_{P,i} + u_{P,r} + u_{S,r} \quad (3E-49)$$

$$v^I = v_{P,i} + v_{P,r} + v_{S,r} \quad (3E-50)$$

The displacement field in Material *II* is described by the combination of a transmitted *P* plane wave attenuated in the direction of wave propagation,

$$u_{P,i}(x, y, t) = T_{P,i} u_0 (\sin \theta_{P,i}) e^{-\alpha_P^{II} (x \sin \theta_{P,i} + y \cos \theta_{P,i})} e^{i(k_P^{II} (x \sin \theta_{P,i} + y \cos \theta_{P,i}) - \omega t)} \quad (3E-51)$$

$$v_{P,i}(x, y, t) = T_{P,i} u_0 (\cos \theta_{P,i}) e^{-\alpha_P^{II} (x \sin \theta_{P,i} + y \cos \theta_{P,i})} e^{i(k_P^{II} (x \sin \theta_{P,i} + y \cos \theta_{P,i}) - \omega t)} \quad (3E-52)$$

and a transmitted *S* plane wave attenuated in the direction of wave propagation,

$$u_{S,i}(x, y, t) = T_{S,i} u_0 (\cos \theta_{S,i}) e^{-\alpha_S^{II} (x \sin \theta_{S,i} + y \cos \theta_{S,i})} e^{i(k_S^{II} (x \sin \theta_{S,i} + y \cos \theta_{S,i}) - \omega t)} \quad (3E-53)$$

$$v_{S,i}(x, y, t) = -T_{S,i} u_0 (\sin \theta_{S,i}) e^{-\alpha_S^{II} (x \sin \theta_{S,i} + y \cos \theta_{S,i})} e^{i(k_S^{II} (x \sin \theta_{S,i} + y \cos \theta_{S,i}) - \omega t)} \quad (3E-54)$$

where

$$(\alpha_P^{II})^2 = \frac{\rho^{II} \omega^2}{2r^{II} \Pi^{II}} \left(\sqrt{\frac{1 + \omega^2 \tau^2}{1 + (r^{II})^{-2} \omega^2 \tau^2}} - \frac{1 + (r^{II})^{-1} \omega^2 \tau^2}{1 + (r^{II})^{-2} \omega^2 \tau^2} \right) \quad (3E-55)$$

$$(\alpha_S^{II})^2 = \frac{\rho^{II} \omega^2}{2r^{II} M^{II}} \left(\sqrt{\frac{1 + \omega^2 \tau^2}{1 + (r^{II})^{-2} \omega^2 \tau^2}} - \frac{1 + (r^{II})^{-1} \omega^2 \tau^2}{1 + (r^{II})^{-2} \omega^2 \tau^2} \right) \quad (3E-56)$$

$$(k_P^II)^2 = \frac{\rho^II \omega^2}{2r^II \Pi^II} \left(\sqrt{\frac{1 + \omega^2 \tau^2}{1 + (r^II)^2 \omega^2 \tau^2}} + \frac{1 + (r^II)^{-1} \omega^2 \tau^2}{1 + (r^II)^2 \omega^2 \tau^2} \right) \quad (3E-57)$$

and

$$(k_S^II)^2 = \frac{\rho^II \omega^2}{2r^II M^II} \left(\sqrt{\frac{1 + \omega^2 \tau^2}{1 + (r^II)^2 \omega^2 \tau^2}} - \frac{1 + (r^II)^{-1} \omega^2 \tau^2}{1 + (r^II)^2 \omega^2 \tau^2} \right) \quad (3E-58)$$

The displacement field in Material II is

$$u^II = u_{P,t} + u_{S,t} \quad (3E-59)$$

$$v^II = v_{P,t} + v_{S,t} \quad (3E-60)$$

Expressions for the relevant stresses in each plane strain standard linear solid are

$$\begin{aligned} \sigma_{yy}^I + \tau^I \sigma_{yy}^I = r^I \Pi^I \frac{\partial v^I}{\partial y} + r^I (\Pi^I - 2M^I) \frac{\partial u^I}{\partial x} + \tau^I \Pi^I \frac{\partial v^I}{\partial y \partial t} \\ + \tau^I (\Pi^I - 2M^I) \frac{\partial u^I}{\partial x \partial t} \end{aligned} \quad (3E-61)$$

$$\sigma_{xy}^I + \tau^I \sigma_{xy}^I = r^I M^I \left(\frac{\partial u^I}{\partial y} + \frac{\partial v^I}{\partial x} \right) + \tau^I M^I \left(\frac{\partial u^I}{\partial y \partial t} + \frac{\partial v^I}{\partial x \partial t} \right) \quad (3E-62)$$

$$\begin{aligned} \sigma_{yy}^II + \tau^II \sigma_{yy}^II = r^II \Pi^II \frac{\partial v^II}{\partial y} + r^II (\Pi^II - 2M^II) \frac{\partial u^II}{\partial x} + \tau^II \Pi^II \frac{\partial v^II}{\partial y \partial t} \\ + \tau^II (\Pi^II - 2M^II) \frac{\partial u^II}{\partial x \partial t} \end{aligned} \quad (3E-63)$$

$$\sigma_{xy}^II + \tau^II \sigma_{xy}^II = r^II M^II \left(\frac{\partial u^II}{\partial y} + \frac{\partial v^II}{\partial x} \right) + \tau^II M^II \left(\frac{\partial u^II}{\partial y \partial t} + \frac{\partial v^II}{\partial x \partial t} \right) \quad (3E-64)$$

Expressions for σ_{xx}^I and σ_{xx}^II are not needed for the computation of the various reflection and transmission coefficients.

The boundary conditions are

$$u^I(x,0,t) = u^II(x,0,t) \quad (3E-65)$$

$$v^I(x,0,t) = v^II(x,0,t) \quad (3E-66)$$

$$\sigma_{yy}^I(x,0,t) = \sigma_{yy}^II(x,0,t) \quad (3E-67)$$

$$\sigma_{xy}^I(x,0,t) = \sigma_{xy}^II(x,0,t) \quad (3E-68)$$

For the special case when

$$\omega\tau^I \ll 1 \quad (3E-69)$$

$$\omega\tau^{II} \ll 1 \quad (3E-70)$$

$$\frac{1-r^I}{\tau^I} = \frac{1-r^{II}}{\tau^{II}} \quad (3E-71)$$

the angles are given by

$$\theta_{P,i} = \theta_{P,r} \quad (3E-72)$$

$$\frac{\sin \theta_{S,r}}{\sin \theta_{P,i}} = \sqrt{\frac{M^I}{\Pi^I}} \quad (3E-73)$$

$$\frac{\sin \theta_{P,t}}{\sin \theta_{P,i}} = \sqrt{\frac{\rho^I \Pi^{II}}{\rho^{II} \Pi^I}} \quad (3E-74)$$

$$\frac{\sin \theta_{S,t}}{\sin \theta_{P,i}} = \sqrt{\frac{\rho^I M^{II}}{\rho^{II} \Pi^I}} \quad (3E-75)$$

and the reflection and transmission coefficients are given by the solution to the following system of equations, eqn. (3E-76):

$$\begin{bmatrix} 1 & \sqrt{\csc^2 \theta_{P,i} - \left(\frac{c_{\max,S}^I}{c_{\max,P}^I}\right)^2} & & \\ -1 & \frac{c_{\max,S}^I}{c_{\max,P}^I} & & \\ a(\Pi^I - 2M^I \sin^2 \theta_{P,i}) & -aM^I \sin 2\theta_{P,i} \left(\frac{c_{\max,S}^I}{c_{\max,P}^I}\right)^{-1} & & \\ -aM^I \sin 2\theta_{P,i} & aM^I \cos 2\theta_{P,i} \left(\frac{c_{\max,S}^I}{c_{\max,P}^I}\right)^{-1} & & \end{bmatrix} \begin{bmatrix} \frac{c_{\max,P}^{II}}{c_{\max,P}^I} & & & \\ -\sqrt{\csc^2 \theta_{P,i} - \left(\frac{c_{\max,P}^{II}}{c_{\max,P}^I}\right)^2} & & & \\ (-\Pi^{II} + 2M^{II} \sin^2 \theta_{P,i}) \left(\frac{c_{\max,P}^{II}}{c_{\max,P}^I}\right)^{-1} & & & \\ -\sin 2\theta_{P,i} \left(\frac{c_{\max,P}^{II}}{c_{\max,P}^I}\right)^{-1} & & & \end{bmatrix} \begin{bmatrix} -\sqrt{\csc^2 \theta_{P,i} - \left(\frac{c_{\max,S}^{II}}{c_{\max,P}^I}\right)^2} & & & \\ -\frac{c_{\max,S}^{II}}{c_{\max,P}^I} & & & \\ M^{II} \sin^2 \theta_{S,i} \left(\frac{c_{\max,S}^{II}}{c_{\max,P}^I}\right)^{-1} & & & \\ -\cos 2\theta_{S,i} \left(\frac{c_{\max,S}^{II}}{c_{\max,P}^I}\right)^{-1} & & & \end{bmatrix} \begin{bmatrix} R_{P,r} \\ R_{S,r} \\ T_{P,t} \\ T_{S,t} \end{bmatrix} = \begin{bmatrix} -1 \\ -\cot \theta_{P,i} \\ a(2M^I \sin^2 \theta_{P,i} - \Pi^I) \\ -M^I \sin 2\theta_{P,i} \end{bmatrix}$$

where

$$c_{\max,P}^I = \sqrt{\Pi^I / \rho^I} \quad (3E-77)$$

$$c_{\max,S}^I = \sqrt{M^I / \rho^I} \quad (3E-78)$$

$$c_{\max,P}^{II} = \sqrt{\Pi^{II} / \rho^{II}} \quad (3E-79)$$

$$c_{\max,S}^{II} = \sqrt{M^{II} / \rho^{II}} \quad (3E-80)$$

and

$$a = \frac{1 + \hat{i}(r^I - 1)/(\omega\tau^I)}{1 + \hat{i}(r^{II} - 1)/(\omega\tau^{II})} \quad (3E-81)$$

Surface Waves

In this section, surface waves on a standard linear solid half-space defined by $y < 0$ will be investigated according to the procedure outlined in [3E-4]. Consider the displacement in the $x-y$ plane of the form

$$u_x = U_{P,x} e^{i\omega(s_{P,x}x + s_{P,y}y - t)} + U_{S,x} e^{i\omega(s_{S,x}x + s_{S,y}y - t)} \quad (3E-82)$$

$$u_y = U_{P,y} e^{i\omega(s_{P,x}x + s_{P,y}y - t)} + U_{S,y} e^{i\omega(s_{S,x}x + s_{S,y}y - t)} \quad (3E-83)$$

where u_n is the component of displacement, $U_{P,n}$ and $U_{S,n}$ are the complex components for each of the P and S modes, $s_{P,n}$ and $s_{S,n}$ are the components of the slowness vector, and where subscript n can be x or y .

The relevant steady-state stresses in the solid are

$$\sigma_{yy}^* = r\Pi^* \frac{\partial v}{\partial y} + r(\Pi^* - 2M^*) \frac{\partial u}{\partial x} \quad (3E-84)$$

$$\sigma_{xy}^* = r\Pi^* \left(\frac{\partial u}{\partial y} + \frac{\partial v}{\partial x} \right) \quad (3E-85)$$

(expressions for σ_{xx}^* is not needed for the computation of the surface wave) where the elastic constants are written in complex form as

$$\Pi^* = \Pi \frac{r + \omega^2 \tau^2 + \hat{i} \omega \tau (r - 1)}{1 + \omega^2 \tau^2} \quad (3E-86)$$

$$M^* = M \frac{r + \omega^2 \tau^2 + \hat{i} \omega \tau (r - 1)}{1 + \omega^2 \tau^2} \quad (3E-87)$$

The viscoelastic Rayleigh wave exists when the surface tractions vanish

$$\sigma_{yy}^* = \sigma_{xy}^* = 0 \quad (3E-88)$$

and

$$s_{P,x} = s_{S,x} = s_x \quad (3E-89)$$

To find the various parameters the following cubic equation must be solved

$$c^3 - 8c^2 + \left(24 - 16 \frac{M}{\Pi} \right) - 16 \left(1 - \frac{M}{\Pi} \right) = 0 \quad (3E-90)$$

where

$$c = \frac{\rho}{s_x^2 M^*} \quad (3E-91)$$

The other parameters are given by

$$s_{S,y}^2 = \frac{\rho}{M^*} - s_x^2 \quad (3E-92)$$

$$s_{P,y}^2 = \frac{\rho}{\Pi^*} - s_x^2 \quad (3E-93)$$

$$U_{S,y} = -U_{S,x} \frac{s_x}{s_{S,y}} \quad (3E-94)$$

$$U_{P,y} = -U_{P,x} \frac{s_{P,y}}{s_x} \quad (3E-95)$$

Because spurious solutions will be generated in the formulation of eqn. (3E-90), the roots of c are admissible if

$$\text{Re}\{s_x\} > 0, \text{Im}\{s_x\} \geq 0 \quad (3E-96)$$

$$\text{Im}\{s_{S,y}\} < 0, \text{Im}\{s_{P,y}\} < 0 \quad (3E-97)$$

and if

$$-4s_{S,y}s_{P,y} = s_x^2 \left(2 - \frac{\rho}{M^* s_x^2} \right)^2 \quad (3E-98)$$

is satisfied.

Numerical observations have shown that for the present standard linear solid viscoelastic model (single relaxation time and single dispersion parameter), there exists only an “elastic-like” Rayleigh wave, with a frequency dependent wavespeed, c_R ,

$$c_R = \frac{1}{\text{Re}\{s_x\}} \quad (3E-99)$$

such that

$$c_R < c_S < c_P \quad (3E-100)$$

The attenuation of the Rayleigh wave is given as

$$\alpha_R = \omega \text{Im}\{s_x\} \quad (3E-101)$$

Figure E.5 and E.6 show the frequency dependence of the phase speed and attenuation for the Rayleigh, P and S waves for the case when $r = 0.55$ and $\nu = 0.30$.

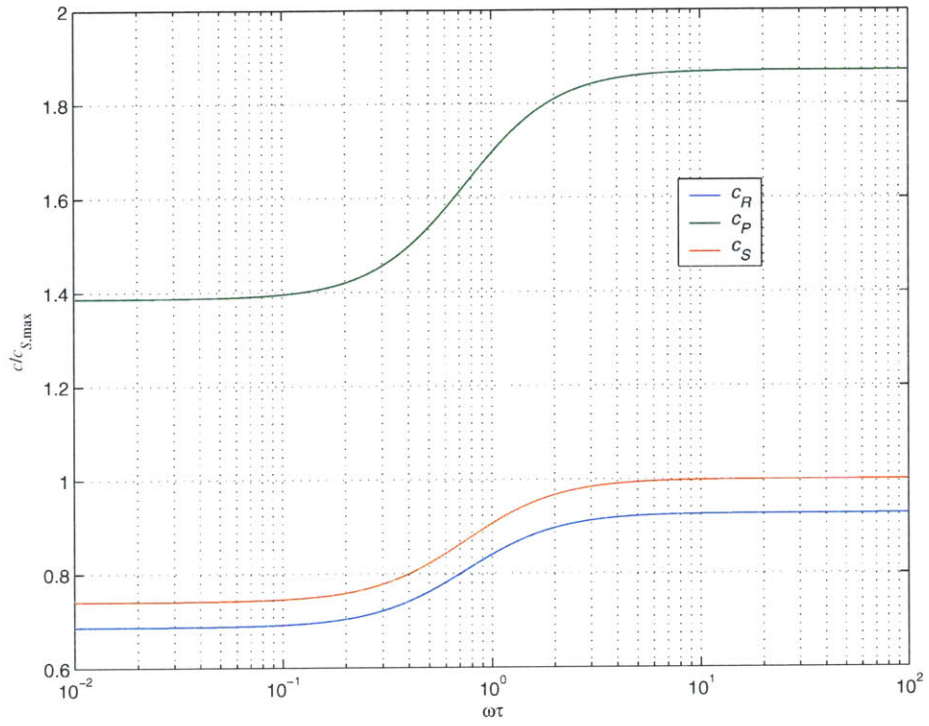


Fig. 3E-5—Frequency dependence of Rayleigh (R), P , and S phase speeds when $r = 0.55$ and $\nu = 0.30$.

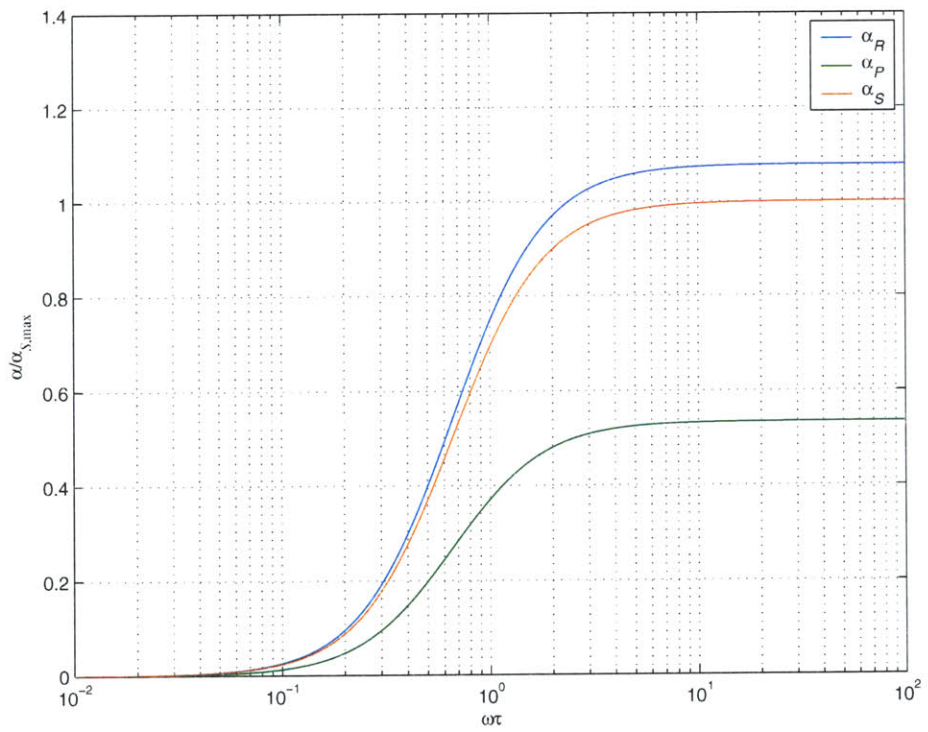


Fig. 3E-6—Frequency dependence of Rayleigh (R), P , and S attenuation when $r = 0.55$ and $\nu = 0.30$.

The particle displacement is expressed as

$$\operatorname{Re}\{u_x\} = \left[\begin{array}{l} \operatorname{Re}\{A_x(y)\} \cos \omega(\operatorname{Re}\{s_x\}x - t) - \\ \operatorname{Im}\{A_x(y)\} \sin \omega(\operatorname{Re}\{s_x\}x - t) \end{array} \right] e^{-\omega \operatorname{Im}\{s_x\}x} \quad (3E-102)$$

$$\operatorname{Re}\{u_y\} = \left[\begin{array}{l} \operatorname{Re}\{A_y(y)\} \cos \omega(\operatorname{Re}\{s_x\}x - t) - \\ \operatorname{Im}\{A_y(y)\} \sin \omega(\operatorname{Re}\{s_x\}x - t) \end{array} \right] e^{-\omega \operatorname{Im}\{s_x\}x} \quad (3E-103)$$

where

$$A_x = e^{i\omega s_{s,y}} + \frac{2}{c-2} e^{i\omega s_{p,y}} \quad (3E-104)$$

$$A_y = -\frac{s_x}{s_{s,y}} \left[e^{i\omega s_{s,y}} + \frac{2}{c-2} e^{i\omega s_{p,y}} \right] \quad (3E-105)$$

The elliptical orbit at a given point is

$$\begin{aligned} & \left(\operatorname{Im}\{A_y\} \operatorname{Re}\{u_x\} + \operatorname{Im}\{A_x\} \operatorname{Re}\{u_y\} \right)^2 \\ & + \left(\operatorname{Re}\{A_y\} \operatorname{Re}\{u_x\} - \operatorname{Re}\{A_x\} \operatorname{Re}\{u_y\} \right)^2 \\ & = \left(\operatorname{Re}\{A_x\} \operatorname{Im}\{A_y\} - \operatorname{Re}\{A_y\} \operatorname{Im}\{A_x\} \right)^2 e^{-2\omega \operatorname{Im}\{s_x\}x} \end{aligned} \quad (3E-106)$$

References:

- 3E-1. R.M. Christensen. *Theory of Viscoelasticity: An Introduction* 2nd ed., pp. 14,15,37,38. Academic Press, New York (1982).
 3E-2. F.J. Lockett. *J. Mech. Phys. Solids*. **10**:53 (1962).
 3E-3. H.F. Cooper, Jr., and E- L. Reiss. *J. Acoust. Soc. Am.* **39**:1133 (1966).
 3E-4. P.K. Currie, M. A. Haynes and P. M. O'Leary. *Q. Appl. Math.* **35**:35 (1977).

APPENDIX 3F—Absorbing Boundaries for Mass-Spring-Dashpot Lattice Model.

In this appendix, absorbing boundaries are formulated and validated by numerical examples.

One-dimensional

The equations governing P wave propagation in a one-dimensional standard linear solid are [3F-1]:

$$\frac{\partial f}{\partial t} = -\frac{f}{\tau} + \frac{r\Pi}{\tau} \frac{\partial^2 u}{\partial x^2} + \Pi \frac{\partial^2 \dot{u}}{\partial x^2} \quad (3F-1)$$

$$\frac{\partial u}{\partial t} = \dot{u} \quad (3F-2)$$

$$\frac{\partial \dot{u}}{\partial t} = \frac{1}{\rho} (f + f_b) \quad (3F-3)$$

where f is a force per unit volume, τ is the relaxation time, r is the dispersion coefficient, Π is an elastic constant, u is the displacement, \dot{u} is the velocity, ρ is the density and f_b is the volumetric body force.

Consider harmonic waves of the form

$$u = e^{-\alpha x} e^{i(kx - \omega t)} \quad (3F-4)$$

where α is the attenuation (Np/unit length), \hat{i} is $\sqrt{-1}$, k is the wavenumber (rad/unit length) and ω is the circular frequency (rad/unit time). Eliminating f and \dot{u} from eqns. (3F-1) through (3F-3) and substituting in (3F-4), and considering the high frequency limit ($\omega\tau \ll 1$) yields the following dispersion relation:

$$\alpha = \frac{1-r}{2\tau_{\max}} \quad (3F-5)$$

$$k = \frac{\omega}{c_{\max}} \quad (3F-6)$$

where

$$c_{\max} = \sqrt{\frac{\Pi}{\rho}} \quad (3F-7)$$

To reduce spurious numerical reflections caused by the truncation of the computational domain, an absorbing layer is proposed. This absorbing layer gradually increases the attenuation coefficient to a predetermined maximum magnitude. In view of eqn. (3F-7), one approach to increase attenuation is to make r and τ monotonically decreasing functions of x in such an absorbing layer.

Consider steady-state wave propagation in a standard linear solid half-space ($x > 0$) having peak magnitude u_0 at $x = 0$ and center frequency ω . It is desired to simulate the physical response in the domain $0 \leq kx \leq 50$, where k is the wavenumber corresponding to ω , and absorb out-going waves beyond the physical domain. Thus equation eqn. (3F-1) is rewritten as

$$\frac{\partial f}{\partial t} = -\frac{f}{\tau(x)} + \frac{r(x)\Pi}{\tau(x)} \frac{\partial^2 u}{\partial x^2} + \Pi \frac{\partial^2 \dot{u}}{\partial x^2} \quad (3F-8)$$

where

$$r(x) = \begin{cases} r, & 0 \leq kx \leq 50 \\ r \exp\left(\ln(r_{\min}/r) \frac{x-50/k}{L}\right), & 50 < kx \leq 50 + kL \end{cases} \quad (3F-9)$$

$$\tau(x) = \begin{cases} \tau, & 0 \leq kx \leq 50 \\ \tau \exp\left(\ln(\tau_{\min}/\tau) \frac{x-50/k}{L}\right), & 50 < kx \leq 50 + kL \end{cases} \quad (3F-10)$$

where r_{\min} and τ_{\min} are the minimum values of r and τ , respectively, and L is the length of the absorbing layer.

Equations (3F-8), (3F-2) and (3F-3) are discretized via the mass spring dashpot lattice model (MSDLM) as

$$\frac{df_i}{dt} = -\frac{1}{\tau_i} f_i + \frac{r_i \Pi}{h^2 \tau_i} (u_{i+1} - 2u_i + u_{i-1}) + \frac{\Pi}{h^2} (\dot{u}_{i+1} - 2\dot{u}_i + \dot{u}_{i-1}) \quad (3F-11)$$

$$\frac{du_i}{dt} = \dot{u}_i \quad (3F-12)$$

$$\frac{d\dot{u}_i}{dt} = \frac{1}{\rho} (f_i + f_{bi}) \quad (3F-13)$$

where h is the grid space and the subscript i is an integer that denotes the value of the preceding variable at $x = (i-1)h$.

Equations (3F-10), (3F-11) and (3F-12) are numerically integrated by the fourth order Runge-Kutta method [3F-2] having stability conditions:

$$\frac{\Delta t}{\tau} \leq 2.78^{**} \quad (3F-14)$$

$$\frac{c_{\max} \Delta t}{h} \leq 1.30 \quad (3F-15)$$

where Δt is the numerical integration time step. In view of eqn. (3F-14), the lower limit for τ_{\min} is

$$\tau_{\min} \geq \frac{\Delta t}{2.78} \quad (3F-15)$$

** 2.78 is an approximation for the exact limit, which is given by

$$-\frac{4}{3} - \frac{10}{3} \frac{\sqrt[3]{2}}{\sqrt[3]{9\sqrt{29}-43}} + \frac{1}{3} \sqrt[3]{4(9\sqrt{29}-43)}.$$

The theoretical lower limit for r_{\min} is zero, but to provide bounds on the exponential function used in eqn. (3F-9), the following is adopted

$$r_{\min} = 0.01r \quad (3F-16)$$

To further reduce any numerical reflection at the boundary of the absorbing layer, an acoustic boundary condition according to [3F-3] is applied at $kx = 100 + kL$.

An MSDLM simulation of a physical domain and an absorbing region in response to a harmonic prescribed displacement at $x = 0$ (u_0 magnitude, ω magnitude) is shown in Fig. 3F-1.

Two-Dimensional

The two-dimensional stress-dynamic equations for a plain-strain standard linear solid, having a single dispersion constant r and single relaxation time τ , and incorporating absorbing boundary conditions are

$$\begin{aligned} \frac{\partial f_x}{\partial t} = & -\frac{1}{\tau(x,y)} f_x + \frac{r(x,y)\Pi}{\tau(x,y)} \frac{\partial^2 u}{\partial x^2} + \frac{r(x,y)(\Pi - M)}{\tau(x,y)} \frac{\partial^2 v}{\partial x \partial y} + \frac{r(x,y)M}{\tau(x,y)} \frac{\partial^2 u}{\partial y^2} \\ & + \Pi \frac{\partial^2 \dot{u}}{\partial x^2} + (\Pi - M) \frac{\partial^2 \dot{v}}{\partial x \partial y} + M \frac{\partial^2 \dot{u}}{\partial y^2} \end{aligned} \quad (3F-16)$$

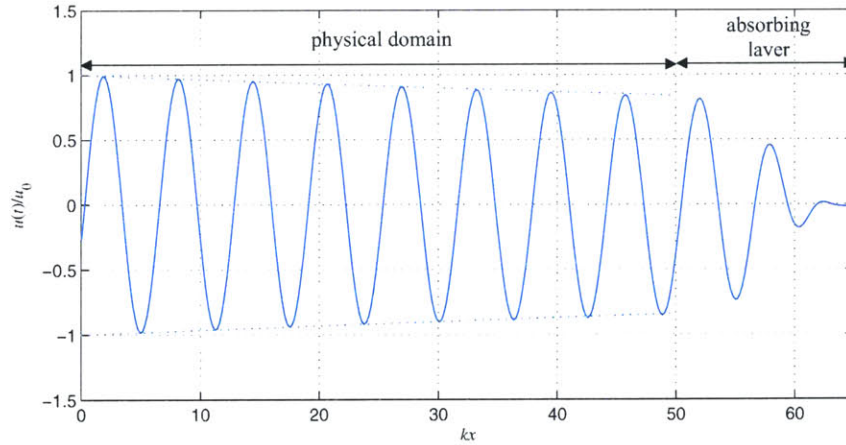


Fig. 3F-1—MSDLM simulation of steady-state one-dimensional standard linear solid showing exact analytical envelope in physical domain and rapid decay in absorbing layer. Here u_0 is displacement magnitude at $x = 0$, k is the wavenumber, $r = 0.652$, $\omega\tau = 50$, $kL = 15$, $\frac{c_{\max}\Delta t}{h} = 1.30$, and

$$\frac{\Delta t}{\tau} = 5.1 \times 10^{-3}.$$

$$\begin{aligned} \frac{\partial f_y}{\partial t} = & -\frac{1}{\tau(x,y)} f_y + \frac{r(x,y)\Pi}{\tau(x,y)} \frac{\partial^2 v}{\partial y^2} + \frac{r(x,y)(\Pi - M)}{\tau(x,y)} \frac{\partial^2 u}{\partial x \partial y} + \frac{r(x,y)M}{\tau(x,y)} \frac{\partial^2 v}{\partial x^2} \\ & + \Pi \frac{\partial^2 \dot{v}}{\partial y^2} + (\Pi - M) \frac{\partial^2 \dot{u}}{\partial x \partial y} + M \frac{\partial^2 \dot{v}}{\partial x^2} \end{aligned} \quad (3F-17)$$

$$\frac{\partial u}{\partial t} = \dot{u} \quad (3F-18)$$

$$\frac{\partial v}{\partial t} = \dot{v} \quad (3F-19)$$

$$\frac{\partial \dot{u}}{\partial t} = \frac{1}{\rho} (f_x + f_{bx}) \quad (3F-20)$$

$$\frac{\partial \dot{v}}{\partial t} = \frac{1}{\rho} (f_y + f_{by}) \quad (3F-21)$$

Equations (3F-16) through (3F-21) are discretized via the MSDLM as

$$\begin{aligned} \frac{df_{i,j}^x}{dt} = & -\frac{1}{\tau_{i,j}} f_{i,j}^x + \frac{r_{i,j}(\Pi - M)}{\tau_{i,j}h^2} (u_{i+1,j} - 2u_{i,j} + u_{i-1,j}) \\ & + \frac{r_{i,j}M}{2\tau_{i,j}h^2} (u_{i+1,j+1} + u_{i-1,j-1} + u_{i+1,j-1} + u_{i-1,j+1} - 4u_{i,j}) \\ & + \frac{r_{i,j}(\Pi - M)}{4\tau_{i,j}h^2} (v_{i+1,j+1} + v_{i-1,j-1} - v_{i+1,j-1} - v_{i-1,j+1}) \\ & + \frac{\Pi - M}{h^2} (\dot{u}_{i+1,j} - 2\dot{u}_{i,j} + \dot{u}_{i-1,j}) \\ & + \frac{M}{2h^2} (\dot{u}_{i+1,j+1} + \dot{u}_{i-1,j-1} + \dot{u}_{i+1,j-1} + \dot{u}_{i-1,j+1} - 4\dot{u}_{i,j}) \\ & + \frac{\Pi - M}{4h^2} (\dot{v}_{i+1,j+1} + \dot{v}_{i-1,j-1} - \dot{v}_{i+1,j-1} - \dot{v}_{i-1,j+1}) \end{aligned} \quad (3F-22)$$

$$\begin{aligned}
 \frac{df_{i,j}^y}{dt} = & -\frac{1}{\tau_{i,j}} f_{i,j}^y + \frac{r_{i,j}(\Pi - M)}{\tau_{i,j}h^2} (v_{i,j+1} - 2v_{i,j} + v_{i,j-1}) \\
 & + \frac{r_{i,j}M}{2\tau_{i,j}h^2} (v_{i+1,j+1} + v_{i-1,j-1} + v_{i+1,j-1} + v_{i-1,j+1} - 4v_{i,j}) \\
 & + \frac{r_{i,j}(\Pi - M)}{4\tau_{i,j}h^2} (u_{i+1,j+1} + u_{i-1,j-1} - u_{i+1,j-1} - u_{i-1,j+1}) \\
 & + \frac{\Pi - M}{h^2} (\dot{v}_{i,j+1} - 2\dot{v}_{i,j} + \dot{v}_{i,j-1}) \\
 & + \frac{M}{2h^2} (\dot{v}_{i+1,j+1} + \dot{v}_{i-1,j-1} + \dot{v}_{i+1,j-1} + \dot{v}_{i-1,j+1} - 4\dot{v}_{i,j}) \\
 & + \frac{(\Pi - M)}{4h^2} (\dot{u}_{i+1,j+1} + \dot{u}_{i-1,j-1} - \dot{u}_{i+1,j-1} - \dot{u}_{i-1,j+1})
 \end{aligned} \tag{3F-23}$$

$$\frac{du_{i,j}}{dt} = \dot{u}_{i,j} \tag{3F-24}$$

$$\frac{dv_{i,j}}{dt} = \dot{v}_{i,j} \tag{3F-25}$$

$$\frac{d\dot{u}_{i,j}}{dt} = \frac{1}{\rho} (f_{i,j}^{bx} + f_{i,j}^x) \tag{3F-26}$$

$$\frac{d\dot{v}_{i,j}}{dt} = \frac{1}{\rho} (f_{i,j}^{by} + f_{i,j}^y) \tag{3F-27}$$

where the subscripts i and j are integers that denotes the value of the corresponding variable at position $x = (i-1)h + c_1$ and $y = (j-1)h + c_2$ (here c_1 and c_2 are constants based on the relative position of the origin with respect to the grid).

Consider the physical domain $-20 \leq kx \leq 20$, $-20 \leq ky \leq 20$ surrounded by an absorbing layer of thickness L . Extending eqns. (9) and (10) to the two-dimensional case yields

$$r(x, y) = \begin{cases} r, & -20 \leq kx \leq 20 \\ & -20 \leq ky \leq 20 \\ r \times \min \left\{ \begin{aligned} & \exp \left(\ln(r_{\min} / r) \frac{|x - 20/k|}{L} \right) \\ & \exp \left(\ln(r_{\min} / r) \frac{|y - 20/k|}{L} \right) \end{aligned} \right\}, & \begin{aligned} & -20 - kL \leq kx \leq 20 + kL \\ & -20 - kL \leq ky \leq 20 + kL \end{aligned} \end{cases} \tag{3F-22}$$

$$\tau(x, y) = \begin{cases} \tau, & -20 \leq kx \leq 20 \\ & -20 \leq ky \leq 20 \\ \tau \times \min \left\{ \begin{aligned} & \exp \left(\ln(\tau_{\min} / \tau) \frac{|x - 20/k|}{L} \right) \\ & \exp \left(\ln(\tau_{\min} / \tau) \frac{|y - 20/k|}{L} \right) \end{aligned} \right\}, & \begin{aligned} -20 - kL \leq kx \leq 20 + kL \\ -20 - kL \leq ky \leq 20 + kL \end{aligned} \end{cases} \quad (3F-23)$$

To further reduce any numerical reflection at the boundary of the absorbing layer, at $kx = \pm 20 \pm kL$ and $ky = \pm 20 \pm kL$, there is a two-dimensional acoustic absorbing boundary condition [3F-3] at the edge of the absorbing layer.

Fig. 3F-2 shows the steady-state response due to a sinusoidal time-varying circular normal stress σ_{rr} at the origin.

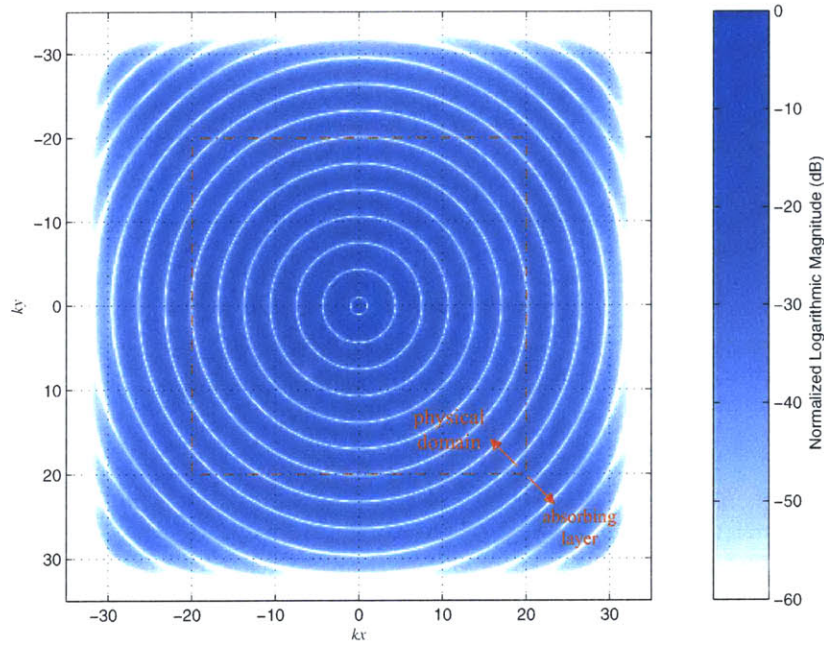


Fig. 3F-2—MSDLM simulation of steady-state wave propagation due to sinusoidal time-varying circular normal stress at origin in two-dimensional plane strain standard linear surrounded by absorbing boundary of thickness L . Here k is wavenumber of P waves, $r = 0.652$, $\nu = 0.377$, $\omega\tau = 50$, $kL = 15$, $\frac{c_{\max} \Delta t}{h} = 1.30$, and $\frac{\Delta t}{\tau} = 5.1 \times 10^{-3}$.

References:

- 3F-1. R.M. Christensen. *Theory of Viscoelasticity: An Introduction* 2nd ed., pp. 14,15,37,38. Academic Press, New York (1982).
- 3F-2. M. Abramowitz and I.A. Stegun (Eds.), *Handbook of Mathematical Functions with Formulas, Graphs and Mathematical Tables*, pp. 896-897. Dover, New York (1965).
- 3F-3. A.C. Reynolds. *Geophysics* **43**:1099 (1978).

CHAPTER 4: ULTRASONIC NONDESTRUCTIVE EVALUATION OF SUBSURFACE CRACKS IN AN ATTENUATING NANOCOMPOSITE

ABSTRACT: Theoretical predictions of specific strength and specific stiffness of nanocomposites make them attractive replacements for alloys and modern fiber reinforced composites in future generations of numerous structures. The reliable and safe utilization of these nanocomposites will require their periodic characterization with nondestructive evaluation.

Analytical mass-spring-dashpot lattice models (MSDLM) for the ultrasonic nondestructive evaluation of an attenuating nanocomposite containing subsurface cracks are developed. The homogenization of the elastic and viscoelastic mechanical properties of the nanocomposite constituents is implied in the use of the MSDLM. Furthermore, numerical accuracy requirements restrict minimum anomaly dimensions to one-twentieth of the characteristic wavelength.

Full-field wave propagation simulations of these models as well as the corresponding model of a pristine nanocomposite are conducted, and their relative surface displacements are presented. The initial temporal and spatial disturbances of these relative surface displacements along with root-mean-square averages of the vertical relative surface displacement reveal guidelines for the characterization of subsurface cracks in nanocomposites and other attenuating materials.

CONTENTS:

4-1	Introduction.....	157
4-2	Analytical Model.....	159
4-3	Numerical Discretization.....	162
	4-3.1 Mass-Spring-Dashpot Lattice Model.....	162
	4-3.2 Verification.....	163
4-4	Normalized Parameters.....	166
4-5	Material and Interrogation Parameters.....	167
4-6	Displacement Field.....	169
4-7	Required Detection Resolution.....	169
4-8	Initial Relative Surface Disturbance.....	172
4-9	Transient Relative Surface Disturbance.....	176
4-10	Conclusions.....	178
4A	MSDLM Discretizations at Various Boundary and Interaction Conditions.....	180
4B	Asymptotic and Numerical Analysis of Scattering and Diffraction of an Incident Longitudinal Wave by a Semi-Infinite Crack.....	190
4C	Spectral Analysis of Transient Relative Vertical Surface Displacement.....	200

NOMENCLATURE

Symbols

b	extensional dashpot coefficient	x''	horizontal coordinate of crack tip of horizontal semi-infinite crack
c	phase speed	z'	vertical coordinate of crack tip of vertical semi-infinite crack
e	base of natural logarithm	z''	vertical coordinate of crack tip of horizontal semi-infinite crack
F	externally applied force per unit depth		
f^x, f^z	horizontal and vertical force per unit volume	α	attenuation (Np/unit length)
f	frequency	Δt	numerical time step
g	extensional spring constant	$\hat{\delta}(x)$	Dirac delta function
h	numerical grid spacing	δ	normalized surface displacement resolution
i, j	indicial notation for grid position	ε	absolute surface displacement detection resolution
k	wavenumber	γ	rotational dashpot coefficient
M	instantaneous modulus governing shear waves	η	rotational spring constant
P	relating to longitudinal waves	κ	ratio of longitudinal phase speed to shear phase speed
\bar{r}	dispersion ratio	λ	wavelength
S	relating to shear waves	ν	Poisson's ratio
T	period corresponding to center frequency	Π	instantaneous modulus governing longitudinal waves
t^*	initial relative surface displacement time	π	ratio of circle's circumference to diameter
u, w	horizontal and vertical displacement	ρ	density
x^*	initial relative surface displacement coordinate	σ	stress
x'	horizontal coordinate of crack tip of vertical semi-infinite crack	τ	relaxation time

Subscripts

<i>center</i>	relating to center
<i>max, peak</i>	relating to greatest magnitude
<i>min</i>	relating to least magnitude
<i>P</i>	relating to longitudinal waves
<i>R</i>	relating to Rayleigh waves
<i>relative</i>	relative to pristine nanocomposite
<i>RMS</i>	relating to root-mean-square
<i>S</i>	relating to shear waves
<i>std.dev.</i>	relating to standard deviation

4-1 INTRODUCTION

Modern composites consist of a matrix (generally polymer, metal, or ceramic) and reinforcement (generally fibers, platelets, or particles) that are combined to produce materials having mechanical properties tailored for specific applications. Substandard fabrication procedures, environmental exposure, and handling or service deterioration can affect their mechanical properties without effect on their visual appearance.

Because composite components are subjected to increasingly demanding structural requirements, their periodic characterization by various nondestructive evaluation (NDE) techniques is an important aspect of ensuring their reliable performance. In NDE, rather than absolute outputs of interrogated structures and materials (e.g., surface displacements, temperatures), it is often more desirable to obtain outputs relative to known pristine structures and materials (e.g., relative displacements or temperature rise) as shown schematically in Fig. 4-1. In ultrasonic NDE, prescribed time-dependent waves are propagated through the interrogated structure. Due to reflections, scattering, and absorption of these waves, perturbations in output surface tractions and/or displacements can be detected, and ideally related to deterioration or inherent characteristics of the component.

Various theoretical and experimental modeling of ultrasonic NDE in engineering materials have been undertaken in the last few decades. For example, Williams *et. al* used theoretical and experimental ultrasonic NDE models for damage characterization in various materials and structures, especially those utilizing composites [4-1 through 4-7]; Achenbach *et. al* investigated the theoretical scattering of time harmonic surface and body waves due to the presence of subsurface cracks in an elastic half-space [4-8 through 4-12]; one-dimensional ultrasonic NDE theoretical models of layered composites have been investigated [4-12, 4-13, 4-14]; and in the last few years, laser ultrasonics has enabled full-field detection of composite surface displacements caused by subsurface anomalies [4-15, 4-16].

Compared with most modern composites, nanocomposites are in their developmental infancy. Nanocomposites, a classification that includes matrixes reinforced by nanoparticles of dimensions less than 100 nm, often exhibit exemplary

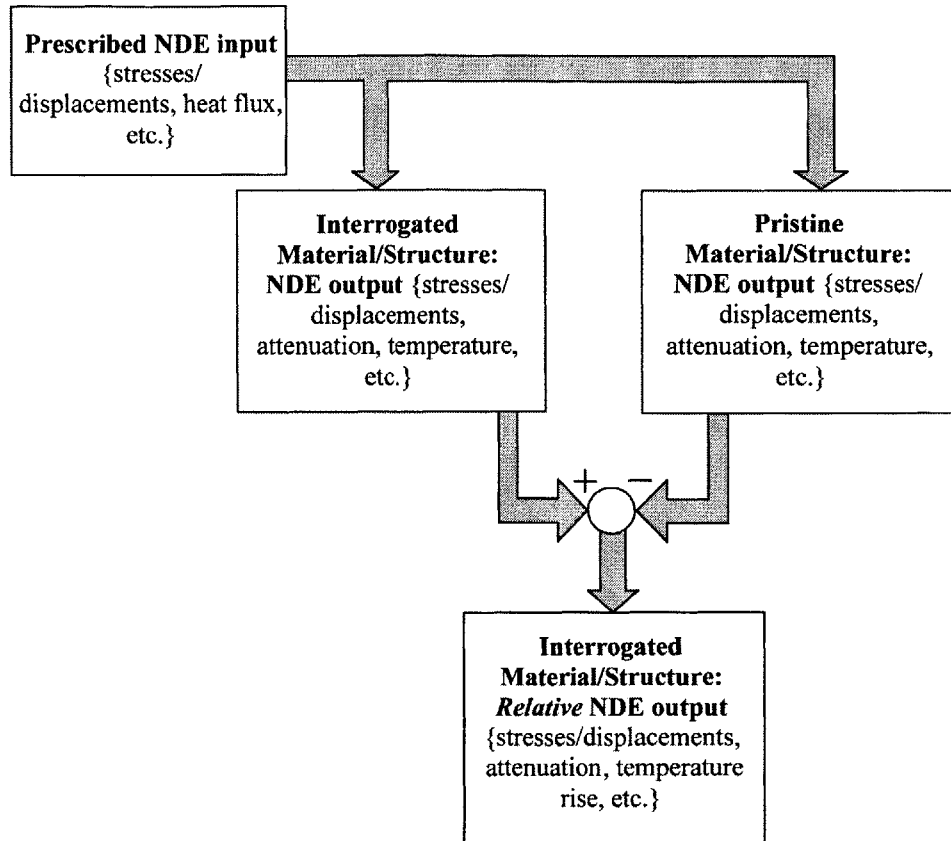


Fig. 4-1—Schematic of relative nondestructive evaluation (NDE) output for interrogated material or structure, with respect to corresponding pristine material or structure.

structural properties. For example, a 5% concentration by weight of nanoparticulate clay embedded in an epoxy matrix typically produces a 20 – 50% increase in strength and stiffness over the pristine matrix [4-17]; single-walled carbon nanotubes (CNTs) have an elastic modulus and yield strength on the order of 10^3 GPa and 50 GPa, respectively [4-18, 4-19]; and future CNT reinforced polymers are projected to have a tensile strength of 2.5 GPa, an elastic modulus of 240 GPa, and a density of 10^3 kg/m³ [4-20].

The application of nanocomposites in structures is very promising. A case study by NASA engineers [4-20] projected an 85% reduction in the weight of a reusable launch vehicle if a CNT reinforced polymer were substituted for the current composites and alloys. A similar case study involving a range of wide-bodied current commercial aircraft predicted a 14% average reduction in structural mass and a 10% average decrease in fuel consumption [4-23].

Nanocomposites often have specific areas—the total surface area of the matrix and

reinforcement phase per unit volume—that are orders of magnitude higher than comparable macrocomposites [4-21]. Furthermore, poor load transfer between the matrix and reinforcement in such nanomaterials as CNT composites produce strengths and stiffnesses far short of theoretical projections. The high specific area, poor load transfer efficiency, and lack of proper reinforcement dispersion in the matrix, combine to produce materials that exhibit significant viscoelastic behavior. For example, Suhr *et. al* [4-22] have shown that the loss modulus is fifteen times higher in a CNT composite at frequencies on the order of 10Hz compared to that in the neat matrix; and Zhou *et. al* [4-21] have modeled and measured the “stick-slip” behavior of CNTs in a polymeric matrix.

When subjected to ultrasonic waves, nanocomposites often have attenuation coefficients that are an *order of magnitude* higher than those of modern carbon fiber reinforced composites. Nanocrystalline metals exhibit attenuation that is five to ten times higher than in the same coarse-grained metals for ultrasonic frequencies up to 20 MHz [4-25]. Attenuation in zirconium-based bulk metallic glass composite increases 5 to 9 times with a 4% volume fraction of CNTs over the undoped glass [4-25]. These results strongly indicate that an accurate model of ultrasonic wave propagation in nanocomposites must include attenuation.

The remainder of the chapter is divided into five main sections: (1) an analytical model for ultrasonic NDE of an attenuating half-space containing subsurface cracks is introduced; (2) numerical discretization of the analytical model and the verification of numerical solutions are described; (3) normalized parameters are formed; (4) specific nanocomposite and ultrasonic investigation parameters are presented; and (5) the parametric investigation of the full-field surface response is summarized.

4-2 ANALYTICAL MODEL

Consider a viscoelastic solid half-space ($z < 0$) containing subsurface semi-infinite cracks. At time $t = 0$, the half-space is subject to a time-varying vertical force per unit depth $F(x,t)$ concentrated at the origin as shown in Fig. 4-2a. The Gaussian-modulated

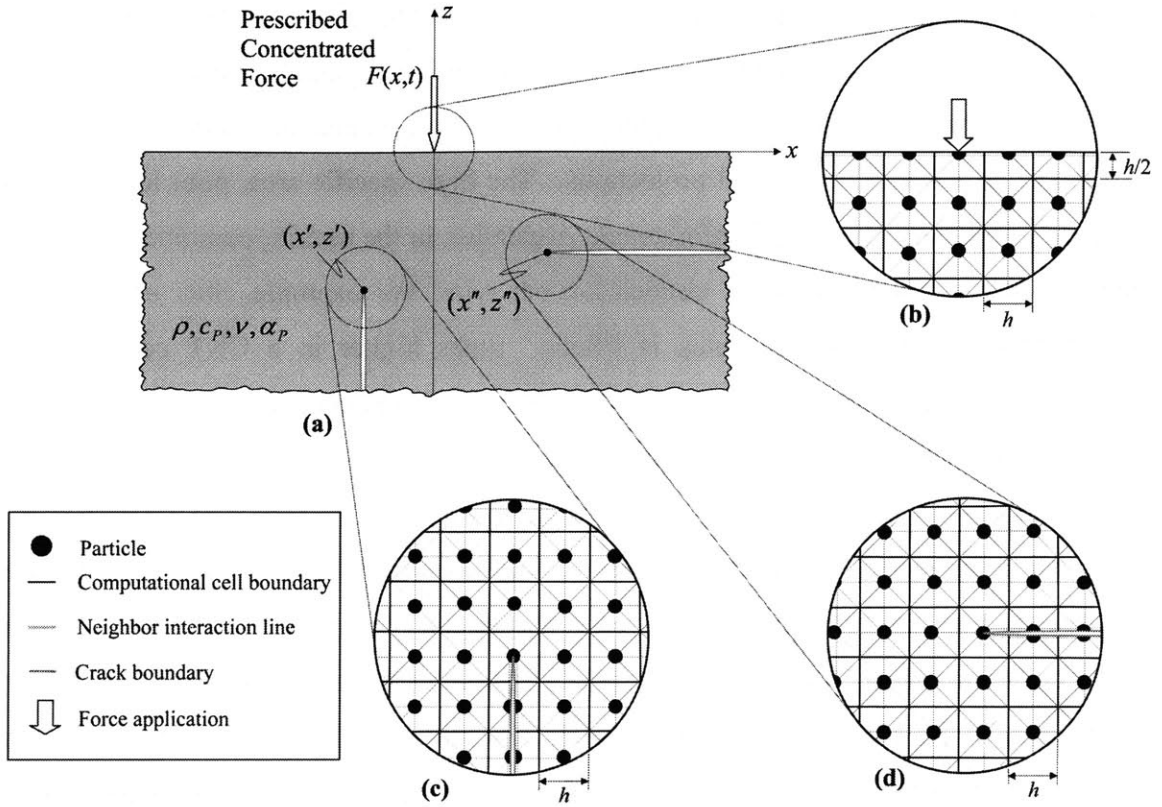


Fig. 4-2—(a) Schematic of half-space containing vertical and horizontal semi-infinite cracks subject to vertical concentrated force $F(x,t)$, where ρ is mass density, c_p is P -wave phase velocity, ν is Poisson's ratio, and α_p is P -wave attenuation. Insets show lattice discretization in vicinity of (b) free surface, (c) vertical crack tip (*Case One*) and (d) horizontal crack tip (*Case Two*), where h is grid space.

cosinusoidal forcing function $F(x,t)$, chosen primarily due to its smoothness and well-defined bandwidth, is given by

$$F(x,t) = F_{peak} \hat{\delta}(x) \exp\left[-\frac{1}{2}(2\pi f_{std.dev.} t - 3)^2\right] \cos(2\pi f_{center} t - 3f_{center} f_{std.dev.}^{-1}) \quad (4-1)$$

where F_{peak} is the peak magnitude of the line force, $\hat{\delta}(x)$ is the Dirac delta function, $f_{std.dev.}$ is the standard deviation frequency, and f_{center} is the center frequency ($f_{center} > 0$).

The function $F(x,t)$ inputs $\frac{3f_{center}}{\pi f_{std.dev.}}$ periods having an envelope greater than

$F_{peak} \exp(-\frac{9}{2})$ and thereafter rapidly decays to a traction-free boundary condition.

The viscoelastic solid is a single relaxation time standard linear solid half-space having a density ρ , frequency independent P -wave phase speed c_p , frequency independent P -wave attenuation α_p , and Poisson's ratio ν . The plane strain stress-

dynamic equations are [4-26]

$$f_{,t}^x = -\tau^{-1} f^x + \tau^{-1} \bar{r} \Pi u_{,xx} + \tau^{-1} \bar{r} (\Pi - M) w_{,xz} + \tau^{-1} \bar{r} M u_{,zz} + \Pi u_{,xxt} + (\Pi - M) w_{,xzt} + M u_{,zzt} \quad (4-2)$$

$$f_{,t}^z = -\tau^{-1} f^z + \tau^{-1} \bar{r} \Pi w_{,zz} + \tau^{-1} \bar{r} (\Pi - M) u_{,xz} + \tau^{-1} \bar{r} M w_{,xx} + \Pi w_{,zzt} + (\Pi - M) u_{,zzt} + M w_{,xxt} \quad (4-3)$$

$$u_{,tt} = \rho^{-1} (f^x + f^{bx}) \quad (4-4)$$

and

$$w_{,tt} = \rho^{-1} (f^z + f^{bz}) \quad (4-5)$$

provided the initial conditions

$$f^x(0) = \Pi u_{,xx}(0) + (\Pi - M) w_{,xz}(0) + M u_{,zz}(0) \quad (4-6)$$

$$f^z(0) = \Pi w_{,zz}(0) + (\Pi - M) u_{,xz}(0) + M w_{,xx}(0) \quad (4-7)$$

are satisfied. Here f^x and f^z are the respective horizontal and vertical forces per unit volume, f^{bx} and f^{bz} are the respective horizontal and vertical body forces per unit volume, τ is the stress relaxation time, u and w are the respective horizontal and vertical components of displacement, \bar{r} is the dispersion coefficient given by

$$\bar{r} = 1 - 2\tau\alpha_p c_p, \quad (4-8)$$

Π is the instantaneous elastic constant given by

$$\Pi = \rho c_p^2 \quad (4-9)$$

and M is the instantaneous shear modulus given by

$$M = \frac{\rho c_p^2}{\kappa^2} \quad (4-10)$$

where κ is given by

$$\kappa = \sqrt{\frac{2-2\nu}{1-2\nu}} \quad (4-11)$$

Additionally, the S -wave speed c_s and S -wave attenuation α_s are given by

$$c_s = \frac{c_p}{\kappa} \quad (4-12)$$

$$\alpha_s = \alpha_p \kappa \quad (4-13)$$

Analytical dispersion relations for this solid are derived and discussed in [4-26].

The boundary conditions at the free surface and along the traction-free cracks are:
 along the free surface $z = 0$

$$\sigma_{xz}(x,0) = 0, \sigma_{zz}(x,0) = F(x,t), \quad -\infty < x < \infty; \quad (4-14)$$

along the vertical crack terminating at position (x', z')

$$\sigma_{xx}(x'^-, z) = \sigma_{xx}(x'^+, z) = \sigma_{xz}(x'^-, z) = \sigma_{xz}(x'^+, z) = 0, \quad z' > z > -\infty; \quad (4-15)$$

and along the horizontal crack terminating at position (x'', z'')

$$\sigma_{zz}(x, z''^-) = \sigma_{zz}(x, z''^+) = \sigma_{xz}(x, z''^-) = \sigma_{xz}(x, z''^+) = 0, \quad x'' < x < \infty. \quad (4-16)$$

4-3 NUMERICAL DISCRETIZATION

4-3.1 Mass-Spring-Dashpot Lattice Model

The half-space described in the previous section is numerically discretized and simulated via the mass-spring-dashpot lattice model (MSDLM) [4-26], an extension of the mass-spring lattice model [4-27,4-28]. In the MSDLM, as shown in Fig. 4-3, the viscoelastic continuum is heuristically discretized into point masses interacting with closest neighbors via extensional and rotational standard linear elements—a spring in

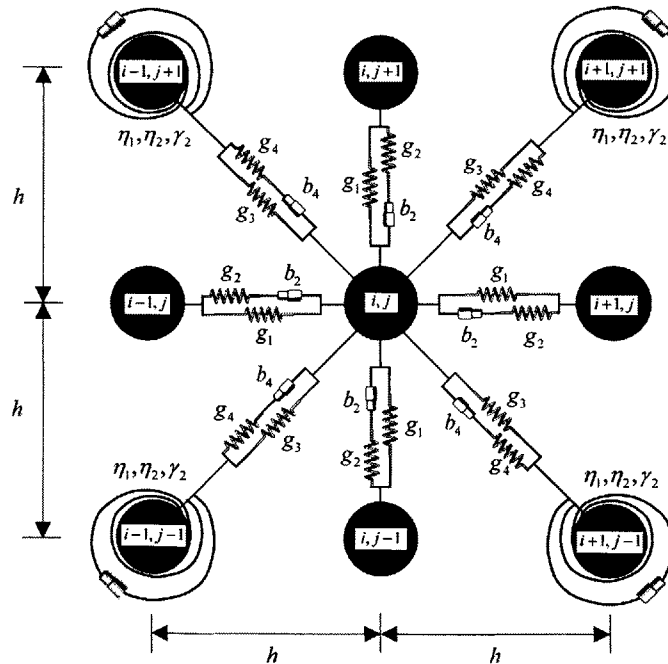


Fig. 4-3—Schematic of MSDLM discretization at interior particle located at position (i, j) . [4-26]

parallel to a spring and dashpot in series. (The various spring and dashpot coefficients are stated explicitly in [4-26].) The two-dimensional lattice discretization in the vicinity of a free surface, horizontal crack tip and vertical crack tip is shown in Figs. 4-2b through 4-2d. In addition to a summary of numerical convergence criteria relating the grid space h and the time step Δt , the discretized MSDLM stress-dynamic equations for particles in the vicinity of various interaction conditions are listed in Appendix A.

4-3.2 Verification

The verification of a few two-dimensional examples involving the reflection of plane waves at planar boundaries is given in [4-26]. Here, the focus of the numerical verification is on two specific problems related to the problem statement—surface wave propagation and crack tip diffraction. For all numerical verification problems, the MSDLM dispersion coefficient \bar{v} is set to unity to simulate an elastic material.

First, consider the time-varying vertical force $F(x,t)$ given in eqn. (4-1) acting on a pristine elastic half-space as shown in Fig. 4-2a. The Rayleigh wavelength corresponding to the center frequency is

$$\lambda_R = \frac{c_R}{f_{center}} \quad (4-17)$$

where the Rayleigh wave velocity c_R is calculated according to [4-29]. The maximum frequency content of $F(x,t)$ is defined (arbitrarily) as when the frequency is three standard deviations above the center frequency, $f_{max} = f_{center} + 3f_{std.dev.}$, where the absolute value of the frequency content has dropped to a value $\exp(-\frac{9}{2})$ relative to the content at the center frequency. Therefore, the minimum wavelength propagating along the surface of the pristine half-space is the Rayleigh wavelength corresponding to f_{max} , or

$$\lambda_{min} = \frac{c_R}{f_{max}} = \frac{\lambda_R}{1 + 3f_{std.dev.}f_{center}^{-1}} \quad (4-18)$$

For numerical accuracy, the MSDLM grid space is set as $h = \lambda_{min} / 20$.

The exact transient solution for the surface displacements is solved by Lamb [4-30]. Figure 4-4 shows the exact and MSDLM horizontal and vertical surface

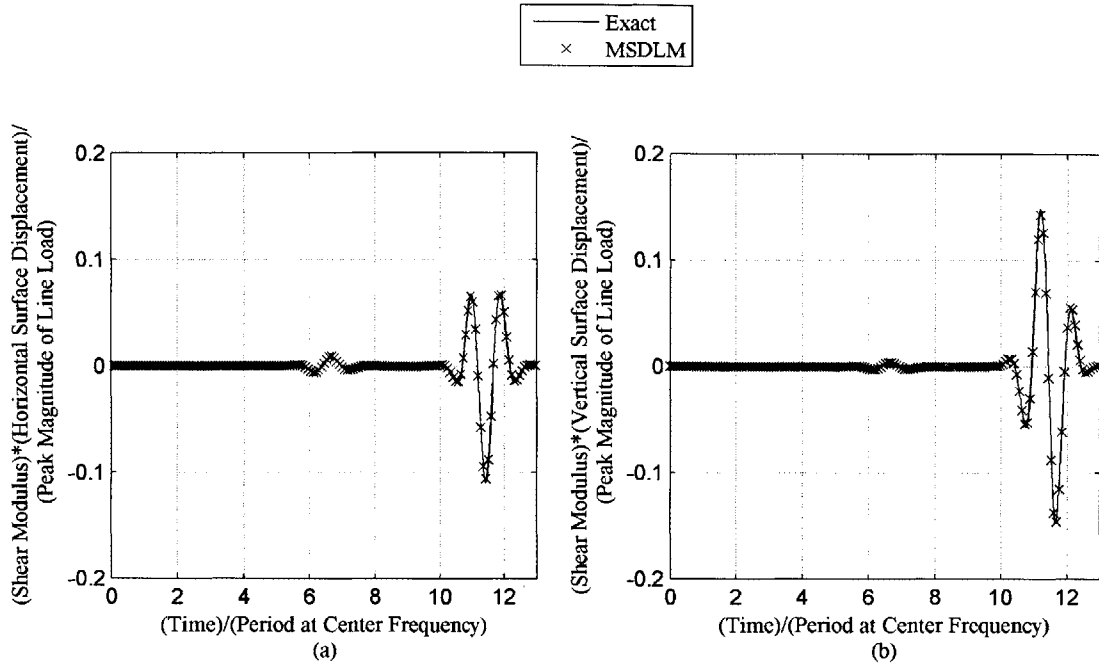


Fig. 4-4—Comparison of exact [4-30] and MSDLM (a) horizontal and (b) vertical surface displacements due to Gaussian-modulated cosinusoidal vertical force (normalized bandwidth $f_{std.dev.}f_{center}^{-1} = 1/3$) concentrated at origin of elastic solid having Poisson's ratio $\nu = 0.30$. Measurements are taken at ten Rayleigh wavelengths from the origin, corresponding to center frequency f_{center} .

displacements at $x = 10\lambda_R$ for an elastic half-space having a Poisson's ratio $\nu = 0.30$ and when the normalized bandwidth $f_{std.dev.}f_{center}^{-1} = 1/3$. (For increased clarity, the numerical solution is shown only at every fifth time step Δt .) The initial disturbance due to the surface P -wave followed by the Rayleigh wave is clearly seen in the figure. A discrete Fourier transform (DFT) [4-31] of the surface displacements reveals that the MSDLM surface displacements have a 1.5% error in amplitude at the center frequency.

Next, consider an unbounded elastic solid containing a semi-infinite crack that terminates at the origin and lies along the positive x -axis as shown in Fig. 4-5. An incident Gaussian-modulated cosinusoidal plane P -wave propagates at an angle of incidence θ_p with respect to the crack having a center P -wavenumber k_p (center P -wavelength $\lambda_p = 2\pi k_p^{-1}$) and standard deviation P -wavenumber $k_{p, std.dev.}$. The minimum wavelength propagated in the model corresponds to Rayleigh wavelength λ_{min} given by

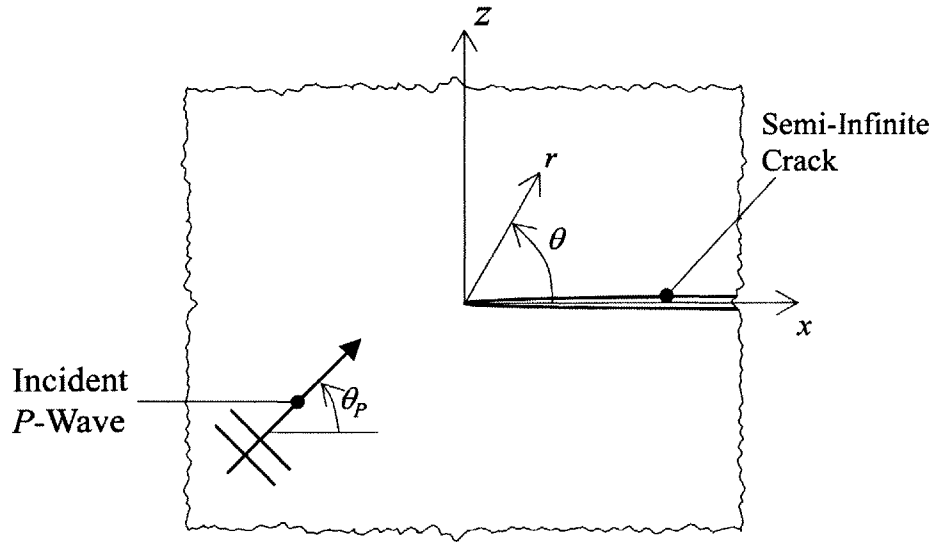


Fig. 4-5—Schematic of incident plane P -wave impinging on vicinity of tip of semi-infinite crack.

$$\lambda_{\min} = \frac{c_R}{c_P} \frac{\lambda_p}{(1 + 3k_{P, \text{std. dev.}} k_P^{-1})} \quad (4-19)$$

For accuracy, the MSDLM grid space is set as $h = \lambda_{\min} / 20$.

The diffracted P and S -wave fields due to an incident harmonic P -plane wave impinging the tip of a semi-infinite crack are given exactly in the form of integral equations [4-32]. An asymptotic analysis of the far field reveals that the diffracted body waves can be thought of as being formed from rays emanating from the crack tip, being inversely proportional to the square root of the distance traveled and directly proportional to the so-called “diffraction coefficients.” The respective diffraction coefficients for P and S -waves, $D_P^P(\theta; \theta_p, \nu)$ and $D_S^P(\theta; \theta_p, \nu)$, are given explicitly in [4-32]. The MSDLM diffraction coefficients are calculated by subtracting the incident and reflected plane waves from the simulated displacement field and performing a DFT on relevant displacements (Appendix 4B).

Figure 4-6 compares the asymptotic and MSDLM diffraction coefficients corresponding to a plane wave having an angle of incidence $\theta_p = 90^\circ$ for a material having $\nu = 0.30$. Here all MSDLM measurements are taken at radii approximately $3\lambda_p$ and $5\lambda_p$. The MSDLM diffraction coefficients are in good qualitative agreement with the

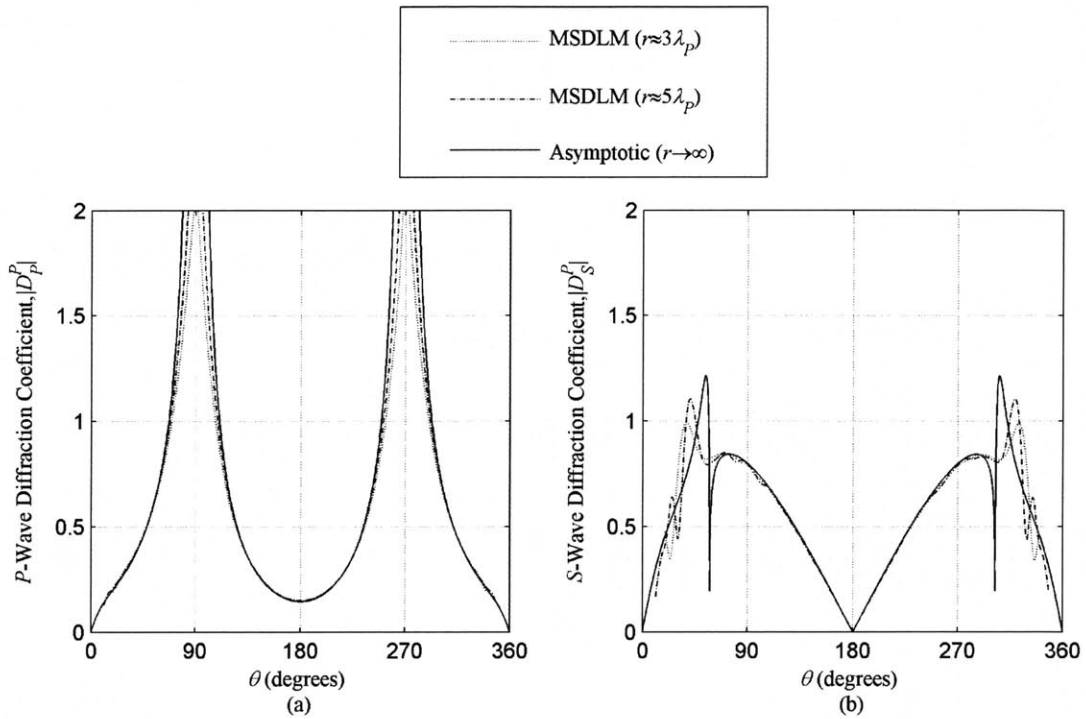


Fig. 4-6—Comparison of asymptotic [4-32] and MSDLM (a) P -wave diffraction coefficient and (b) S -wave diffraction coefficient due to incident P -wave having angle of incidence $\theta_p = 90^\circ$ interacting with semi-infinite crack embedded in elastic solid having Poisson's ratio $\nu = 0.30$. Here normalized bandwidth of spatial disturbance is $k_{p, std. dev.} k_p^{-1} = 1/3$ and MSDLM measurements are taken at radii approximately three and five P -wavelengths λ_p , corresponding to center wavenumber k_p .

asymptotes. In general, as the radius increases the near field effects diminish; that is, the MSDLM diffraction coefficients more closely approximate the asymptotes. The oscillatory amplitude behavior in Fig. 4-6b is due to a secondary shear wave created by the interaction of the P -wave with the traction-free surface of the crack; such a secondary shear wave is commonly referred to as a head wave.

4-4 NORMALIZED PARAMETERS

The relative surface displacements on an attenuating half-space containing a vertical or horizontal semi-infinite crack is written in normalized functional form as

$$\frac{M}{F_{peak}} u_{relative} = fc n_1 \left\{ \frac{x}{\lambda_R}, \frac{t}{T}, \nu, \frac{\pi}{\alpha_p \lambda_p}, \frac{f_{std. dev.}}{f_{center}}, \frac{\hat{x}}{\lambda_R}, \frac{\hat{z}}{\lambda_R} \right\} \quad (4-20)$$

$$\frac{M}{F_{peak}} w_{relative} = fc n_2 \left\{ \frac{x}{\lambda_R}, \frac{t}{T}, \nu, \frac{\pi}{\alpha_p \lambda_p}, \frac{f_{std.dev.}}{f_{center}}, \frac{\hat{x}}{\lambda_R}, \frac{\hat{z}}{\lambda_R} \right\} \quad (4-21)$$

where the normalized parameters are divided into five groups:

- the normalized relative surface displacements: $(M/F_{peak})(u_{relative})$ and $(M/F_{peak})(w_{relative})$, where $u_{relative}$ and $w_{relative}$ are given by

$$u_{relative} = u - u_{pristine} \quad (4-22)$$

$$w_{relative} = w - w_{pristine} \quad (4-23)$$

namely, the difference between the horizontal and vertical surface displacements on the interrogated nanocomposite, u and w , respectively, and the horizontal and vertical surface displacements on an identically loaded pristine nanocomposite, $u_{pristine}$ and $w_{pristine}$;

- the independent coordinates: the normalized surface coordinate x/λ_R and the normalized time t/T , where T is the period corresponding to the center frequency;
- the material properties of the half-space: the Poisson's ratio ν and the normalized penetration depth parameter $\pi/(\alpha_p \lambda_p)$, which is the number of wavelengths at the center frequency required for a wave to attenuate by a factor $\exp(-\pi)$;
- the normalized bandwidth of the surface loading $f_{std.dev.}/f_{center}$;
- and the normalized location of the crack tip: \hat{x}/λ_R and \hat{z}/λ_R , which represents either a vertical or horizontal orientation.

It has been shown [4-14] that numerical errors due to the dispersion in attenuation and phase speed are less than 1% if the following non-dimensional requirement is satisfied:

$$\frac{\pi}{\alpha_p \lambda_p} > 2\pi f_{center} \tau > 5 \quad (4-24)$$

4-5 MATERIAL AND INTERROGATION PARAMETERS

The interrogated material is a hypothetical polymeric composite having a 60% volume fraction of CNTs [4-20], in which the mechanical properties of this future-generation composite are predicted to obey the micromechanical “rule-of-mixtures.”

Henceforth, this material will be denoted “nanocomposite.” The orders of magnitude for P -wave phase velocity and density are $c_p \sim 10^4$ m/s and $\rho \sim 10^3$ kg/m³, respectively, and the estimated Poisson’s ratio and P -wave attenuation are $\nu = 0.30$ and $\alpha_p \sim 10$ Np/m, respectively. Furthermore, the nanocomposite is assumed to be interrogated at a center frequency $f_{center} \sim 10$ MHz and normalized bandwidth $f_{std.dev.}/f_{center} = 1/3$, and having a peak force per unit depth $F_{peak} \sim 100$ N/m. Accordingly, the normalized penetration depth is $\pi\alpha_p^{-1}\lambda_p^{-1} = 100$. Table 4-1 summarizes the order of magnitudes for the various parameters for the ultrasonic interrogation of the nanocomposite.

The nanocomposite is discretized and simulated via a 401×401 MSDLM grid in the region defined by $-5\lambda_R \leq x \leq 5\lambda_R$ and $-10\lambda_R \leq z \leq 0$. The corresponding simulations cover 1242 time steps over the time period $0 \leq t \leq 20T$. Furthermore, absorbing boundaries [4-26] are situated at $x = \pm 5\lambda_R$ and $z = -10\lambda_R$ to simulate the semi-infinite half-space.

In the numerical examples that follow, two cases of subsurface cracks embedded in the nanocomposite halfspace are highlighted. *Case One* is a vertical semi-infinite crack terminating at coordinates $x' = -2.5\lambda_R$ and $z' = -5\lambda_R$. *Case Two* is a horizontal semi-infinite crack terminating at coordinates $x'' = -2.5\lambda_R$ and $z'' = -5\lambda_R$. (Refer to Fig. 4-2.)

Table 4-1—Orders of magnitude for various parameters involved in ultrasonic interrogation of hypothetical carbon nanotube-based nanocomposite [4-20].

Material Properties	Density $\rho \sim 10^3$ kg/m ³
	P -wave phase velocity $c_p \sim 10^4$ m/s
	Poisson’s ratio $\nu = 0.30$
	P -wave attenuation $\alpha_p \sim 10$ Np/m
	Normalized penetration depth $\frac{\pi}{\alpha_p \lambda_p} = 100$
Interrogation Parameters	Peak line force per unit depth $F_{peak} \sim 100$ N/m
	Center frequency $f_{center} \sim 10^7$ Hz
	Normalized bandwidth $f_{std.dev.}/f_{center} = 1/3$
Output Surface Parameters	Rayleigh wavelength $\lambda_R \sim 10^{-3}$ m
	Elastic far-field surface displacement $u \sim 10^{-10}$ m

4-6 DISPLACEMENT FIELD

Figures 4-7 and 4-8 show the displacement field throughout the nanocomposite half-space for *Cases One* and *Two*. The *P* and *S*-waves radiating into the nanocomposite, as well as the Rayleigh waves propagating along the free surfaces can be clearly seen in both cases. In Fig. 4-7, the diffraction from the vertical crack tip is observed. In Fig. 4-8, the multiple reflections from the parallel free surfaces and the diffraction from the horizontal crack tip are clearly visible. For both *Cases One* and *Two* the *relative* surface displacements are zero until the *P*-wave interacts with the crack and returns to the surface.

4-7 REQUIRED DETECTION RESOLUTION

Figure 4-9 shows the maximum *relative* vertical surface displacement of a nanocomposite having identical elastic material properties and ultrasonic interrogation parameters as *Cases One* and *Two*, except that the normalized penetration depth varies from 10 (an extremely attenuative material) to ∞ (a perfectly elastic non-attenuative material). For both the horizontal and vertical cracks, the maximum relative vertical surface displacement monotonically increases with increasing penetration depth to an asymptotic value for a perfectly elastic material. For a fixed penetration depth, the maximum relative vertical surface displacement for the horizontal crack is roughly two orders of magnitudes higher than the corresponding value for the vertical crack.

Consider an experimental noncontact monitoring system capable of detecting an absolute displacement as low as ε . A normalized surface displacement resolution, denoted by δ , is defined as the minimum detectable surface displacement divided by a specified experimental measurement range (ideally, the range that maximizes experimental contrast). It is assumed that the experimental measurement range is tuned to maximize the elastic far-field Rayleigh wave amplitude, which is approximately equal to $0.2F_{peak}M^{-1}$ [4-30], the relationship between the normalized and absolute displacement resolution is

$$0.2\delta = \varepsilon \frac{M}{F_{peak}} \quad (25)$$

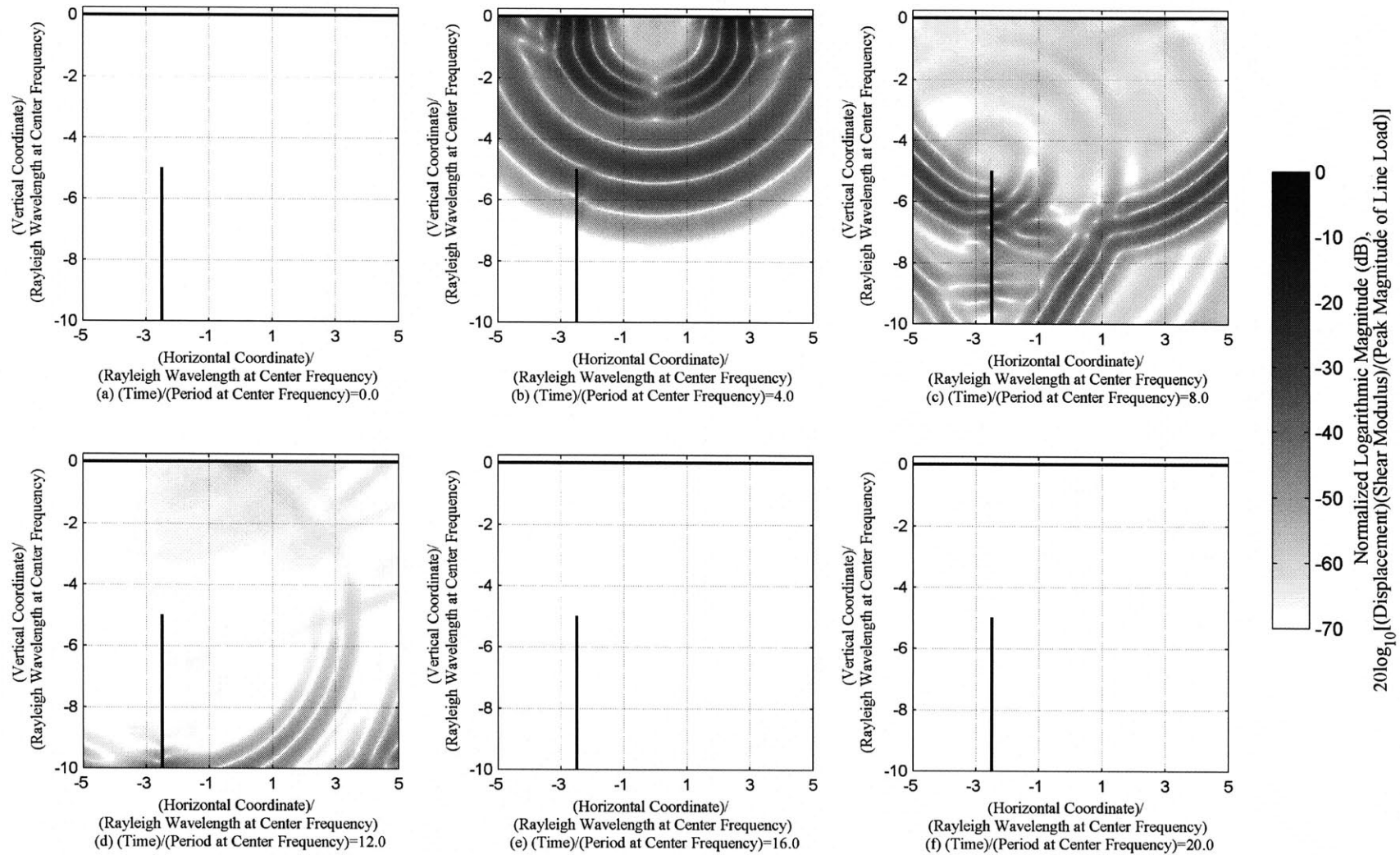


Fig. 4-7—Snapshots of displacement field for *Case One*, where nanocomposite is subject to concentrated Gaussian-modulated cosinusoidal vertical force per unit depth at origin.

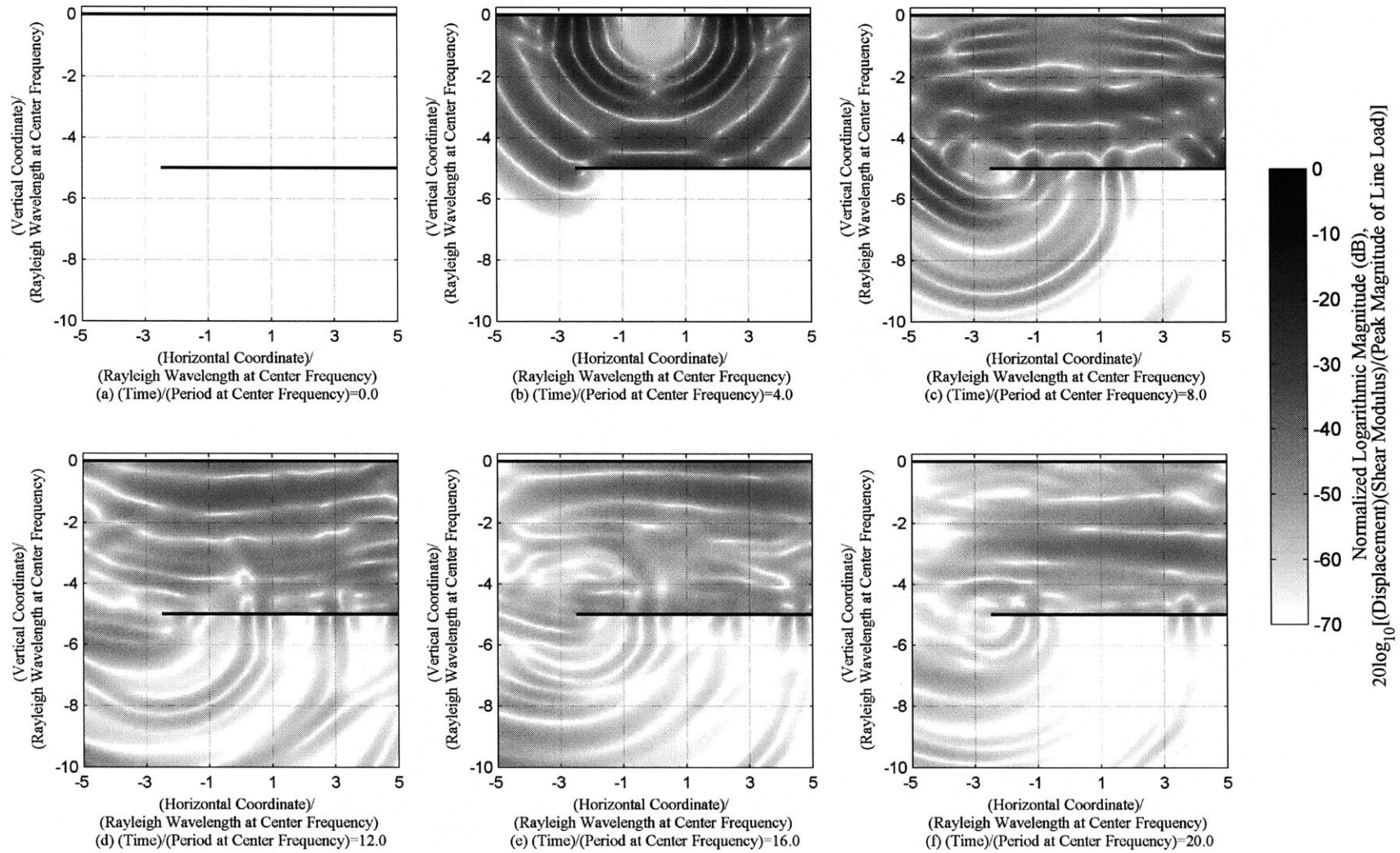


Fig. 4-8—Snapshots of displacement field for *Case Two*, where nanocomposite is subject to concentrated Gaussian-modulated cosinusoidal vertical force per unit depth at origin.

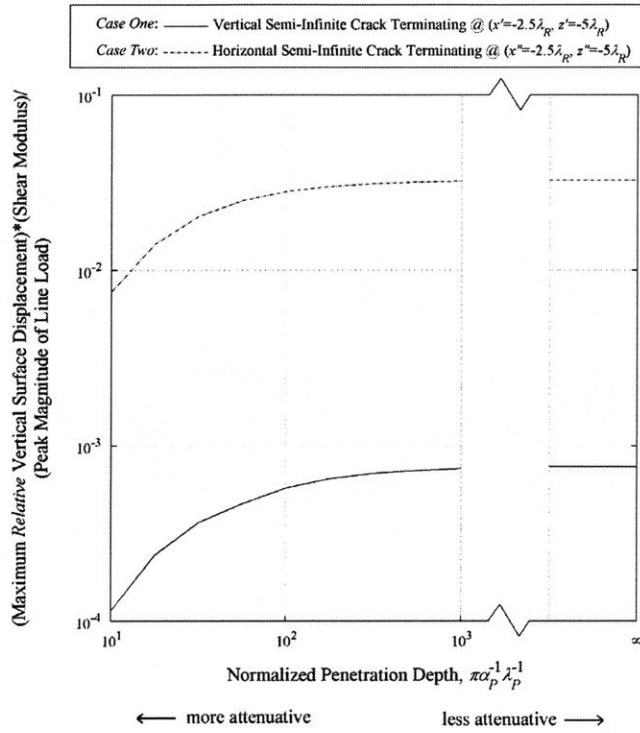


Fig. 4-9—Maximum relative vertical surface displacement as a function of normalized penetration depth for *Cases One* and *Two*. Here λ_R is Rayleigh wavelength at center frequency, α_p is P -wave attenuation, and λ_p is P -wavelength at center frequency.

Thus, the required normalized detection resolution is of the same order of magnitude as the contours of maximum vertical surface displacement shown in Fig. 4-9.

4-8 INITIAL RELATIVE SURFACE DISTURBANCE

In order to further characterize the relative vertical surface displacement response, two parameters are proposed based upon δ . The time when the normalized relative vertical surface response initially equals 0.2δ is defined as t^* . Additionally, the surface coordinate at which the initial 0.2δ surface displacement appears is defined as x^* . Figure 4-10 shows a schematic that interrelates parameters δ , t^* , and x^* . The normalized functional forms of t^* and x^* are

$$\frac{t^*}{T} = fc n_3 \left\{ \delta, \nu, \frac{\pi}{\alpha_p \lambda_p}, \frac{f_{std.dev.}}{f_{center}}, \frac{\hat{x}}{\lambda_R}, \frac{\hat{z}}{\lambda_R} \right\} \quad (4-26)$$

$$\frac{x^*}{\lambda_R} = fc n_4 \left\{ \delta, \nu, \frac{\pi}{\alpha_p \lambda_p}, \frac{f_{std.dev.}}{f_{center}}, \frac{\hat{x}}{\lambda_R}, \frac{\hat{z}}{\lambda_R} \right\} \quad (4-27)$$

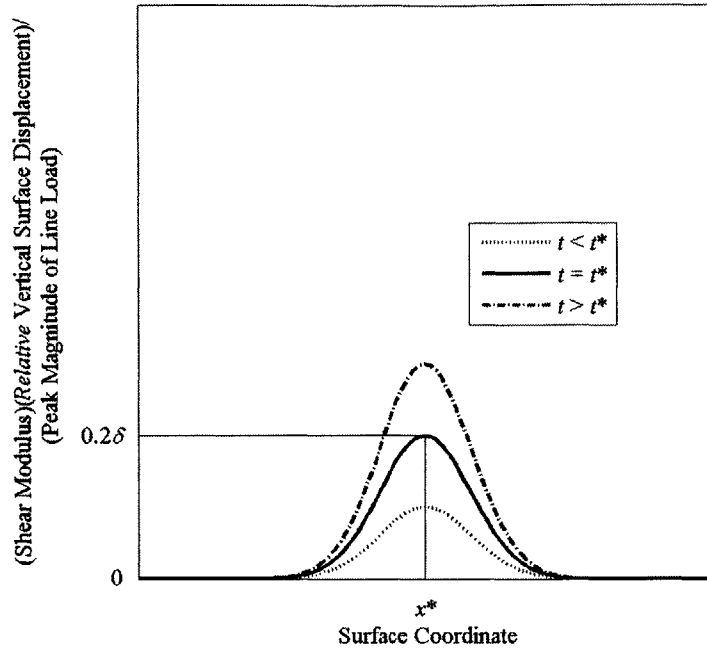


Fig. 4-10—Schematic of relative vertical surface displacement at time t^* and in vicinity of surface coordinate x^* based on normalized detection resolution δ .

For the vertical semi-infinite crack, the relative surface displacements are zero until $t \approx t^*$, which is equal to the time necessary for the fastest wave, the P -wave, to interact with the sub-surface vertical crack-tip and return to the surface. Thus, approximate relationships for eqns. (4-26) and (4-27) are derived by using a simple ray analogy for the P -waves, which minimize the origin/crack-tip/surface distance. As $\delta \rightarrow 0$, which suggests infinitely fine resolution of surface displacements, the normalized relationship between x^* , t^* , x' , and z' are given by the following equations

$$\frac{z'}{\lambda_R} = \frac{1}{2} \left(\frac{c_R}{c_P} \right) \left(\frac{t^*}{T} \right)^{-1} \left(\frac{x'}{\lambda_R} \right)^2 - \frac{1}{2} \left(\frac{c_R}{c_P} \right)^{-1} \left(\frac{t^*}{T} \right) \quad (4-28)$$

and

$$\frac{x^*}{\lambda_R} = \frac{x'}{\lambda_R} \quad (4-29)$$

where c_R/c_P is a function of ν only ($c_R/c_P = 0.50$ for $\nu = 0.30$). Equation (4-28) is an expression for trajectories of constant t^* in the $x' - z'$ plane; the trajectories consist of

ever-flattening cascading parabolas in increasing t^* .

The results for t^* and x^* as a function of the vertical crack-tip location are shown in Fig. 4-11 for $\delta \rightarrow 0$ (dashed contour lines) and $\delta = 10^{-6}$ (solid contour lines), where excellent agreement with eqns. (4-28) and (4-29) is displayed. Figure 4-11 suggests that the location of a vertical semi-infinite crack tip can be graphically determined by overlaying contours of t^* and x^* on a single set of axes and noting the point of intersection.

For the horizontal semi-infinite crack, as $\delta \rightarrow 0$, the path that minimizes the origin/crack/surface distance depends upon the quarter-space location of the crack. If $x'' \geq 0$, that is, if the crack does not cross the line $x = 0$, the normalized relationship between x^* , t^* , x'' , and z'' follows from eqns. (4-28) and (4-29) as

$$\frac{z''}{\lambda_R} = \frac{1}{2} \left(\frac{c_R}{c_P} \right) \left(\frac{t^*}{T} \right)^{-1} \left(\frac{x''}{\lambda_R} \right)^2 - \frac{1}{2} \left(\frac{c_R}{c_P} \right)^{-1} \left(\frac{t^*}{T} \right), \quad \frac{x''}{\lambda_R} \geq 0 \quad (4-30)$$

and

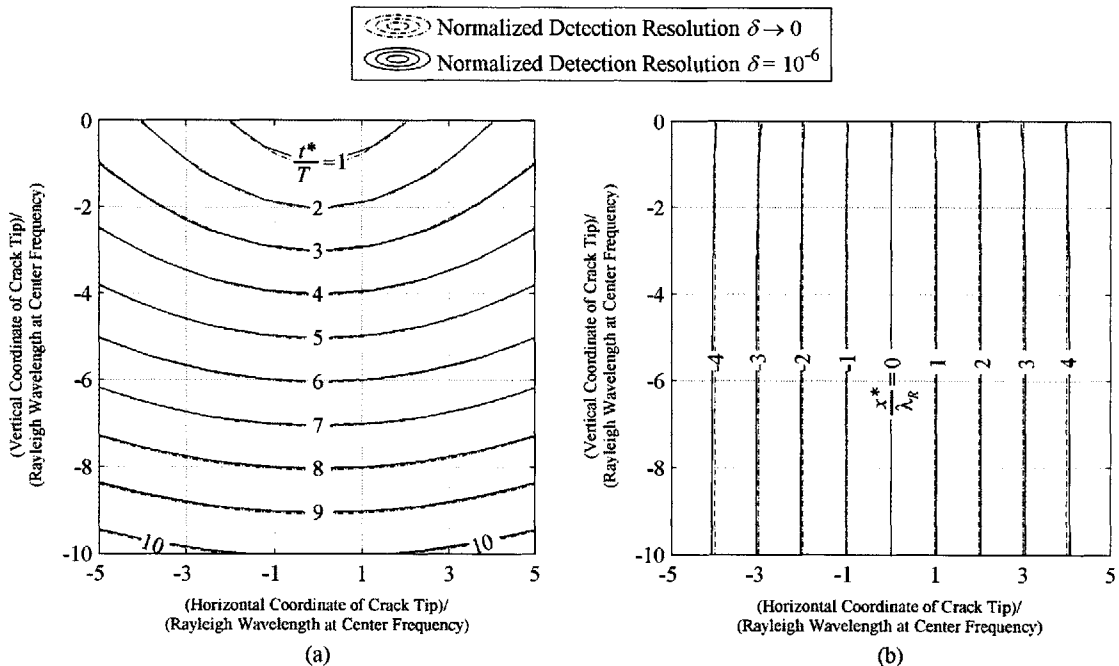


Fig. 4-11—(a) Initial reaction time t^* normalized by period at center frequency T and (b) initial reaction surface coordinate x^* normalized by Rayleigh wavelength at center frequency λ_R as function of location of vertical crack tip embedded in nanocomposite for normalized detection resolutions $\delta \rightarrow 0$ (dashed contour lines) and $\delta = 10^{-6}$ (solid contour lines).

$$\frac{x^*}{\lambda_R} = \frac{x''}{\lambda_R}, \quad \frac{x''}{\lambda_R} \geq 0 \tag{4-31}$$

If $x'' < 0$, that is, if the crack crosses the line $x = 0$, the minimum P -wave path is simply twice the origin/crack depth distance. In this case, the normalized relationship between x^* , t^* , x'' , and z'' is

$$\frac{z''}{\lambda_R} = -\frac{1}{2} \left(\frac{c_R}{c_P} \right)^{-1} \left(\frac{t^*}{T} \right), \quad \frac{x''}{\lambda_R} < 0 \tag{4-32}$$

$$\frac{x^*}{\lambda_R} = 0, \quad \frac{x''}{\lambda_R} < 0 \tag{4-33}$$

Figure 4-12 shows contours of t^* and x^* as a function of the horizontal crack-tip location for $\delta \rightarrow 0$ (dashed contour lines) and $\delta = 10^{-6}$ (solid contour lines). Fig. 4-12 suggests that, based solely on measurements of t^* and x^* , in general only the depth of crack can be determined; a scanning of the line load must be undertaken.

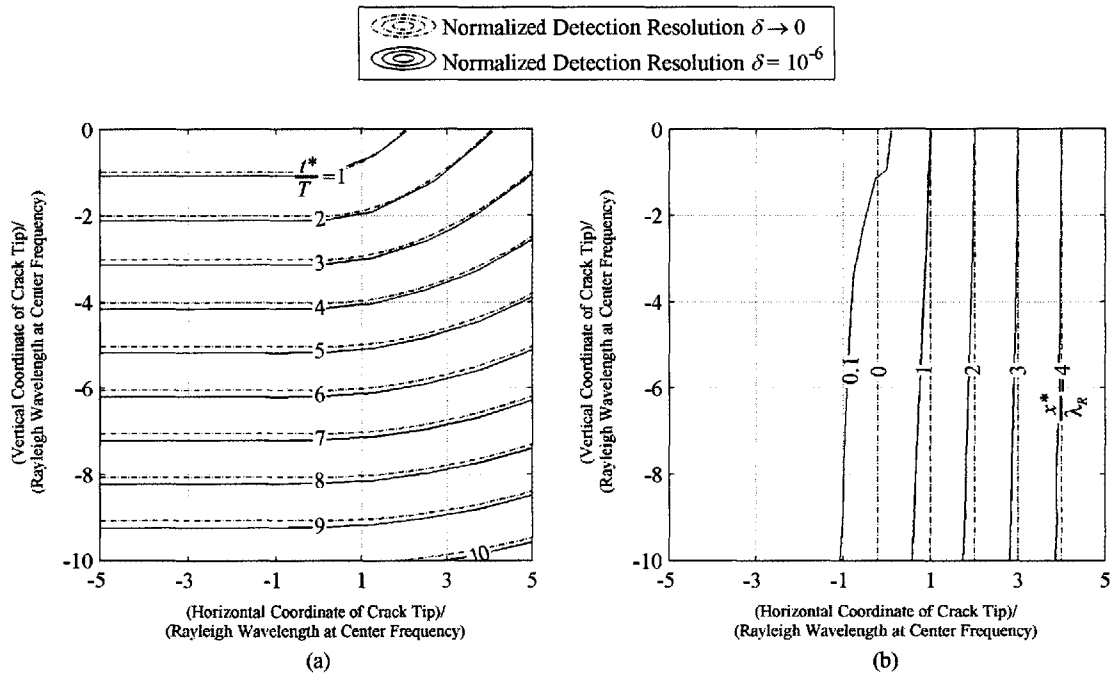


Fig. 4-12—(a) Initial reaction time t^* normalized by period at center frequency T and (b) initial reaction surface coordinate x^* normalized by Rayleigh wavelength at center frequency λ_R as function of location of horizontal crack tip embedded in nanocomposite for normalized detection resolutions $\delta \rightarrow 0$ (dashed contour lines) and $\delta = 10^{-6}$ (solid contour lines).

4-9 TRANSIENT RELATIVE SURFACE DISPLACEMENT

The transient full-field *relative* vertical surface displacement in the spatial window $-5\lambda_R \leq x \leq 5\lambda_R$ and time period $0 \leq t \leq 20T$ is characterized by the corresponding root-mean-square value given by

$$w_{relative}^{RMS} = \sqrt{\frac{1}{N_x N_t} \sum_{m=1}^{N_x} \sum_{n=1}^{N_t} |w_{relative}(x_m, t_n)|^2} \quad (4-34)$$

where $N_x = 401$ horizontal grid points, $N_t = 1242$ time steps, and where

$$x_m = h \left(m - 1 - \frac{N_x - 1}{2} \right) \quad (4-35)$$

and

$$t_n = \Delta t(n - 1) \quad (4-36)$$

(An alternative way of analyzing the transient relative surface displacements in wavenumber-frequency space is detailed in Appendix 4C.)

Figure 4-13 shows $w_{relative}^{RMS}$ as a function of crack-tip location for vertical and horizontal semi-infinite cracks. A few observations are noted. First, for a fixed horizontal coordinate of the crack tip, $w_{relative}^{RMS}$ monotonically decreases with increasing crack depth. Second, for a vertical crack, for a fixed depth $w_{relative}^{RMS}$ has a relative minimum for a vertical crack located directly under the origin. Third, for a horizontal crack, for a fixed depth $w_{relative}^{RMS}$ monotonically decreases with increasing horizontal coordinate.

In the preceding analysis, it has been assumed that the line load remains fixed at the origin. However, the above analysis is valid if a scanning line load function $F_{scan}(x, t)$ is defined by

$$F_{scan}(x, t) = \sum_{p=0}^{\infty} F(x - c_{scan}t, t - pT_{scan}) \quad (4-37)$$

that is, the line load is scanned on the surface of the nanocomposite with a scanning speed c_{scan} and period T_{scan} , provided $c_{scan} \ll c_R$ and $T_{scan} \gg 20T$. According to eqns.

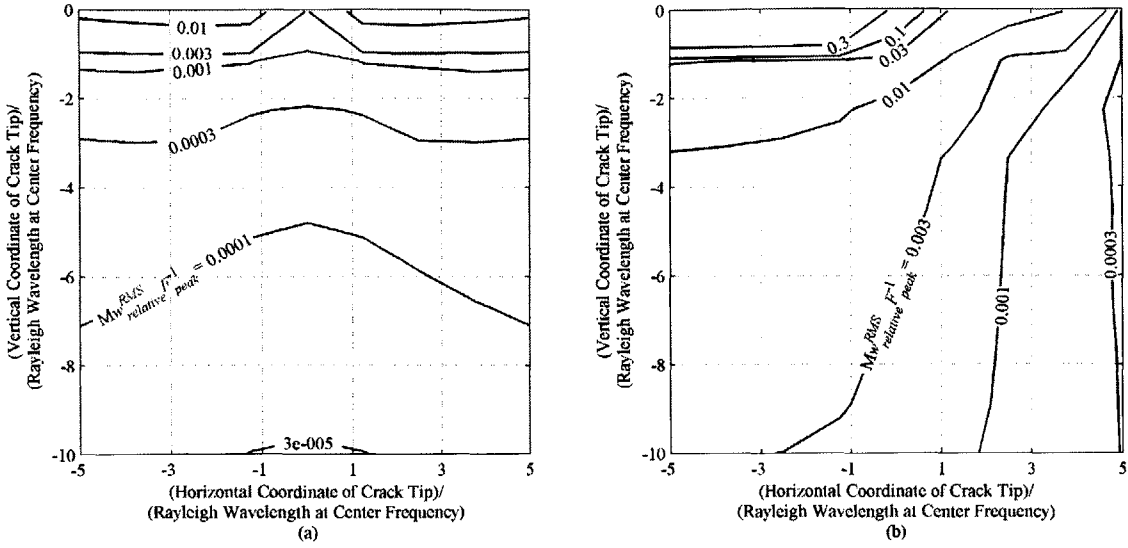


Fig. 4-13—Root-mean-square *relative* vertical surface displacement $w_{relative}^{RMS}$, normalized by shear modulus M and peak force per unit length F_{peak} , as function of crack tip location in nanocomposite for (a) vertical semi-infinite cracks and (b) horizontal semi-infinite cracks.

(4-1) and (4-37), the line load is above the origin at time $t = 0$. The relative horizontal position of the line load with respect to the horizontal coordinate of the crack tip is

$$x_{relative} = x' - c_{scan}t \quad (4-38)$$

for vertical cracks and

$$x_{relative} = x'' - c_{scan}t \quad (4-39)$$

for horizontal cracks. In this case $x_{relative} > 0$ if the line load is to the right of the horizontal crack tip location.

Figure 14 shows $w_{relative}^{RMS}$ as a function of $x_{relative}$ for *Cases One* and *Two*. A few observations are noted.

First, the peak magnitude of $w_{relative}^{RMS}$ for *Case Two* is two orders of magnitude larger than the peak magnitude of $w_{relative}^{RMS}$ for *Case One*. Second, for *Case Two*, $w_{relative}^{RMS}$ monotonically decreases with decreasing $x_{relative}$. Third, for *Case One*, $w_{relative}^{RMS}$ is symmetric with respect to $x_{relative} = 0$, that is, when the line load is directly above the vertical crack. This symmetry is due primarily to the diffraction coefficient of a crack subjected to normal plane wave radiation being much smaller than the diffraction

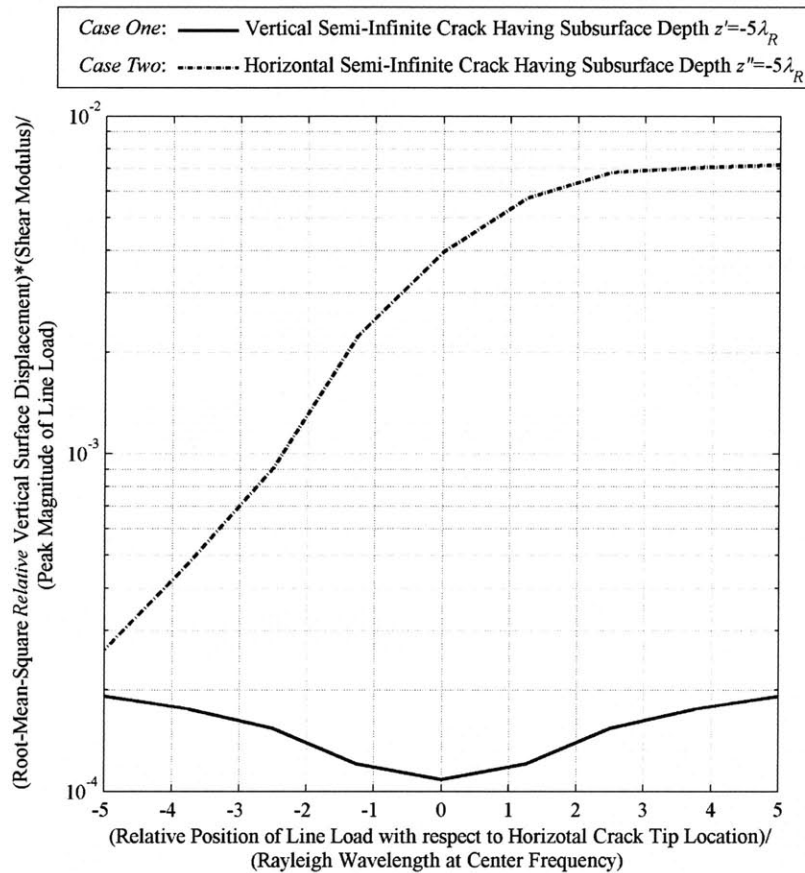


Fig. 14—Root-mean-square *relative* vertical surface displacement as function of relative position of line load with respect to the horizontal crack tip location for vertical and horizontal semi-infinite cracks having same depth as *Case One* and *Case Two*.

coefficient of a crack subjected to plane wave radiation that is slightly to moderately oblique [4-32]. Thus, a scanning measurement would produce distinctly different signatures for horizontal and vertical semi-infinite cracks, having crack tips at equal depths.

4-10 CONCLUSIONS

Analytical mass-spring-dashpot lattice models for the ultrasonic nondestructive evaluation of an attenuating nanocomposite containing subsurface cracks were developed. Full-field wave propagation simulations of these models as well as the the simulations for a corresponding model of a pristine nanocomposite were conducted, and their relative surface displacements were presented. The initial temporal and spatial disturbances of these relative surface displacements along with root-mean-square averages of the relative vertical surface displacement reveal guidelines for the characterization of subsurface cracks in nanocomposites and other attenuating materials.

References:

- 4-1. J.H. Williams, Jr. and N.R. Lampert. *Mater. Eval.* **38**:68 (1980).
- 4-2. J.H. Williams, Jr., and B. Doll. *Mater. Eval.* **40**:1374 (1982).
- 4-3. J.H. Williams, Jr, H. Kiragulle and S.S. Lee. *Mater. Eval.* **44**:455 (1986).
- 4-4. L.-W. Cai and J.H. Williams, Jr. *Ultrason.* **37**:435 (1999).
- 4-5. L.-W. Cai and J.H. Williams, Jr. *Ultrason.* **37**:463 (1999).
- 4-6. R.J. Nagem, J.M. Seng and J.H. Williams, Jr. *Mater. Eval.* **58**:1065 (2000).
- 4-7. R.J. Nagem, J.M. Seng and J.H. Williams, Jr. *Mater. Eval.* **58**:1310 (2000).
- 4-8. D.A. Mendelsohn, J.D. Achenbach and L.M. Keer. *Wave Mot.* **2**:277 (1980).
- 4-9. J.D. Achenbach and R.J. Brind. *J. Sound Vib.* **76**:43 (1981).
- 4-10. R.J. Brind and J.D. Achenbach. *J. Sound Vib.* **78**:555 (1981).
- 4-11. J.D. Achenbach, W. Lin and L.M. Keer. *IEEE Trans. Sonics Ultrason.* **SU-30**:270 (1983).
- 4-12. L.-W. Cai and J.H. Williams, Jr. *Mater. Eval.* **63**:434 (2005).
- 4-13. L.-W. Cai and J.H. Williams, Jr. *Mater. Eval.* **63**:657 (2005).
- 4-14. P.D. Small, A.F. Thomas, and J.H. Williams, Jr. submitted for publication (2005).
- 4-15. D. Cerniglia, B.B. Djordjevic, and V. Nigrelli. *IEEE Ultrasonics Symposium* 751-754 (2001).
- 4-16. T. Stratoudaki, C. Edwards, S. Dixon and S.B. Palmer. *Proc. of SPIE Int. Soc. Opt. Eng.* **5046**:89 (2003).
- 4-17. J.-J. Luo and I.M. Daniel. *Compos. Sci. Technol.* **63**:1607 (2003).
- 4-18. E.T. Thostenson, Z. Ren and T.-W. Chou. *Compos. Sci. Technol.* **61**:1899 (2001).
- 4-19. D. Srivastava, C. Wei and K. Cho. *Appl. Mech. Rev.* **56**:215 (2003).
- 4-20. C.E. Harris, C.E., M.J. Shuart and H.R. Gray. *SAMPE J.* **38**:33 (2002).
- 4-21. S.E. O'Donnell, K.R. Sprong and B.M. Haltli. *Collection of Technical Papers - AIAA 4th Aviation Technology, Integration, and Operations Forum,ATIO* **2**:693 (2004).
- 4-22. X. Zhou, E. Shin, K.W. Wang and C.E. Bakis. *Compos. Sci. Technol.* **64**:2425 (2004).
- 4-23. J. Suhr, N. Koratkar, P. Keblinski and P. Ajayan. *Nat. Mater.* **4**:134 (2005).
- 4-24. M.J. Lang, M. Duarte-Dominguez, R. Birringer, R. Hempelmann, H. Natter, and W. Arnold. *NanoStruct. Mater.* **12**:811 (1999).
- 4-25. Z. Bian, R.J. Wang, D.Q. Zhao, M.X. Pan, Z.X. Wang and W.H. Wang. *Appl. Phys. Lett.* **82**:2790 (2003).
- 4-26. A.F. Thomas, H. Yim and J.H. Williams, Jr. submitted for publication (2005).
- 4-27. H. Yim and Y. Choi. *Mater. Eval.* **58**:889 (2000).
- 4-28. H. Yim and Y. Sohn. *IEEE Trans. Ultrason. Ferroelectr. Freq. Control.* **47**:549 (2000).
- 4-29. K. Graff. *Wave Motion in Elastic Solids*, p. 325. Dover, New York (1991).
- 4-30. Lamb, H. *Philosophical Transactions of the Royal Society of London. Series A, Containing Papers of a Mathematical or Physical Character.* **203**:1 (1904).
- 4-31. A.V. Oppenheim and R.W. Schaffer. *Discrete-Time Signal Processing*, pp. 559-588, 621. Prentice Hall, Upper Saddle River, New Jersey, 1999.
- 4-32. J.D. Achenbach, A.K. Gautesen, and H. McMaken. *Ray Methods for Waves in Elastic Solids*, pp. 109-128,146,147. Pitman Advanced Publishing Program, Boston (1982).

APPENDIX 4A—MSDLM Discretizations at Various Boundary and Interaction Conditions

This appendix details the stress-dynamic equations for the MSDLM discretization of a single relaxation time, single dispersion ratio standard linear solid [4A-1] in the vicinity of various interaction conditions.

Interior Particle

The MSDLM discretized stress-dynamic equations for an interior particle located at position (i, j) , as shown in Fig. 4A-1, are

$$\begin{aligned}
 \frac{df_{i,j}^x}{dt} = & -\frac{f_{i,j}^x}{\tau} + \frac{\bar{r}(\Pi - M)}{\tau h^2} (u_{i+1,j} - 2u_{i,j} + u_{i-1,j}) \\
 & + \frac{\bar{r}M}{2\tau h^2} (u_{i+1,j+1} + u_{i-1,j-1} + u_{i+1,j-1} + u_{i-1,j+1} - 4u_{i,j}) \\
 & + \frac{\bar{r}(\Pi - M)}{4\tau h^2} (w_{i+1,j+1} + w_{i-1,j-1} - w_{i+1,j-1} - w_{i-1,j+1}) \\
 & + \frac{\Pi - M}{h^2} (\dot{u}_{i+1,j} - 2\dot{u}_{i,j} + \dot{u}_{i-1,j}) \\
 & + \frac{M}{2h^2} (\dot{u}_{i+1,j+1} + \dot{u}_{i-1,j-1} + \dot{u}_{i+1,j-1} + \dot{u}_{i-1,j+1} - 4\dot{u}_{i,j}) \\
 & + \frac{\Pi - M}{4h^2} (\dot{w}_{i+1,j+1} + \dot{w}_{i-1,j-1} - \dot{w}_{i+1,j-1} - \dot{w}_{i-1,j+1})
 \end{aligned} \tag{4A-1}$$

$$\begin{aligned}
 \frac{df_{i,j}^z}{dt} = & -\frac{f_{i,j}^z}{\tau} + \frac{\bar{r}(\Pi - M)}{\tau h^2} (w_{i,j+1} - 2w_{i,j} - w_{i,j-1}) \\
 & + \frac{\bar{r}M}{2\tau h^2} (w_{i+1,j+1} + w_{i-1,j-1} + w_{i+1,j-1} + w_{i-1,j+1} - 4w_{i,j}) \\
 & + \frac{\bar{r}(\Pi - M)}{4\tau h^2} (u_{i+1,j+1} + u_{i-1,j-1} - u_{i+1,j-1} - u_{i-1,j+1}) \\
 & + \frac{\Pi - M}{h^2} (\dot{w}_{i,j+1} - 2\dot{w}_{i,j} - \dot{w}_{i,j-1}) \\
 & + \frac{M}{2h^2} (\dot{w}_{i+1,j+1} + \dot{w}_{i-1,j-1} + \dot{w}_{i+1,j-1} + \dot{w}_{i-1,j+1} - 4\dot{w}_{i,j}) \\
 & + \frac{\Pi - M}{4h^2} (\dot{u}_{i+1,j+1} + \dot{u}_{i-1,j-1} - \dot{u}_{i+1,j-1} - \dot{u}_{i-1,j+1})
 \end{aligned} \tag{4A-2}$$

$$\frac{du_{i,j}}{dt} = \dot{u}_{i,j} \tag{4A-3}$$

$$\frac{dw_{i,j}}{dt} = \dot{w}_{i,j} \quad (4A-4)$$

$$\frac{d\dot{u}_{i,j}}{dt} = \frac{1}{\rho} (f_{i,j}^{bx} + f_{i,j}^x) \quad (4A-5)$$

$$\frac{d\dot{w}_{i,j}}{dt} = \frac{1}{\rho} (f_{i,j}^{bz} + f_{i,j}^z) \quad (4A-6)$$

Free Surface

The MSDLM discretized stress-dynamic equations for a particle located on the longitudinal free surface at position (i, j) , as shown in Fig. 4A-2, are

$$\begin{aligned} \frac{df_{i,j-\frac{1}{2}}^x}{dt} = & -\frac{f_{i,j-\frac{1}{2}}^x}{\tau} + \frac{\bar{r}(\Pi - M)}{\tau h^2} (u_{i-1,j} - 2u_{i,j} + u_{i+1,j}) \\ & + \frac{\bar{r}M}{\tau h^2} (u_{i+1,j-1} + u_{i+1,j-1} - 2u_{i,j}) \\ & + \frac{\bar{r}(\Pi - M)}{2\tau h^2} (w_{i-1,j-1} - w_{i+1,j-1}) + \frac{\bar{r}(3M - \Pi)}{4\tau h^2} (w_{i-1,j} - w_{i+1,j}) \\ & + \frac{\Pi - M}{h^2} (\dot{u}_{i-1,j} - 2\dot{u}_{i,j} + \dot{u}_{i+1,j}) + \frac{M}{h^2} (\dot{u}_{i+1,j-1} + \dot{u}_{i+1,j} - 2\dot{u}_{i,j}) \\ & + \frac{\Pi - M}{2h^2} (\dot{w}_{i-1,j-1} - \dot{w}_{i+1,j-1}) + \frac{3M - \Pi}{4h^2} (\dot{w}_{i-1,j} - \dot{w}_{i+1,j}) \end{aligned} \quad (4A-7)$$

$$\begin{aligned} \frac{df_{i,j-\frac{1}{2}}^z}{dt} = & -\frac{f_{i,j-\frac{1}{2}}^z}{\tau} + \frac{2\bar{r}(\Pi - M)}{\tau h^2} (w_{i,j-1} - w_{i,j}) \\ & + \frac{\bar{r}M}{\tau h^2} (w_{i+1,j-1} + w_{i-1,j-1} - 2w_{i,j}) \\ & + \frac{\bar{r}(\Pi - M)}{2\tau h^2} (u_{i-1,j-1} - u_{i+1,j-1}) + \frac{\bar{r}(3M - \Pi)}{4\tau h^2} (u_{i+1,j} - u_{i-1,j}) \\ & + \frac{2(\Pi - M)}{h^2} (\dot{w}_{i,j-1} - \dot{w}_{i,j}) + \frac{M}{h^2} (\dot{w}_{i+1,j-1} + \dot{w}_{i-1,j-1} - 2\dot{w}_{i,j}) \\ & + \frac{\Pi - M}{2h^2} (\dot{u}_{i-1,j-1} - \dot{u}_{i+1,j-1}) + \frac{3M - \Pi}{4h^2} (\dot{u}_{i+1,j} - \dot{u}_{i-1,j}) \end{aligned} \quad (4A-8)$$

$$\frac{du_{i,j}}{dt} = \dot{u}_{i,j} \quad (4A-9)$$

$$\frac{dw_{i,j}}{dt} = \dot{w}_{i,j} \quad (4A-10)$$

$$\frac{d\dot{u}_{i,j}}{dt} = \frac{2}{\rho} (f_{i,j-\frac{1}{2}}^x + f_{i,j}^{sx}) \quad (4A-11)$$

$$\frac{d\dot{w}_{i,j}}{dt} = \frac{2}{\rho} \left(f_{i,j-\frac{1}{2}}^z + f_{i,j}^{sz} \right) \quad (4A-12)$$

Crack Tips

The MSDLM discretized stress-dynamic equations for a particle located on the crack tip of a horizontal semi-infinite crack, as shown in Fig. 4A-2, are

$$\begin{aligned} \frac{df_{i,j}^x}{dt} = & -\frac{f_{i,j}^x}{\tau} + \frac{\bar{r}(\Pi - M)}{th^2} \left(0.5u_{i+1,j^+} + 0.5u_{i+1,j^-} - 2u_{i,j} + u_{i-1,j} \right) \\ & + \frac{\bar{r}(3M - \Pi)}{2th^2} \left(w_{i+1,j^+} - w_{i+1,j^-} \right) \\ & + \frac{\bar{r}M}{2th^2} \left(u_{i+1,j+1} + u_{i-1,j-1} + u_{i+1,j-1} + u_{i-1,j+1} - 4u_{i,j} \right) \\ & + \frac{\bar{r}(\Pi - M)}{4th^2} \left(w_{i+1,j+1} + w_{i-1,j-1} - w_{i+1,j-1} - w_{i-1,j+1} \right) \\ & + \frac{\Pi - M}{h^2} \left(0.5\dot{u}_{i+1,j^+} + 0.5\dot{u}_{i+1,j^-} - 2\dot{u}_{i,j} + \dot{u}_{i-1,j} \right) \\ & + \frac{3M - \Pi}{2h^2} \left(u_{i+1,j^+} - u_{i+1,j^-} \right) \\ & + \frac{M}{2h^2} \left(\dot{u}_{i+1,j+1} + \dot{u}_{i-1,j-1} + \dot{u}_{i+1,j-1} + \dot{u}_{i-1,j+1} - 4\dot{u}_{i,j} \right) \\ & + \frac{\Pi - M}{4h^2} \left(\dot{w}_{i+1,j+1} + \dot{w}_{i-1,j-1} - \dot{w}_{i+1,j-1} - \dot{w}_{i-1,j+1} \right) \end{aligned} \quad (4A-13)$$

$$\begin{aligned} \frac{df_{i,j}^z}{dt} = & -\frac{f_{i,j}^z}{\tau} + \frac{\bar{r}(\Pi - M)}{th^2} \left(w_{i,j+1} - 2w_{i,j} - w_{i,j-1} \right) \\ & + \frac{\bar{r}(3M - \Pi)}{2th^2} \left(u_{i+1,j^-} - u_{i+1,j^+} \right) \\ & + \frac{\bar{r}M}{2th^2} \left(w_{i+1,j+1} + w_{i-1,j-1} + w_{i+1,j-1} + w_{i-1,j+1} - 4w_{i,j} \right) \\ & + \frac{\bar{r}(\Pi - M)}{4th^2} \left(u_{i+1,j+1} + u_{i-1,j-1} - u_{i+1,j-1} - u_{i-1,j+1} \right) \\ & + \frac{\Pi - M}{h^2} \left(\dot{w}_{i,j+1} - 2\dot{w}_{i,j} - \dot{w}_{i,j-1} \right) \\ & + \frac{3M - \Pi}{2h^2} \left(\dot{u}_{i+1,j^-} - \dot{u}_{i+1,j^+} \right) \\ & + \frac{M}{2h^2} \left(\dot{w}_{i+1,j+1} + \dot{w}_{i-1,j-1} + \dot{w}_{i+1,j-1} + \dot{w}_{i-1,j+1} - 4\dot{w}_{i,j} \right) \\ & + \frac{\Pi - M}{4h^2} \left(\dot{u}_{i+1,j+1} + \dot{u}_{i-1,j-1} - \dot{u}_{i+1,j-1} - \dot{u}_{i-1,j+1} \right) \end{aligned} \quad (4A-14)$$

$$\frac{du_{i,j}}{dt} = \dot{u}_{i,j} \quad (4A-15)$$

$$\frac{dw_{i,j}}{dt} = \dot{w}_{i,j} \quad (4A-16)$$

$$\frac{d\dot{u}_{i,j}}{dt} = \frac{1}{\rho} (f_{i,j}^{bx} + f_{i,j}^x) \quad (4A-17)$$

$$\frac{d\dot{w}_{i,j}}{dt} = \frac{1}{\rho} (f_{i,j}^{bz} + f_{i,j}^z) \quad (4A-18)$$

The MSDLM discretized stress-dynamic equations for a particle located on the crack tip of a vertical semi-infinite crack, as shown in Fig. 4A-4, are

$$\begin{aligned} \frac{df_{i,j}^x}{dt} = & -\frac{f_{i,j}^x}{\tau} + \frac{\bar{r}(\Pi - M)}{2h^2} (u_{i+1,j} - 2u_{i,j} + u_{i-1,j}) \\ & + \frac{\bar{r}(3M - \Pi)}{2\tau h^2} (w_{i^+,j-1} - w_{i^-,j-1}) \\ & + \frac{\bar{r}M}{2\tau h^2} (u_{i+1,j+1} + u_{i-1,j-1} + u_{i+1,j-1} + u_{i-1,j+1} - 4u_{i,j}) \\ & + \frac{\bar{r}(\Pi - M)}{4\tau h^2} (w_{i+1,j+1} + w_{i-1,j-1} - w_{i+1,j-1} - w_{i-1,j+1}) \\ & + \frac{\Pi - M}{h^2} (\dot{u}_{i+1,j} - 2\dot{u}_{i,j} + \dot{u}_{i-1,j}) \\ & + \frac{3M - \Pi}{2\tau h^2} (\dot{w}_{i^+,j-1} - \dot{w}_{i^-,j-1}) \\ & + \frac{M}{2h^2} (\dot{u}_{i+1,j+1} + \dot{u}_{i-1,j-1} + \dot{u}_{i+1,j-1} + \dot{u}_{i-1,j+1} - 4\dot{u}_{i,j}) \\ & + \frac{\Pi - M}{4h^2} (\dot{w}_{i+1,j+1} + \dot{w}_{i-1,j-1} - \dot{w}_{i+1,j-1} - \dot{w}_{i-1,j+1}) \end{aligned} \quad (4A-19)$$

$$\begin{aligned}
 \frac{df_{i,j}^z}{dt} = & -\frac{f_{i,j}^z}{\tau} + \frac{\bar{r}(\Pi - M)}{ch^2} (w_{i,j+1} - 2w_{i,j} - 0.5w_{i^-,j-1} - 0.5w_{i^+,j-1}) \\
 & + \frac{\bar{r}(3M - \Pi)}{2ch^2} (u_{i^-,j-1} - u_{i^+,j-1}) \\
 & + \frac{\bar{r}M}{2ch^2} (w_{i+1,j+1} + w_{i-1,j-1} + w_{i+1,j-1} + w_{i-1,j+1} - 4w_{i,j}) \\
 & + \frac{\bar{r}(\Pi - M)}{4ch^2} (u_{i+1,j+1} + u_{i-1,j-1} - u_{i+1,j-1} - u_{i-1,j+1}) \\
 & + \frac{\Pi - M}{h^2} (\dot{w}_{i,j+1} - 2\dot{w}_{i,j} - 0.5\dot{w}_{i^-,j-1} - 0.5\dot{w}_{i^+,j-1}) \\
 & + \frac{3M - \Pi}{2h^2} (\dot{u}_{i^-,j-1} - \dot{u}_{i^+,j-1}) \\
 & + \frac{M}{2h^2} (\dot{w}_{i+1,j+1} + \dot{w}_{i-1,j-1} + \dot{w}_{i+1,j-1} + \dot{w}_{i-1,j+1} - 4\dot{w}_{i,j}) \\
 & + \frac{\Pi - M}{4h^2} (\dot{u}_{i+1,j+1} + \dot{u}_{i-1,j-1} - \dot{u}_{i+1,j-1} - \dot{u}_{i-1,j+1})
 \end{aligned} \tag{4A-20}$$

$$\frac{du_{i,j}}{dt} = \dot{u}_{i,j} \tag{4A-21}$$

$$\frac{dw_{i,j}}{dt} = \dot{w}_{i,j} \tag{4A-22}$$

$$\frac{d\dot{u}_{i,j}}{dt} = \frac{1}{\rho} (f_{i,j}^{bx} + f_{i,j}^x) \tag{4A-23}$$

$$\frac{d\dot{w}_{i,j}}{dt} = \frac{1}{\rho} (f_{i,j}^{bz} + f_{i,j}^z) \tag{4A-24}$$

Convergence

The stress-dynamic equations (4A-1) through (4A-24) are numerically integrated via the standard 4th order Runge-Kutta algorithm [4A-2]. Numerical analysis [4A-3] has shown that the stability requirements relating the grid spacing h and the time step Δt are

$$\frac{c_P \Delta t}{h} \leq 1.30 \tag{4A-19}$$

$$\frac{\Delta t}{\tau} \leq 2.78 \tag{4A-20}$$

Furthermore, the accuracy condition required to limit the numerical dissipation and phase speed error to less than 1% is

$$\frac{\lambda_{\min}}{h} \geq 20 \quad (4A-21)$$

where λ_{\min} is the minimum effective wavelength propagating in the model.

Because $0 < \bar{r} \leq 1$, the penetration depth of the material, $\pi\alpha_p^{-1}\lambda_p^{-1}$, (that is, the number of wavelengths required for a plane wave to decay by a factor $\exp(-\pi)$) must satisfy

$$\frac{\pi}{\alpha_p\lambda_p} > \omega\tau \quad (4A-22)$$

It has been shown that materials with penetration depths as low as 5 can be accurately modeled in this manner; materials having a penetration depth lower than five exhibit significant dispersion [4A-3].

References:

- 4A-1. A.F. Thomas, H. Yim and J.H. Williams, Jr. submitted for publication (2005).
- 4A-2. M. Abramowitz and I.A. Stegun (Eds.), *Handbook of Mathematical Functions with Formulas, Graphs and Mathematical Tables*, pp. 896-897. Dover, New York (1965).
- 4A-3. P.D. Small, A.F. Thomas, and J.H. Williams, Jr. submitted for publication (2005).

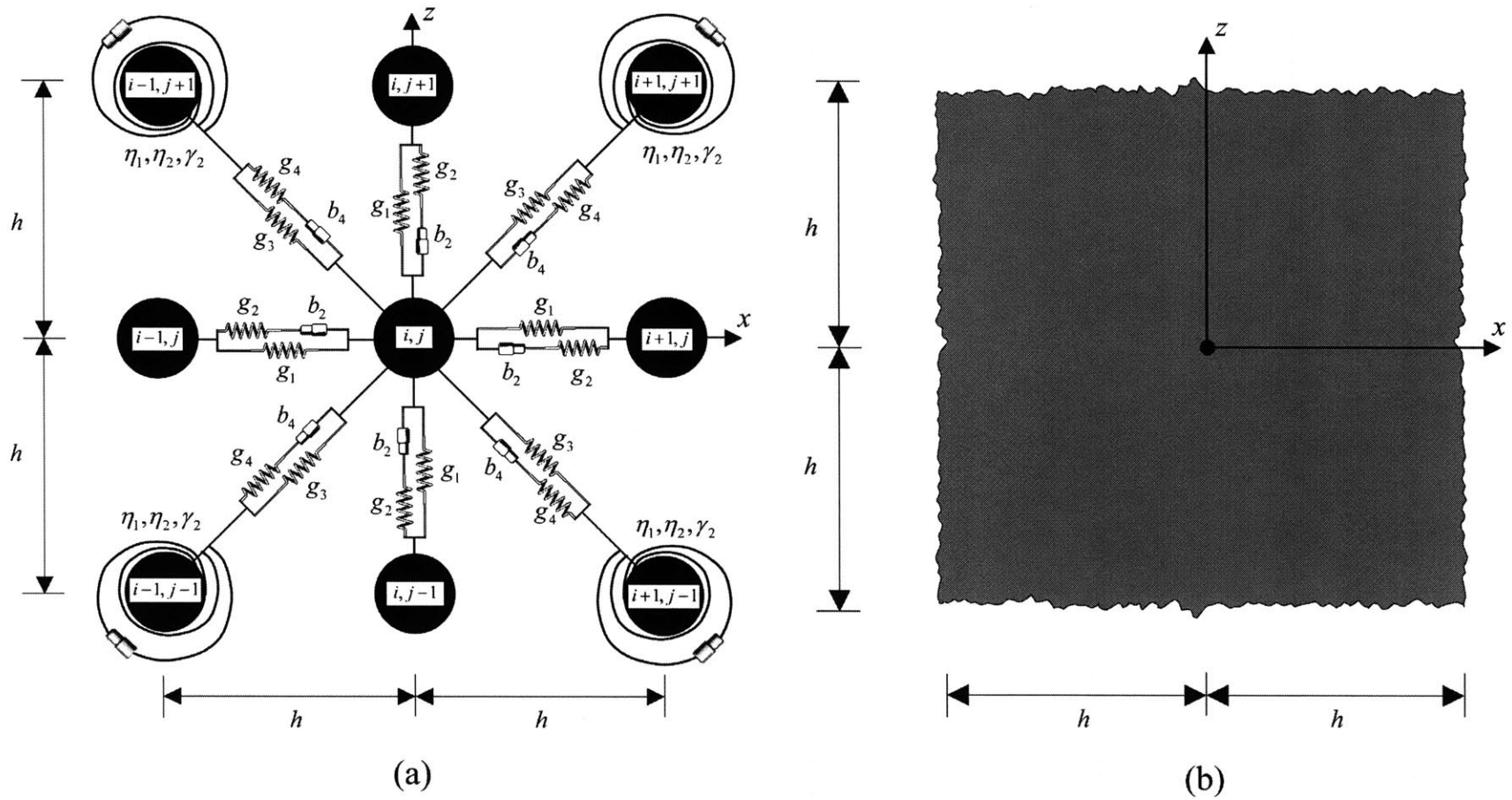


Fig. 4A-1—(a) MSDLM discretization of interior particle at position (i, j) and (b) corresponding continuum element centered at the origin.

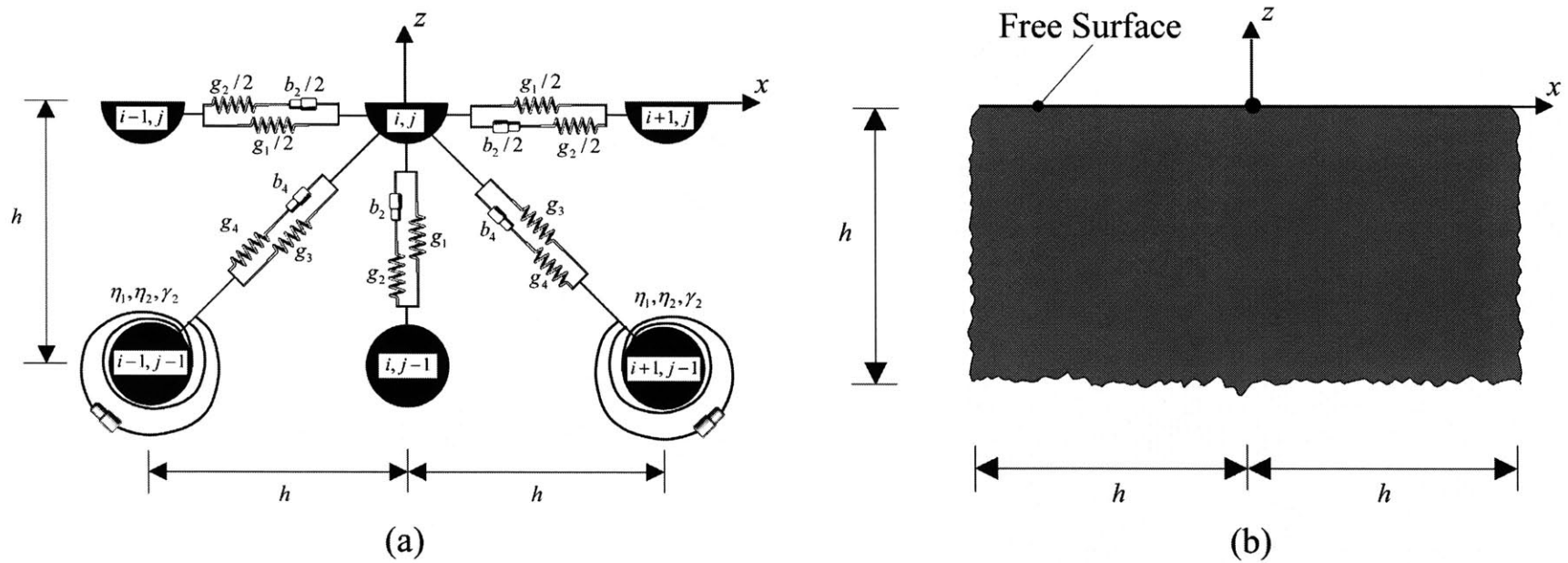


Fig. 4A-2—(a) MSDLM discretization of particle located on free surface at position (i, j) and (b) corresponding continuum element bounded by the origin.

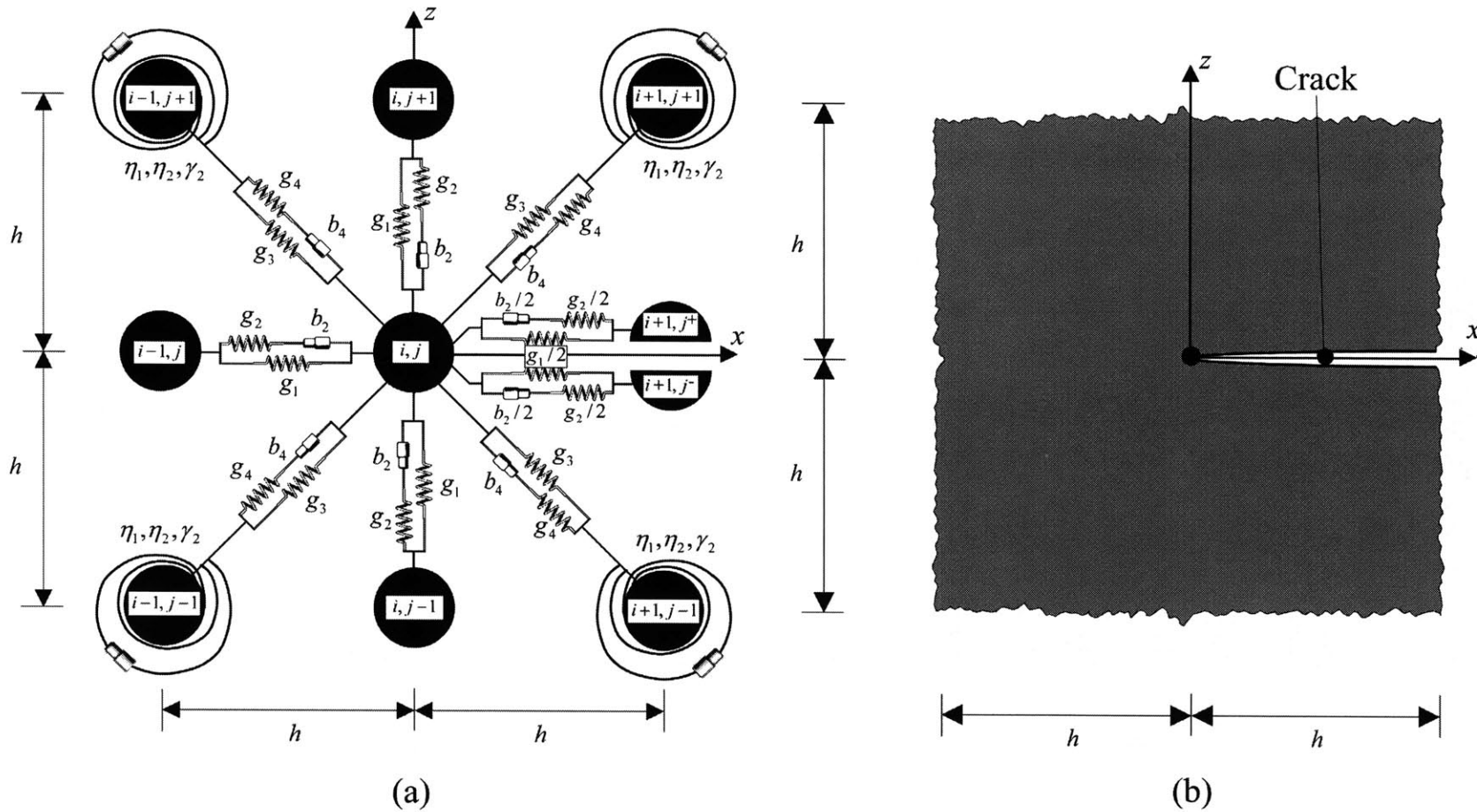


Fig. 4A-3—(a) MSDLM discretization of particle located on tip of horizontal crack at position (i, j) and (b) corresponding continuum element centered at the origin.

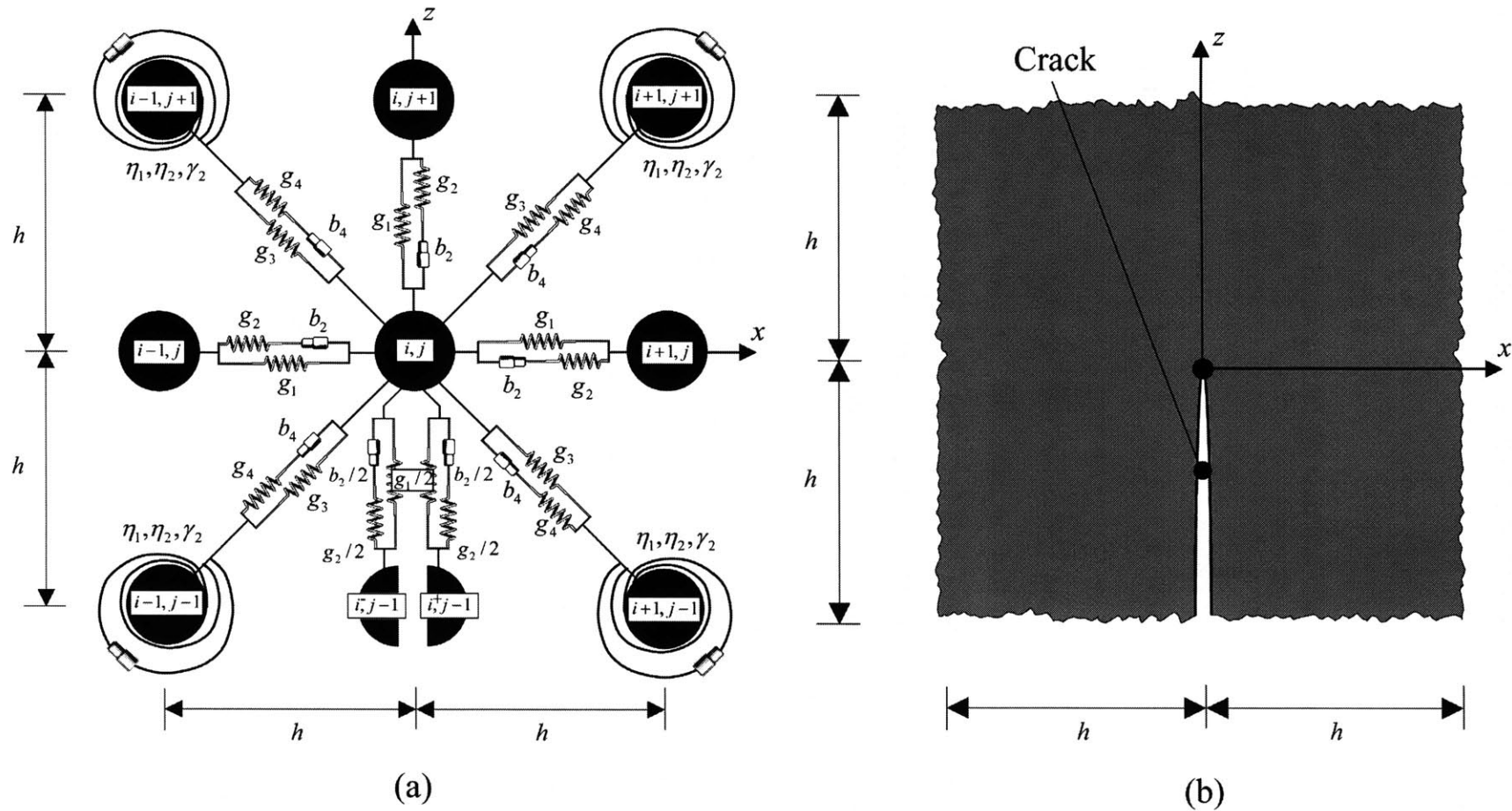


Fig. 4A-4—(a) MSDLM discretization of particle located on tip of vertical crack at position (i, j) and (b) corresponding continuum element centered at the origin.

APPENDIX 4B—Asymptotic and Numerical Analysis of Scattering and Diffraction of an Incident Longitudinal Wave by a Semi-Infinite Crack

Introduction

Consider an isotropic elastic solid in a state of plane strain having density ρ , Lamè constants λ and μ , and containing a semi-infinite crack that terminates at the origin and lies along the positive x -axis as shown in Fig. 4B-1. An incident harmonic plane P -wave of circular frequency ω and oriented at an angle θ_p with respect to the horizontal, impinges upon the crack edge. The asymptotic analyses of the scattered field (that is, the part of the field that can be treated with geometrical elastodynamics) and the diffracted field (that is, the part of the field that interacts with the crack edge) are given by Achenbach, Gautesen and McMaken [4B-1]. The first section of this appendix summarizes their solutions. The second section is a verification of the mass-spring-dashpot lattice model (MSDLM) [4B-2] applied to crack-tip scattering.

Asymptotic Solution [4B-1]

In this section, as part of the nomenclature conventions, superscripts are used in conjunction with vectors, while subscripts are used in conjunction with scalars. As a special case of scalars, reflection and diffraction coefficient use both superscripts and subscripts, with the superscripts indicating the incident form of irradiation and subscripts indicating the reflected form of irradiation.

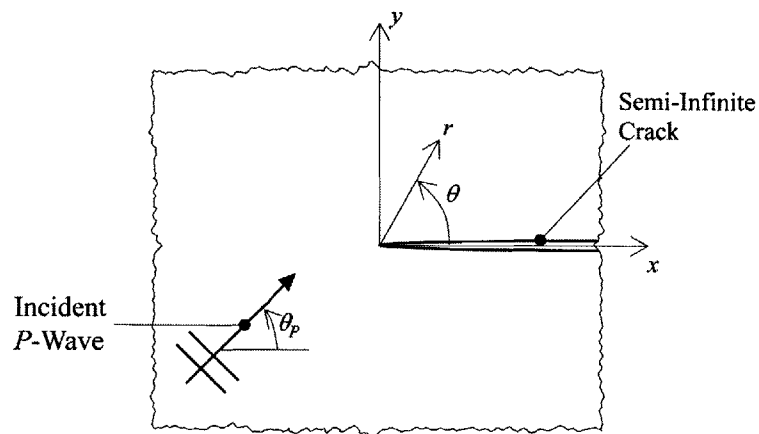


Fig. 4B-1—Schematic of incident plane P -wave impinging on vicinity of tip of semi-infinite crack.

Problem Formulation

The incident field is

$$\mathbf{u}^P = u_{peak} \mathbf{d}^P \exp(\hat{i} k_P \mathbf{p}^P \cdot \mathbf{x}) \quad (4B-1)$$

where u_{peak} is the peak amplitude and script P denotes properties relating to a P -wave,

$$\mathbf{d}^P = (\cos \theta_P, \sin \theta_P) \quad (4B-2)$$

$$\hat{i} = \sqrt{-1} \quad (4B-3)$$

$$k_P = \frac{\omega}{c_P} = \frac{\omega}{\sqrt{(\lambda + 2\mu) / \rho}} \quad (4B-4)$$

and

$$\mathbf{p}^P = (\cos \theta_P, \sin \theta_P) \quad (4B-5)$$

Here, ω is the circular frequency, and throughout the remainder of the section on the steady-state analysis, the time variation $\exp(-\hat{i} \omega t)$ is omitted.

The total field can be written as

$$\mathbf{u}^t = \mathbf{u}^{ge} + \mathbf{u}^d \quad (4B-6)$$

where the superscripts t , ge and d represent the total, geometrical elastodynamic, and diffracted fields, respectively.

Geometrical Elastodynamic Field

The geometrical elastodynamic field is

$$\begin{aligned} \mathbf{u}^{ge} = & u_{peak} \mathbf{d}^P \exp(\hat{i} k_P \mathbf{p}^P \cdot \mathbf{x}) H[\text{sgn}(\theta - \theta_P)] \\ & + u_{peak} R_P^P(\theta_L) \mathbf{d}^{rP} \exp(\hat{i} k_P \mathbf{p}^{rP} \cdot \mathbf{x}) H[\text{sgn}(\theta + \theta_P - 2\pi)] \\ & + u_{peak} R_S^P(\theta_P) \mathbf{d}^{rS} \exp(\hat{i} k_S \mathbf{p}^{rS} \cdot \mathbf{x}) H[\text{sgn}(\theta + \theta_{rS} - 2\pi)] \end{aligned} \quad (4B-7)$$

where $H[\cdot]$ denotes the Heaviside step-function,

$$R_P^P(\theta_P) = \frac{\sin(2\theta_P) \sin(2\theta_{rS}) - \kappa_S^2 \cos^2(2\theta_{rS})}{\sin(2\theta_P) \sin(2\theta_{rS}) + \kappa_S^2 \cos^2(2\theta_{rS})} \quad (4B-8)$$

script rP denotes the properties related to the scattered longitudinal waves,

$$\mathbf{d}^{rP} = (\cos \theta_P, -\sin \theta_P) \quad (4B-9)$$

$$\mathbf{p}^{rP} = (\cos \theta_P, -\sin \theta_P) \quad (4B-10)$$

$$R_S^P(\theta_P) = -\frac{2\kappa_S \sin(2\theta_P) \cos(2\theta_{rS})}{\sin(2\theta_P) \sin(2\theta_{rS}) + \kappa_S^2 \cos^2(2\theta_{rS})} \quad (4B-11)$$

script rS denotes the properties related to the scattered vertically-polarized transverse waves,

$$\mathbf{d}^{rS} = (-\sin \theta_S, \cos \theta_S) \quad (4B-12)$$

$$k_S = \frac{\omega}{c_S} = \frac{\omega}{\sqrt{\mu/\rho}} \quad (4B-13)$$

$$\mathbf{p}^{rS} = (\cos \theta_S, -\sin \theta_S) \quad (4B-14)$$

Here θ_{rS} satisfies

$$\cos \theta_{rS} = \frac{\cos \theta_P}{\kappa_S} \quad (4B-15)$$

$$\kappa_S = \sqrt{\frac{\lambda + 2\mu}{\mu}} = \sqrt{\frac{2 - 2\nu}{1 - 2\nu}} \quad (4B-16)$$

where ν is Poisson's ratio.

Diffracted Field

The diffracted far-field is

$$\begin{aligned} \mathbf{u}^d &= \frac{u_{peak}}{\sqrt{k_P r}} D_P^P(\theta; \theta_P) \mathbf{d}_P^P \exp(\hat{i} k_P r) \\ &+ \frac{u_{peak}}{\sqrt{k_S r}} D_S^P(\theta; \theta_P) \mathbf{d}_S^P \exp(\hat{i} k_S r) \\ &+ u_{peak} D_{RS}^P(\theta_P) \mathbf{d}_{RS}^P \exp(\hat{i} k_R r) \\ &+ u_{peak} D_{RA}^P(\theta_P) \mathbf{d}_{RA}^P \exp(\hat{i} k_R r) \end{aligned} \quad (4B-17)$$

where for the diffraction coefficients of the body waves ($\beta = P, S$)

$$D_\beta^P(\theta; \theta_P) = -\frac{1}{2} \kappa_\beta Z F_\beta^P(\theta) \{E_1^P(\theta_P) E_1^\beta(\theta) G_{S\beta}^P(\theta) + E_2^P(\theta_P) E_2^\beta(\theta) G_{P\beta}^P(\theta)\} \quad (4B-18)$$

Here

$$\kappa_\beta = \frac{c_P}{c_\beta} \quad (4B-19)$$

$$Z = \sqrt{\frac{2}{\pi}} \exp(\hat{i} \frac{\pi}{4}) \quad (4B-20)$$

$$E_1^P(\theta) = \sin(2\theta) \quad (4B-21)$$

$$E_2^P(\theta) = \kappa_S^2 - 2\cos^2\theta \quad (4B-22)$$

$$E_1^S(\theta) = \cos(2\theta) \quad (4B-23)$$

$$E_2^S(\theta) = \sin(2\theta) \quad (4B-24)$$

$$G_{\gamma\beta}^P(\theta) = \sqrt{\cos\theta_p + \kappa_\gamma} \sqrt{\kappa_\gamma - \kappa_\beta \cos\theta} \quad (4B-25)$$

$$F_\beta^P(\theta) = \frac{\kappa_\beta^2}{2(\kappa_S^2 - 1)(\cos\theta_L - \kappa_\beta \cos\theta)H_P^+(\theta_p)H_\beta^-(\theta)} \quad (4B-26)$$

$$H_\beta^\pm(\theta) = (\kappa_R \pm \kappa_\beta \cos\theta)K^+(\pm\kappa_\beta \cos\theta) \quad (4B-27)$$

$$\ln K^+(\xi) = -\frac{1}{\pi} \int_1^{\kappa_S} \frac{1}{\xi + t} \tan^{-1} \left\{ \frac{4t^2 \sqrt{\kappa_S^2 - t^2} \sqrt{t^2 - 1}}{(\kappa_S^2 - 2t^2)^2} \right\} dt \quad (4B-28)$$

$$k_R = \kappa_R k_P \quad (4B-29)$$

and where κ_R is the solution ζ to

$$(\kappa_S^2 - 2\zeta^2)^2 + 4\zeta^2 \sqrt{1 - \zeta^2} \sqrt{\kappa_S^2 - \zeta^2} = 0 \quad (4B-30)$$

The diffraction vectors are

$$\mathbf{d}_p^P = (\cos\theta, \sin\theta) \quad (4B-31)$$

$$\mathbf{d}_s^P = (-\sin\theta, \cos\theta) \quad (4B-32)$$

and the diffraction coefficients of the symmetric and anti-symmetric Rayleigh waves are

$$D_{RS}^P(\theta_p) = -\hat{i} E_2^P(\theta_p) F_0^P \sqrt{\kappa_R - 1} \sqrt{\cos\theta_p + 1} \quad (4B-33)$$

$$D_{RA}^P(\theta_p) = -\hat{i} E_1^P(\theta_L) F_0^P \sqrt{\kappa_R - \kappa_S} \sqrt{\cos\theta_p + \kappa_S} \quad (4B-34)$$

Here

$$F_0^P = \frac{1}{2(1 - \kappa_S^{-2})(\cos\theta_p - \kappa_R)H_P^+(\theta_p)K^+(-\kappa_R)} \quad (4B-35)$$

and the diffraction vectors are

$$\mathbf{d}_{RS}^P = (0, 1) \quad (4B-36)$$

$$\mathbf{d}_{RA}^P = (1, 0) \quad (4B-37)$$

MSDLM Verification

Figure 4-1 is discretized according to the MSDLM [4B-2] and the P and S dispersion coefficients are set to unity to simulate an elastic material. Instead of a harmonic incident P -wave impinging upon the crack, the incident plane P -wave has the form

$$\mathbf{u}^P = u_{peak} \mathbf{d}^P \exp\left[-\frac{1}{2}(k_{P, std. dev.} \xi)^2\right] \cos(k_P \xi) \quad (4B-38)$$

where $k_{P, std. dev.}$ is the standard deviation P -wavenumber, k_P is the center P -wavenumber, and

$$\xi = x \cos \theta_P + y \sin \theta_P - c_P t \quad (4B-39)$$

Thus, at time $t = 0$, the plane containing the peak amplitude interacts with the crack tip. The wavelength of the P -wave corresponding to the center wavenumber is

$$\lambda_P = \frac{2\pi}{k_P} \quad (4B-40)$$

and the minimum effective wavelength, which corresponds to the minimum effective Rayleigh wavelength traveling along the crack face, is

$$\lambda_{min} = \frac{c_R}{c_P} \frac{\lambda_P}{(1 + 3k_{P, std. dev.} k_P^{-1})} \quad (4B-41)$$

where $c_R = c_P \kappa_R^{-1}$. For accuracy, the MSDLM grid space is set as $h = \frac{\lambda_{min}}{20}$.

Figures 4B-2 and 4B-3 show snapshots of the diffracted MSDLM displacement fields due to a plane P -wave having incident angles of 0° and 90° , respectively, in an elastic material having $\nu = 0.30$ when the normalized bandwidth is $k_{P, std. dev.} k_P^{-1} = 1/3$. For clarity, the geometric elastodynamic field (that is, the incident and reflected plane waves) have been subtracted from the images leaving only the waves resulting from the crack tip diffraction. (Because of the incomplete subtraction of the incident and reflected plane waves in Figs. 4B-2 and 4B-3, there are visible displacements two to three orders of magnitude less than the peak displacement.) Here the center circular frequency is equal to $\omega_c = k_P c_P$. The circular P and S wave fronts emanating from the crack tip, as well as the head waves trailing behind the P waves and the Rayleigh waves traveling along the upper and lower faces of the crack can be clearly seen.

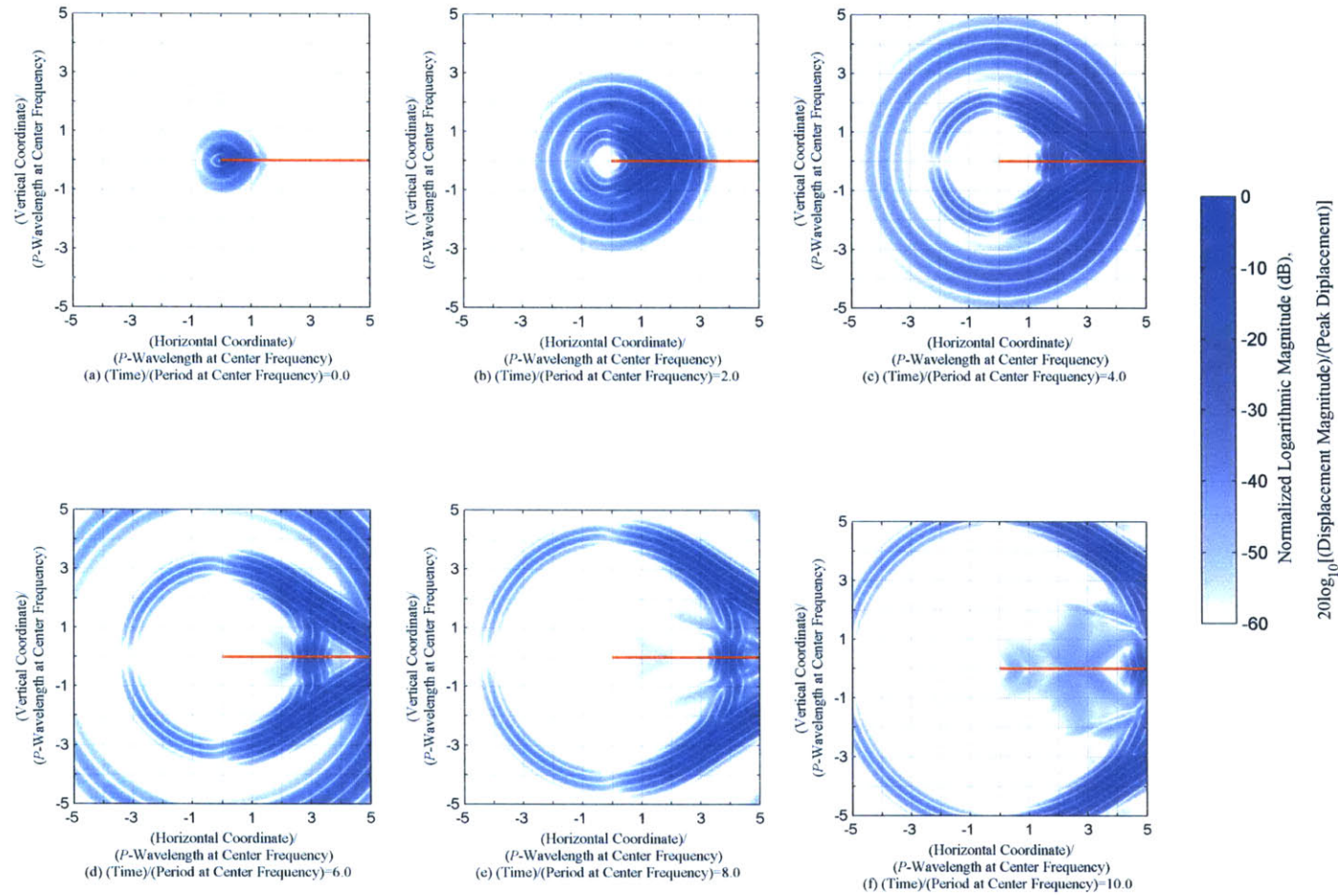


Fig. 4B-2—Snapshots of diffracted waves due to incident P -wave having angle of incidence $\theta_p = 0^\circ$ interacting with semi-infinite crack embedded in elastic solid having Poisson’s ratio $\nu = 0.30$ and where normalized bandwidth of spatial disturbance is $k_{p,\sigma}k_p^{-1} = 1/3$. (Incident plane wave has been subtracted out of images.)

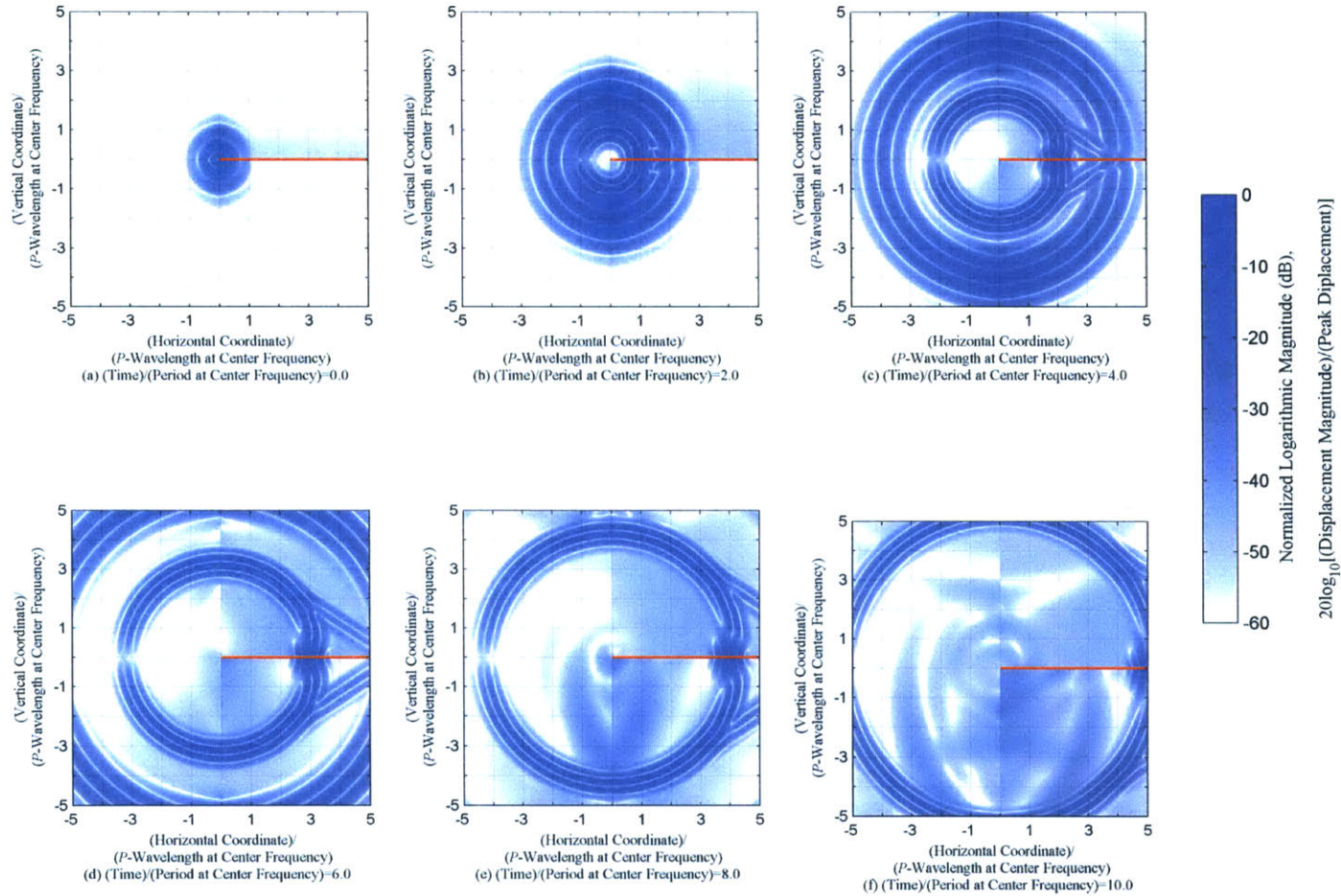


Fig. 4B-3—Snapshots of the diffracted waves due to incident P -wave having angle of incidence $\theta_p = 90^\circ$ interacting with semi-infinite crack embedded in elastic solid having Poisson's ratio $\nu = 0.30$ and where normalized bandwidth of spatial disturbance is $k_{P,\sigma}k_p^{-1} = 1/3$. (Incident and reflected plane waves have been subtracted out of images.)

Figure 4B-4 shows the time histories of the displacement at the crack tip and the radial and tangential displacements at a point located at $r = 4\lambda_p$ and $\theta = 45^\circ$ due to an incident P -wave oriented at $\theta_p = 90^\circ$. The frequency content of each wave packet is found by taking a 1024-point discrete Fourier transform of the displacement history using the time window

$$-\frac{3}{\omega_c} \frac{k_{P, \text{std.dev.}}}{k_P} \leq t \leq \frac{3}{\omega_c} \frac{k_{P, \text{std.dev.}}}{k_P} \quad (4B-42)$$

for the incident wave at the crack tip; the time window

$$\frac{r}{c_P} - \frac{3}{\omega_c} \frac{k_{P, \text{std.dev.}}}{k_P} \leq t \leq \frac{r}{c_P} + \frac{3}{\omega_c} \frac{k_{P, \text{std.dev.}}}{k_P} \quad (4B-43)$$

for the radial displacement history; and the time window

$$\frac{r}{c_P} \kappa_S - \frac{3}{\omega_c} \frac{k_{P, \text{std.dev.}}}{k_P} \leq t \leq \frac{r}{c_P} \kappa_S + \frac{3}{\omega_c} \frac{k_{P, \text{std.dev.}}}{k_P} \quad (4B-44)$$

for the transverse displacement history. The respective discrete Fourier transforms of the incident wave, the radial displacement, and the transverse displacement are denoted as $U_i(\omega)$, $U_r(\omega)$,

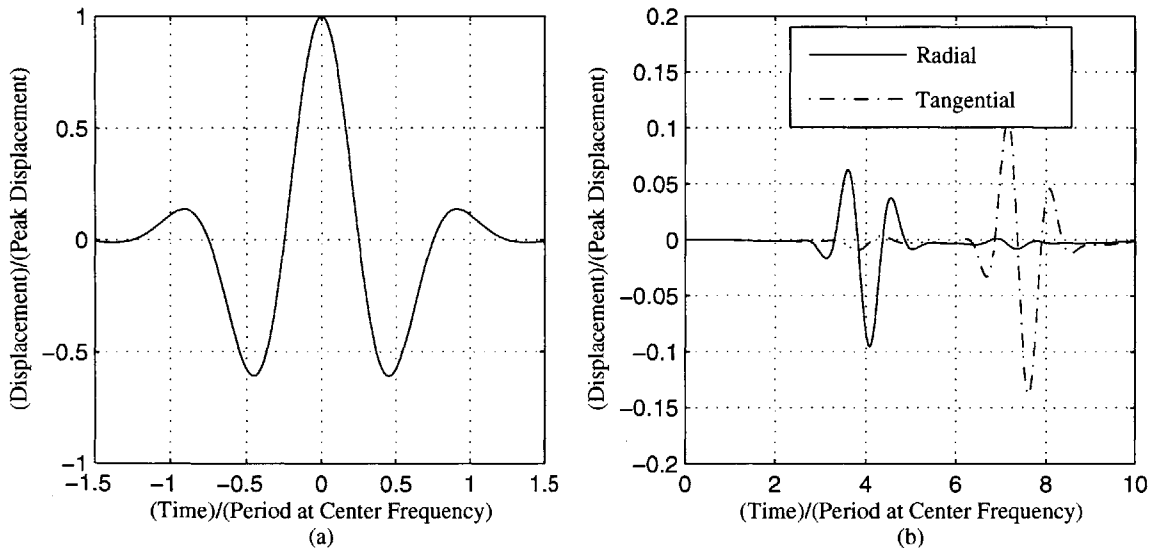


Fig. 4B-4—Displacement time histories at (a) crack tip of incident wave and (b) radial and tangential displacements of diffracted wave at radius of four P -wavelengths and angle $\theta = 45^\circ$. Here displacements are due to incident P -wave having angle of incidence $\theta_p = 90^\circ$ interacting with semi-infinite crack embedded in elastic solid having Poisson's ratio $\nu = 0.30$ and where normalized bandwidth of spatial disturbance is $k_{P, \text{std.dev.}} k_P^{-1} = 1/3$.

and $U_i(\omega)$. The absolute value of the MSDLM diffraction coefficients are formed according to

$$\left|D_P^p(\theta; \theta_p, \nu)\right|_{MSDLM} = \sqrt{k_p r} \frac{|U_r(\omega_c)|}{|U_i(\omega_c)|} \quad (4B-45)$$

$$\left|D_S^p(\theta; \theta_p, \nu)\right|_{MSDLM} = \kappa_S \sqrt{k_p r} \frac{|U_t(\omega_c)|}{|U_i(\omega_c)|} \quad (4B-46)$$

Figures 4B-5 and 4B-6 compare the asymptotic diffraction coefficients, eqn. (4B-17), and MSDLM diffraction coefficients at angles of incidence $\theta_p = 0^\circ$ and $\theta_p = 90^\circ$, respectively, for a material having $\nu = 0.30$. The MSDLM measurements are shown at $r \approx 3\lambda_p$, $r \approx 4\lambda_p$, and $r \approx 5\lambda_p$. The P -wave diffraction coefficients are in excellent qualitative agreement with the asymptotes. The S -wave diffraction coefficients are in excellent qualitative agreement with the asymptotes in the range of $55^\circ < \theta < 305^\circ$. In the ranges $0^\circ < \theta < 55^\circ$ and $305^\circ < \theta < 360^\circ$, the S -wave fronts are interfered by the head waves and Rayleigh waves (e.g., see Figs. 4-2e and 4-3e) that result in the oscillation of the computed S -wave diffraction coefficients. If the head waves and Rayleigh waves were effectively subtracted out of the images, the MSDLM simulations would achieve a better agreement with asymptotic solutions.

References:

- 4B-1. J.D. Achenbach, A.K. Gautesen and H. McMaken. *Ray Methods for Waves in Elastic Solids*. pp. 109-132, 146-147. Pitman Advanced Publishing Program, Boston (1982).
- 4B-2. A.F. Thomas, H. Yim, and J.H. Williams, Jr. submitted for publication (2005).

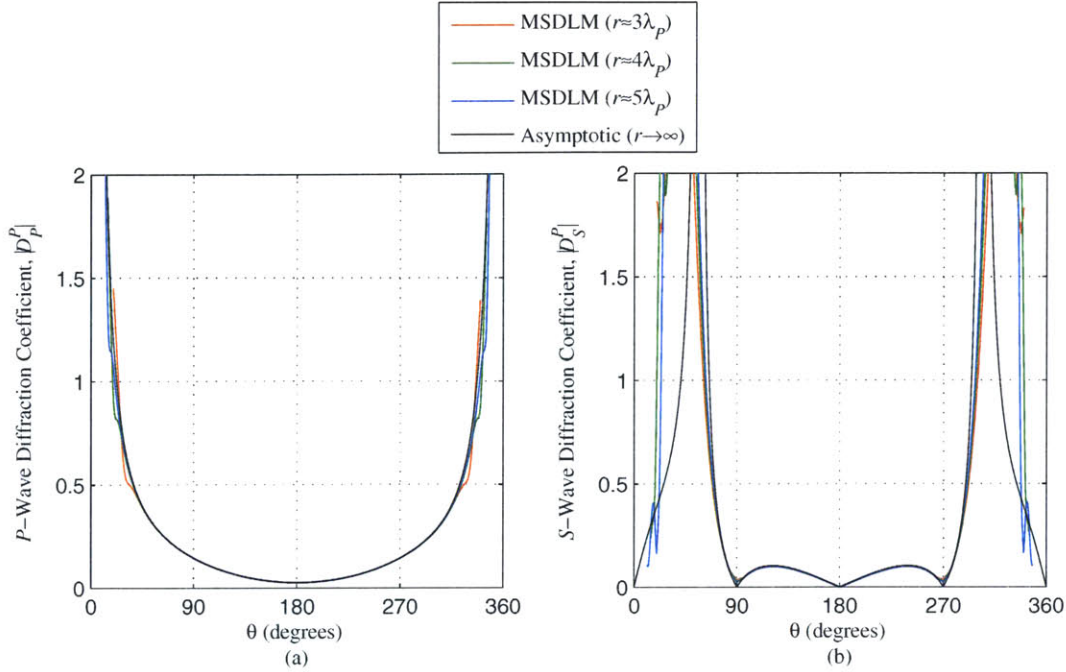


Fig. 4B-5—Comparison of asymptotic [B-1] and MSDLM (a) P -wave diffraction coefficient and (b) S -wave diffraction coefficient due to incident P -wave having angle of incidence $\theta_p = 0^\circ$ interacting with semi-infinite crack embedded in elastic solid having Poisson's ratio $\nu = 0.30$ and where normalized bandwidth of spatial disturbance is $k_{P, std. dev.} k_P^{-1} = 1/3$. MSDLM measurements are taken at radii approximately three, four, and five P -wavelengths λ_p .

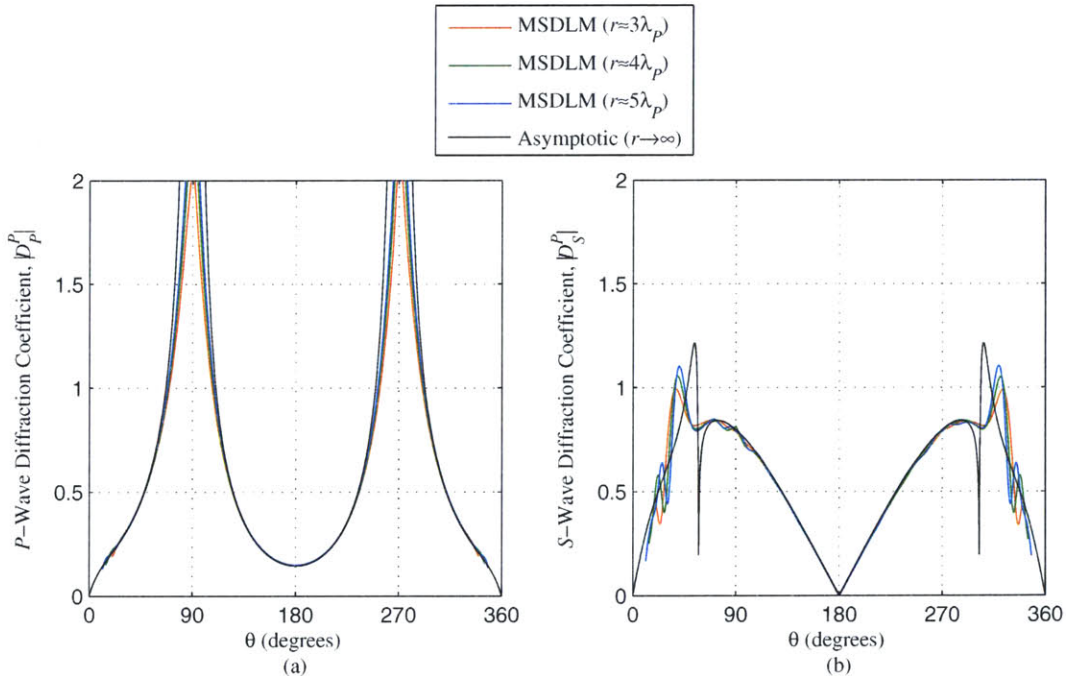


Fig. 4B-6—Comparison of asymptotic [B-1] and MSDLM (a) P -wave diffraction coefficient and (b) S -wave diffraction coefficient due to incident P -wave having angle of incidence $\theta_p = 90^\circ$ interacting with semi-infinite crack embedded in elastic solid having Poisson's ratio $\nu = 0.30$ and where normalized bandwidth of spatial disturbance is $k_{P, std. dev.} k_P^{-1} = 1/3$. MSDLM measurements are taken at radii approximately three, four, and five P -wavelengths λ_p .

APPENDIX 4C—Spectral Analysis of Transient Relative Vertical Surface Displacement

Consider a half-space ($z < 0$) composed of a hypothetical polymeric composite having a 60% volume fraction of CNTs [4C-1] subject to ultrasonic interrogation. Table 4C-1 summarizes the orders of magnitude for the various parameters for the ultrasonic interrogation of the nanocomposite.

The transient surface displacement relative to a pristine half-space, $w_{relative}(x, t)$, due to a narrow-banded concentrated surface load (center frequency f_c) is analyzed for its wavenumber and frequency content via a spatial discrete Fourier transform (DFT) [4C-2]. According to Parseval's relation [4C-2], the sum of the squares of $w_{relative}(x, t)$ and its corresponding two-dimensional DFT, $W_{relative}(k, f)$, are related by

$$\sum_{p=1}^{N_x} \sum_{q=1}^{N_t} |w_{relative}(x_p, t_q)|^2 = \frac{1}{N_k N_f} \sum_{r=1}^{N_k} \sum_{s=1}^{N_f} |W_{relative}(k_r, f_s)|^2 \quad (4C-1)$$

where N_x is the number of horizontal grid points, N_t is the number of time points, N_k is the number points used in the spatial DFT ($N_k \geq N_x$), and N_f is the number points used in the temporal DFT ($N_f \geq N_t$). Further,

$$x_p = h \left(p - 1 - \frac{N_x - 1}{2} \right) \quad (4C-2)$$

$$t_q = \Delta t (q - 1) \quad (4C-3)$$

$$k_r = \frac{2\pi}{N_k h} (r - 1) \quad (4C-4)$$

$$f_s = \frac{1}{N_f \Delta t} (s - 1) \quad (4C-5)$$

where h is the grid spacing and Δt is the numerical time step. Because the right-hand side of eqn. (4C-1) is a numerical integration of the spectral “power” density function over the zero wavenumber to the wavenumber corresponding to the Nyquist criterion, π/h , and over the zero frequency to the Nyquist frequency $1/(2\Delta t)$, the quantity described in eqn. (4C-1) is called the spectral “energy”. The total spectral energy is

subdivided into nine designations, which are listed in Table 4C-2.

The nanocomposite half-space is numerically simulated via a MSDLM $N_x \times N_x$ spatial grid over N_t time steps [4C-3]. In the numerical examples that follow, $N_x = N_k = 401$ and $N_t = N_f = 1249$.

Figure 4C-1 shows the spectral energy content subdivisions for two cases: *Case One* is a vertical semi-infinite crack terminating at coordinates $x' = -2.5\lambda_R$ and $z' = -5\lambda_R$, *Case Two* is a horizontal semi-infinite crack terminating at coordinates $x'' = -2.5\lambda_R$ and $z'' = -5\lambda_R$, where λ_R is the Rayleigh wavelength at the center frequency. It is noted that $L_k M_f$ dominates the spectral energy content for both *Cases One* and *Two*. The five designations containing high-range wavenumber or high-range frequency— $L_k H_f$, $M_k H_f$, $H_k H_f$, $H_k M_f$ and $H_k L_f$ —are more than two orders of magnitude below $L_k M_f$ and can thus be neglected.

References:

- 4C-1. C.E. Harris, C.E., M.J. Shuart and H.R. Gray. *SAMPE J.* **38**:33 (2002).
- 4C-2. A.V. Oppenheim and R.W. Schafer. *Discrete-Time Signal Processing*, pp. 559-588, 621. Prentice Hall, Upper Saddle River, New Jersey, 1999.
- 4C-3. A.F. Thomas, H. Yim and J.H. Williams, Jr. submitted for publication (2005).

Table 4C-1—Orders of magnitude for various parameters involved in ultrasonic interrogation of hypothetical carbon nanotube-based nanocomposite [4C-1].

Material Properties	Density $\rho \sim 10^3 \text{ kg/m}^3$
	P-wave phase velocity $c_p \sim 10^4 \text{ m/s}$
	Poisson's ratio $\nu = 0.30$
	P-wave attenuation $\alpha_p \sim 10 \text{ Np/m}$
	Normalized penetration depth $\frac{\pi}{\alpha_p \lambda_p} = 100$
Interrogation Parameters	Peak line force per unit depth $F_{peak} \sim 100 \text{ N/m}$
	Center frequency $f_c \sim 10^7 \text{ Hz}$
	Normalized bandwidth $f_\sigma / f_c = 1/3$
Output Surface Parameters	Rayleigh wavelength $\lambda_R \sim 10^{-3} \text{ m}$
	Elastic far-field surface displacement $u \sim 10^{-10} \text{ m}$

Table 4C-2—Spectral energy subdivisions in wavenumber-frequency space.

	Low-range wavenumbers $0 \leq k < 0.3k_R$	Mid-range wavenumbers $0.3k_R \leq k < 1.7k_R$	High-range wavenumbers $1.7k_R \leq k < 20k_R$
High-range frequencies $1.7f_c \leq f < 31f_c$	$L_k H_f$	$M_k H_f$	$H_k H_f$
Mid-range frequencies $0.3f_c \leq f < 1.7f_c$	$L_k M_f$	$M_k M_f$	$H_k M_f$
Low-range frequencies $0 \leq f < 0.3f_c$	$L_k L_f$	$M_k L_f$	$H_k L_f$

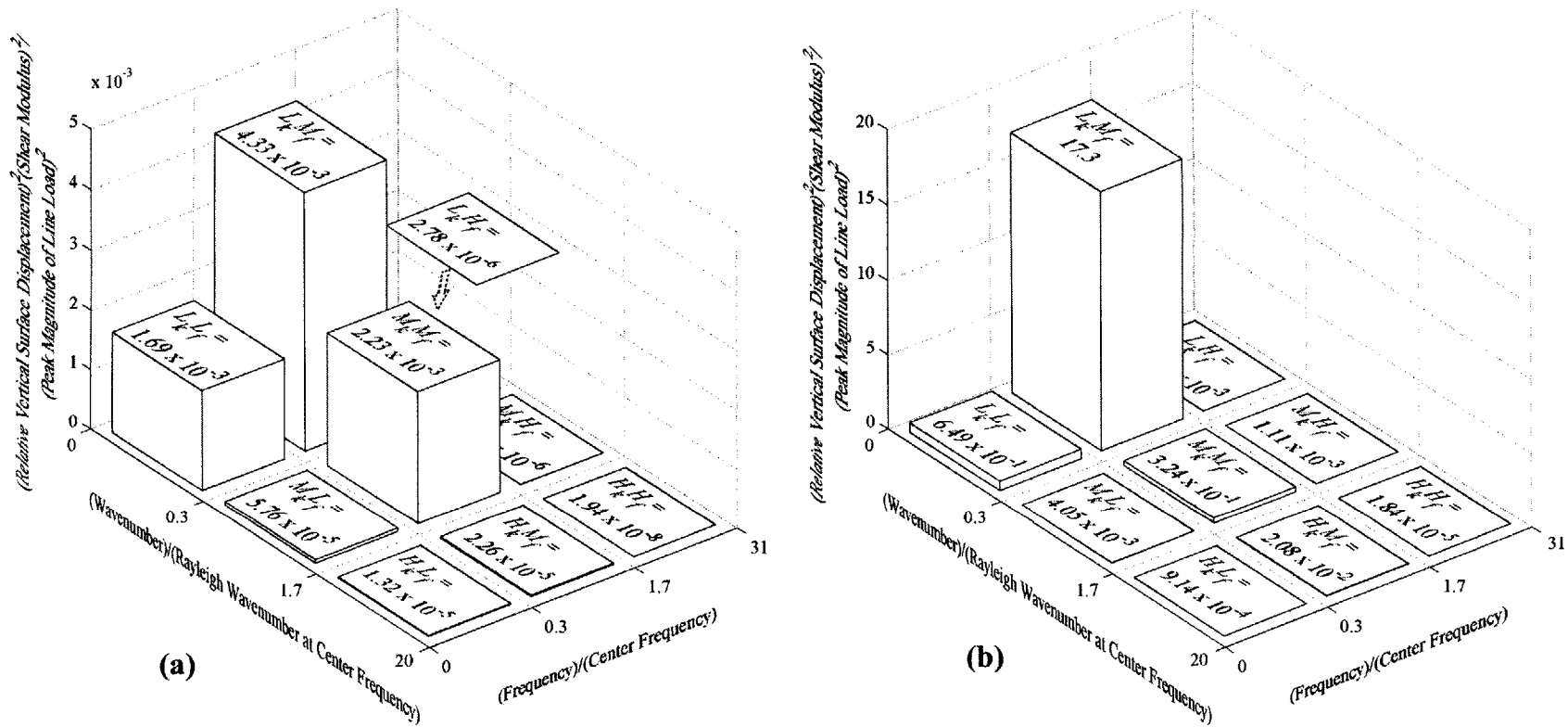


Fig. 4C-1—Spectral energy content of relative vertical surface displacement in wavenumber-frequency space for (a) Case One and (b) Case Two. Spectral energy is subdivided into 9 designations indicially defined by $X_k Y_f$, where X and Y can be any of L (low-range), M (mid-range), or H (high-range), and where k is wavenumber and f is frequency.

CHAPTER 5: THESIS CONCLUSION

CONTENTS:

5-1	Summary of Achievements.....	207
5-2	Recommendations.....	207

5-1 SUMMARY OF ACHIEVEMENTS

This thesis detailed the development of a computational lattice model, called the mass-spring-dashpot lattice model (MSDLM), to simulate and visualize ultrasonic wave phenomena in attenuating materials. This development involved an investigation of numerical errors inherent in the elastic model upon which the MSDLM is based, the mass-spring lattice model (MSLM). Finally, mass-spring-dashpot lattice models were used in the theoretical nondestructive evaluation of subsurface cracks in an attenuating nanocomposite. The main contributions of the thesis are summarized in the following points.

- The MSLM convergence of phase speed for plane waves traveling at oblique angles was investigated.
- The formulation and verification of correction terms for the precise implementation of MSLM traction boundaries was presented.
- The stress-dynamic equations for a standard linear solid viscoelastic model and its accompanying dispersion relations were derived.
- The formulation of the MSDLM for the simulation and visualization of ultrasonic wave phenomena in attenuating materials containing reflecting and absorbing boundaries was introduced.
- The nondestructive evaluation of subsurface cracks in an attenuating nanocomposite was modeled via lattice methods.

5-2 RECOMMENDATIONS

Lattice modeling can provide a framework for the effective simulation and visualization for engineering problems that are outside the scope of this thesis. Recommendations for further refinement of the MSDLM include:

- Development of MSDLM for anisotropic media.
- Development of MSDLM containing a fractional derivative dashpot to allow for more realistic attenuation modeling.

Recommendations for further applications of MSDLM include:

- Investigation of subsurface cracks of finite length.
- Investigation of distributed anomalies.

